Study on Cyber-physical System for Direct Current Circuit Breaker Based on Atmospheric Arc Plasma Movement

Tokyo City University

Graduate School of Integrative Science and Engineering

Electrical Engineering and Chemistry

High Current and Energy DX Laboratory

2091201 Zhenwei Ren

March 2023

Content

Symbol

A [A·m^{-2}·K^{-2}]	: Richardson-Dushman constant
$A_{x,y,z}$ [T·m]	: Vector potential (subscript indicating direction)
$B_{x,y,z}$ [T]	: Magnetic flux density (subscript indicating direction)
C [%]	: Contaminate proportion of metal vapor
C_p [J·kg^{-1}·K^{-1}]	: Constant pressure specific heat
D [m^2·s^{-1}]	: Diffusion coefficient
e [C]	: Elementary charge
$E_{x,y,z}$ [V·m^{-1}]	: Electric field (subscript indicating direction)
E_{Air} [eV]	: Ionization energy of air
E_{eh} [J]	: Energy exchange between the electrons and heavy particles
F [V·m^{-1}]	: Electric field applied on the electrode surface
g [m·s^{-2}]	: Gravitational acceleration
h [J·kg]	: Enthalpy
h_{arc} [W·m^{-2}·K^{-1}]	: Heat transfer coefficient
h_P [J·s]	: Planck constant
I [A]	: Arc current
$j_{x,y,z}$ [A·m^{-2}]	: Current density (subscript indicating direction)
J_F [A·m^{-2}]	: Current density derived from the field emission
J_T [A·m^{-2}]	: Current density derived from the thermal emission
k [J·K^{-1}]	: Boltzmann constant
L [m]	: Arc length
L_{vol} [m]	: Thickness of the control volume of the gas on the electrode surface
m_{Cu} [kg]	: Generated mass of Cu
m_e [kg]	: Weight of an electron
m_h [kg]	: Mass of a heavy particles
M [kg·mol^{-1}]]	: Atomic weight
M_{air} [kg·mol^{-1}]	: Molecular weights of air
M_{Cu} [kg·mol^{-1}]	: Molecular weights of Cu
n_A	: Vertical direction of anode surface
n_C	: Vertical direction of cathode surface
n_{Cu} [kg·m^{-3}·s^{-1}]	: Condensation rate of Cu
n_e [m^{-3}]	: Density of electrons
n_h [m^{-3}]	: Number density of heavy particles

P [Pa] : Pressure
P_{atm} [Pa] : Atmospheric pressure
P_v [Pa] : Saturation vapor pressure
q_A [W·m^{-2}] : Enthalpy flux on anode surface
q_C [W·m^{-2}] : Enthalpy flux on cathode surface
Q_{Cu} [J·kg^{-1}] : Heat of the phase change for Cu
Q_{rad} [W·m^{-3}] : Radiation power
R [Ω] : Arc resistance
R_C [kg·m^{-3}·s^{-1}·K^{-1}] : Coefficient of the condensation rate
S [m^2] : Arc cross-sectional area
S [W·m^{-3}] : Energy source term of vaporization and condensation on the electrode surface
t [s] : Time
T [K] : Temperature
T_A [K] : Temperature of anode surface
T_C [K] : Temperature of cathode surface
T_{Cu} [K] : Boiling point of Cu
T_e [K] : Electron temperature
T_h [K] : Heavy particles temperature
T_{vol1} [K] : Temperature of vol_1
u [m·s] : Flow velocity of X direction
U [V] : Arc voltage
U_s [V] : Electrode fall voltage
V_{arc} [V/m·s] : Increment rate of the arc voltage per unit length
v [m·s] : Flow velocity of Y direction
v_{Cu} [kg·m^{-3}·s^{-1}] : Vaporization rate of Cu
vol_1 [m^3] : Volume of the control volume of the gas on the electrode surface
vol_2 [m^3] : Volume of the control volume of the electrode on the electrode surface
w [m·s] : Flow velocity of Z direction
y [m] : Location of Y direction
x [m] : Location of X direction
z [m] : Location of Z direction
α[W·m^{-2}·K^{-4}] : Stefan-Boltzmann constant
β_{air} : Dimensionless constants of air
β_{Cu} : Dimensionless constants of Cu
Δt [s] : Time step
Δy [m] : Sheath thickness
$\Delta\phi$ [eV] : Schottky effect
ε_0 [F·m^{-1}] : Permittivity of free space
ε_A : Surface emissivity of the anode
ε_C : Surface emissivity of the cathode
η_{air} : Viscosity coefficients of air
η_{Cu} : Viscosity coefficients of Cu
κ [W·m^{-1}·k^{-1}] : Thermal conductivity
λ_D [m] : Debye length
μ [H·m^{-1}] : Magnetic permeability

ρ_0 [kg·m^{-3}] : Mass density at 300 K
ρ_{air} [kg·m^{-3}] : Mass density of air
ρ_{Cu} [kg·m^{-3}] : Mass density of Cu
ρ [kg·m^{-3}] : Mass density
σ [S·m^{-1}] : Electrical conductivity
σ_{arc} [S] : Arc electrical conductivity
σ_{eff} [S·m^{-1}] : Effective electrical conductivity
ϕ [V] : Potential
ϕ_A [eV] : Work function of anode
ϕ_C [eV] : Work function of cathode
ϕ_{Ce} [eV] : Effective work function of cathode
ϕ_S [V] : Electric potential of the sheath edge
ϕ_W [V] : Electric potential of the electrode surface
$\pi\overline{\Omega_{eh}}$ [m^2] : cross-section between the electrons and the heavy particles

Chapter1 Introduction

1.1 Conception diagram of Society 6.0

Following the hunting society (Society 1.0), agricultural society (Society 2.0), industrial society (Society 3.0), and information society (Society 4.0), it was proposed to construct the current society (Society 5.0) by highly integrating cyber space and physical space, which final goal is to solve social problems while ensuring economic development [1]. However, what will the future society (Society 6.0) be like after the solve problems were solved and the economy was developed? It should be a society full of opportunity and excitement supported by sustainable infrastructure. Then, it will lead to another question, what is a sustainable infrastructure? The sustainable infrastructure should be constructed by the next-generation products according to IoT technology [2] and M2M technology [3], which can able to provide a sufficient and unlimited environment for us to enjoy our life. Naturally, it will get to the question of how to create the next-generation product? Throughout the past and present, great products have always been created by the fusing of knowledge from different fields. Obtaining knowledge of a specific field requires someone to dive into the fundamental phenomenon and fully utilize existing technology, then become an expert. Based on the above discussion, the conception diagram of Society 6.0 can be expressed as Fig. 1.

To be more specific, the construction of Society 6.0 should be started by different individuals, who locate their interested field and try to become an expert in that field. Then, the next-generation products can be generated through the cooperation and inspiration of knowledge from different fields. Those next-generation products will connect and constitute a sustainable infrastructure, which can provide a sufficient and unlimited environment for us to enjoy a life full of opportunity and excitement. This process will form a positive circle to create Society 6.0.

In this study, the development of the next-generation direct current circuit breaker (DCCB) was focused on. This study was divided into three phases, the first phase was developing the numerical simulation based on the experimental data and figures, which implemented the transformation from the physical space to the cyber space. The second phase was analyzing the arc plasma movement and its physical properties variation under various circumstances in cyber space. The third phase was constricting the AI models to improve the data analysis efficiency and reduce the cost. Moreover, the concept of a cyber-physical system for developing the next-generation DCCB was proposed based on the obtained research achievements.

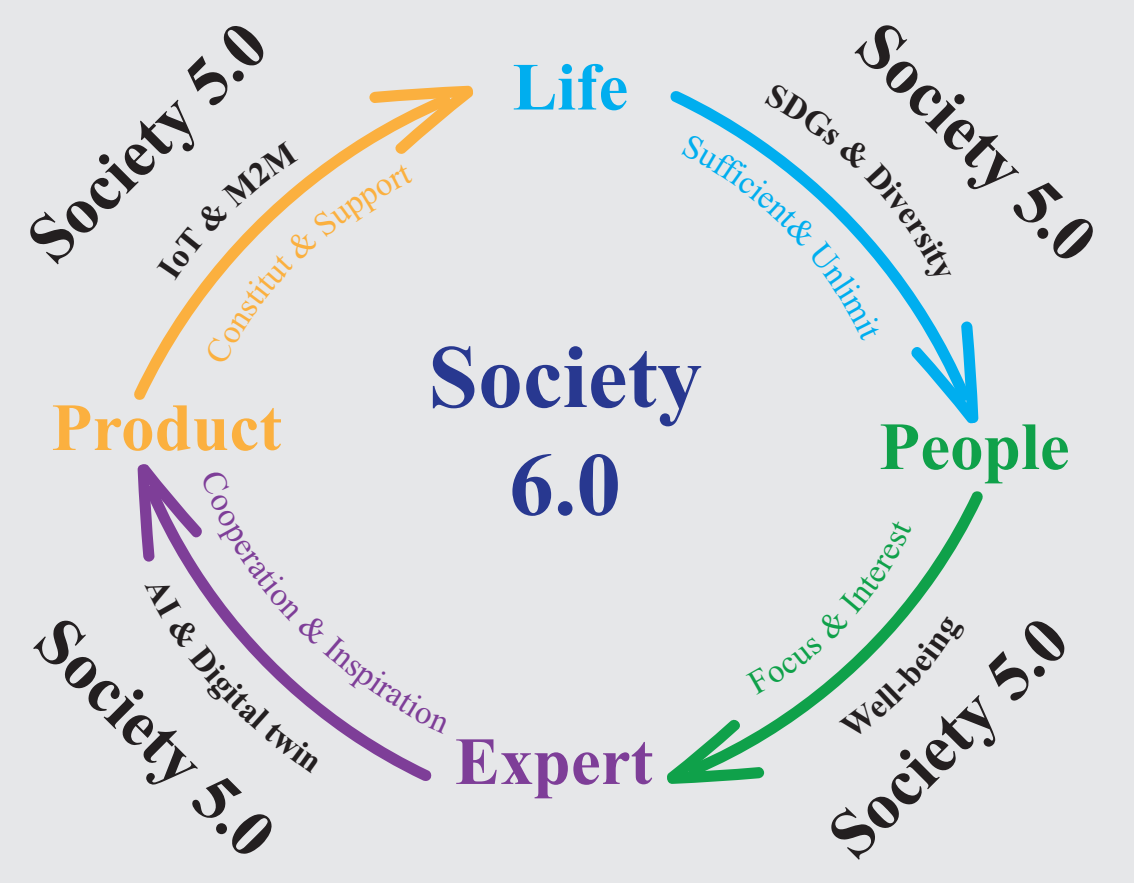

Fig. 1 Conception diagram of Society 6.0.

1.2 Application instances of DCCB and problems

As the fourth state of matter, the research and application of plasma status have a long history and mainly focused on two fields, which are stable control (such as arc welding [4], arc plasma torch [5], arc therapy [6], and so on) and rapidly extinguish (such as circuit breaker [7][8][9]).

This study focuses on the direct current circuit breaker (DCCB) which is primarily used in electric railway systems [10][11][12], electric vehicle [13][14][15][16], solar photovoltaic system [17][18], and so forth. In the case of fault, the moving contact departs from the fixed contact and an arc will be generated between them. Under the influence of its magnetic field, the arc shifts from the contacts to the arc runner and moves toward the splitter plates. Because of the electrode voltage drop and arc length increment, the total voltage of the arc will increase and lead to arc quenching. The most priority object of the DCCB is to extinguish the arc as rapidly as possible, which means that the behavior of the arc plasma is the fundamental key factor in determining the performance of the DCCB. Much research about the arc plasma movement and its physical property variation was reported [19][20][21][22][23][24][25].

In general, there are three phases of the arc plasma during the interruption process of DCCB, which are arc generation, arc motion, and arc re-strike as shown in Fig. 2. When the failure current is detected, the connected cathode and anode electrode depart and a molten metal bridge forms between them [26][27]. The temperature of the molten metal bridge and the electrode surface increase because of the Joule heating, and the molten metal bridge explodes along with the arc plasma generates in this area [28][29][30]. Those phenomena occur during the electrode opening process and are defined as the arc generation phase in this study as shown in Fig. 2(a). After the arc plasma generation, it stagnates in the inter-electrode area and causes serious damage to the electrode while remaining the flow of the failure current. For interrupting the failure current, it had been proposed to apply an external magnetic field to drive the arc plasma into the extinguished chamber [31][32][33][34]. These processes are defined as the arc motion phase in this study as shown in Fig. 2(b). However, the arc plasma sometimes re-strikes back to the inter-electrode area, because of the residue of metal vapor and high-temperature gas as shown in Fig. 2(c-1). Sometimes, the arc plasma reignites after its extinguished, because of the existence of electrical potential differences between electrodes as shown in Fig. 2(c-2). These phenomena are defined as the arc re-strike phase in this study as shown in Fig. 2(c).

The improvement of DCCB technology is focusing on four aspects. The first is to decrease the interrupt time which is the rapidity characteristic. The second is to prevent the occurrence of a re-strike phenomenon which is the reliability characteristic. The third is to interrupt the large failure current which is the high capacity characteristic. Forth is to implement the interruption process in a small space which is the miniaturization characteristic. However, the above four characteristics are difficult to simultaneously satisfied.

In the application of DCCB in the electric railway system, the consideration of miniaturization characteristics is usually neglected, because it is set at a specified location. DCCB for electric railway systems usually interrupts the failure current at kilo amperes level which satisfies the

high capacity characteristic. However, it usually needs to interrupt the arc plasma several times in one single interruption, because the arc reignites after its extinguish due to the residue of high-temperature gas and metal vapor at the ignition location, which leads to the satisfaction of rapidity and reliability characteristics become its priority.

The miniaturization characteristic is the most important factor of DCCB when it is applied in an electric vehicle because the serval DCCBs are assembled. For achieving the fast charging technology to reduce the charging time, it is crucially to develop a DCCB able to interrupt large charging current when a failure occurred. However, the arc plasma tends to stagnate in the inter-electrode area at the large current situation, because of space insufficient for stretching the arc plasma. Hence, the satisfaction of high capacity characteristics is its priority, and the focus on rapidity and reliability characteristics becomes second.

Based on the above explanation and the problems of the current DCCB, it is essential to develop a next-generation DCCB that simultaneously satisfies the rapidity, reliability, miniaturization, and high-capacity characteristics of various application scenarios.

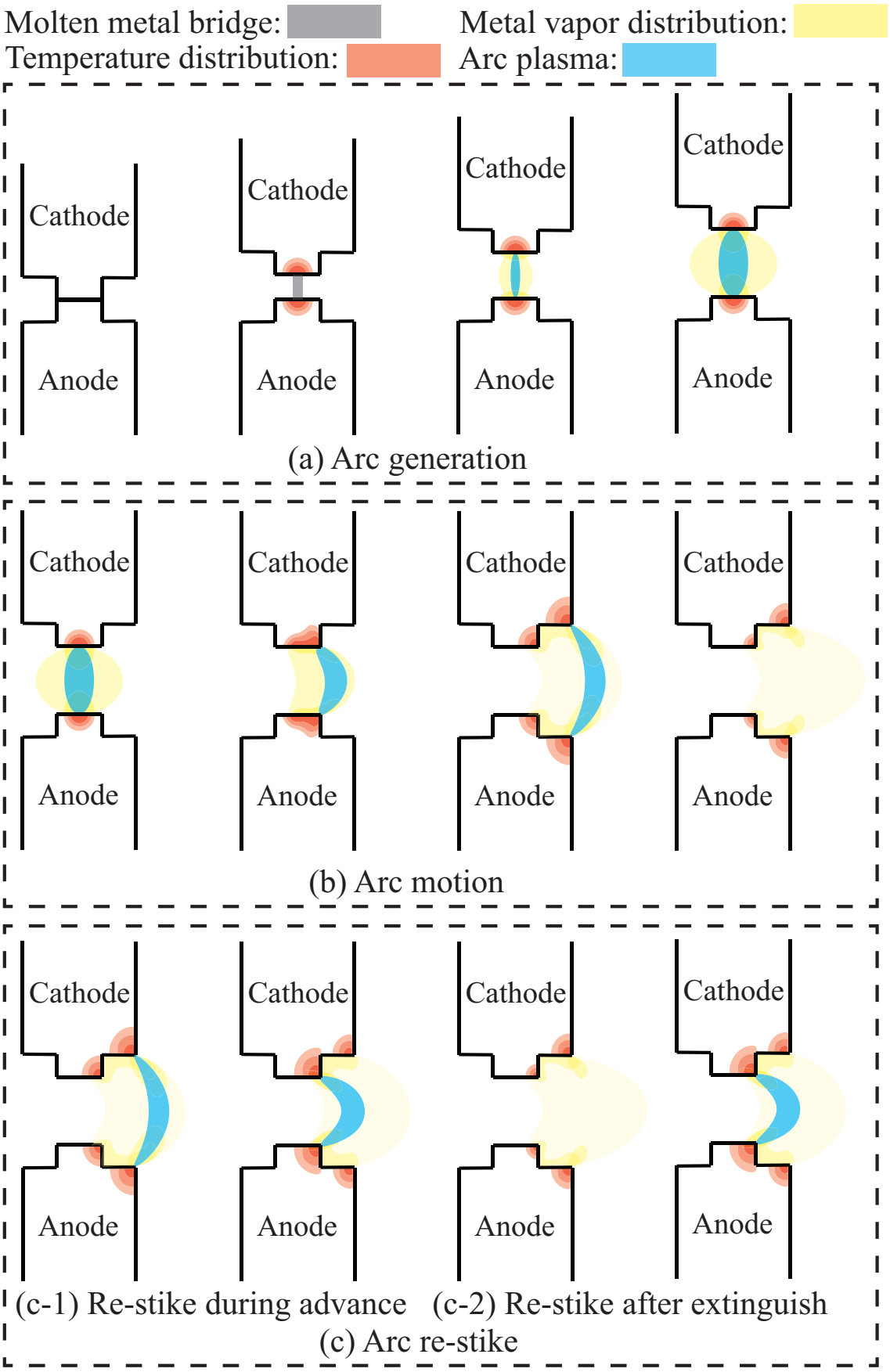

Fig. 2 Schematic of three phases of DCCB during interruption process.

1.3 Expected performances and modern manufacturing method of next-generation DCCB

Recently, there has rapid advancement in the development process of digital transformation for shortening the manufacturing cycle and promoting the product iteration in smart manufacturing [35] as shown in Fig. 3. The efficiency of design and prototyping, as the most time-consuming parts of the manufacturing cycle, needs to be significantly improved with the assistance of big data [36] and digital twin technology [37].

For the fabrication of a next-generation DCCB, four characteristics need to be achieved: rapidity, reliability, high capacity, and miniaturization. It is necessary to elucidate the mechanism of arc plasma movement and the variation in its physical properties variation in a DCCB for constructing an accurate virtual model using the digital twin technology, which can provide guidelines for production design. For achieving the construction of a digital twin technology for developing the next-generation DCCB, firstly, the elucidation of fundamental arc plasma movement (cathode spot, anode spot, and arc column) and its physical property variation are essential. Hence, a three-dimensional electromagnetic thermal fluid simulation program was developed, and movements of arc plasma in parallel electrodes with different intensities of external magnetic field applications were simulated. Secondly, the interruption process of arc plasma based on the actual product was implemented under various conditions.

After elucidating the fundamental arc plasma movement and its physical property variation, it is necessary to establish a database of various DCCB interruption circumstances. Because of the large amount of analytical work, an artificial intelligence (AI) model was constructed for differentiating the interruption results to improve the analysis efficiency. Further, another AI model was constructed to predicate the interruption result based on the preliminary stage of the simulation result, which can decrease the requirement of calculation consuming time and power.

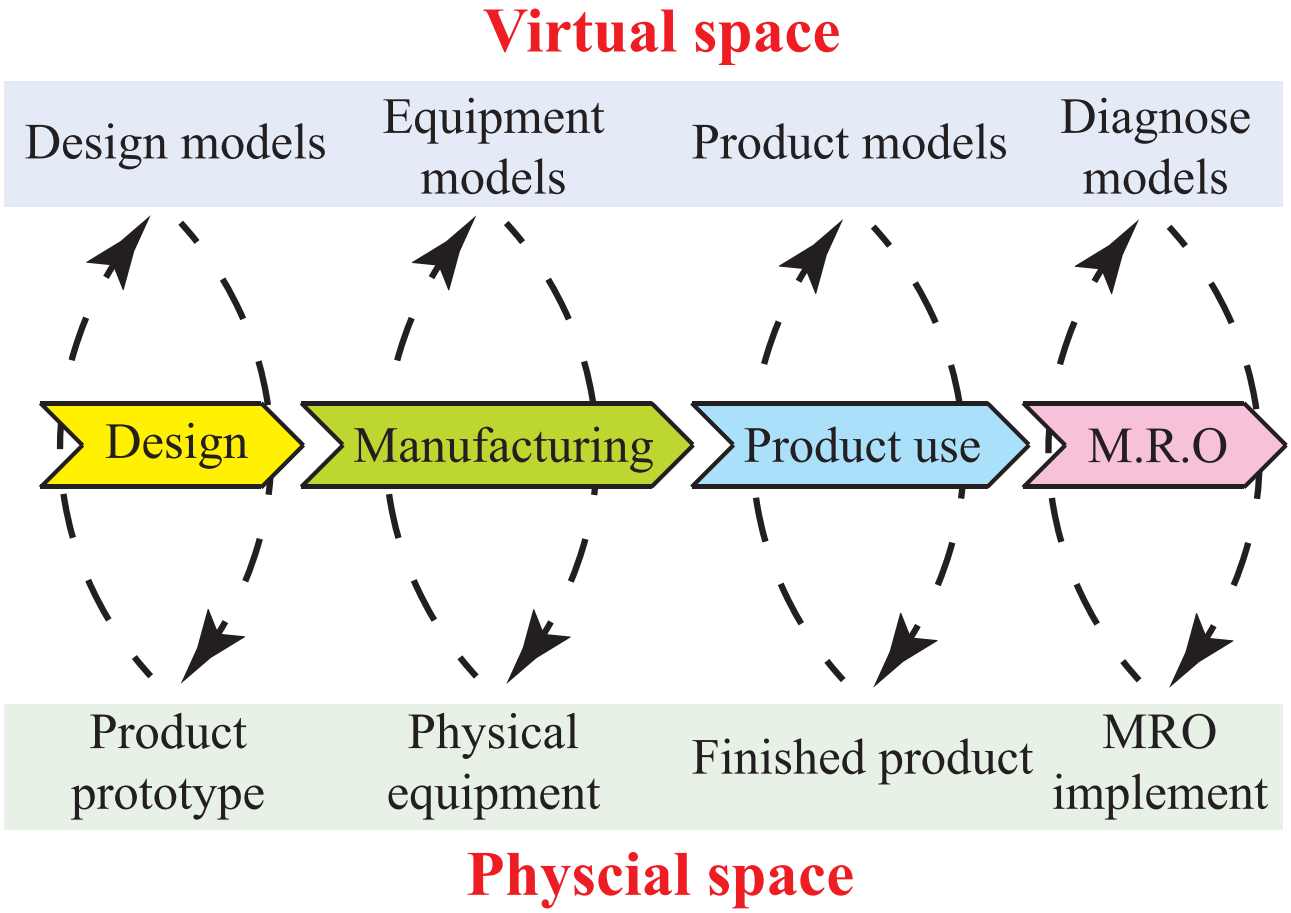

Fig. 3 Schematic of digital twin technology in manufacturing.

1.4 Atmospheric arc plasma movement in parallel electeodes

1.4.1 Basic movement and schematic of arc plasma with applying external magnetic field

As the most commonly used method of controlling or extinguishing the arc plasma, arc plasma movement by applying an external magnetic field is well analyzed and reported [38][39][40][41]. In the most simplified condition, arc plasma is generated between a pair of parallel electrodes and advances under the influence of its self-electromagnetic field and applied external magnetic field. However, the arc does not move smoothly between the electrodes, the anode spot stagnates on the ignited point when the arc column and cathode spot move forward [42]. Because of this arc movement characteristic, a large amount of metal vapor generates from the anode and causes the re-ignite phenomenon to occur on the cathode side as shown in Fig. 4(a) [43]. Even the cathode spot sometimes moves backward, it mostly advances continuously as shown in Fig. 4(b) [43]. On the other hand, the movement of the anode spot is intermittently and well-known as the re-strike phenomenon and the process has been described as follows. Firstly, the arc column bends and extends under the influence of electromagnetic force derived from the electrodes and the arc itself. Secondly, the cathode spot is drawn by the arc column and jumps continuously and uniformly in a small step. In the meantime, the arc column keeps extending and the anode spot stagnates on the anode. Thirdly, the arc column contacts with the anode surface and heats this area which leads to the new anode spot appearing along with the original anode spot disappearing. The above processes are shown in Fig. 5 [38].

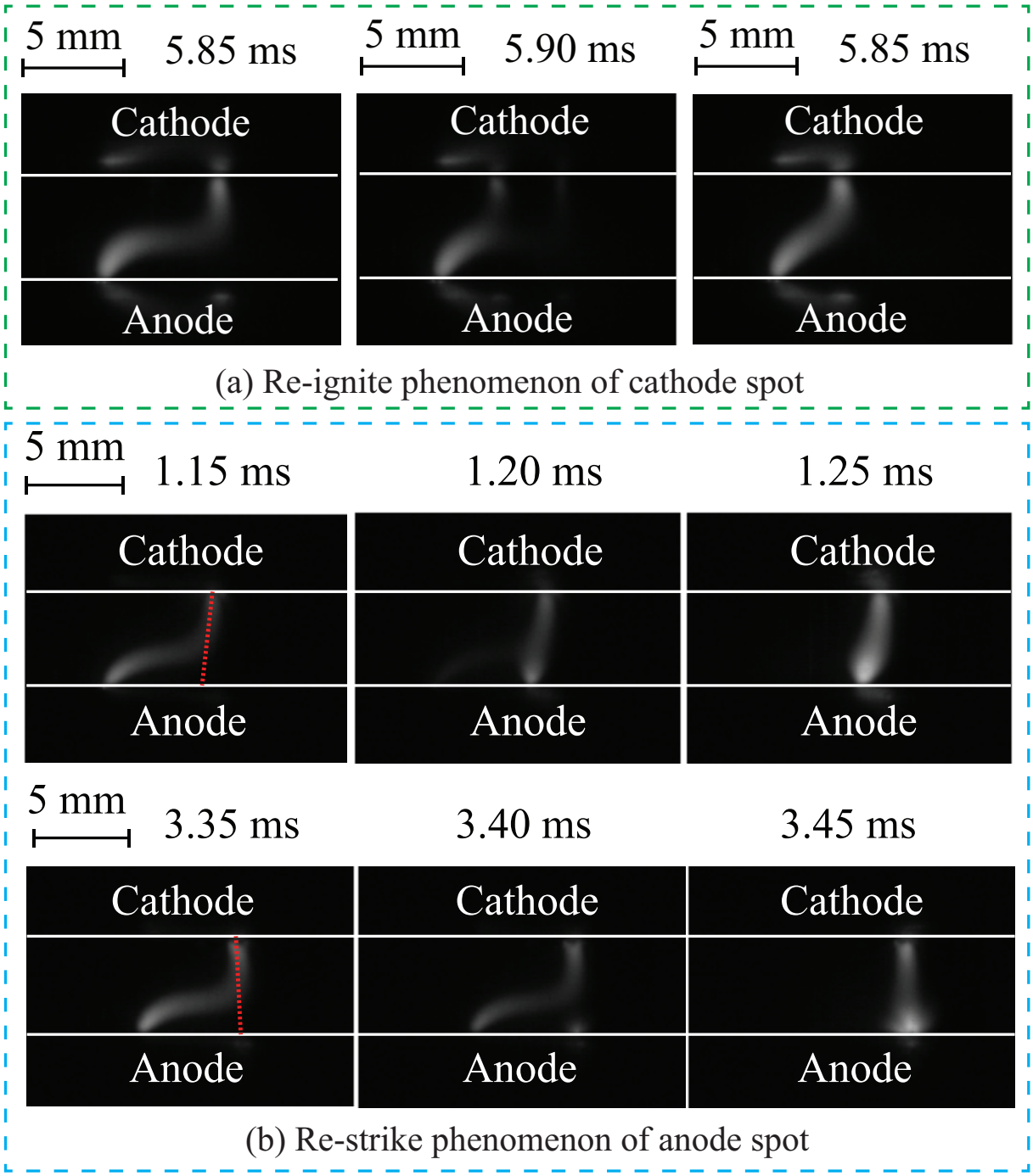

Fig. 4 Experiment figures of the arc plasma advancement in a parallel electrode [43].

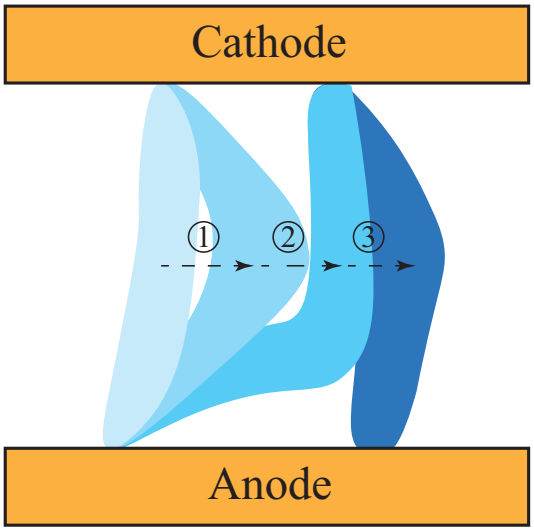

Fig. 5: Schematic of arc structure during the re-strike phenomenon occurred between two parallel electrodes [38].

1.4.2 Hypothesis models and schematic of cathode and anode spots movement

It is assumed that the cathode spot movement is dominated by self and external magnetic forces, and the hypothesis models of cathode spot advancement in different conditions are proposed in Fig. 6 [44]. There are three models presented, model (a) is the case without an external magnetic field applied, the cathode spot does not move because the self-electromagnetic forces derived from the arc plasma form an electromagnetic force balance on the cathode spot area. Model (b) is applying a weak external magnetic field density to the arc plasma, the charged particles are transported by the external magnetic field and lead to the current density on the center point and advanced side (which is the right side in this study) becoming stronger. However, the self-electromagnetic force is still stronger than the external magnetic force on the advanced side, which leads to the direction of total electromagnetic force still pointing backward and the cathode spot remaining stagnation. Model (c) is applying a strong external magnetic field density to the arc plasma, the current density on the advanced side significantly increases and the external magnetic force is stronger than the self-electromagnetic force on the advanced side, which leads to the direction of total electromagnetic force points forward and lead to the cathode spot advance. It should be noted that the cathode spot movement in this chapter is based on the electrical conductivity distribution near the cathode surface as explained in Chapter 2.6.2.

In this study, the electrode material is copper; therefore, electron emission from the cathode is not only derived from thermal emission but also field emission [45][46]. Thus, is necessary to consider both thermal and field emissions to accurately simulate the cathode spot movement. Fig. 7 [47] shows a schematic of cathode spot advancement where the cathode spot advances toward the right and the time increases from Fig. 7 (a) [44] to Fig. 7 (c) [44]. It is assumed that the charged particles advance under the influence of the electromagnetic force derived from the self or external magnetic field, which causes the current density of the field emission on the advanced side to increase. Because of the increment in the current density, the Joule heating on the advanced side also increases, and the cathode spot advances in a macro view. In this study, the Richardson–Shottky formula [45] and the Fowler–Nordheim formula [48][49] are used for considering the thermal field emission, and the details about the specific setting are narrated in Chapter 2.5.

Regarding the anode side, the arc column bends toward the anode under the influence of the electrode jet or the electromagnetic force, which causes the re-strike phenomenon, as shown in Fig. 8 [47]. It assumes that the new anode spot is located where its electrical conductivity is higher than that at its periphery, and the cause of this electrical conductivity increment is important for elucidating the re-strike phenomenon occurrence. In this study, a thermal non-equilibrium model [50][51] was used to analyze the electron and heavy particles (ions and neutral particles) temperature distributions immediately before the re-strike phenomenon occurrence. Moreover, the electrical conductivity was calculated based on the electron or heavy particles (ions and neutral particles) temperature, to determine the triggering factor of the electrical conductivity increment.

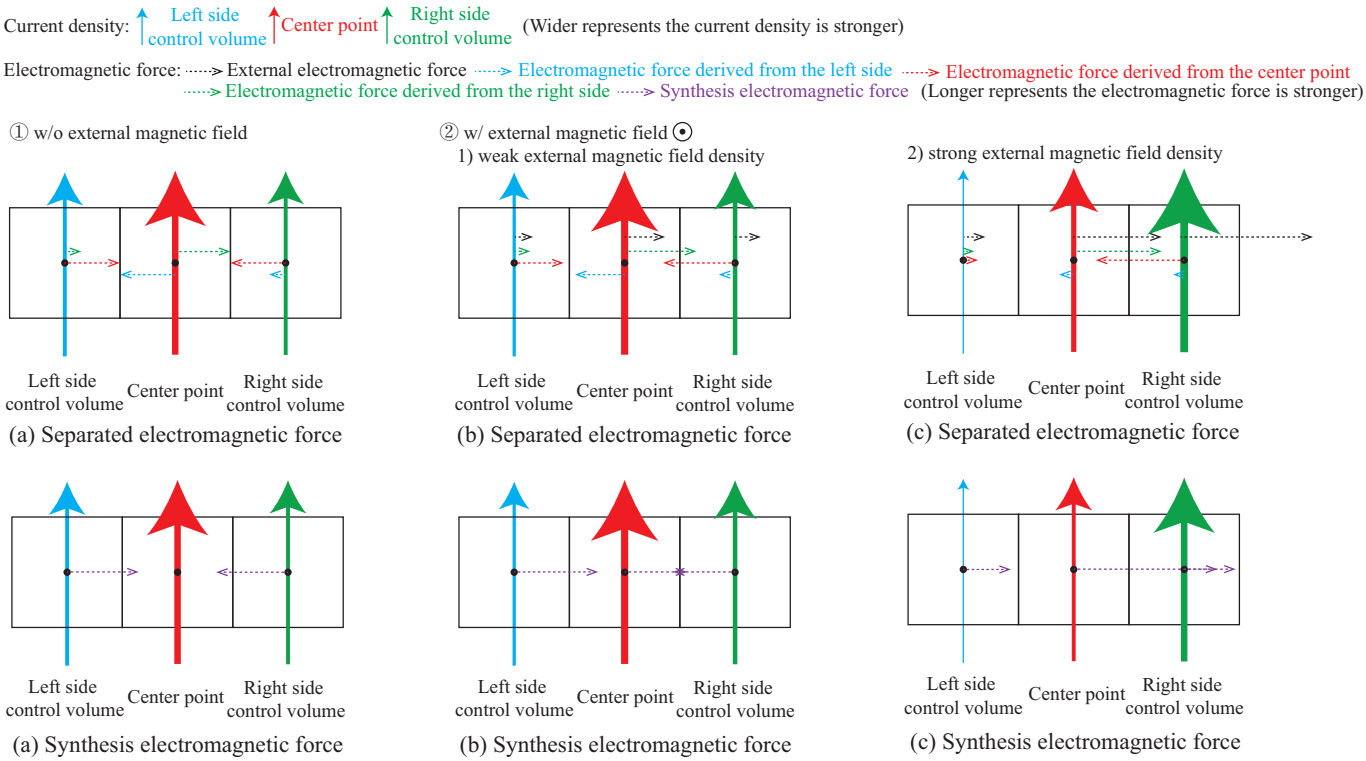

Fig. 6 Hypothesis models of cathode spot different advancing conditions [44].

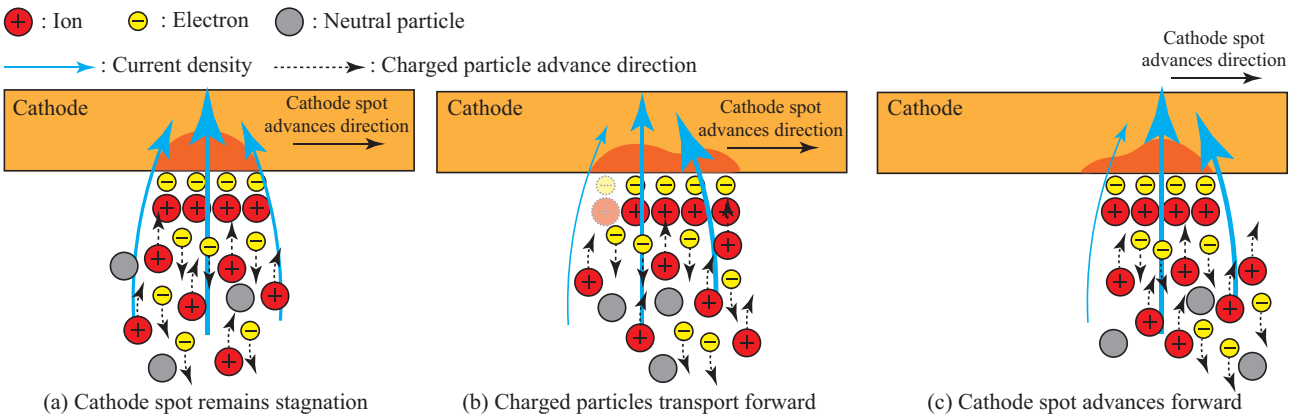

Fig. 7 Schematic of cathode spot advancement with time variation [47].

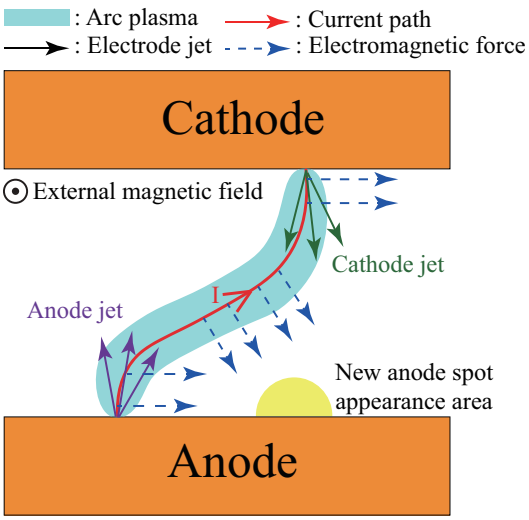

Fig. 8 Schematic of anode spot advancement before re-strike phenomenon occurrence [47].

1.5 Atmospheric arc plasma movement during interruption process of DCCB

An arc is generated during the DC switching process, and the rapid extinguishing of the arc is essential to protect the electrical circuits of EVs. However, the installation environment limits the DCCs from extinguishing the arc in a small, closed space. It has been reported that the metal vapor generated from the electrodes can significantly influence the arc movement in such a space, thus confining the arc from stretching toward the extinguishing chamber.

The contamination of metal vapor in the arc plasma can significantly increase the gas's electrical conductivity [52][53][54] because the metal vapor (Cu atom) is generated from the electrodes, and its lower ionization voltage causes an increase in electron-number density [55]. Therefore, it is hypothesized that the arc stretches into the extinguishing chamber under the effect of an external magnetic field; however, the metal vapor (atom and ion) remains on the electrode surface and the area between them owing to the residual temperature of the electrode surface, even after the arc column moves forward. The gas electrical conductivity of these areas remains high, which causes the probability of the reattachment phenomenon (anode spot moves from the outer corner to the inner corner) occurring to increase, and elongates the stretching time of the arc into the extinguishing chamber. A schematic of the arc movement with and without consideration of the metal vapor is shown in Fig. 9 [56].

The increment rate of the arc voltage per unit length (V_{arc} [V/m·s]) is used as an important index of the DCCB performance. The arc voltage can be described by Eq. 1. In this equation, U [V], I [A], R [Ω], L [m], S [m^2], and σ_{arc} [S] are the voltage, current, resistance, length, cross-sectional area, and electrical conductivity of the arc, respectively. The arc current was fixed in the calculation programs in this study, which means that the increment rate of the arc voltage per unit length was determined by the change in length, cross-sectional area, and electrical conductivity of the arc.

· General equation of arc voltage

$$U = IR = IL\frac{1}{S\sigma_{arc}} \tag{1}$$

Based on the discussion above, electrode-opening-velocity-dependence models of the increment rate of the arc voltage per unit length without an external magnetic field are established and shown in Fig. 10 [57]. Compared to the case of the standard electrode opening velocity, the increment rate of the arc length becomes more rapid when the electrode opening velocity is high. In addition, the cross-sectional area of the arc decreases because the current path should be concentrated to maintain the arc stability, which results in a high gas temperature of the arc center and a high electrical conductivity of the arc. As a result, the arc voltage increment rate increases along with the electrode opening velocity increment because the increment of the arc length is dominant in this circumstance. In contrast, the increment rate of the arc length becomes smoother when the electrode opening velocity is low. The cross-sectional area of the arc increases because there is sufficient time for it to expand, which leads to the current density

dispersion and electrical conductivity reduction. However, the difference in the arc voltage increment rate at different electrode opening velocities decreases when an external magnetic field is applied because the increment rate of the arc length significantly increases.

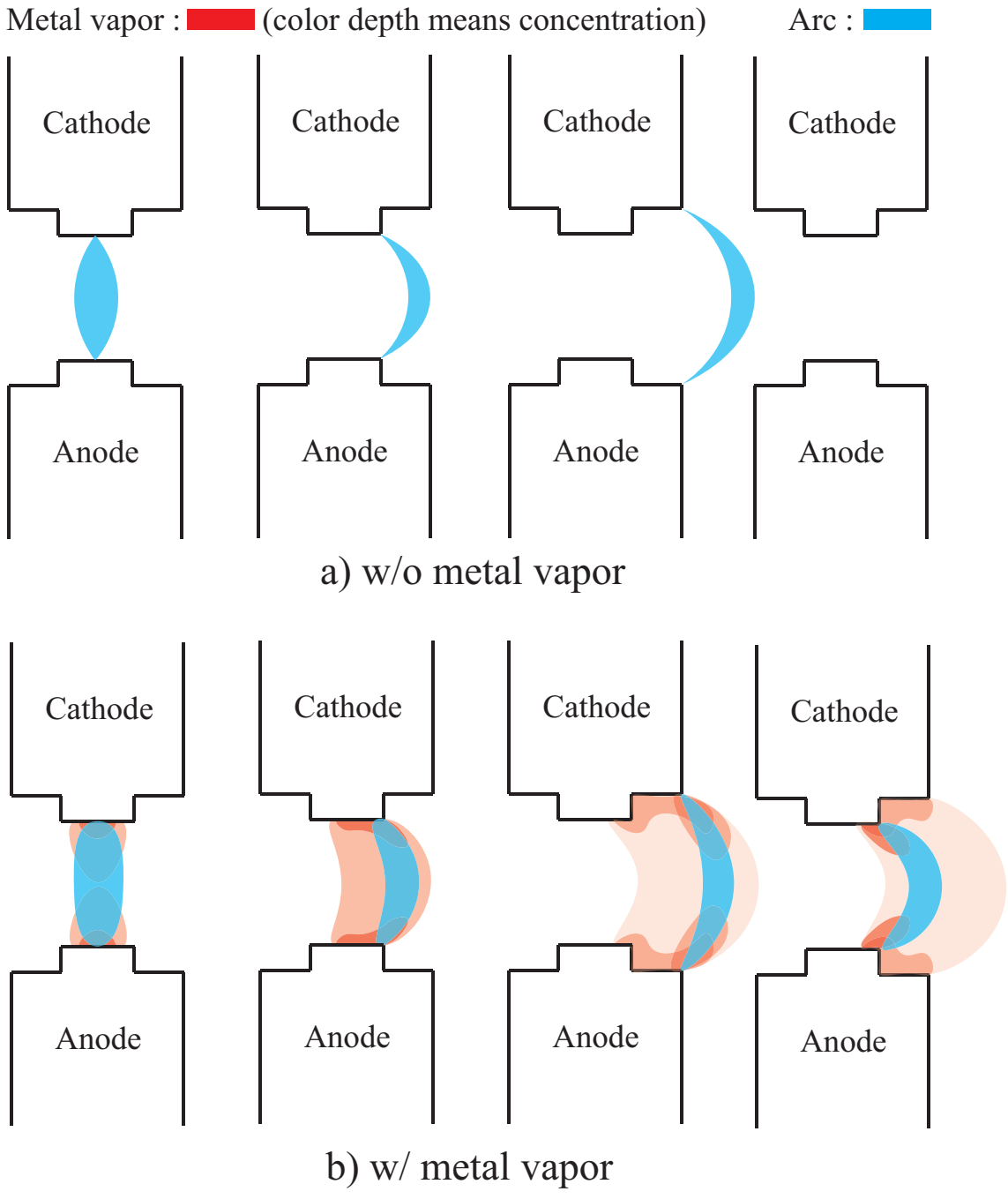

Fig. 9 Schematic of arc movement comparison without and with metal vapor [56].

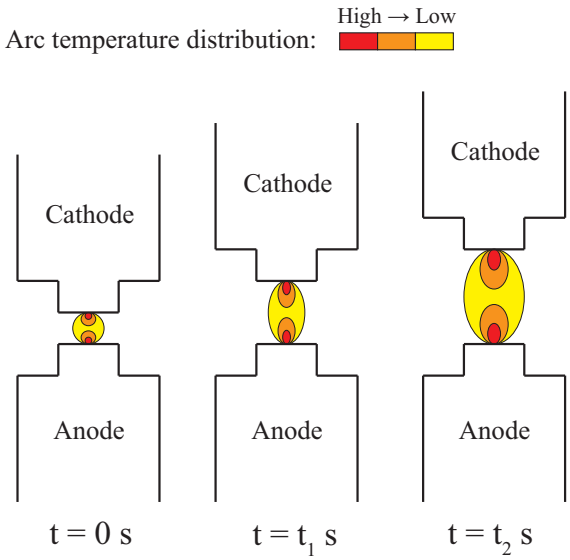

(a) Standard electrode opening velocity situation

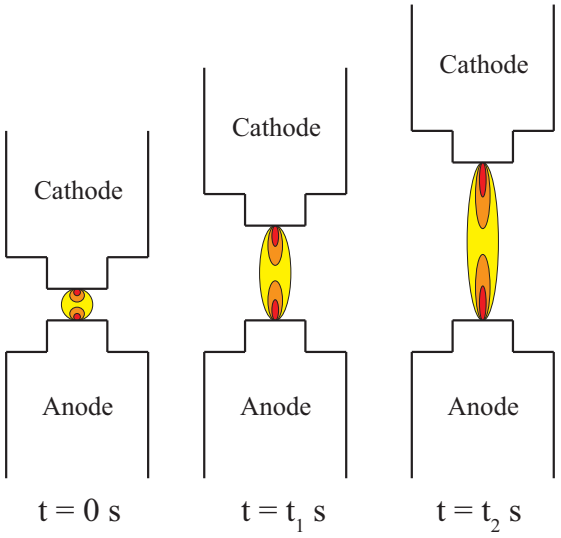

(b) Fast electrode opening velocity situation

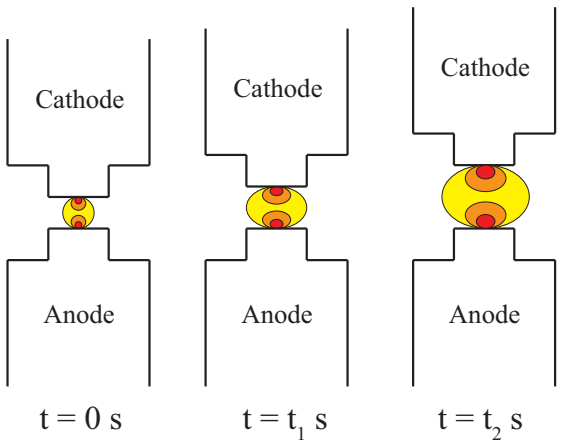

(c) Slow electrode opening velocity situation

Fig. 10: Hypothetical models of the arc form change for different electrode opening velocities without external magnetic field application [57].

1.6 Object, task, and goal of study

Fig. 11 presents the flow of this study. Firstly, the application and problem of current DCCB were searched and summarized four characteristics (rapidity, reliability, miniaturization, and high capacity) of DCCB. Based on the searched problem and demand, it gets to the conclusion of the need for next-generation DCCB is simultaneously satisfying four characteristics.

Therefore, the object of this study is to propose a design for next-generation DCCB that simultaneously satisfies four characteristics. The tasks for achieving the about object include: elucidating the movement and physical property variation of the magnetic driven arc, constructing the numerical simulation for simulating the interruption process of DCCB, and developing an AI model for differentiating and predicting the interruption result.

To be specific, the behavior of atmospheric arc plasma between parallel electrodes with external magnetic field application was discussed in Chapter 3. The behavior of atmospheric arc plasma inside DCCB with external magnetic field application was discussed in Chapter 4. The development of AI models for shorting the DCCB manufacturing cycle and the construction of a cyber-physical system for next-generation DCCB was discussed in Chapter 5.

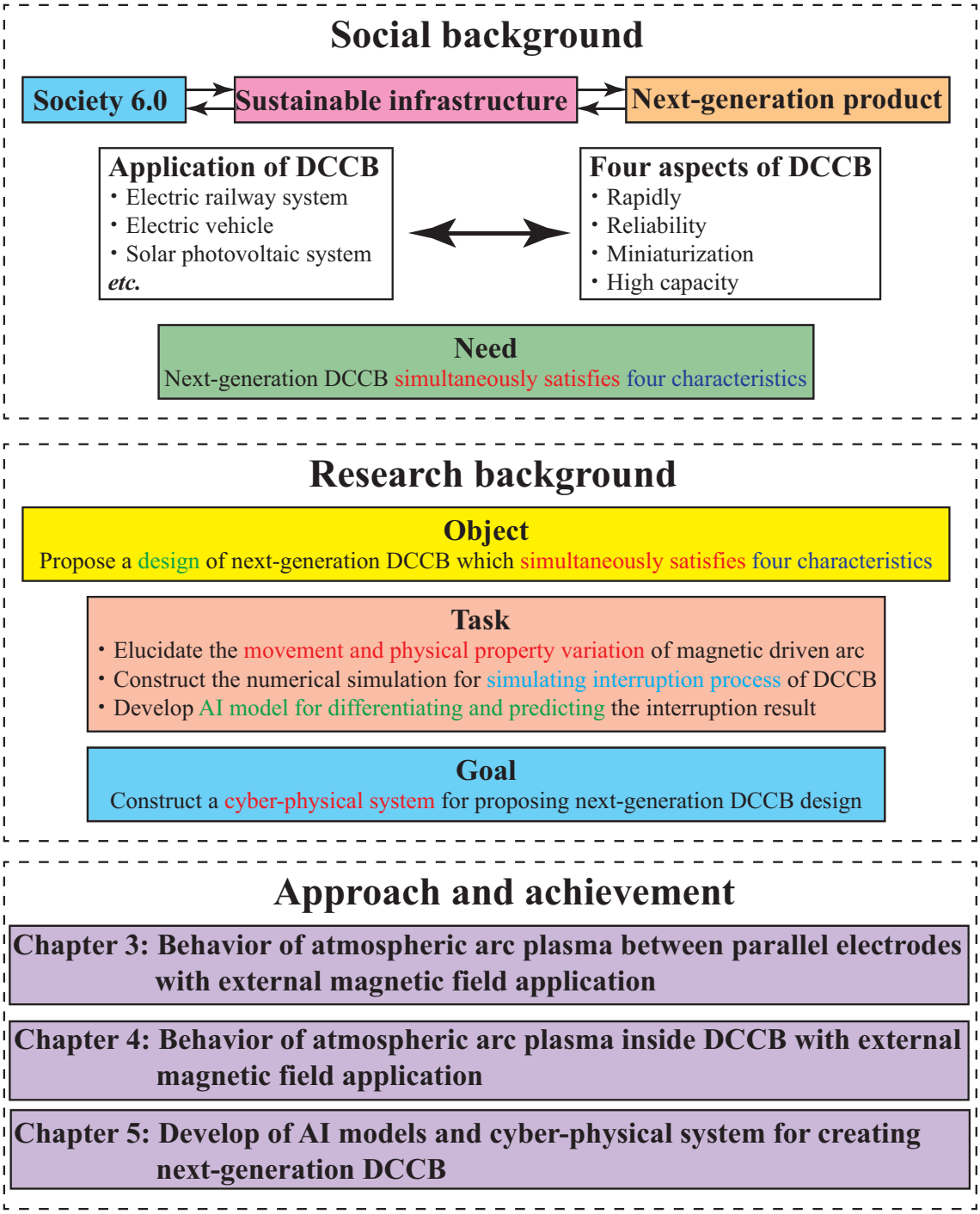

Fig. 11 Flow of this research.

1.7 Structure of thesis

Fig. 12 presents the structure of this thesis, and the detail is explained as follows.

In Chapter 1, the application and problem of the current DCCB were presented, the hypothesis models of magnetic driven arc were constructed, and the object, task, and goal of this study were declared.

In Chapter 2, the basic information about the numerical simulation used in this study was explained. Specifically, the treatment of the gas-electrode interface and the setting of the preliminary stage of the interruption process.

In Chapter 3, the simulation result of magnetic driven arc movement in parallel electrodes was analyzed. The experimental data elucidated and verified the mechanism of electrode spot movement.

In Chapter 4, the simulation result of the interruption process of DCCB was analyzed. The arc plasma movement, interruption circumstances, and physical properties variation inside the DCCB were elucidated.

In Chapter 5, the AI model for differentiating and predicting the interruption result of DCCB was developed. A cyber-physical system for designing the next-generation DCCB was constructed.

In summary, the object, task, and goal of this study were reviewed and the obtained main results were summarized.

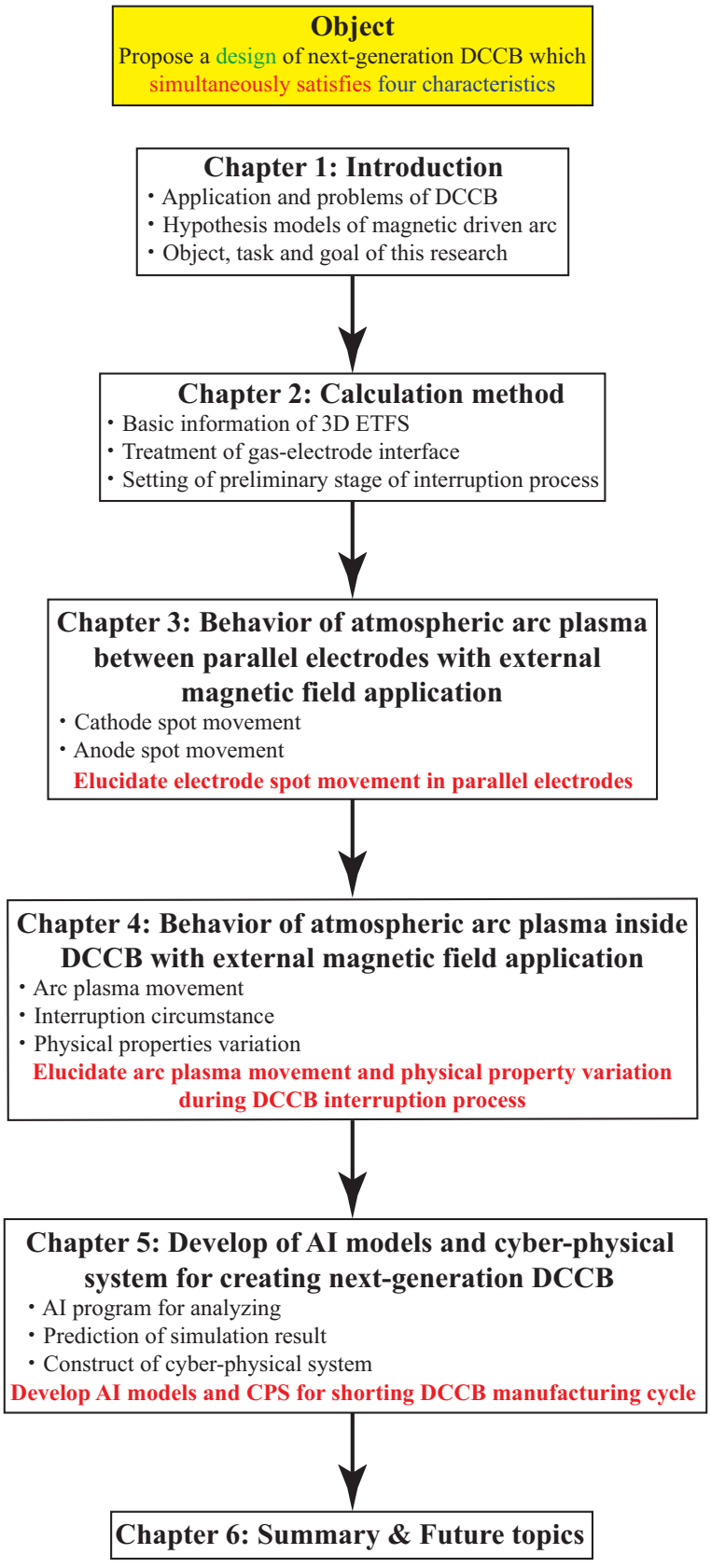

Fig. 12 Structure of this thesis.

Chapter2 Calculation method

2.1 Basic assumption and governing equation

In this study, the Local Thermodynamic Equilibrium (LTE) is assumed to be satisfied with setting the gas pressure to 0.1 MPa as uncompressed gas for the following reasons. Firstly, the temperature of arc plasma is usually considered to be in the order of 15,000–20,000 K, and the electron and ion number densities are in the order of 10^{23} m^{-3} [58]. Secondly, a strong collision coupling for the energy exchange between the electrons and heavy particles, including chemical reactions such as ionization and recombination [59][60]. The environmental gas is air and the air arc plasma is always assumed to be a laminar flow because the Reynolds number of air arc is normally thought to be small.

Moreover, the particle compositions (N_2, N_2^+, N, N^+, O_2, O_2^+, O^-, O, O^+, NO, NO^+, Cu, Cu^+) from 300 K to 30,000 K (every 100 K) at different metal vapor mixture rates (0, 0.01, 0.1, 1, 3, 5, 10, 20, 40, 70, and 100 mol%) at 0.1 MPa were calculated. The plasma properties, such as electron density, the number density of neutral particles, mass density, enthalpy, specific heat, electrical conductivity, thermal conductivity, viscosity, and radiative emission coefficient were calculated based on the particle composition using the Chapman-Enskog theory [61]. Because the gas temperature and metal vapor mixture rate were discontinuous, the plasma properties between the determinate values were calculated using a linear approximation[62]. The interval values of the physical properties of the electrode (copper in this study), such as mass density, enthalpy, specific heat, electrical conductivity, and thermal conductivity, were also calculated using a linear approximation based on the temperature variation.

The governing equations are mass conservation, momentum conservation, energy conservation, current continuity, Maxwell, and metal vapor conservation equation. These equations are solved across the entire calculation area including the arc plasma and the electrodes [63]. Over the entire calculation area, the aforementioned equations were discretized by the finite volume method and calculated by the tridiagonal matrix algorithm method [64][50][51]. The semi-implicit method was used to analyze the pressure and velocity fields for the revised pressure-linked equations [65][66]. The details of the governing equations are as follows:

· Mass conservation equation

$$\frac{\partial \rho}{\partial t} + \frac{\partial}{\partial x}(\rho u) + \frac{\partial}{\partial y}(\rho v) + \frac{\partial}{\partial z}(\rho w) = 0 \tag{2}$$

Where $\rho\,[\mathrm{kg \cdot m^{-3}}]$ is the mass density, t [s] is the time, x, y, z [m] are the locations of each

direction, u, v, w [m·s] are the flow velocities of each direction.

· Momentum conservation equation (x direction)

$$\begin{aligned} & \frac{\partial \rho u}{\partial t} + \frac{\partial}{\partial x}(\rho u^2) + \frac{\partial}{\partial y}(\rho uv) + \frac{\partial}{\partial z}(\rho uw) \\ = \; & -\frac{\partial P}{\partial x} + j_y B_z - j_z B_y + \left(\frac{\partial}{\partial x}(\eta \frac{\partial u}{\partial x})\right) + \left(\frac{\partial}{\partial y}(\eta \frac{\partial u}{\partial y})\right) \\ & + \left(\frac{\partial}{\partial z}(\eta \frac{\partial u}{\partial z})\right) \end{aligned} \tag{3}$$

· Momentum conservation equation (y direction)

$$\begin{aligned} & \frac{\partial \rho v}{\partial t} + \frac{\partial}{\partial x}(\rho uv) + \frac{\partial}{\partial y}(\rho v^2) + \frac{\partial}{\partial z}(\rho vw) \\ = \; & -\frac{\partial P}{\partial y} + j_z B_x - j_x B_z + \left(\frac{\partial}{\partial x}(\eta \frac{\partial v}{\partial x})\right) + \left(\frac{\partial}{\partial y}(\eta \frac{\partial v}{\partial y})\right) \\ & + \left(\frac{\partial}{\partial z}(\eta \frac{\partial v}{\partial z})\right) \end{aligned} \tag{4}$$

· Momentum conservation equation (z direction)

$$\begin{aligned} & \frac{\partial \rho w}{\partial t} + \frac{\partial}{\partial x}(\rho uw) + \frac{\partial}{\partial y}(\rho vw) + \frac{\partial}{\partial z}(\rho w^2) \\ = \; & -\frac{\partial P}{\partial z} + j_y B_x - j_x B_y + \left(\frac{\partial}{\partial x}(\eta \frac{\partial w}{\partial x})\right) + \left(\frac{\partial}{\partial y}(\eta \frac{\partial w}{\partial y})\right) \\ & + \left(\frac{\partial}{\partial z}(\eta \frac{\partial w}{\partial z})\right) + (\rho_0 - \rho) g \end{aligned} \tag{5}$$

Where P [Pa] is the pressure, j [A·m^{-2}] is the current density and the subscript indicating direction, B [T] is the magnetic flux density vector and the subscript indicating direction, ρ_0 [kg·m^{-3}] is the mass density at 300 K, g [m·s^{-2}] is the gravitational acceleration.

· Energy conservation equation

$$\begin{aligned} & \frac{\partial \rho h}{\partial t} + \frac{\partial}{\partial x}(\rho uh) + \frac{\partial}{\partial y}(\rho vh) + \frac{\partial}{\partial z}(\rho wh) \\ = \; & \frac{\partial}{\partial x}\left(\frac{\kappa}{C_p}\frac{\partial h}{\partial x}\right) + \frac{\partial}{\partial y}\left(\frac{\kappa}{C_p}\frac{\partial h}{\partial y}\right) + \frac{\partial}{\partial z}\left(\frac{\kappa}{C_p}\frac{\partial h}{\partial z}\right) \\ + \; & j_x E_x + j_y E_y + j_z E_z - Q_{rad} \end{aligned} \tag{6}$$

Where h [J·kg] is the enthalpy, κ [W·m^{-1}·k^{-1}] is the thermal conductivity, C_p [J·kg^{-1}·K^{-1}] is the constant pressure specific heat, E [V·m^{-1}] is the electric field and subscript means direction. The radiation is calculated [59][67][120][69] based on the particle composition, partition function, collision cross-section, and properties (wavelength, transition probability, statistical weight, and energy) of each particle from the database [70]. The absorption is calculated only within the control volume and depends on the temperature and the radial dimension of the control volume (the absorption length is set as 0.25 mm according to the size of the control

volume) based on Ref. [67]. Subsequently, the radiative emission coefficient can be obtained from the calculated radiation and absorption. This coefficient reflects the energy balance, as shown in Eq. 6 as Q_{rad} [W·m^{-3}].

· Current continuity equation

$$\frac{\partial}{\partial x}(j_x) + \frac{\partial}{\partial y}(j_y) + \frac{\partial}{\partial z}(j_z) = 0 \tag{7}$$

· Current density

$$j_x = \sigma E_x, j_y = \sigma E_y, j_z = \sigma E_z \tag{8}$$

Where σ [S·m^{-1}] is the electrical conductivity.

· Electric field

$$E_x = -\frac{\partial \phi}{\partial x}, E_y = -\frac{\partial \phi}{\partial y}, E_z = -\frac{\partial \phi}{\partial z} \tag{9}$$

Where ϕ [V] is the potential.

· Maxwell-Amphale equation (x direction)

$$\frac{\partial^2 A_x}{\partial x^2} + \frac{\partial^2 A_x}{\partial y^2} + \frac{\partial^2 A_x}{\partial z^2} = -\mu j_x \tag{10}$$

· Maxwell-Amphale equation (y direction)

$$\frac{\partial^2 A_y}{\partial x^2} + \frac{\partial^2 A_y}{\partial y^2} + \frac{\partial^2 A_y}{\partial z^2} = -\mu j_y \tag{11}$$

· Maxwell-Amphale equation (z direction)

$$\frac{\partial^2 A_z}{\partial x^2} + \frac{\partial^2 A_z}{\partial y^2} + \frac{\partial^2 A_z}{\partial z^2} = -\mu j_z \tag{12}$$

Where A [T·m] is the vector potential and the subscript indicating direction, μ [H·m^{-1}] is the magnetic permeability.

· Magnetic flux density

$$B_x = \frac{\partial A_z}{\partial y} - \frac{\partial A_y}{\partial z}, B_y = \frac{\partial A_x}{\partial z} - \frac{\partial A_z}{\partial x}, B_z = \frac{\partial A_y}{\partial x} - \frac{\partial A_x}{\partial y} \tag{13}$$

· Metal vapor conservation equation

$$\begin{aligned} &\frac{\partial \rho C}{\partial t} + \frac{\partial}{\partial x}(\rho u C) + \frac{\partial}{\partial y}(\rho v C) + \frac{\partial}{\partial z}(\rho w C) \\ = \;& \frac{\partial}{\partial x}(D\frac{\partial \rho C}{\partial x}) + \frac{\partial}{\partial y}(D\frac{\partial \rho C}{\partial y}) + \frac{\partial}{\partial z}(D\frac{\partial \rho C}{\partial z}) \end{aligned} \tag{14}$$

· Diffusion coefficient

$$D = \frac{2\sqrt{2}(1/M_{air} + 1/M_{Cu})^{0.5}}{((\rho_{air}^2/\beta_{air}^2\eta_{air}^2 M_{air})^{0.25} + (\rho_{Cu}^2/\beta_{Cu}^2\eta_{Cu}^2 M_{Cu})^{0.25})^2} \tag{15}$$

Here, C [%] is the contaminate proportion of Cu vapor on the electrode surface which will be discussed in detail at Chapter 2.3, D [$m^2 \cdot s^{-1}$] is the diffusion coefficient, M_{air} [$kg \cdot mol^{-1}$] and M_{Cu} [$kg \cdot mol^{-1}$] are the molecular weights of air and Cu, respectively, ρ_{air} [$kg \cdot m^{-3}$] and ρ_{Cu} [$kg \cdot m^{-3}$] are the mass density of air and Cu, respectively, β_{air} and β_{Cu} are the dimensionless constants defined by $\beta_i = (D\rho_i)/\eta_i$ where i indicates the atomic species, which theoretically range between 1.2 and 1.543, $\beta_{air} = \beta_{Cu} = 1.385$ is assumed based on the mean value of the experimental data [71]. η_{air} and η_{Cu} are the viscosity coefficients of air and Cu, respectively.

2.2 Flow chart, calculation area and conditions

Fig. 13 shows the calculation flow chart. The cathode, arc plasma, and anode are integrated as one, and the interactions between them are considered and calculated by a three-dimensional electromagnetic thermal fluid simulation. At every advancement of the time step, the physical properties (temperature, flow velocity, pressure, electric potential, and vector potential) of the previous time step will be used as the initial values and implement the iterative calculation. The variable rates of enthalpy, electric potential, flow velocity, and mass will be decreased along with the calculation times, and the program will be defined as convergence when the above variation rates are smaller than 10^{-4}, or calculation times of this time step exceeds a set value.

For elucidating the cathode spot, anode spot, and arc plasma movements, a simple calculation area of the parallel electrode was constructed [43][44][47] based on the actual experimental equipment, which is a three-dimensional rectangular coordinate system, and the length of x, y, and z are both 25 mm. The shape of the electrodes is triangular and the inter-electrode distance is 5 mm. Arc current is set to 10, 30, 50, 100, or 150 A and the initial position of the arc is 10 mm in the Y direction. The applied external magnetic field density is 0, 0.05, 1, 2, or 3 mT, which points toward the $-$ X direction. The schematic of the parallel electrode calculation area is shown in Fig. 14 [44] along with its mesh distribution, which is non-uniform and has sparse distribution at the periphery (control volume is a 0.5 mm cube), and dense distribution at the center (control volume is a 0.25 mm cube). Table 1 [44] shows the detail of the boundary setting, which is a Neumann boundary.

For elucidating the interruption process of the DCCB, a symmetrical three-dimensional calculation area based on the actual product [13] was constructed [56][57][72] for simplicity and rapid calculation. It is a three-dimensional rectangular coordinate system with the x, y, and z dimensions being 20, 20, and 27 mm, respectively. The electrode had a protruding surface to imitate the actual shape of the DCCB, and the arc current was set to 135 A based on Ref. [13]. To mimic the interruption process as faithful to the actual process as possible, the vapor generates from the molten metal bridge, electrode opening process, and the application of recovery voltage was taken into consideration in this study, which is exhaustively explained in Chapter 2.8.1 and 2.8.2. Meanwhile, the arc plasma movement in the case of applying 0-10 mT external magnetic field towards the -X direction was implemented. The calculation area is shown in Fig. 15 [57] and its boundary conditions are shown in Table 2 [56].

Table 1 Boundary conditions of parallel electrode calculation area [44].

Plane	T	ϕ_S	ϕ_R	u	v	w	P_r	A_x	A_y	A_z	C
abcd	$\frac{\partial T}{\partial z}=0$	$\frac{\partial \phi}{\partial z}=0$	$\frac{\partial \phi}{\partial z}=0$ $(\sigma=0)$	0	0	0	0	$\frac{\partial A_x}{\partial z}=0$	$\frac{\partial A_y}{\partial z}=0$	$\frac{\partial A_z}{\partial z}=0$	0
AadD/ bBCc	$\frac{\partial T}{\partial z}=0$	$\frac{\partial \phi}{\partial z}=0$	$\frac{\partial \phi}{\partial z}=0$	$\frac{\partial u}{\partial z}=0$	$\frac{\partial v}{\partial z}=0$	$\frac{\partial \rho w}{\partial z}=0$	$\frac{\partial P_r}{\partial z}=0$	$\frac{\partial A_x}{\partial z}=0$	$\frac{\partial A_y}{\partial z}=0$	$\frac{\partial A_z}{\partial z}=0$	$\frac{\partial C}{\partial z}=0$
efgh	$\frac{\partial T}{\partial z}=0$	$\phi=0$	$\frac{\partial \phi}{\partial z}=0$ $(\sigma=0)$	0	0	0	0	$\frac{\partial A_x}{\partial z}=0$	$\frac{\partial A_y}{\partial z}=0$	$\frac{\partial A_z}{\partial z}=0$	0
EehH/ fFGg	$\frac{\partial T}{\partial z}=0$	$\frac{\partial \phi}{\partial z}=0$	$\frac{\partial \phi}{\partial z}=0$	$\frac{\partial u}{\partial z}=0$	$\frac{\partial v}{\partial z}=0$	$\frac{\partial \rho w}{\partial z}=0$	$\frac{\partial P_r}{\partial z}=0$	$\frac{\partial A_x}{\partial z}=0$	$\frac{\partial A_y}{\partial z}=0$	$\frac{\partial A_z}{\partial z}=0$	$\frac{\partial C}{\partial z}=0$
abJKI	$\frac{\partial T}{\partial y}=0$	$\frac{\partial \phi}{\partial y}=0$	$\frac{\partial \phi}{\partial y}=0$	0	0	0	0	$\frac{\partial A_x}{\partial y}=0$	$\frac{\partial A_y}{\partial y}=0$	$\frac{\partial A_z}{\partial y}=0$	0
AaIKJbB FfjkieE	$\frac{\partial T}{\partial y}=0$	$\frac{\partial \phi}{\partial y}=0$	$\frac{\partial \phi}{\partial y}=0$	$\frac{\partial u}{\partial y}=0$	$\frac{\partial \rho v}{\partial y}=0$	$\frac{\partial w}{\partial y}=0$	$\frac{\partial P_r}{\partial y}=0$	$\frac{\partial A_x}{\partial y}=0$	$\frac{\partial A_y}{\partial y}=0$	$\frac{\partial A_z}{\partial y}=0$	$\frac{\partial C}{\partial y}=0$
eikjf	$\frac{\partial T}{\partial y}=0$	$\frac{\partial \phi}{\partial y}=0$	$\phi=0$	0	0	0	0	$\frac{\partial A_x}{\partial y}=0$	$\frac{\partial A_y}{\partial y}=0$	$\frac{\partial A_z}{\partial y}=0$	0
dcLNM	$\frac{\partial T}{\partial y}=0$	$\frac{\partial \phi}{\partial y}=0$	$\frac{\partial \phi}{\partial y}=0$ $(\sigma=0)$	0	0	0	0	$\frac{\partial A_x}{\partial y}=0$	$\frac{\partial A_y}{\partial y}=0$	$\frac{\partial A_z}{\partial y}=0$	0
DdMNL cCGgl nmhH	$\frac{\partial T}{\partial y}=0$	$\frac{\partial \phi}{\partial y}=0$	$\frac{\partial \phi}{\partial y}=0$	$\frac{\partial u}{\partial y}=0$	$\frac{\partial \rho v}{\partial y}=0$	$\frac{\partial w}{\partial y}=0$	$\frac{\partial P_r}{\partial y}=0$	$\frac{\partial A_x}{\partial y}=0$	$\frac{\partial A_y}{\partial y}=0$	$\frac{\partial A_z}{\partial y}=0$	$\frac{\partial C}{\partial y}=0$
hmnlg	$\frac{\partial T}{\partial y}=0$	$\frac{\partial \phi}{\partial y}=0$	$\frac{\partial \phi}{\partial y}=0$ $(\sigma=0)$	0	0	0	0	$\frac{\partial A_x}{\partial y}=0$	$\frac{\partial A_y}{\partial y}=0$	$\frac{\partial A_z}{\partial y}=0$	0
ADHE	$\frac{\partial T}{\partial x}=0$	$\frac{\partial \phi}{\partial x}=0$	$\frac{\partial \phi}{\partial x}=0$	$\frac{\partial \rho u}{\partial x}=0$	$\frac{\partial v}{\partial x}=0$	$\frac{\partial w}{\partial x}=0$	$\frac{\partial P_r}{\partial x}=0$	$\frac{\partial A_x}{\partial x}=0$	$\frac{\partial A_y}{\partial x}=0$	$\frac{\partial A_z}{\partial x}=0$	$\frac{\partial C}{\partial x}=0$
BCGF	$\frac{\partial T}{\partial x}=0$	$\frac{\partial \phi}{\partial x}=0$	$\frac{\partial \phi}{\partial x}=0$	$\frac{\partial \rho u}{\partial x}=0$	$\frac{\partial v}{\partial x}=0$	$\frac{\partial w}{\partial x}=0$	$\frac{\partial P_r}{\partial x}=0$	$\frac{\partial A_x}{\partial x}=0$	$\frac{\partial A_y}{\partial x}=0$	$\frac{\partial A_z}{\partial x}=0$	$\frac{\partial C}{\partial x}=0$

Table 2 Boundary conditions of opposite electrode calculation area [56].

Plane	T	ϕ	u, v, w	P_r	A_x	A_y	A_z	C
ABCD	300	$\frac{\partial \phi}{\partial z}=0$	0	0	$\frac{\partial A_x}{\partial z}=0$	$\frac{\partial A_y}{\partial z}=0$	$\frac{\partial A_z}{\partial z}=0$	0
EFHG	$\frac{\partial T}{\partial z}=0$	$\frac{\partial \phi}{\partial z}=0$	0	0	$\frac{\partial A_x}{\partial z}=0$	$\frac{\partial A_y}{\partial z}=0$	$\frac{\partial A_z}{\partial z}=0$	0
abcd	300	$\frac{\partial \phi}{\partial z}=0$	0	0	$\frac{\partial A_x}{\partial z}=0$	$\frac{\partial A_y}{\partial z}=0$	$\frac{\partial A_z}{\partial z}=0$	0
efgh	$\frac{\partial T}{\partial z}=0$	$\phi=0$	0	0	$\frac{\partial A_x}{\partial z}=0$	$\frac{\partial A_y}{\partial z}=0$	$\frac{\partial A_z}{\partial z}=0$	0
AadD	300	$\frac{\partial \phi}{\partial y}=0$	0	0	$\frac{\partial A_x}{\partial y}=0$	$\frac{\partial A_y}{\partial y}=0$	$\frac{\partial A_z}{\partial y}=0$	0
BbcC	300	$\frac{\partial \phi}{\partial y}=0$	0	0	$\frac{\partial A_x}{\partial y}=0$	$\frac{\partial A_y}{\partial y}=0$	$\frac{\partial A_z}{\partial y}=0$	0
ABba	300	$\frac{\partial \phi}{\partial x}=0$	0	0	$\frac{\partial A_x}{\partial x}=0$	$\frac{\partial A_y}{\partial x}=0$	$\frac{\partial A_z}{\partial x}=0$	0
DCcd	300	$\frac{\partial \phi}{\partial x}=0$	0	0	$\frac{\partial A_x}{\partial x}=0$	$\frac{\partial A_y}{\partial x}=0$	$\frac{\partial A_z}{\partial x}=0$	0

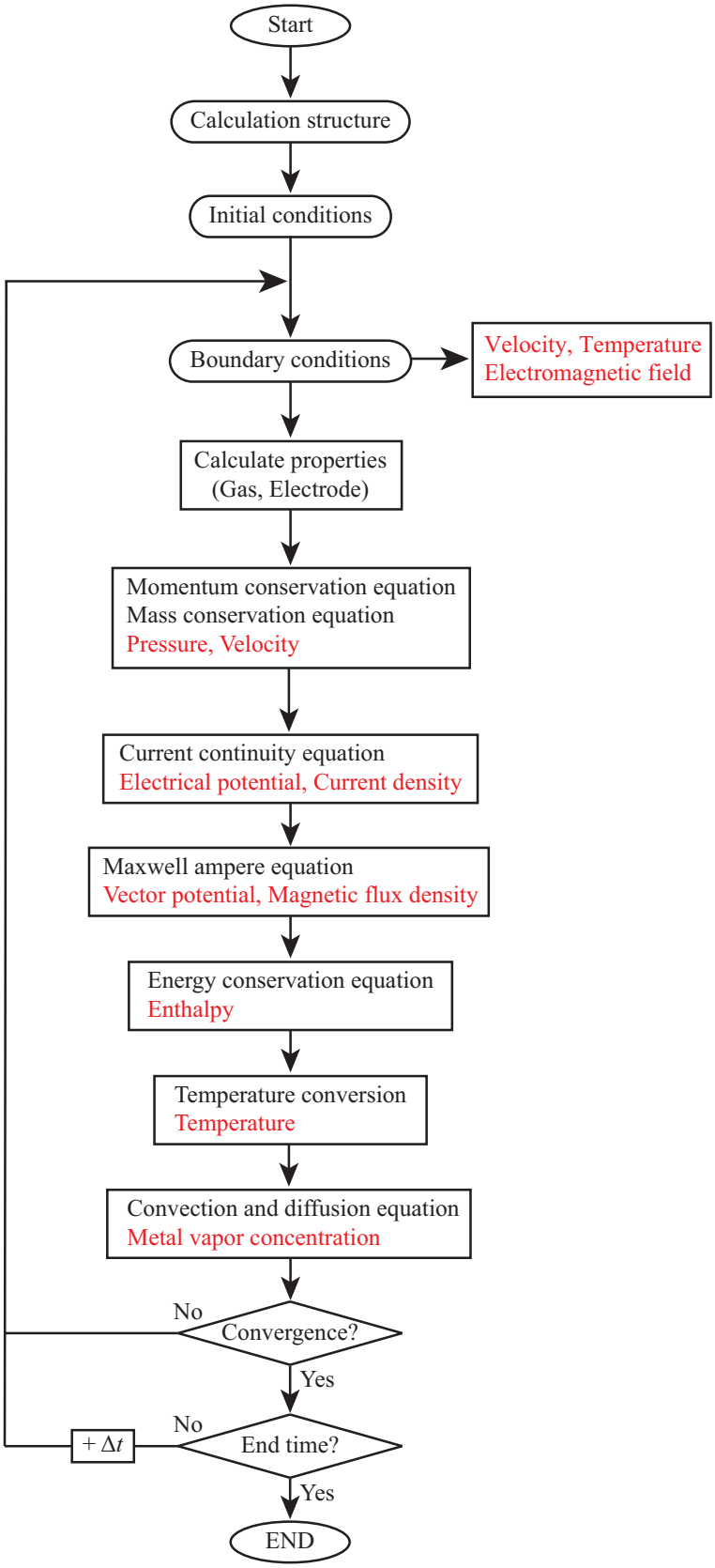

Fig. 13 Calculation flow chart.

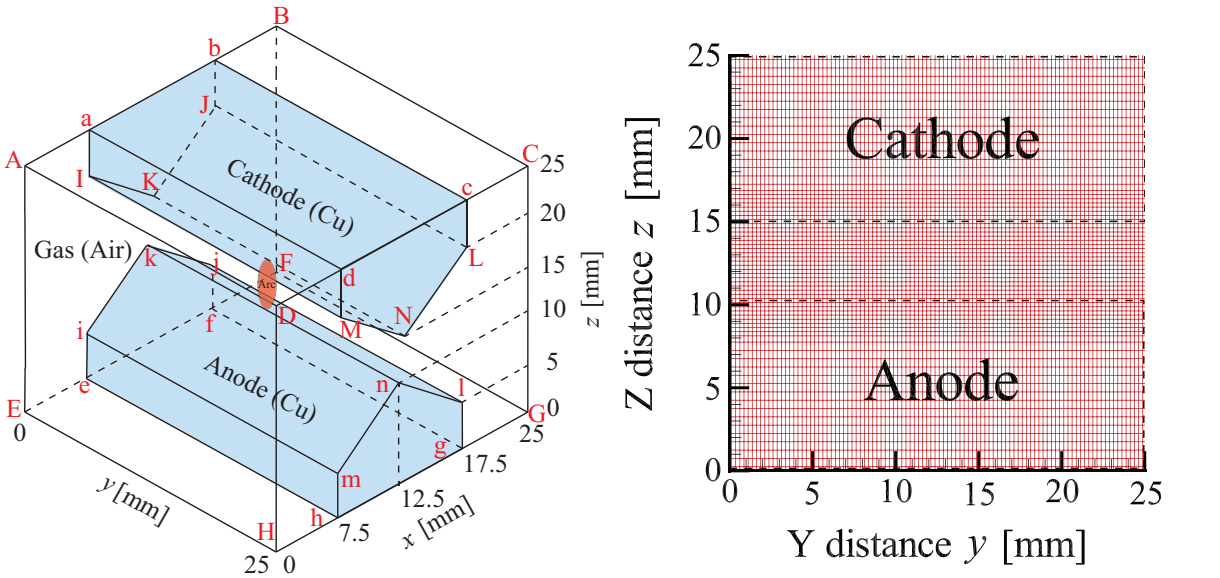

(a) Three-dimensional view (b) Two-dimensional view fo YZ plane

Fig. 14 Calculation area and mesh distribution of parallel electrode [44].

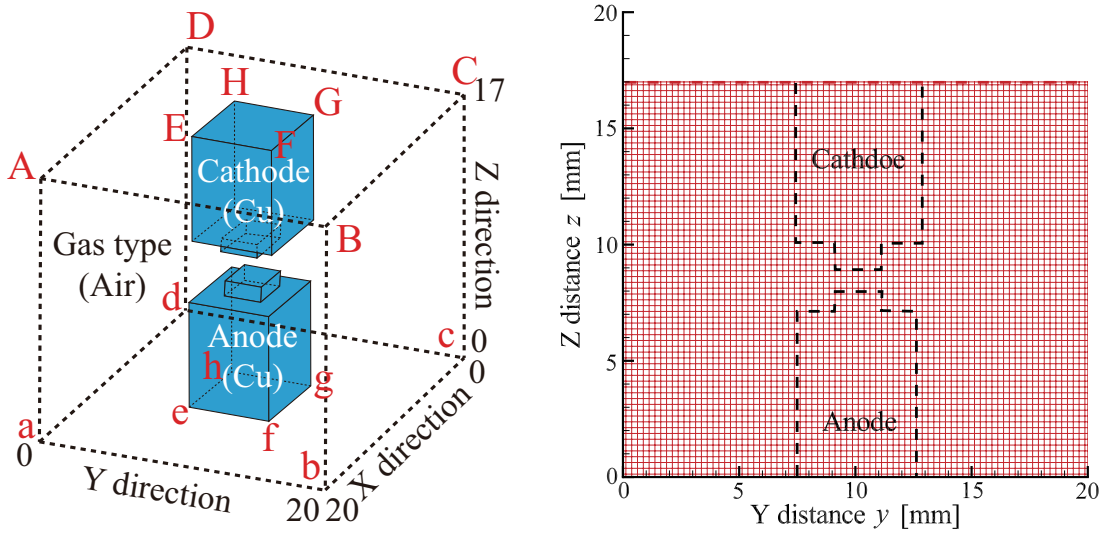

(a) Three-dimensional view (b) Two-dimensional view fo YZ plane

Fig. 15 Calculation area and mesh distribution of opposite electrode [57].

2.3 Metal vapor generation and energy balance of gas-electrode interface

2.3.1 Saturation vapor pressure model and vaporization rate model

In this study, two calculation methods for calculating the generation of metal vapor from the electrode were used, which are the saturation vapor pressure model and the vaporization rate model.

Firstly, the saturation vapor pressure model will be introduced. In this model, the quantity of the metal vapor is calculated from the concentration of metal vapor in the molten pool on the electrode, and the mass density of the arc which is contaminated by the metal vapor. At every time step, the saturation vapor pressure is calculated based on the molten pool surface temperature. This saturation vapor pressure and the surrounding pressure are used to calculate the concentration of metal vapor on the molten pool surface. Using this concentration of metal vapor as the initial value along with the flow diffusion equation, the concentration distribution of metal vapor can be obtained [73][74]. Fig. 16 is the calculation method of metal vapor generation. The equations used to calculate the initial metal vapor concentration are shown as follows.

· Contaminate proportion of metal vapor on the electrode surface (saturation vapor pressure model)

$$C_{pressure} = \frac{\rho_{Cu} M_{Cu}}{\rho_{Cu} M_{Cu} + (P_{atm} - P_v) M_{air}} \tag{16}$$

Here, P_{atm} [Pa] is the atmospheric pressure, and P_v [Pa] is the saturation vapor pressure of Cu.

Secondly, the vaporization rate model will be introduced. In this model, the metal vapor concentration on the electrode surface is calculated based on the temperature difference between the arc plasma and the electrode. For better understanding, the schematic about the control volume on electrode surface is shown in Fig. 17 [56].

· Contaminate proportion of metal vapor on the electrode surface (vaporization rate model)

$$C_{rate} = \frac{m_{Cu} + \rho_{Cu} vol_1}{m_{Cu} + \rho vol_1} \tag{17}$$

Here, m_{Cu} [kg] is the generated mass of Cu and vol_1 [m^3] is the volume of the control volume of the gas on the electrode surface.

· Generated mass of metal vapor

$$m_{Cu} = v_{Cu} vol_2 \Delta t \tag{18}$$

In the equation above, v_{Cu} [$kg \cdot m^{-3} \cdot s^{-1}$] is the vaporization rate of Cu, vol_2 [m^3] is the volume of the control volume of the electrode on the electrode surface, and Δt [s] is the time step.

· Vaporization rate of Cu

$$v_{Cu} = \frac{h_{arc}(T - T_{Cu})}{Q_{Cu} L_{vol}} \tag{19}$$

Here, h_{arc} [W·m^{-2}·K^{-1}] is the heat transfer coefficient, which is assumed to be 10^5 according to Ref. [75]; however, the heat transfer coefficient between the arc plasma and electrode was calculated using the membrane temperature theory [76], which deduced the heat transfer coefficient according to the thermal conductivity of atmospheric gas. T [K] is the temperature; T_{Cu} [K] is the boiling point of Cu, which is 2,835 K; Q_{Cu} [J·kg^{-1}] is the heat of the phase change for Cu, which equals to the heat of melting sums heat of vaporization, which is 4,936 according to Ref. [75]; and L_{vol} [m] is the thickness of the control volume of the gas on the electrode surface.

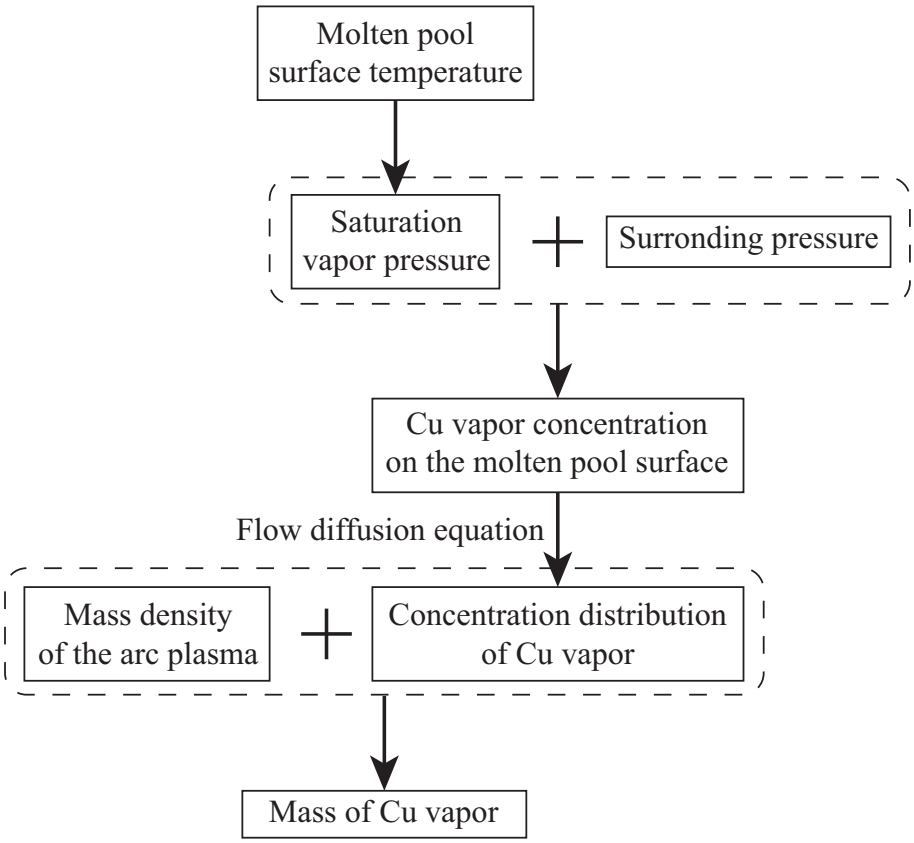

Fig. 16 Calculation flow of Cu vapor generation in saturation vapor pressure model.

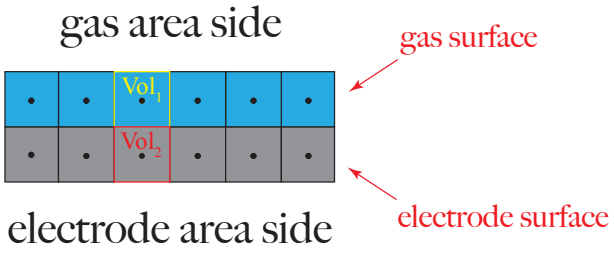

Fig. 17 Schematic of the control volumes on electrode surface [56].

2.3.2 Energy exchange on electrode surface

The energy conservation equation presented as Eq. 6 shows the general calculation of energy during the whole calculation area. The energy exchange between the arc plasma and electrode surface is considered and feedback to the energy equation as generation term during the calculation. The following equations show the heat conduction from arc plasma, ion heating (at the cathode side), electron cooling (at the cathode side), electron condensation heating (at the anode side), radiation emission, and vaporization and condensation on the electrode surface.

· Energy exchange on the cathode surface

$$q_C = \kappa \frac{\partial T}{\partial n_C} + j_i(E_{Air} - \phi_{Ce}) - j_e\phi_C - \varepsilon_C \alpha {T_C}^4 + S \tag{20}$$

· Energy exchange on the anode surface

$$q_A = \kappa \frac{\partial T}{\partial n_A} + j\phi_A - \varepsilon_A \alpha {T_A}^4 + S \tag{21}$$

· Current density of electron

$$j_e = AT^2 exp(-\frac{e\phi_{Ce}}{\partial kT}) \tag{22}$$

· Current density of ion

$$j_i = j - j_e \tag{23}$$

Where the q_C and q_A [W·m^{-2}] are the enthalpy flux on the cathode and anode surface, respectively. It will divide the length of control volume before feedback to the energy equation as a generic term, to maintain the consistency of the unit. n_C and n_A are the vertical direction of the cathode and anode surface, respectively. E_{Air} [eV] is the ionization energy of air, ϕ_{Ce} [eV] is the effective work function of cathode, ϕ_C and ϕ_A [eV] are the work function of cathode and anode, respectively. ε_C and ε_A are the surface emissivity of the cathode and anode, respectively. α[W·m^{-2}·K^{-4}] is the Stefan-Boltzmann constant, and T_C and T_A [K] is the temperature of cathode and anode surface, respectively. S [W·m^{-3}] is the energy source term of vaporization and condensation on the electrode surface, which will explain in detail at Eq. 25. A [A·m^{-2}·K^{-2}] is the Richardson-Dushman constant, e [C] is the elementary charge, and k [J·K^{-1}] is the Boltzmann constant.

The condensation of metal vapor is assumed to occur on the electrode surface when its temperature is less than the boiling point, as shown below.

· Condensation rate of metal vapor

$$n_{Cu} = CR_C(T_{vol1} - T_{Cu}) \tag{24}$$

Here, n_{Cu} [kg·m^{-3}·s^{-1}] is the condensation rate of Cu; R_C [kg·m^{-3}·s^{-1}·K^{-1}] is the coefficient of the condensation rate, which is assumed to be 1.0 according to Ref. [75]; and T_{vol1} [K] is the temperature of vol_1 as shown in Fig. 17 [56]. To consider the vaporization and condensation

on the electrode surface, the vaporization and condensation rates of Cu were used to calculate the energy source term.

· Energy source of metal vapor vaporization and condensation

$$S = -(v_{Cu} + n_{Cu})Q_{Cu} \tag{25}$$

The minus sign represents the energy loss of the electrode. The energy source term corresponds to Eq. 20 and Eq. 21.

2.4 Arc root model for simulating non-local thermal equilibrium effect on electrode surface

For considering the non-local thermal equilibrium effect on electrode surfaces, the effective electrical conductivity of a thin-layer element was adopted to calculate the electrical conductivity between the arc column and the electrode [77][78], which is described from Eq. 26 to Eq. 28. Moreover, the effective electrical conductivity was integrated with the electrical conductivity of control volume on the electrode surface for reflecting the effect of electrode fall voltage, because the sheath thickness (around 10^{-7} m) is smaller than the control volume length (2.5×10^{-4} m), which Fig. 18 [47] shows the diagram of this treatment.

· Effective electrical conductivity

$$\sigma_{eff} = J\frac{\Delta y}{U_s} \tag{26}$$

where σ_{eff} [S·m^{-1}] is the effective electrical conductivity, U_s [V] is the electrode fall voltage, and Δy [m] is the sheath thickness, which can be calculated using the Debye length as follow [79][80]:

· Sheath thickness

$$\Delta y = \frac{\sqrt{2}}{3}exp(\frac{1}{4})(ln\frac{eM}{2\pi m_e})^{\frac{3}{4}}\lambda_D \tag{27}$$

where M [kg·mol^{-1}]] is the atomic weight, m_e [kg] is the weight of an electron, and λ_D [m] is the Debye length.

· Debye length

$$\lambda_D = \sqrt{\frac{\varepsilon_0 kT_e}{n_e e^2}} \tag{28}$$

where ε_0 [F·m^{-1}] is the permittivity of free space, T_e [K] is the electron temperature, and n_e [m^{-3}] is the density of electrons.

The electrode fall voltage can be calculated using the electric potential difference between the sheath edge and the electrode surface as follows [80]:

· Electrode fall voltage

$$U_s = \phi_W - \phi_S = (\frac{kT_e}{2e})(ln(\frac{0.43M}{m_e}) - 1) \tag{29}$$

where ϕ_W [V] is the electric potential of the electrode surface and ϕ_S [V] is the electric potential of the sheath edge.

Based on the above equations, the effective electrical conductivity is determined by the atomic weight, the density of electrons, and electron temperature. The first two physical properties can be obtained at each calculation cycle. However, accurate calculation or measurement of the electron temperature on an electrode surface is difficult; therefore, a simple treatment of the electron temperatures on the cathode and anode surfaces was adopted. Specifically, the electrode fall voltages of the cathode and anode side are approximately 15 V and 5 V [81][82][83][84], respectively. Based on that research results, the electron temperatures on the

cathode and anode surfaces were set as 6,000 K and 2,000 K, respectively, for obtaining the above electrode fall voltages using Eq. 29. Under these settings in a stationary calculation, the electrode fall voltages of the cathode and the anode were 16.7 V and 5.56 V, respectively.

R: Resistance; L: Length of control volume; S: Area of control volume;
σ: Electrical conductivity; ρ: Electrical resistivity;
1: Sheath region; 2: Region beside sheath area

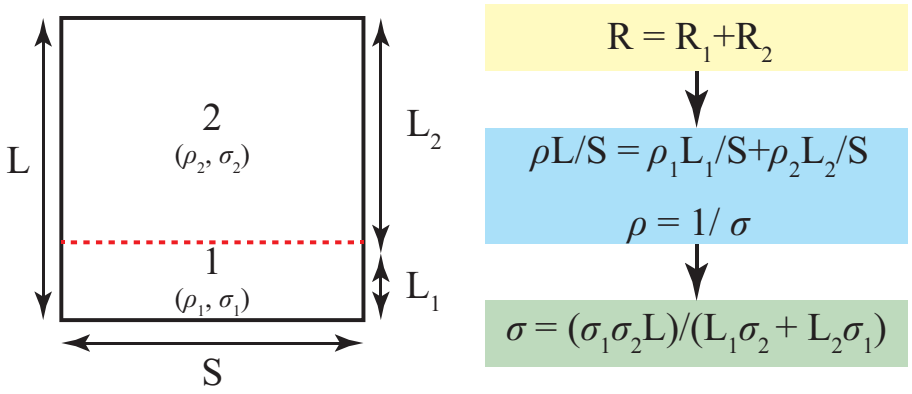

Fig. 18: Treatment of electrical conductivity of control volume on electrode surface for reflecting electrode fall voltage [47].

2.5 Thermal field theory application and current density setting on cathode surface

The current density contributions from the thermal and field emission are calculated separately and subsequently integrated. The thermal emission from the cathode surface is expressed as follows [45]:

· Richardson-Schottky formula

$$J_T = \frac{4\pi m_e e(k_B T)^2}{h_P^3} exp \frac{-e(\phi_C - \Delta\phi)}{kT} \tag{30}$$

where J_T [A·m^{-2}] is the current density derived from the thermal emission, h_P [J·s] is the Planck constant, and $\Delta\phi$ [eV] is the Schottky effect, which is described as follows:

· Schottky effect

$$\Delta\phi = (\frac{eF}{4\pi\varepsilon_0})^{\frac{1}{2}} \tag{31}$$

where F [V·m^{-1}] is the electric field applied on the electrode surface, which is determined by dividing the electrode fall voltage by the sheath thickness, as presented in Chapter. 2.4.

The current density component from the field emission, can be calculated using the following equation [48][49]:

· Fowler–Nordheim formula

$$J_F = \frac{e^3 F^2}{8\pi h_P \phi t(y)^2} exp(\frac{-8\sqrt{3m_e}\phi^{\frac{3}{2}} v(y)}{3h_P eF}) \tag{32}$$

where J_F [A/m^2] is the current density derived from the field emission, and $t(y)$ and $v(y)$ are distinct tabulated functions of the work function of the electrode and the electric field applied on the electrode surface, respectively, which are correspondingly set as 1.110721 and 0.

2.6 Calculation setting for simulating cathode spot movement

2.6.1 Current density distribution setting on cathode surface

Except for the non-local thermal equilibrium effect on the cathode surface, it is also necessary to implement a special treatment on the cathode surface for the cathode spot size. There were two different methods were implemented in this study.

Firstly, the cathode spot size was decided by the electrical conductivity distribution on the cathode surface as shown in Fig. 19 [44]. To be specific, the control volume which has the highest electrical conductivity on the electrode surface is located in every calculation cycle and the electrical conductivity of other control volumes is set to 0. Then the current density of this located control volume (J_0) is calculated and compares to the standard value ($J_T = 10^{10}$ A/m^2 [85]). If this current density is higher than the standard value, the electrical conductivity of the surrounding control volumes is removed, and their current densities are calculated base on their electrical conductivities and compare to the standard value as well. When the current density of the control volume is lower than the standard value, the size of the electrode spot is set.

Secondly, the cathode spot size was decided by the calculated current density based on thermal field emission theory as shown in Fig. 20 [47] (the schematic is a two-dimensional model for good understanding, whereas the used calculation model is a three-dimensional model). First, the current of the control volume that has the highest total current density based on the thermal field emission theory is calculated. Second, if this current is larger than the set current, then the current density of the control volume is calculated using the setting arc current and its cross-sectional area; otherwise, the currents of its peripheral control volumes are calculated. Third, the summarized current of these control volumes is compared with the setting arc current, and if the former is larger than the latter, the current density of the peripheral control volumes is calculated using the current difference and its area. Based on the above procedure, the size of the cathode spot is automatically adjusted in different conditions.

As for the anode side, the anode spot size was decided by the electrical conductivity distribution on the anode surface which is similar to Fig. 19 [44]. Except from the standard value of current density was set as $J_T = 10^6$ A/m^2 instead of $J_T = 10^{10}$ A/m^2.

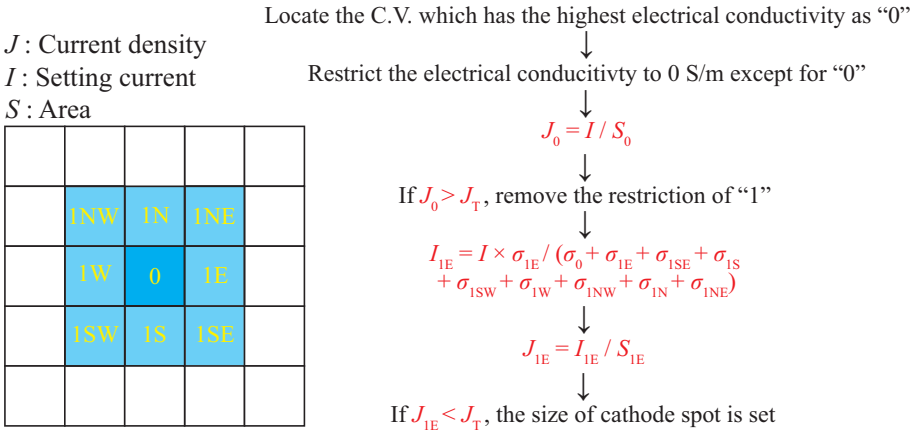

Fig. 19 Restriction of the electrical conductivity on electrode surface [44].

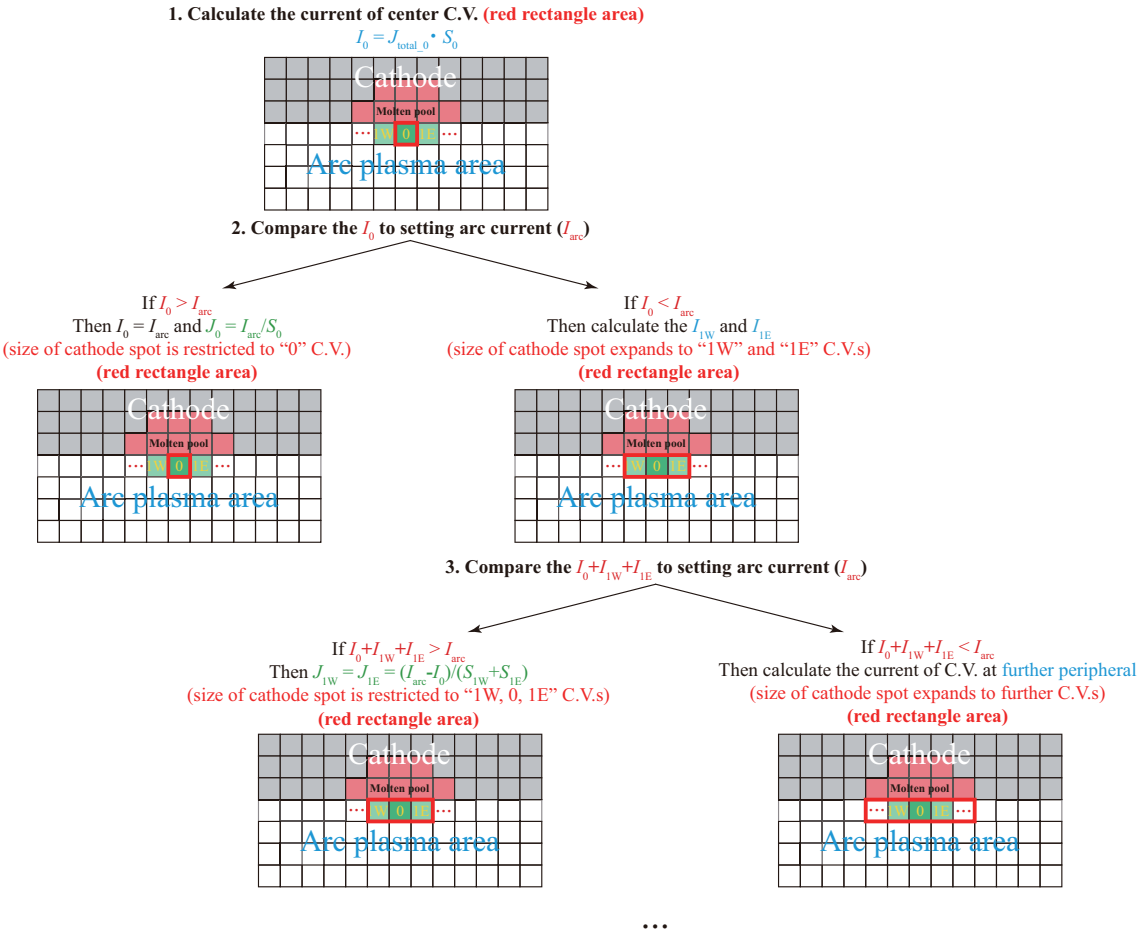

Fig. 20 Restriction method of current density on cathode surface at each calculation cycle [47].

2.6.2 Cathode spot advancement method

Because the calculation setting of the cathode spot size was based on two different methods, it has two different advancement methods as well.

In the case of cathode spot size was decided by the electrical conductivity distribution on the cathode surface, the cathode spot movement was assumed to be decided by the electrical conductivity distribution of the arc plasma area which near around the cathode surface as shown in Fig. 21. To be specific, the electrical conductivity of the control volume where two layers away from the cathode surface were compared, and the control volume which has the highest electrical conductivity was located. Then, the new center point of the cathode spot on the cathode will be set to have the same horizontal location based on the aforementioned control volume. The reason for this calculation setting is based on the mechanism of magnetic driven arc between two parallel electrodes [86]. By the above setting, the cathode spot based on the charged particle movement of arc plasma can be simulated.

In the case of cathode spot size was decided by the thermal field emission theory, the cathode spot movement was assumed to be triggered by the increment of field emission current density because of the charged particles' transport. To this end, a method of comparing the current density derived from the field emission to a threshold was proposed and shown in Fig. 22 [47]. To be specific, the field emission current density of control volume on the cathode surface is calculated and located in the center control volume which has the highest field emission current density. Then, the center control volume shifts to the control volume for which the current density derived from the field emission is larger than the threshold and the closest to the original center control volume on the advanced side. In this study, the threshold is set as 25%, 50%, or 75% of the current density derived from the field emission in the stationary calculation, which is 1.25×10^{13}, 2.5×10^{13}, or 3.75×10^{13} A/m^2, respectively, in the case of arc current was set as 50 A. The cathode spot keeps advancing by repeating the above steps. The reason for selecting 25%, 50%, or 75% as the current density threshold for cathode spot movement, is because the charged particles are transported forward under the influence of the electrical field derived from the self and external magnetic field. The transport of charged particles leads to the current density derived from the field emission keep increasing. However, the timing of the occurrence of cathode spot movement remains un-clarified, three thresholds were set in this study to simulate the cathode spot movement for finding out the feasibility and application scope of this calculation method.

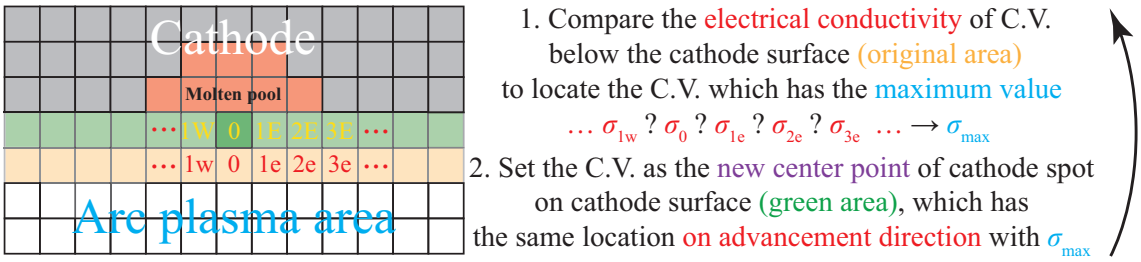

Fig. 21: Calculation setting for simulating cathode spot advancement based on electrical conductivity distribution at each calculation cycle.

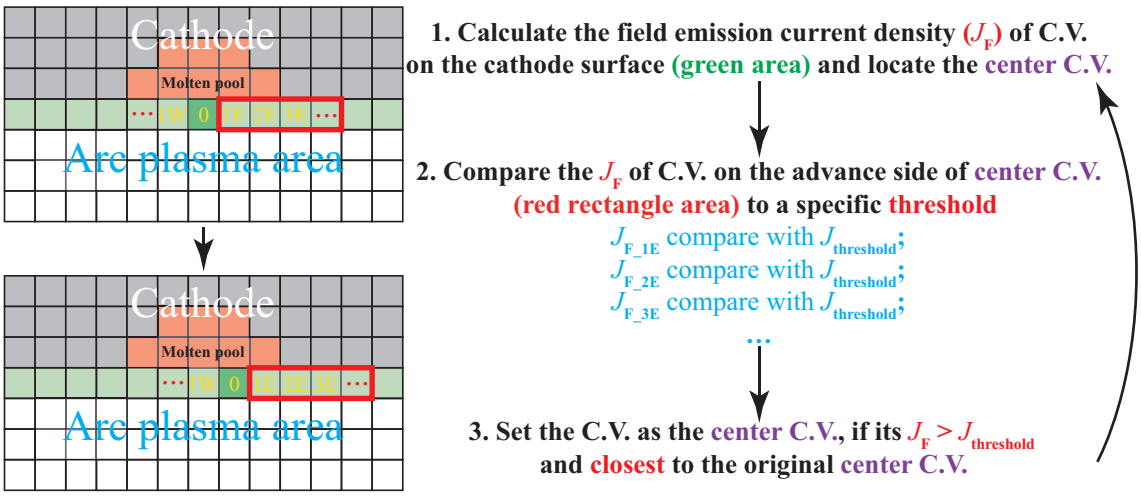

Fig. 22: Calculation setting for simulating cathode spot advancement based on thermal field emission theory at each calculation cycle [47].

2.7 Calculation setting for simulating re-strike phenomenon occurrence on anode side

2.7.1 Mimicking re-strike occurrence based on experiment figures

To simulate the re-strike phenomenon as similar as possible to the experimental result, the experimental figure of arc form right before the re-strike phenomenon occurrence is used as a sample to ignite the arc by setting a virtual arc as an initial value of the stationary calculation. To be specific, the thinning process has been performed on this figure by the photo processing software known as Popimaging and ImageJ. Based on the thinning process result, the control volumes are selected and their temperature is set to 15,000 K for creating a current path to generate the arc. The above process are shown in Fig. 23. To control the arc stagnates on the original anode spot, the electrical conductivity of the control volume on the anode surface is controlled after igniting the arc, and this process is shown in Fig. 24.

As for simulating the re-strike phenomenon, the calculation results of the stationary calculation are used as the initial values to run the transient calculation. Also, the electrical conductivity of the control volume at the anode surface is restricted to 0 S/m except for the original anode spot after the arc is ignited. After a given period, the restriction of the re-strike point area electrical conductivity is removed and the original anode spot area electrical conductivity is set to 0 S/m. The location of the re-strike point is set at $y = 15.10$ mm (in the case of without external magnetic field) and 8.75 mm (in the case of 3 mT external magnetic field applied) according to the experimental figures. To simulate the Cu vapor generated from the new anode spot after the re-strike phenomenon occurrence, the temperature distribution of the anode electrode in the stationary calculation is extracted and assigned to the new anode spot area after the re-strike phenomenon occurred (the cathode side has the same calculation setting as well). Fig. 25 shows the model of above setting process.

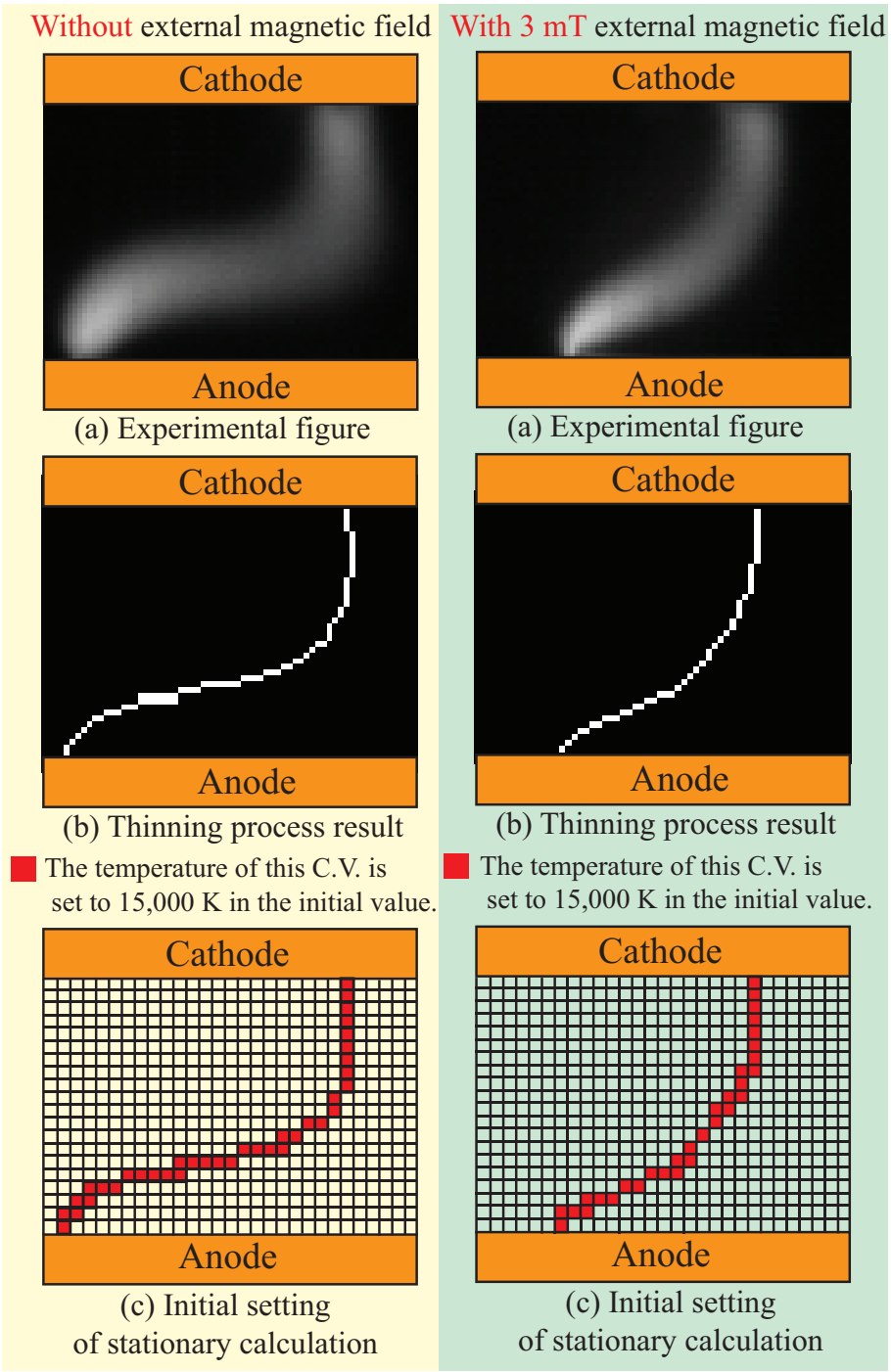

Fig. 23 Setting process of the virtual arc as an initial value at stationary calculation.

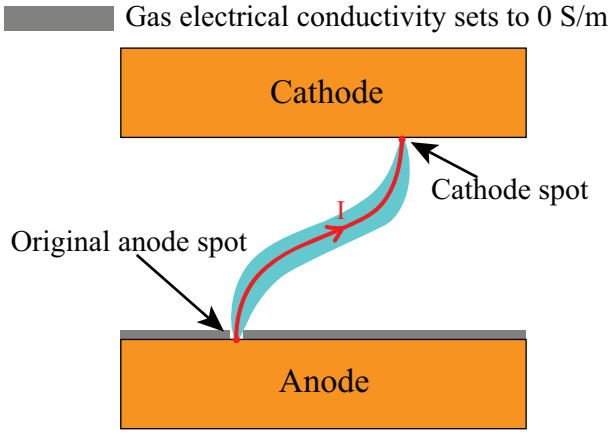

Fig. 24 Schematic of electrical conductivity control setting at stationary calculation.

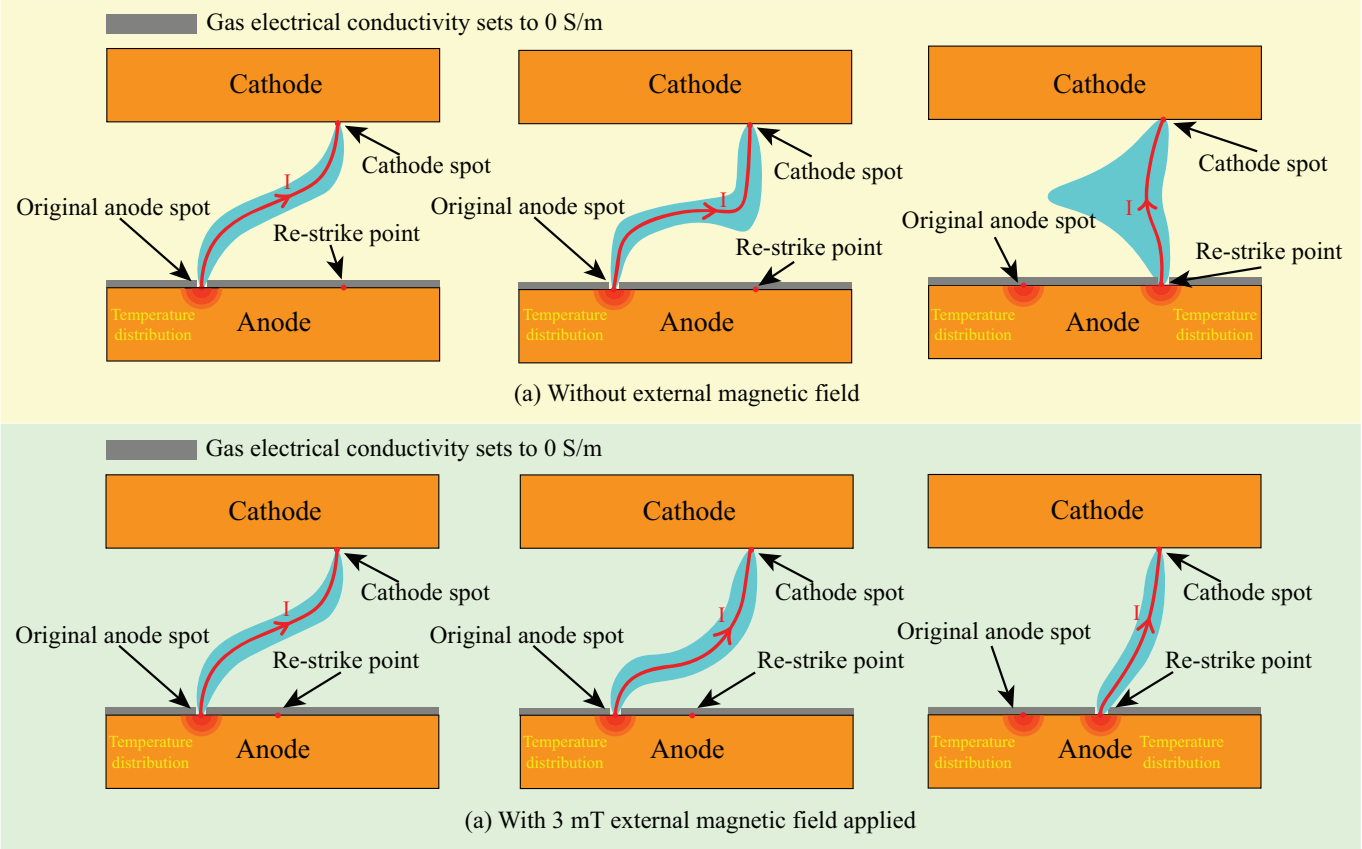

Fig. 25 Setting process of simulating the re-strike phenomenon at transient calculation.

2.7.2 Re-strike phenomenon based on electrical conductivity distribution

Moreover, the electrical conductivity distribution on the anode surface will be influenced by the charged particles' movement which is feedback as the effective electrical conductivity. Therefore, the re-strike phenomenon occurrence based on the electrical conductivity variation on the anode surface was simulated as well. To be specific, the electrical conductivity of the control volume on the anode surface was calculated, and locate the center control volume which has the highest electrical conductivity. Then, the center control volume shifts to the control volume that has the maximum electrical conductivity on the anode surface, while being closest to the original center control volume, as illustrated in Fig. 26 [47].

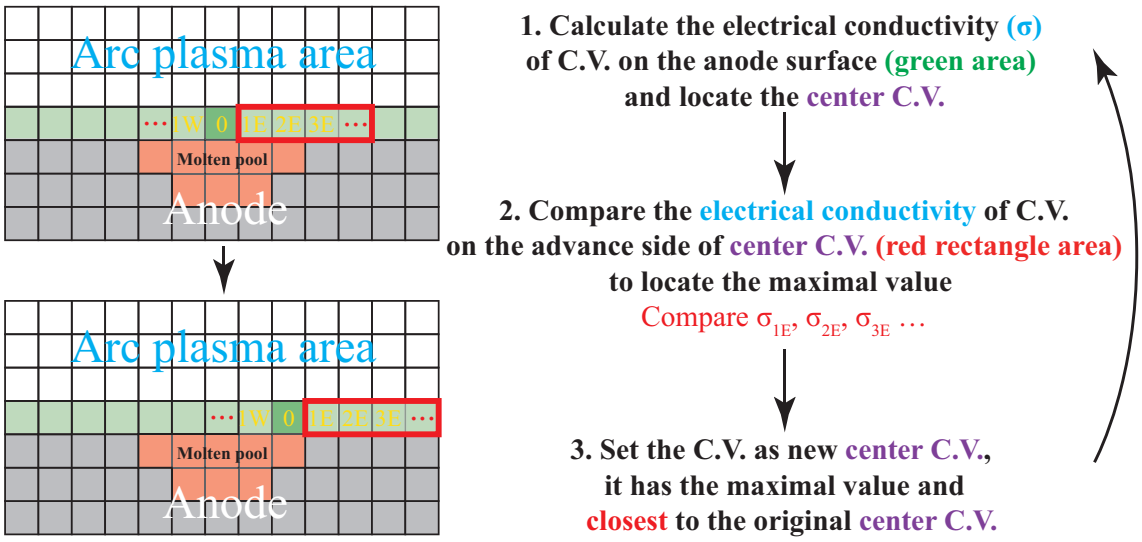

Fig. 26: Calculation setting for simulating re-strike phenomenon occurrence based on electrical conductivity distribution at each calculation cycle [47].

2.7.3 Thermal non-equilibrium model for analyzing physical property variation before re-strike occurrence

For analyzing the triggering factor of the increment in the electrical conductivity and causing the re-strike phenomenon, the simulation results (local thermal equilibrium model) at the time immediately before the re-strike phenomenon occurrence are used as the initial values to implement the thermal non-equilibrium model. The time step is set as 10 μs for capturing the temperature variation. Specifically, the electron and heavy particles (ions and neutral particles) temperatures are calculated using different energy conservations, as expressed as follows [50][51][87][88][89][90][91].

· Energy conservation equation of electrons

$$\begin{aligned} & \frac{\partial(n_e v \frac{5}{2} k_B T_e)}{\partial t} + \bigtriangledown \cdot (n_e v \frac{5}{2} k_B T_e) \\ = \; & - \bigtriangledown \cdot (-\kappa \bigtriangledown T_e) - E_{eh} - Q_{rad} + \sigma E^2 \end{aligned} \tag{33}$$

where E_{eh} [J] is the energy exchange between the electrons and heavy particles (ions and neutral particles), which can be described as follows:

· Energy exchange between electrons and heavy particles

$$\begin{aligned} E_{eh} = & \sum_{j \neq e} \frac{3}{2} k_B (T_e - T_h) \frac{2 m_e m_h}{(m_e + m_h)^2} \\ & \times n_e n_h \pi \overline{\Omega_{eh}} \sqrt{\frac{8 k_B T_e (m_e + m_h)}{\pi m_e m_h}} \end{aligned} \tag{34}$$

where T_h [K] is the heavy particles (ions and neutral particles) temperature, m_h [kg] is the mass of a heavy particles (ions and neutral particles), and n_h [m^{-3}] is the number density of heavy particles (ions and neutral particles), $\pi\overline{\Omega_{eh}}$ [m^2] is the cross-section between the electrons and the heavy particles (ions and neutral particles).

· Energy conservation equation of heavy particles

$$\frac{\partial \rho h}{\partial t} + \bigtriangledown \cdot (\rho v h) = - \bigtriangledown \cdot (-\frac{\kappa}{C_p} \bigtriangledown h) + E_{eh} \tag{35}$$

2.8 Calculation method and setting for mimicking DCCB interruption process

2.8.1 Preliminary stage of DCCB interruption process

For simulating the metal vapor generated from the molten metal bridge, two transient programs with different time steps are used. To be specific, the first transient program has a one-time step which was 6.94 s to mimic the temperature increases from 300 K to 2,835 K, which is the boiling point of electrode material in this study (copper). The diagram of this phase was presented in Fig. 27, and the temperature distribution of the electrodes right before the breaking of the molten metal bridge can be obtained as the simulation result of this transient program.

As for the second transient program, its time step was set as 6.25, 8.00, 12.5, or 25.0 μs for catching the swift variation of the arc plasma phenomenon and its physical property variation. In this transient program, the cathode moves upward 1 control volume (which is a 0.25 mm cube) from the second to ninth time step to mimic the electrode opening process as shown in Fig. 28, in which the electrode opening velocity was 40, 30, 20, or 10 m/s based on the setting time step. To maintain the continuance of the physical properties on the cathode surface after each movement, the physical properties of control volumes on the cathode surface were calculated using the values of its previous location as initial values, such as A base on a, B base on a, and C base on b as presented in Fig. 28(b).

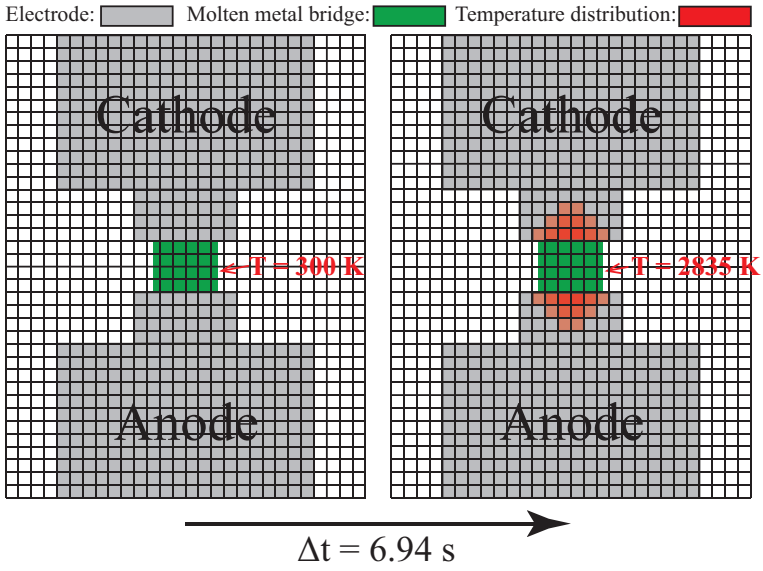

Fig. 27: Diagram of simulation setting for obtaining temperature distribution of electrodes after the molten metal bridge is broken.

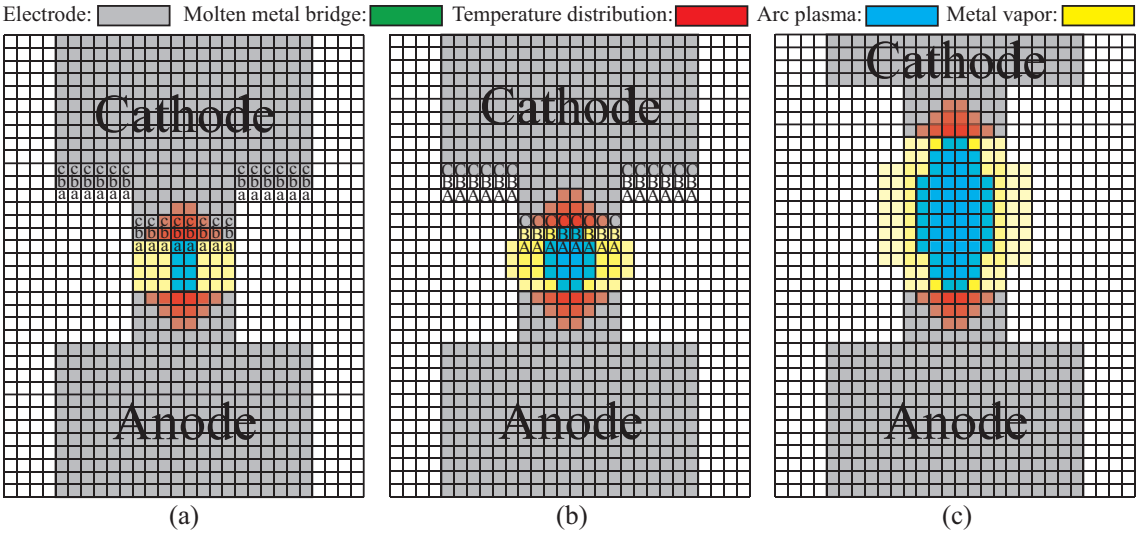

Fig. 28: Diagram of simulation setting for mimicking electrode opening process. (a) First time step. (b) Second time step. (c) Ninth time step.

2.8.2 Application of recovery voltage during DCCB interruption process

For simulating the effect of recovery voltage (RV) on the arc plasma extinguish process, the current of the cathode section was 2.5 mm away from the cathode convex was referenced to decide whether to apply the RV or not. The arc plasma tends to re-strike or reignite between the electrodes in the inter-electrode area which has a high residue temperature even after the arc plasma is stretched into the extinguishing chamber. To be specific, the total resistance of the inter-electrode area was calculated, and the instantaneous recovery current caused by the application of recovery voltage can be obtained. Then, the current density distribution of the inter-electrode area was decided based on the instantaneous recovery current and the electrical conductivity of each control volume in this area, as shown in Fig. 29.

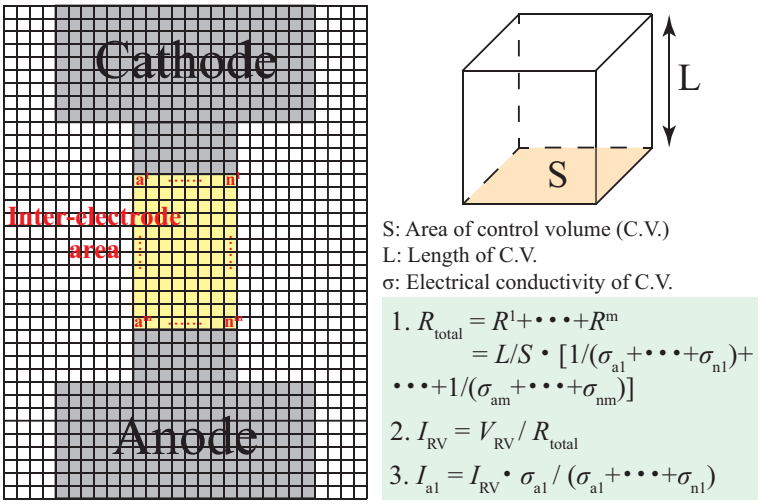

Fig. 29 Diagram of calculation method of recovery voltage application.

Chapter3 Behavior of atmospheric arc plasma between parallel electrodes with external magnetic field application

3.1 Cathode spot movement of atmospheric arc plasma after ignition

3.1.1 Stagnation of cathode spot in the case of without or with a weak external magnetic field applied

For verifying the hypothesis model (a) and (b) of Chapter 1.4.2, the current density and electromagnetic force of the cathode spot area were analyzed in the case of inter-electrode distance is 5 mm and arc current is 10 A in a straight current path model. Fig. 30 [44] shows the temperature distribution with applying 0 or 0.05 mT external magnetic field. The cathode spot did not move in both circumstances, and the current density and electromagnetic force of the cathode spot area were shown in Fig. 31 [44] and Fig. 32 [44]. It can see that the current densities of the two side control volumes were approximately equal in the case without an external magnetic field applied, and the difference in the current density between these two side control volumes increased when a 0.05 mT external magnetic field was applied, because the charged particles are transported by the external magnetic field and moved forward. Also, the electromagnetic force on the right side control volume became weaker when a 0.05 mT external magnetic field was applied, however, its direction still pointed against the advanced direction, which prevents the cathode spot from advancing. As a result, the directions of electromagnetic force on the two sides of the cathode spot were opposite, which forms an electromagnetic force balance and leads to the cathode spot remaining in stagnation.

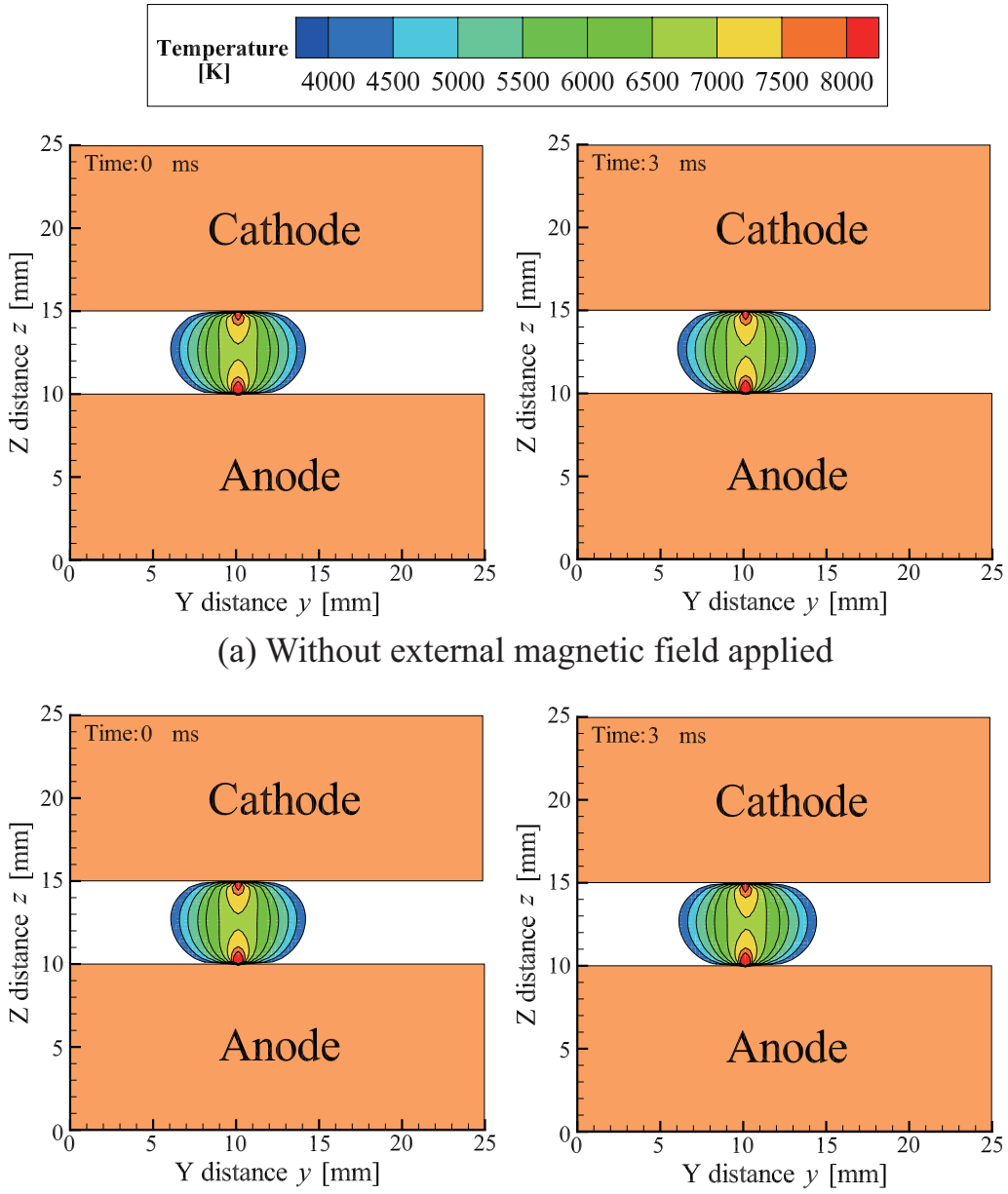

Fig. 30: Temperature distributions with different applied external magnetic field density [44]. (Current path model: straight, arc current: 10 A, applied external magnetic field density: 0/0.05 mT)

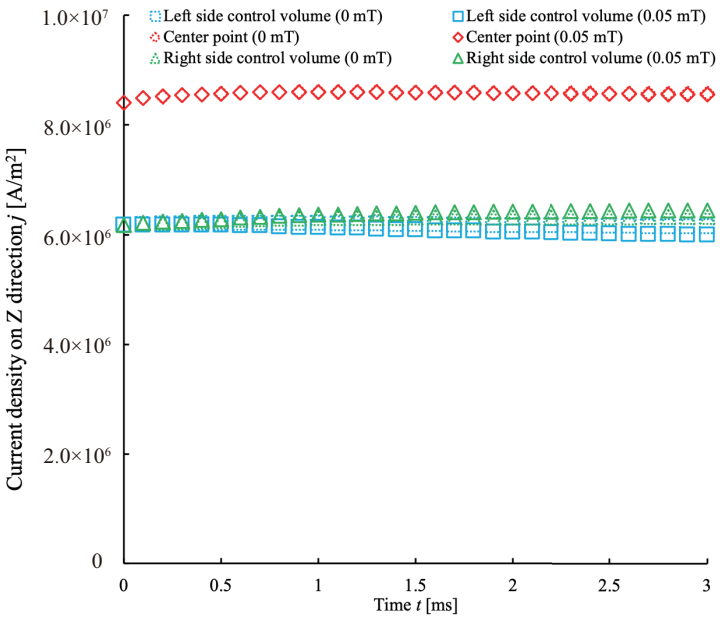

Fig. 31: Current densities of cathode spot area with different applied external magnetic field density [44].
(Current path model: straight, arc current: 10 A, applied external magnetic field density: 0/0.05 mT)

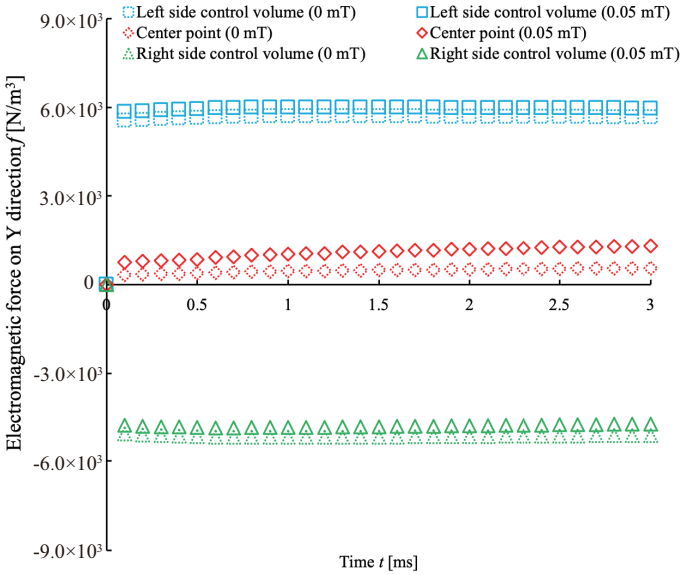

Fig. 32: Electromagnetic forces of cathode spot area with different applied external magnetic field density [44].
(Current path model: straight, arc current: 10 A, applied external magnetic field density: 0/0.05 mT)

3.1.2 Movement of cathode spot in the case of with strong external magnetic field applied

As for verifying the hypothesis model (c) of Chapter 1.4.2, the temperature and current density distribution of the cathode spot area in the case of inter-electrode distance is 5 mm and arc current is 30 A in a straight current path model with applied 1 mT external magnetic field density were presented in Fig. 33 [44], it can see that the cathode spot advanced. Fig. 34 [44] shows the electromagnetic force of the cathode spot area during the cathode spot advance process. It can see that the cathode spot first step (C.S.F.S.) occurred when the direction of electromagnetic force on the right side control volume points forward.

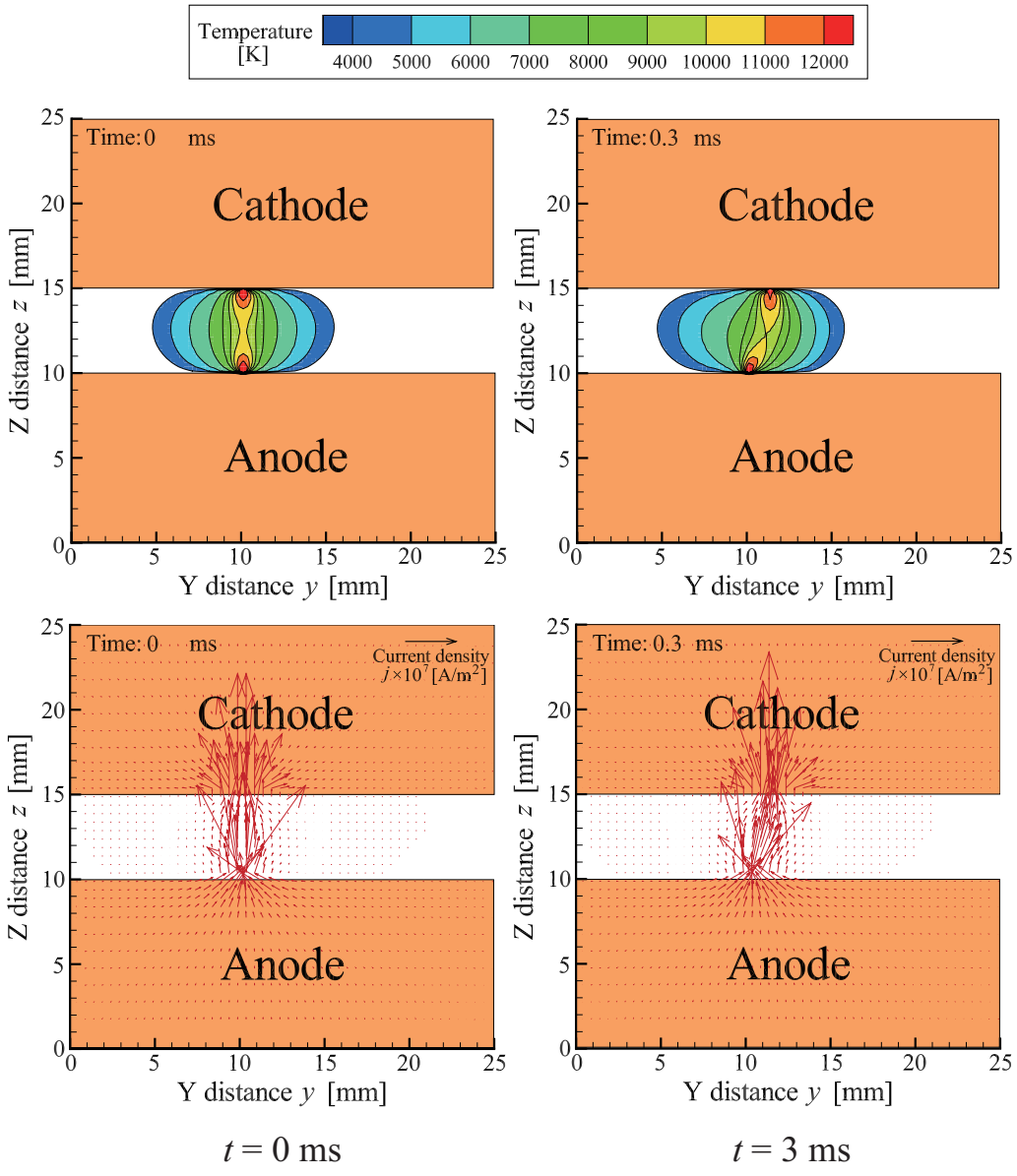

Fig. 33: Temperature and current density distributions in the case of applying 1 mT external magnetic field density [44].
(Current path model: straight, arc current: 30 A, applied external magnetic field density: 1 mT)

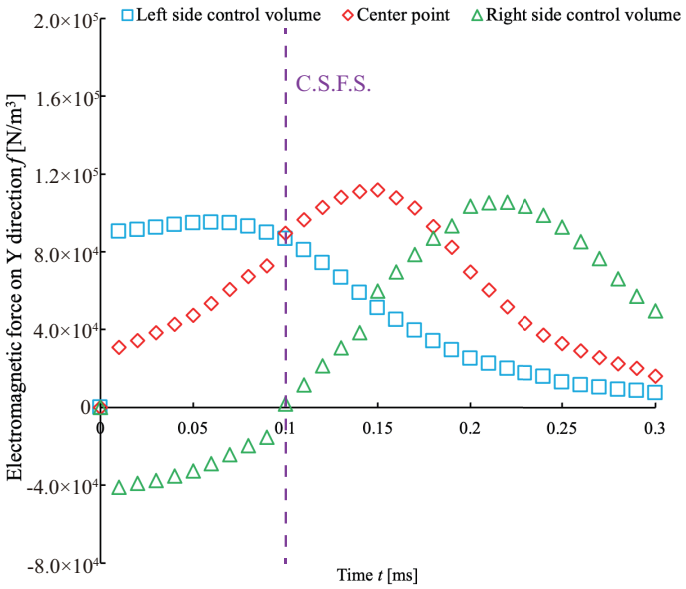

Fig. 34: Electromagnetic forces of cathode spot area in the case of applying 1 mT external magnetic field density [44].
(Current path model: straight, arc current: 30 A, applied external magnetic field density: 1 mT)

3.1.3 Dominating factor of cathode spot movement

For finding out the change of electromagnetic forces of the cathode spot area which causes the cathode spot advancement, the self and external electromagnetic force of the cathode spot area in the case of 0.05 mT (10 A) or 1 mT (30 A) applied at straight current path model were analyzed and shown in Fig. 35 [44] and Fig. 36 [44]. According to Fig. 35 [44] and Fig. 36 [44], it can see that the self electromagnetic force is in domination on the cathode spot area no matter the cathode spot advanced or not. Therefore, the effect of the external electromagnetic force is to transport the charged particles forward and broke the electromagnetic force balance which is formed by the self electromagnetic force derived from the arc plasma itself. As a result, the cathode spot's first step occurred when the direction of total electromagnetic force on the right side of the cathode spot pointed forward.

The comparison of C.S.F.S. velocity (the length of control volume divides the time of C.S.F.S. occurrence) between straight and reentry current path in the case of applied 1 mT external magnetic field was shown in Table 3 [44]. It can see that the C.S.F.S. occurred faster in the case of the reentry current path model, because the self electromagnetic force was increased due to the magnetic field derived from electrodes which promote the cathode spot movement. The comparison of self electromagnetic force of these two current path models in the case of 30 A was shown in Fig. 37 [44].

According to Table 3 [44], the rapid of C.S.F.S. significantly increased along with the arc current increasing, because the increments of self and external electromagnetic forces benefit the charged particles transport forward. Fig. 38 [44] and Fig. 39 [44] show the comparison of self and external magnetic force of cathode spot area in different arc current when the current path is straight. It can see that the increment of external electromagnetic force was slight and the increment of self electromagnetic force was significant, which implies that the effect of the external electromagnetic force is to break the electromagnetic force balance and the velocity of the cathode spot is dominated by the self electromagnetic force.

Fig. 40 [44] shows the relation between flow velocity and electromagnetic force of right side control volume before C.S.F.S. occurrence in difference arc current and current path model. It can see that the electromagnetic force of the right side control volume before C.S.F.S. occurrence became stronger when the arc current became higher, because the cathode jet became stronger which obstructs the advance of charged particles. And the flow velocity was slower in the case of the reentry current path model, because the direction of the cathode jet became more forward-leaning.

Table 3 Velocity of cathode spot first step in different conditions (m/s) [44].

	Straight current path model	Reentry current path model
10 A	0.50	0.58
30 A	3.75	4.69
50 A	4.69	7.50
100 A	6.25	9.38
150 A	9.38	18.75

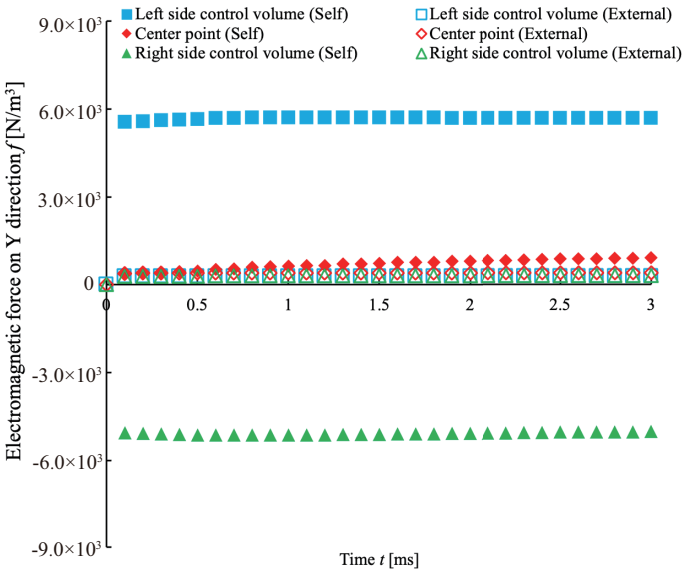

Fig. 35: Self and external electromagnetic force of cathode spot area with applied 0.05 mT external magnetic field density [44].
(Current path model: straight, arc current: 10 A, applied external magnetic field density: 0.05 mT)

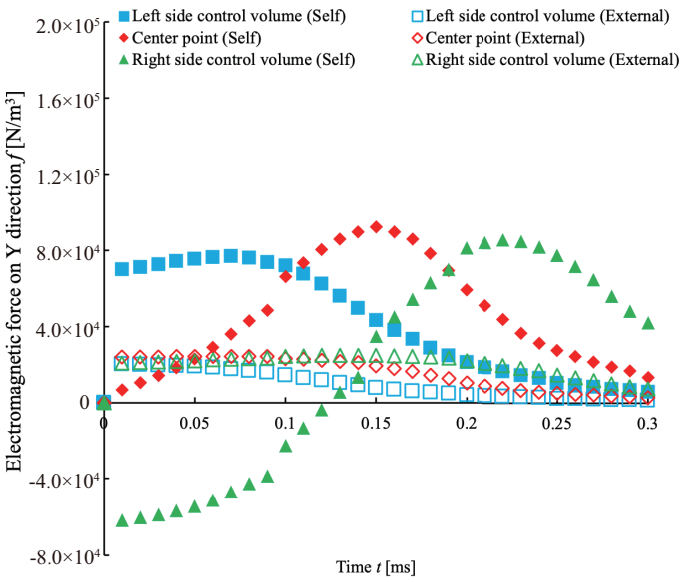

Fig. 36: Self and external electromagnetic force of cathode spot area with applied 1 mT external magnetic field density [44].
(Current path model: straight, arc current: 30 A, applied external magnetic field density: 1 mT)

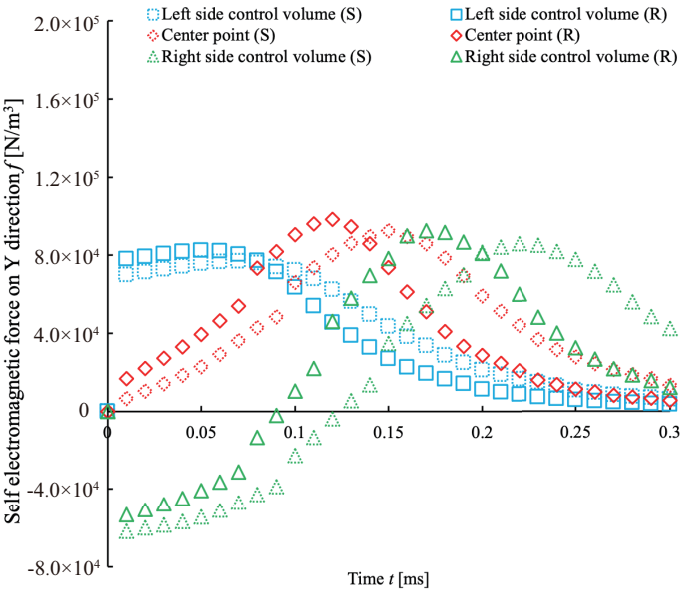

Fig. 37: Self electromagnetic force of cathode spot area in different current path models [44].
(Current path model: straight/reentry, arc current: 30 A, applied external magnetic field density: 1 mT)

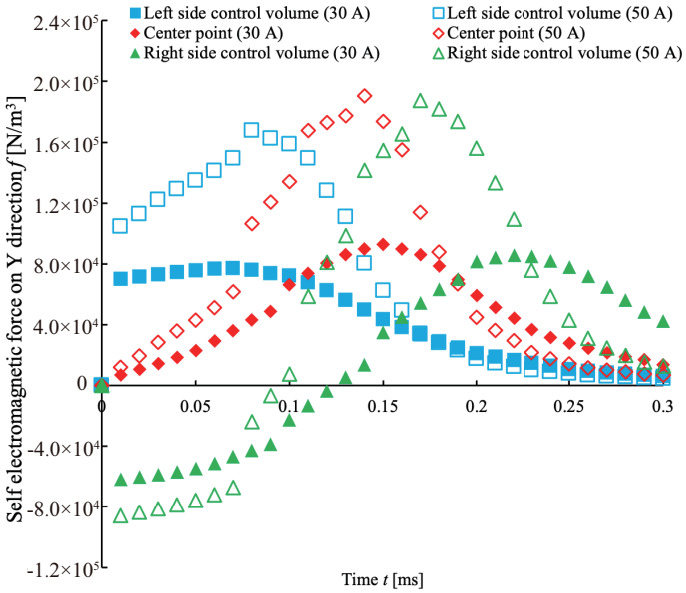

Fig. 38: Self electromagnetic force of cathode spot area in different arc current [44].
(Current path model: straight, arc current: 30/50 A, applied external magnetic field density: 1 mT)

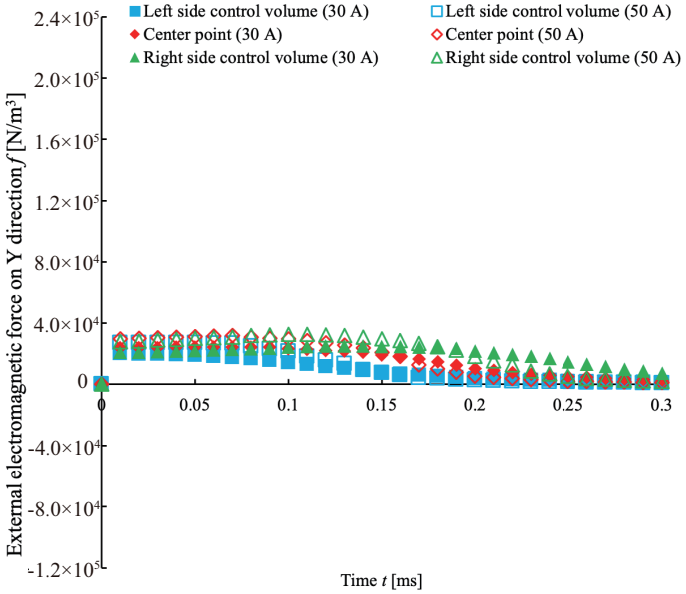

Fig. 39: External electromagnetic force of cathode spot area in different arc current [44].
(Current path model: straight, arc current: 30/50 A, applied external magnetic field density: 1 mT)

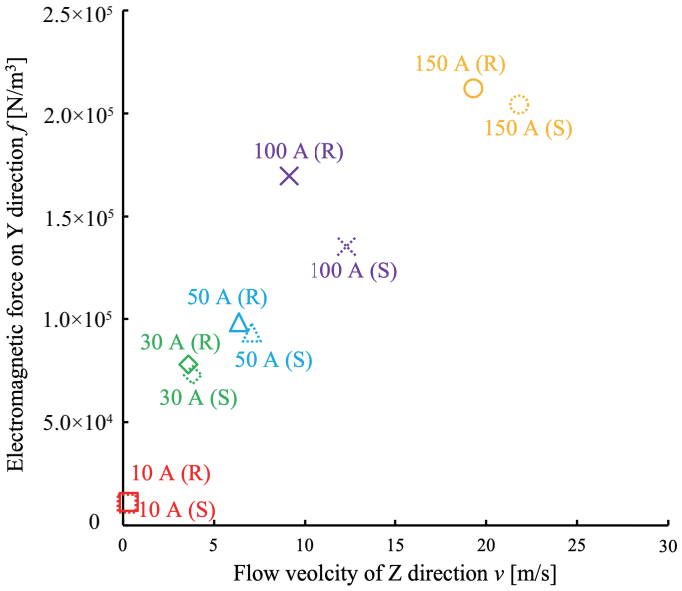

Fig. 40: Relation between flow velocity and electromagnetic force of right side control volume before C.S.F.S. occurrence in difference conditions [44].

3.2 Continuous cathode spot movement with applying external magnetic field

Based on the hypothesis presented in Chapter 1.4.2, the cathode spot movement is assumed to be governed by the charged particles, which are influenced by two factors in the cathode surface area. One is the electromagnetic force derived from the self or external magnetic field, which points to the advanced direction (right side in this study) and promotes the cathode spot movement. Another is the initial velocity of charged particles which reflects in the simulation result as a cathode jet, which points downward and obstructs the charged particles from moving forward. Therefore, the cathode spot velocity should increase with the threshold decrement because less charged particle transport is required. However, this tendency was incompatible in the case of the 25% threshold with 0 or 1 mT external magnetic field applied, as shown in Table 4 [47] which lists the cathode spot velocities in different scenarios.

For observing the influence of driving electromagnetic force and cathode jet to the cathode spot velocity by applying different external magnetic field intensities. The division factor (driving electromagnetic force divided by flow velocity of cathode jet), applied external magnetic field intensity, and cathode spot velocity is summarized in Fig. 41 [47]. The cathode spot velocity should be in proportion to the division factor regardless of the applied external magnetic field intensity, and this tendency was incompatible in the case of the 25% threshold with 1 or 3 mT external magnetic field applied. The reason for the deviation in the case of the 25% threshold was caused by the distribution of field emission current density of control volume on the cathode surface, in which the current density derived from the field emission of the control volume next to the center one was larger than 25% threshold (1.25×10^{13} A/m^2) even before the cathode spot movement. As a result, the calculated cathode spot velocity in the case of the 25% threshold became inaccurate. The analyzed results of cathode spot movement implied that the method of using field emission current density as a threshold to simulate the cathode spot movement has a minimum standard, which was 50% in this study.

Table 4 Cathode spot velocities in different cases [47].

Threshold	25%			50%			75%		
E.M.F.I.* [mT]	0	1	3	0	1	3	0	1	3
C.S.V.** [m/s]	3.33	9.60	49.0	4.71	9.81	45.7	4.58	9.44	43.5

* E.M.F.I.: External magnetic field intensity

** C.S.V.: Cathode spot velocity

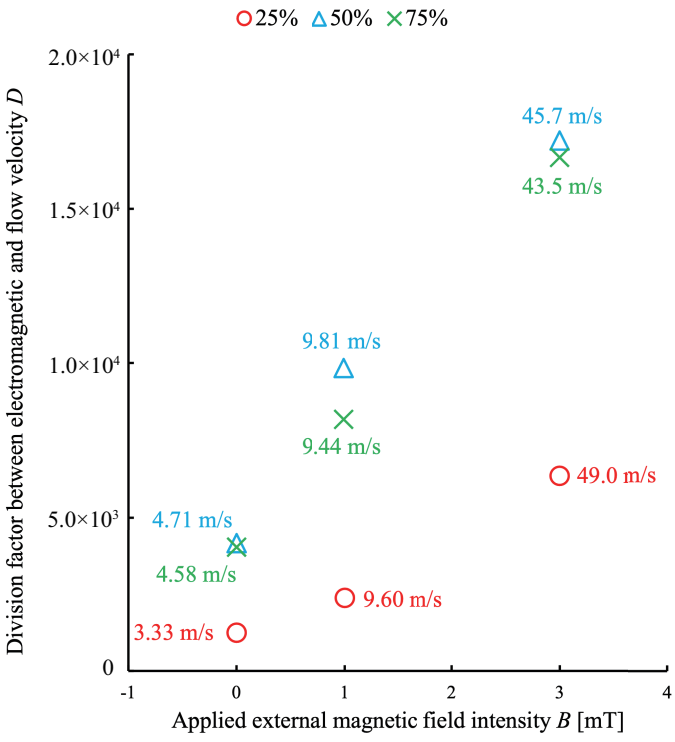

Fig. 41 Division factors between electromagnetic force and flow velocity in different cases [47].

3.3 Re-strike phenomenon of atmospheric arc plasma during advancement

3.3.1 Simulation result of re-strike phenomenon based on experimental figures

Based on the presented calculation setting in Chapter 2.7.1, the re-strike phenomenon was simulated based on experimental figures. According to the simulation results, a new anode spot appears on the re-strike point when the restriction removal time is 100 or 150 μs. The temperature distribution, electrical conductivity distribution, flow velocity distribution, and Cu vapor concentration distribution during the re-strike phenomenon when the restriction removal time is 100 μs are shown in Fig. 42 [43]. From the figure, it can be seen that the distribution of temperature and electrical conductivity are similar, which means that the electrical conductivity of the arc region is dominated by temperature. According to the flow velocity distribution, it can be seen that a vortex is formed because of the cathode and anode jets. Under the influence of this vortex-shaped flow velocity distribution, the high-temperature gas gets away from the anode surface around the original anode spot area, which leads to a reduction in the conductive area, and the current density of the original anode spot gets stronger. As a result, the original anode spot temperature keeps increasing, and the distance between the arc column and re-strike point becomes shorter because of the cathode jet, which increases the electric field strength, thus making it more likely for the re-strike phenomenon to occur. It can be observed that the flow velocity from the anode increases drastically when the new anode spot appears, which is the result of two effects: the formation of an anode jet due to the constriction of the new current path, and the gas expansion caused by the rapid heating of the arc column [92]. Cu vapor is generated from the electrode spots and diffuses into the arc area and its periphery under the influence of the vortex-shaped flow velocity distribution, which increases the electrical conductivity of those areas. The Cu vapor concentration over 1% of the area keeps expanding around the original anode spot because of the increase in the original anode spot temperature.

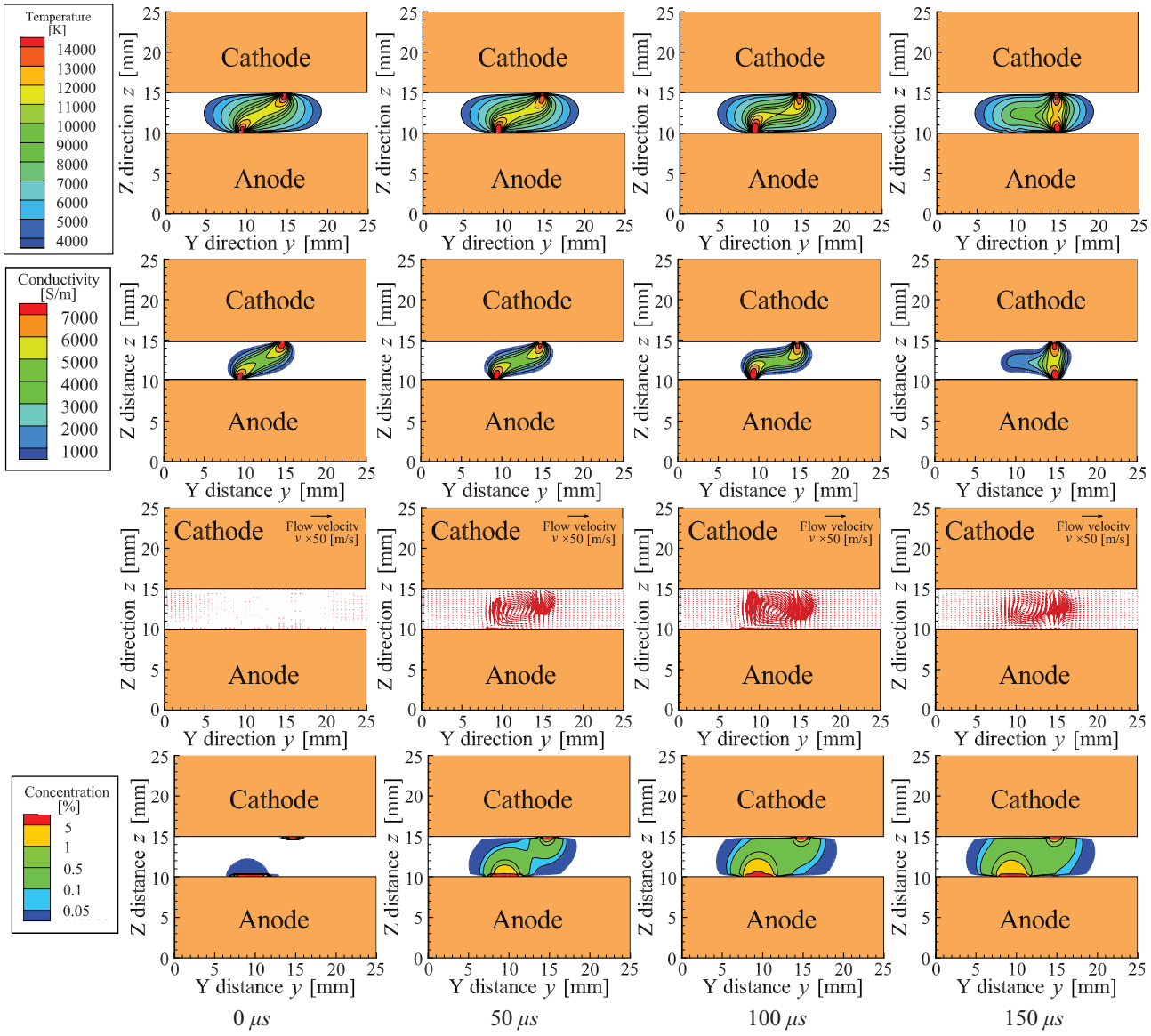

Fig. 42: Temperature distribution, electrical conductivity distribution, flow velocity distribution, and Cu vapor concentration of the magnetically driven arc during the new current path formed in the case where the restriction removal time is 100 μs [43].

3.3.2 Elucidate occurrence conditions of re-strike phenomenon based on experimental figures

Fig. 43 [43] presents the electrical conductivities of the spots immediately above the original anode spot and re-strike point ($z = 10.5$ mm), along with the time variable in the case where the restriction removal time is 100 μs. It can be observed that the electrical conductivity of the original anode spot area increases before the re-strike phenomenon occurs, because of the increase in the original anode spot temperature. The electrical conductivity of the re-strike point area increases drastically after the new anode spot appears. However, it barely changes before the re-strike phenomenon occurs; even the high-temperature gas and Cu vapor are transported toward the re-strike point area under the influence of the cathode jet. Fig. 44 [43] presents the temperature and Cu vapor concentration of the re-strike point area changes with time, which indicates that the increase in temperature and Cu vapor concentration is minimal and not sufficient to cause a significant increase in the electrical conductivity. In other words, the occurrence of the re-strike phenomenon is not dominated by the change of the electrical conductivity. Fig. 45 [43] shows that the electrical potential difference and the electric field density between the re-strike point and the arc column (the control volume with a temperature of 10,000 K, immediately above the re-strike point) when the arc stagnated on the original anode spot. According to Fig. 45 [43], the electrical potential difference between these two points remains constant as the electric field density increases, because of the decreasing distance between the two points. The electric field density is 30.9 V/cm and the distance is 2.35mm immediately before the re-strike phenomenon occurrence.

In case the restriction removal time is 50 μs, the same quantitative analysis can be done. From Fig. 46 [43], it can be observed that the electrical conductivity of the original anode spot area increased before the restriction was removed because of the increase in the original anode spot temperature. A rapid reduction in the area′s electrical conductivity is observed after the restriction of the re-strike point area electrical conductivity is removed and setting the original anode spot area′s electrical conductivity to 0 S/m, since no current passes through this area anymore. After 80 μs, the electrical conductivity remained steady because of the residual temperature on the anode surface even after the original anode spot disappeared. The electric field density between the re-strike point and arc column (the control volume whose temperature is 10,000K and immediately above the re-strike point) continues to increase when the arc stagnated on the original anode spot because the distance between those two points decreases and hence it is affected by the cathode jet. However, the electric field density was not strong enough (the electric field density is 24.9 V/cm and the distance is 2.75 mm) to cause an electrical breakdown when the restriction of the re-strike point area′s electrical conductivity is removed; therefore, a new current path cannot be formed and the current continuity is destroyed.

Based on the analysis of the simulation results, the process of the re-strike phenomenon can be described as follows: immediately before the re-strike phenomenon occurs, the arc form is affected by the electrode jets. The distance between the re-strike point and the arc column becomes short because of the cathode jet, which leads to an increase in the electric field density

between them. When the electric field density exceeds a certain value, electrical breakdown occurs and a new current path forms; along with this, the original anode spot disappears.

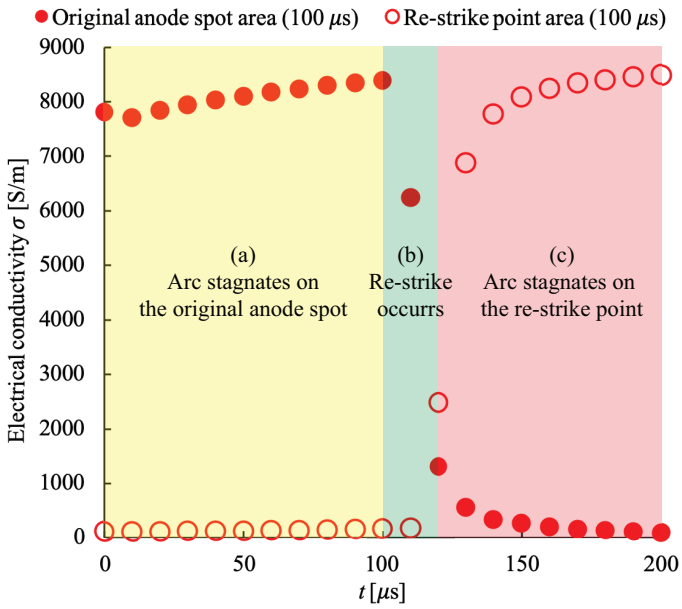

Fig. 43: Electrical conductivities of original anode spot area and re-strike point area when the restriction removal time is 100 μs [43].

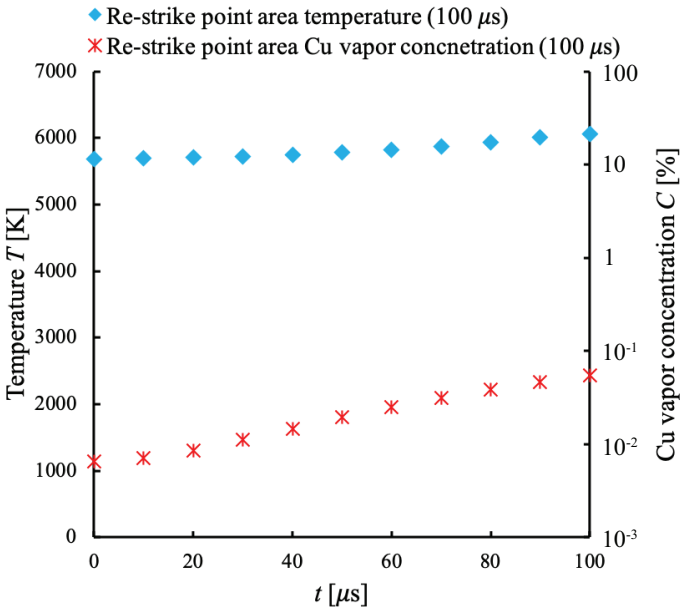

Fig. 44: Temperature and Cu vapor concentration of re-strike point area change with time when the restriction removal time is 100 μs [43].

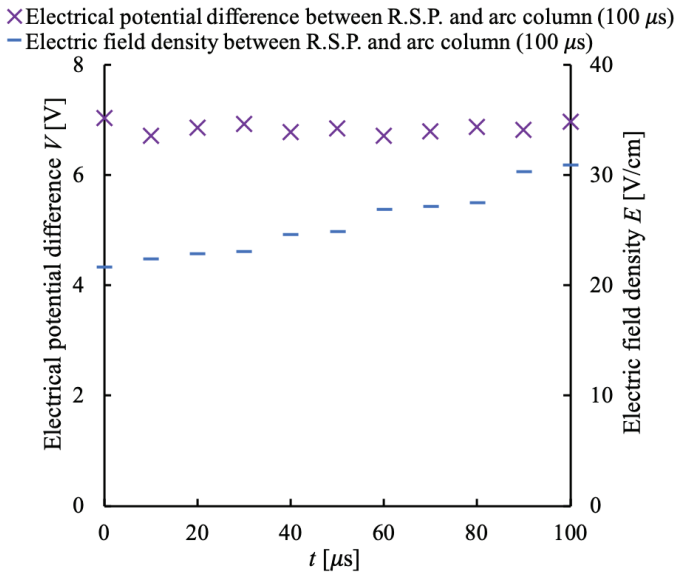

Fig. 45: Electrical potential difference and electric field density between the re-strike point and arc column when the restriction removal time is 100 μs [43].

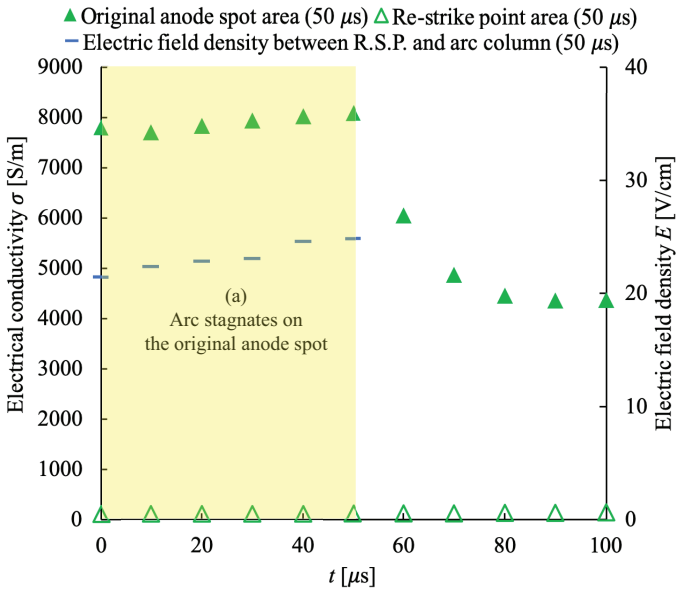

Fig. 46: Electrical conductivity and electrical field density change with time when the restriction removal time is 50 μs [43].

3.3.3 Occurrence of re-strike phenomenon based on electrical conductivity distribution and particles' temperatures variation

Fig. 47 [47] shows the temperature, metal vapor concentration, and current density variation of two re-strike phenomenon occurrences when using 50% of the current density derived from the field emission in the stationary calculation as the cathode spot movement threshold. This simulation of magnetically driven arc (with 1 mT applied external magnetic field) was under the assumption of local thermal equilibrium. A series of temperature residues existed on the cathode surface because of the remainder of the high concentration of the metal vapor even after the cathode spot advanced. This phenomenon did not occur on the anode side because the advanced strides and velocities of the cathode and anode spots were different. Moreover, the metal vapor concentration during anode spot advancement was transported toward the re-strike point area according to Fig. 47(b) [47], and this variation was caused by the influence of convection flow from arc plasma, which was dominated by the cathode jet as shown in Fig. 48 [47].

The simulation results show that the re-strike phenomenon can be simulated based on the electrical conductivity change on the anode surface. It can observe that the current density of the re-strike point area increased before the re-strike occurred as shown in the blue dotted line circle at Fig. 47(c) [47], which is decided by electrical conductivity and electrical field ($J = \sigma E$). Moreover, the high-temperature gas and metal vapor were transported toward the re-strike point area by a strong cathode jet according to Fig. 47(a) and (b) [47]. It is reasonable to assume the occurrence of the re-strike phenomenon was caused by electrical conductivity increment. For finding out the kind of charged particle for this current density increment, the simulation results of 0.7 ms (local thermal equilibrium model) were used as the initial values to implement the thermal non-equilibrium model as shown in Chapter 2.7.3. In this model, the electrical conductivity was calculated from the electron or heavy particles (ions and neutral particles) temperature. Fig. 49 [47] shows the current density distribution variation when the electrical conductivity was calculated based on electron temperature (Fig. 49(a) [47]), or the electrical conductivity was calculated based on heavy particles (ions and neutral particles) temperature (Fig. 49(b) [47]). The current density of the re-strike point area became high when the electrical conductivity was based on the heavy particles (ions and neutral particles) temperature as shown in the green dotted line circle in Fig. 49(b) [47], whereas the current density barely changed if the electrical conductivity was determined from the electron temperature as shown in the blue dotted line circle at Fig. 49(a) [47].

It was assumed that the current density increment is caused by the electrical conductivity increment because of the transport of high-temperature gas and metal vapor. Therefore, Fig. 50 [47] presents the variation of electrical conductivity in the re-strike point area with time, when it was based on the electron or heavy particles (ions and neutral particles) temperature. The electrical conductivity of the re-strike point area did not change when it was obtained from the electron temperature, whereas it increased when it was based on the heavy particles (ions and neutral particles) temperature. However, the increment in the electrical conductivity was small and insufficient to cause the occurrence of the re-strike phenomenon, which suggests

the reason for the current density increment of the re-strike point area was caused by the electrical field increment (based on $J = \sigma E$). Fig. 51 [47] shows the variation in the electron and heavy particles (ions and neutral particles) temperatures when the electrical conductivity was calculated based on the heavy particles (ions and neutral particles) temperature. The electron temperature distribution did not change according to Fig. 51(a) [47], whereas the heavy particles (ions and neutral particles) temperature distribution advanced along with time variation as shown in Fig. 51(b) [47]. This variation of temperature distribution suggests that the advance of the heavy particles (ions and neutral particles) led to the distance between the arc column and anode surface decreasing, and increased the electric field between the arc column and the anode surface, eventually causing the occurrence of the re-strike phenomenon.

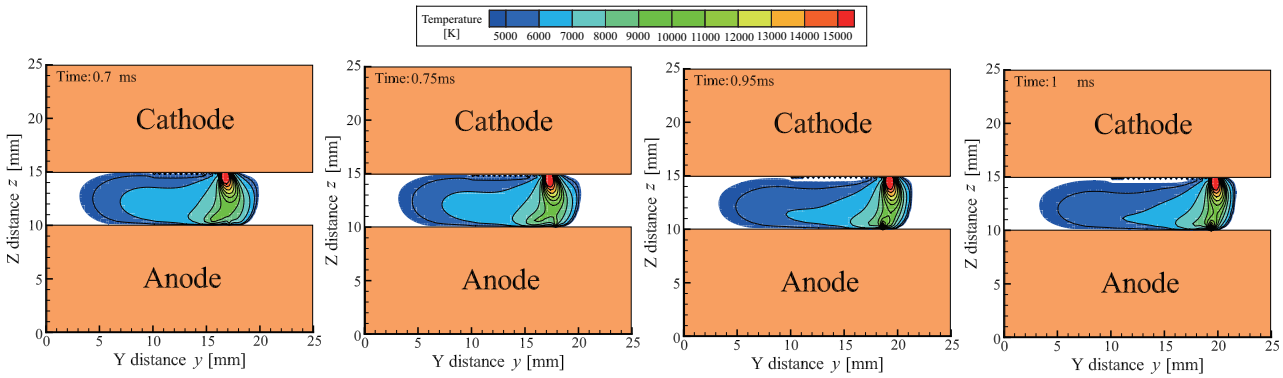

(a) Temperature distribution variation under assumption of local thermal equilibrium.

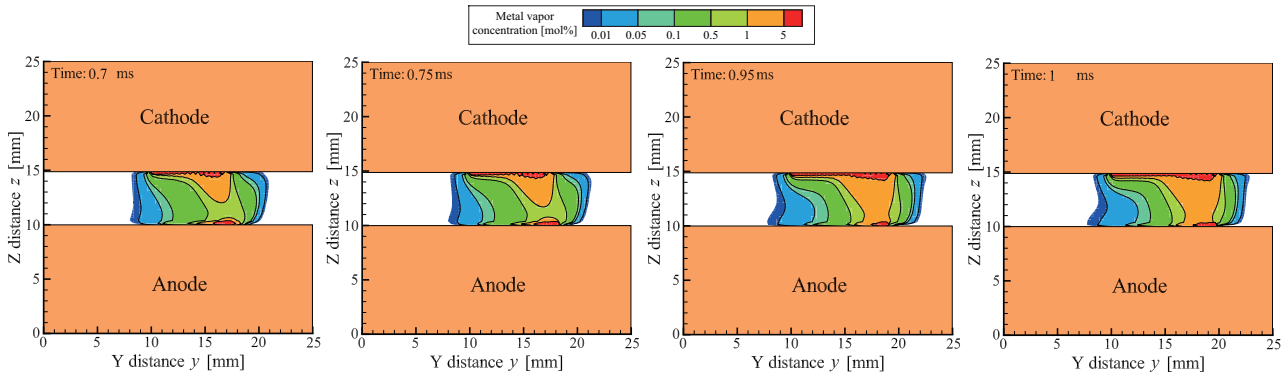

(b) Metal vapor concentration distribution variation under assumption of local thermal equilibrium.

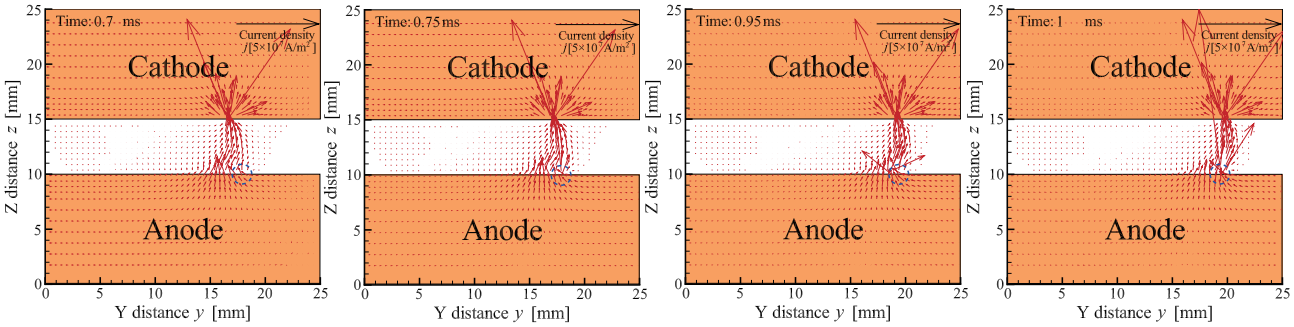

(c) Current density distribution variation under assumption of local thermal equilibrium.

Fig. 47: Temperature, metal vapor concentration and current density distribution of re-strike phenomenon under assumption of local thermal equilibrium [47].

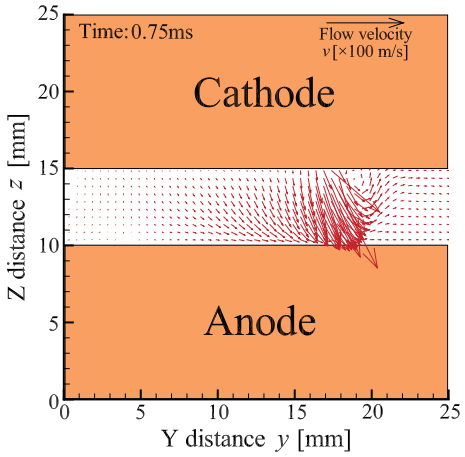

Fig. 48 Flow velocity distribution of magnetically driven arc [47].

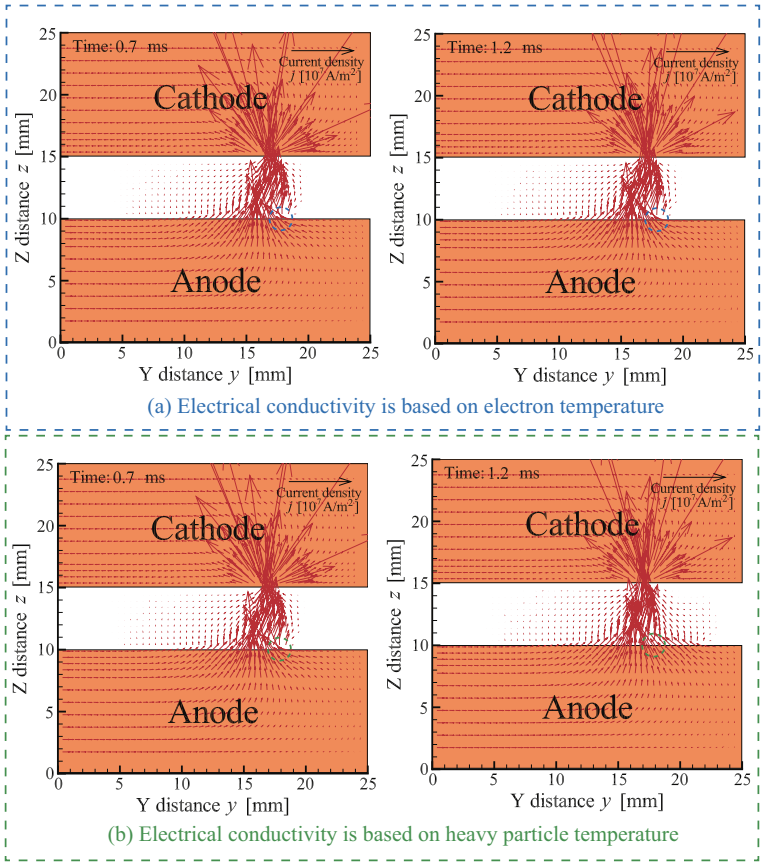

Fig. 49: Current density distribution of electrical conductivity based on electron or heavy particles temperature [47].

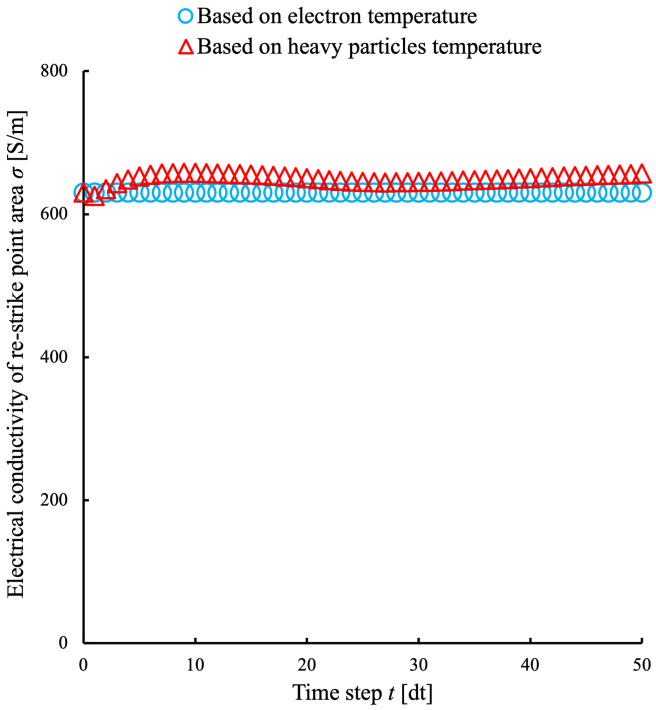

Fig. 50: Electrical conductivity variation in re-strike point area with time-based on different temperatures [47].

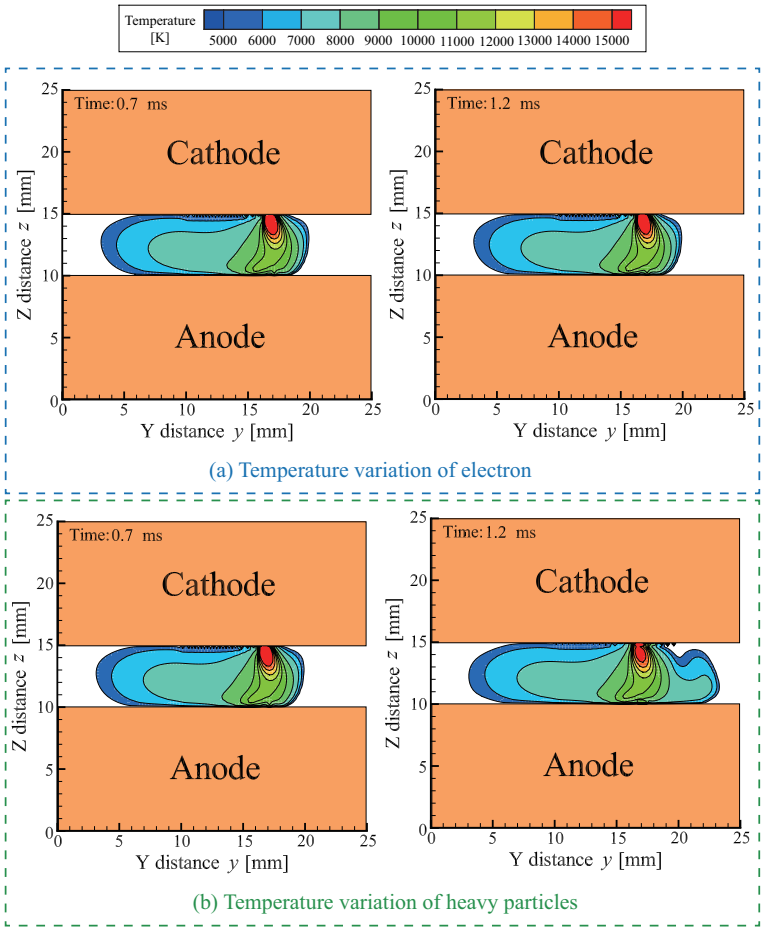

Fig. 51: Variation of temperature distribution of electron and heavy particles when electrical conductivity based on heavy particles temperature [47].

3.4 Comparison of simulation and experimental results

The calculation results of the temperature distribution and Cu vapor concentration distribution when the new anode spot appeared to resemble the experimental figures of the arc movement and Cu vapor movement(used a 520 nm bandpass filter), which indicates that this calculation can simulate the re-strike phenomenon accurately. Compare between the calculation results and experimental figures in the case of without external magnetic field and with 3 mT external magnetic field applied are shown in Fig. 52 and Fig. 53, respectively.

For verifying the appropriateness of the calculation models, experiments were conducted under the same setting conditions, and the experimental and photography conditions are shown in Table 5 [47]. The arc voltage is measured by an oscilloscope (Digital Phosphor oscilloscope DPO 4034 (Tektronix)). The experimental arrangement is shown in Fig. 54 [47], and the comparison of the arc voltages in different arc plasma lengths obtained from simulation and experiments is displayed in Fig. 55 [47]. Numbers 1-11 in Fig. 55 [47] correspond to the experimental figures of arc plasma during its advancement that is presented in Fig. 56 [47], where the top figures are the original figures and the bottom ones are the results of the thinning process. Fig. 57 [47] shows the location of experimental figures on the arc voltage waveform, and the voltage value in Fig. 57 [47] is the voltage of arc column which equals to the total arc voltage minus the electrode fall voltage for showing the voltage fluctuates.

From the experimental results, the total electrode fall voltage of the cathode and the anode can be calculated using the arc plasma length and its voltage, as presented in Fig. 55 [47], and the obtained value was 23.4 V. In the simulation, the electrode fall voltages of the cathode and the anode were obtained as 16.7 V and 5.56 V, respectively. Hence, the simulation total electrode fall voltage of the cathode and the anode was 22.3 V, which was similar to the experimental result.

However, the length of the re-strike stride between the original anode spot and the re-strike point was shorter than the experimental result, which suggests that the calculation setting of the anode spot movement based on the maximum electrical conductivity on the anode surface is insufficient, and further consideration of the stagnation of the anode spot is required.

Table 5 Experimental and photography conditions [47].

Experimental condition		Photography conditions	
Arc current	DC 50 A	High speed video camera	FASTCAM-NOVA S6
Environment gas	Air	Photography speed	40,000 fps
Inter-electrode distance	5 mm	Pixel	640×240
Length of electrode	300 mm	F-value	11
Angle of electrode	90°	Neutral density filter	ND400, ND4

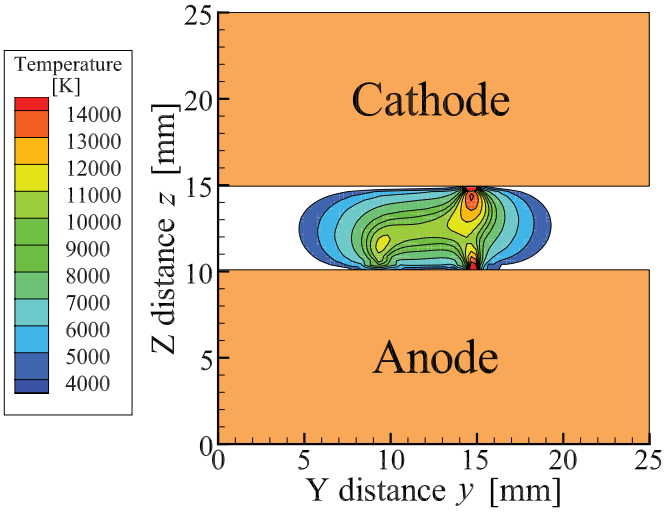

Temperature distribution of calculation result

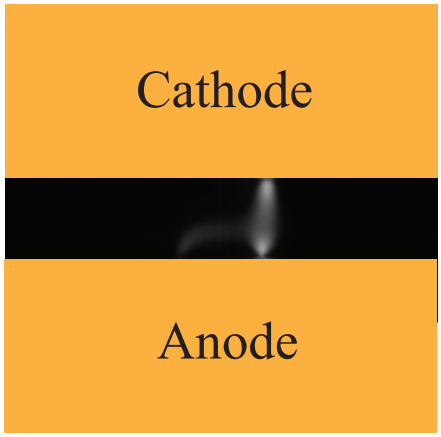

Arc movement of experimental figure

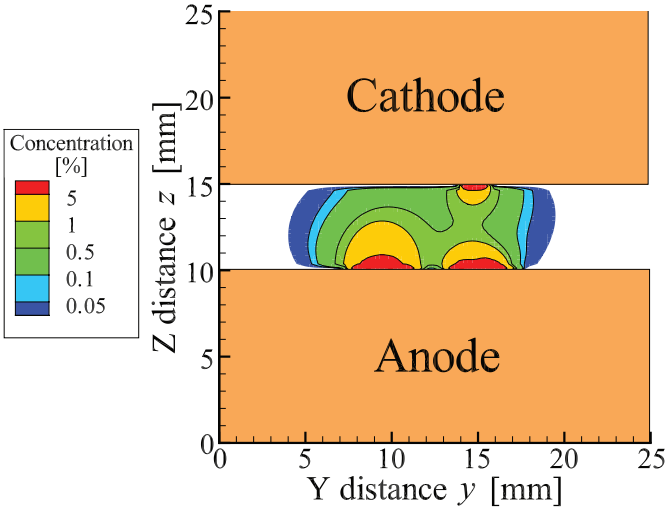

Cu vapor concentration distribution of calculation result

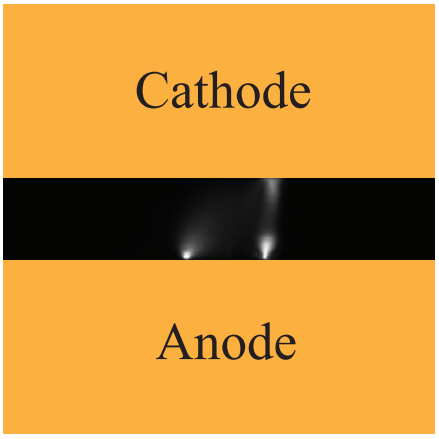

Cu vapor movement of experimental figure

Fig. 52: Compare the calculation results and experimental figures in the case without an external magnetic field.

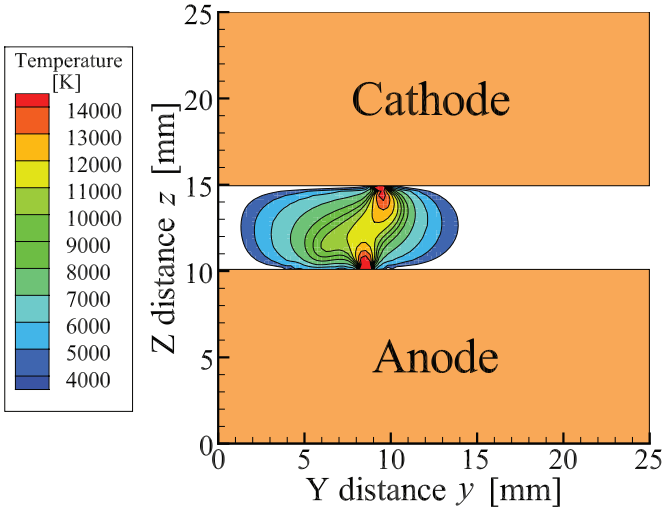

Temperature distribution of calculation result

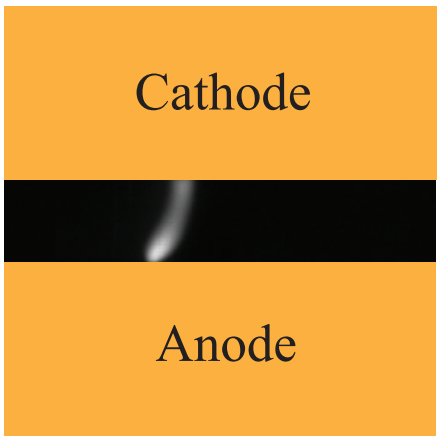

Arc movement of experimental figure

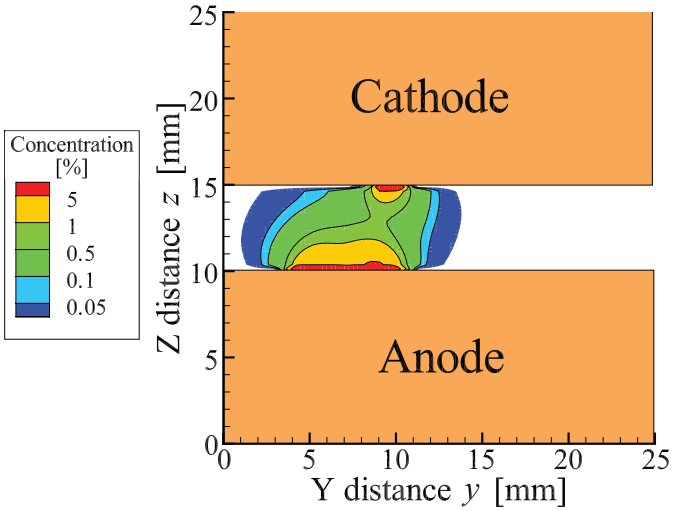

Cu vapor concentration distribution of calculation result

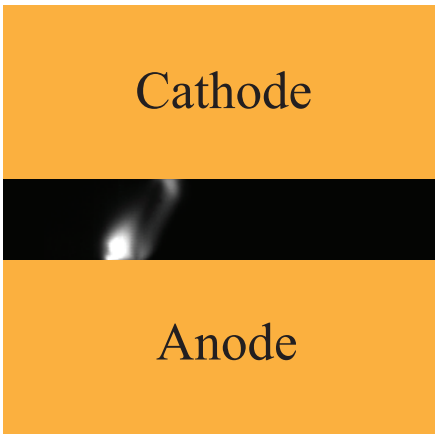

Cu vapor movement of experimental figure

Fig. 53: Compare the calculation results and experimental figures in the case of 3 mT external magnetic field applied.

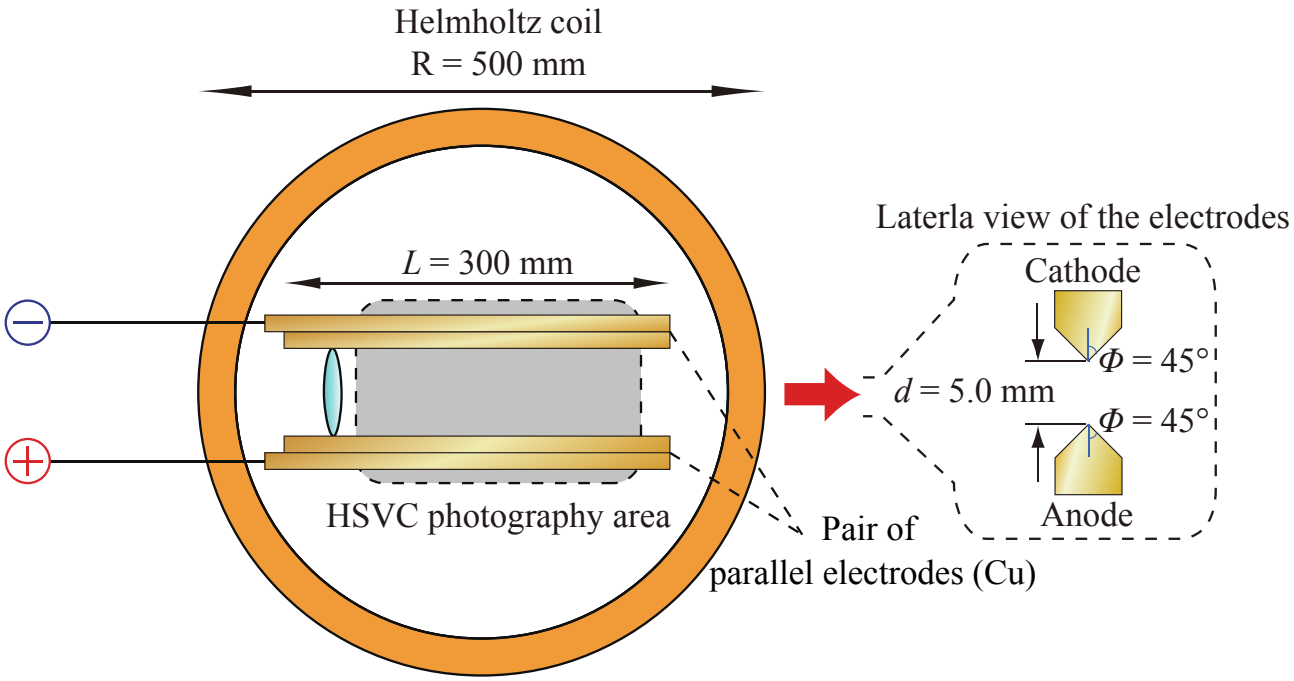

Fig. 54 Experimental arrangement of magnetically driven arc [47].

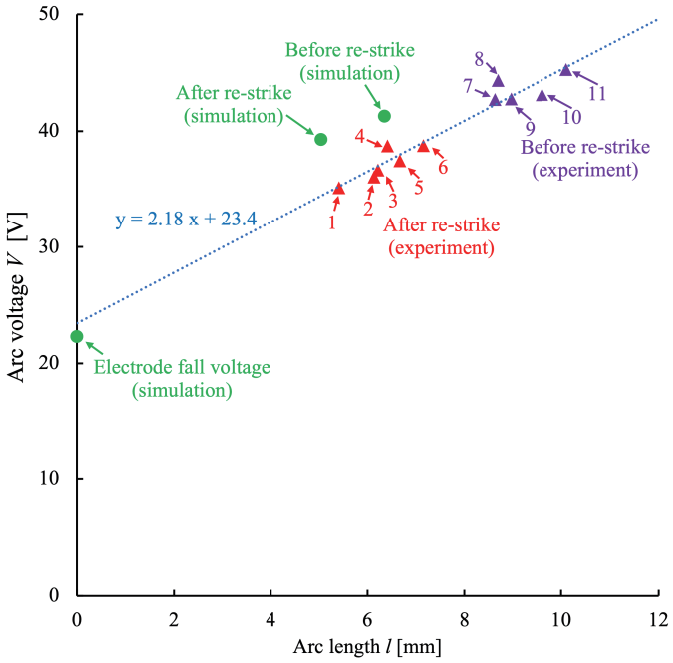

Fig. 55: Comparison of arc voltages at different arc plasma lengths obtained from simulation and experiments [47].

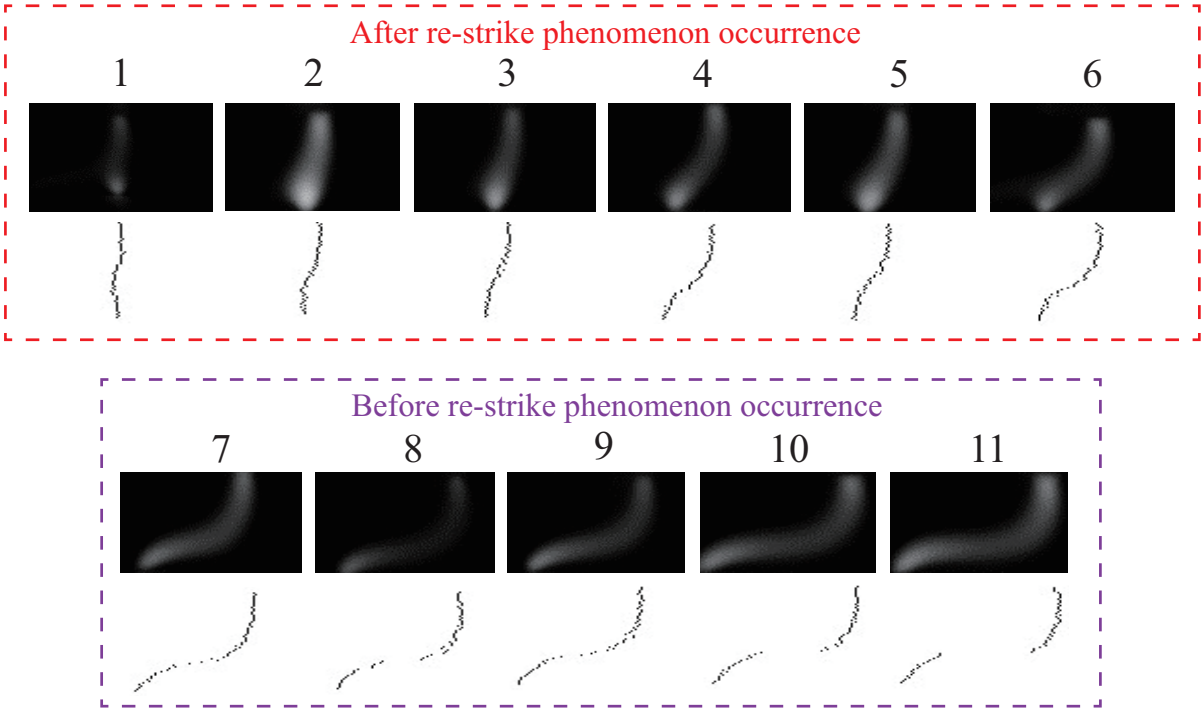

Fig. 56 Experimental figures of arc plasma used for calculating electrode fall voltage [47].

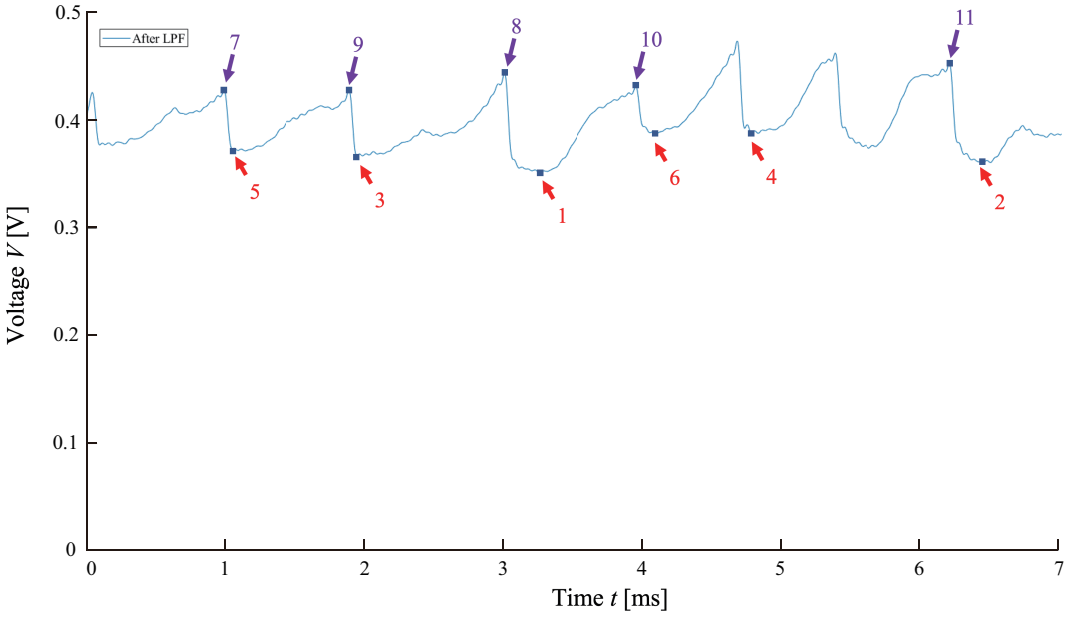

Fig. 57 Location of experimental figures on the arc voltage waveform [47].

Chapter4 Behavior of atmospheric arc plasma inside DCCB with external magnetic field application

4.1 Analysis of adverse influence of metal vapor to arc movement with external magnetic field applied

4.1.1 Adverse influence of metal vapor to arc plasma movement

The arc movements between electrodes without and with consideration of metal vapor were simulated. The physical properties of the arc plasma, such as gas temperature, flow velocity, and metal vapor concentration, are shown in Fig. 58 to Fig. 63 [56]. The electrode spots discussed in this study are defined as the high-temperature plasma area on the electrode surface, and their movements are dominated by changes in the physical properties of the calculation area, especially the electrical conductivity. The electrode jets are defined as the strong flow velocity derived from the electrode spot, and their movements are dominated by the arc form, which is affected by the electromagnetic force. In addition, the temperature of the control volume of the arc decreases while the arc stretches into the extinguishment chamber, especially at the center part. As a result, the section of the current path increased and the current of each control volume decreased. Eventually, the current of the arc section became insufficient to maintain the current continuity condition. This calculation result is defined as arc extinguishment in this calculation.

According to the simulation results shown in Fig. 58 [56] and Fig. 59 [56], the arc requires additional time to stretch into the extinguishing chamber to extinguish with consideration of the metal vapor. It can also be observed that the cathode spot shifts to the inner corner on the backward side after ignition, and then smoothly moves to the inner corner and the outer corner on the forward side while considering the metal vapor. Conversely, the reattachment phenomenon occurs multiple times at two corners on the anode side from 2.0-4.0 ms in consideration of the metal vapor. The vector distribution in this manuscript is the integration result of each isothermal surface (reflected as the color of the vector). According to Fig. 60 [56], it can be observed that a downward flow velocity is formed when the cathode spot stagnates at the inner corner on the back side while considering metal vapor, owing to the comprehensive effect of cathode jet and electromagnetic force derived from the external magnetic field. When the arc remains between the electrodes, the flow velocity becomes strong and prompts the arc to

advance into the extinguishing chamber. The directions of flow velocity around the electrodes point toward the upper right and lower right, which benefits the electrode spots shift from the inner corner to the outer corner. Thereafter, the electrode spots both shifts to the outer corner, and the flow velocity distribution becomes radial, thus accelerating the arc elongation and arc extinguishment.

According to Fig. 61 [56], a diversion of current path generates on the inner corner (at 3.9 ms) before the occurrence of reattachment phenomenon. Furthermore, few strong vectors are formed in the inter corner because the electric field intensity is strong on the electrode edge. The magnetic field of the arc plasma area was dominated by an external magnetic field, as shown in Fig. 62 [56]; however, the self-magnetic field derived from the arc became stronger near the electrode, which changed the direction of magnetic flux on this area.

It can be observed in Fig. 63 [56] that high metal vapor concentration area exists around the cathode surface on the cathode side, because the cathode spot stagnates at the inner corner on the backward side, and the generated metal vapor is transported by the synthetic flow. As for the anode side, a high metal vapor concentration area exists between the inner and outer corners on the forward side, which causes the reattachment phenomenon to occur several times. Furthermore, the metal vapor is generated from the electrodes and diffuses into the extinguishing chamber. It rebounds toward the electrodes when it bumps into the boundary.

Based on the above analyses, the arc's sluggish movement considering metal vapor can be attributed to two reasons: first, the cathode spot shifted to the inner corner on the backward side after ignition, and second, multiple occurrences of the reattachment phenomenon at the anode side.

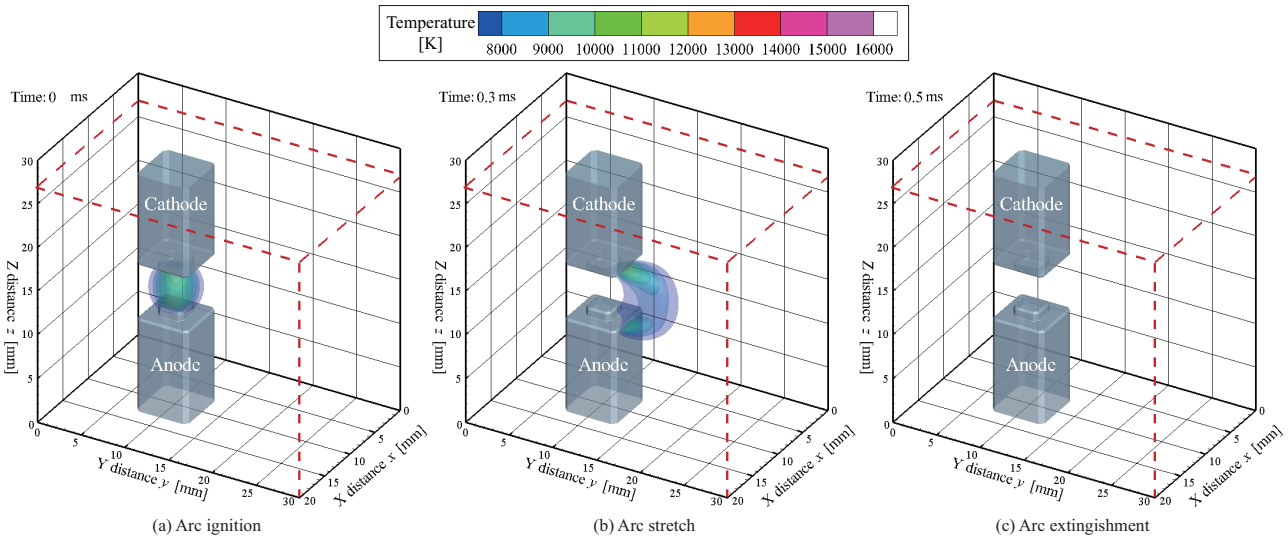

(a) Arc ignition (b) Arc stretch (c) Arc extingishment

Fig. 58 Variation of temperature distribution without metal vapor [56].

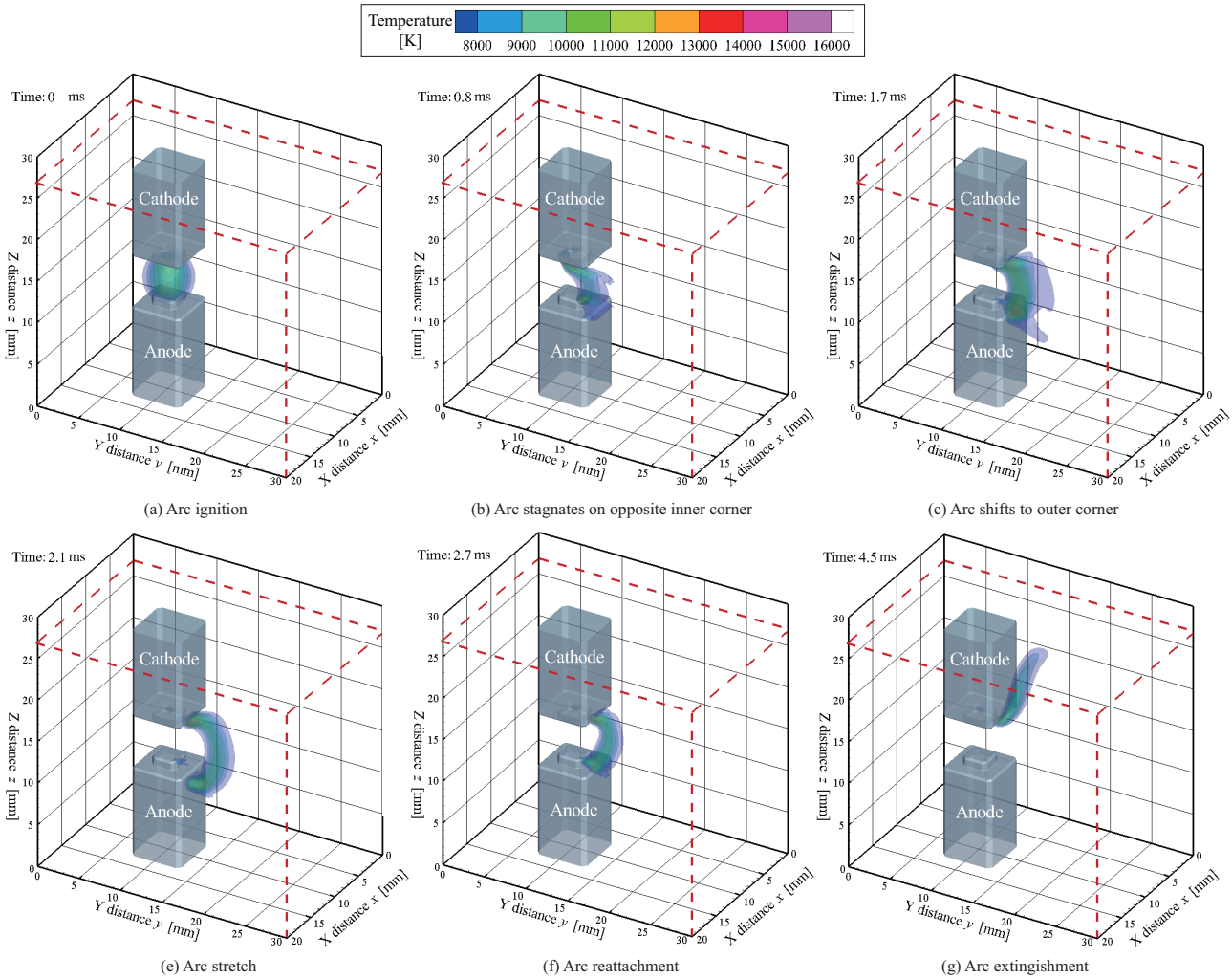

(a) Arc ignition (b) Arc stagnates on opposite inner corner (c) Arc shifts to outer corner

(e) Arc stretch (f) Arc reattachment (g) Arc extingishment

Fig. 59 Variation of temperature distribution with metal vapor [56].

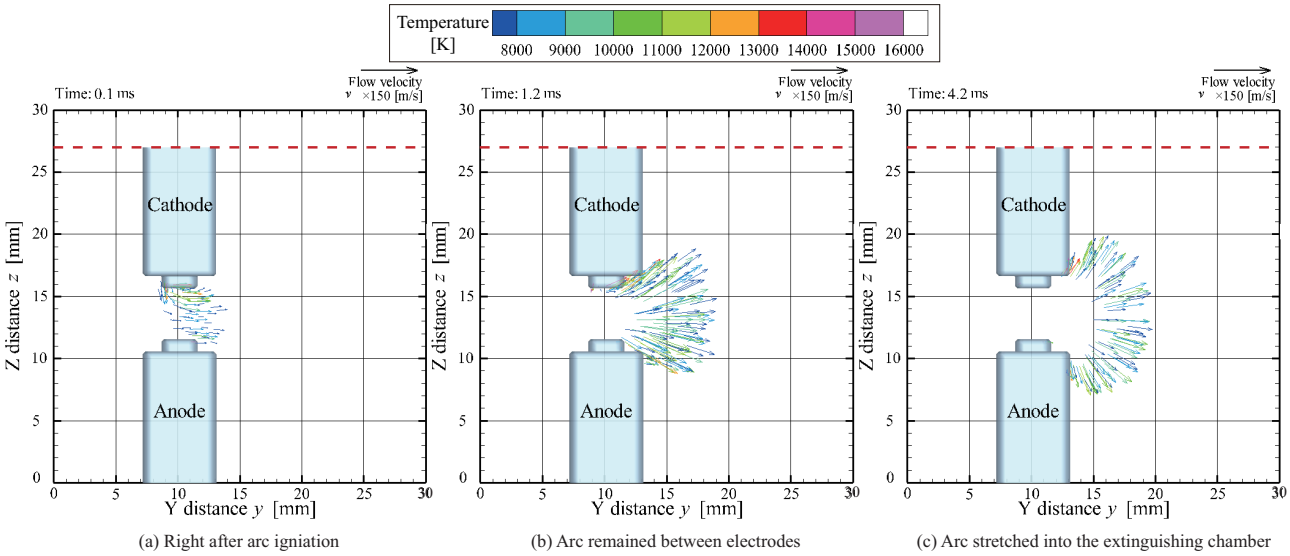

(a) Right after arc igniation (b) Arc remained between electrodes (c) Arc stretched into the extinguishing chamber

Fig. 60 Variation of flow velocity distribution with metal vapor [56].

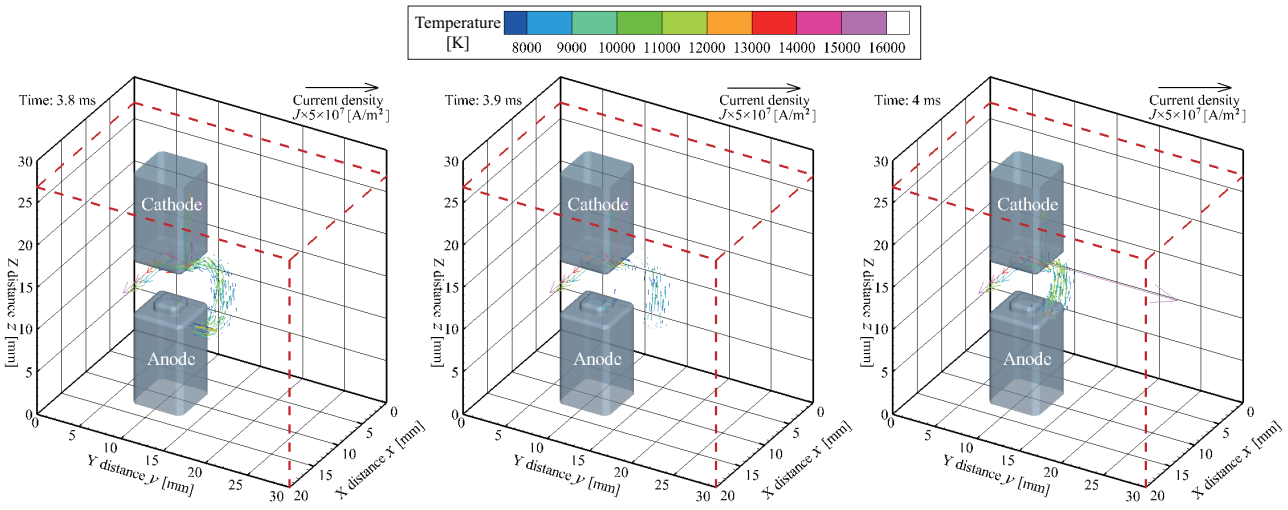

Fig. 61 Variation of current density distribution with metal vapor [56].

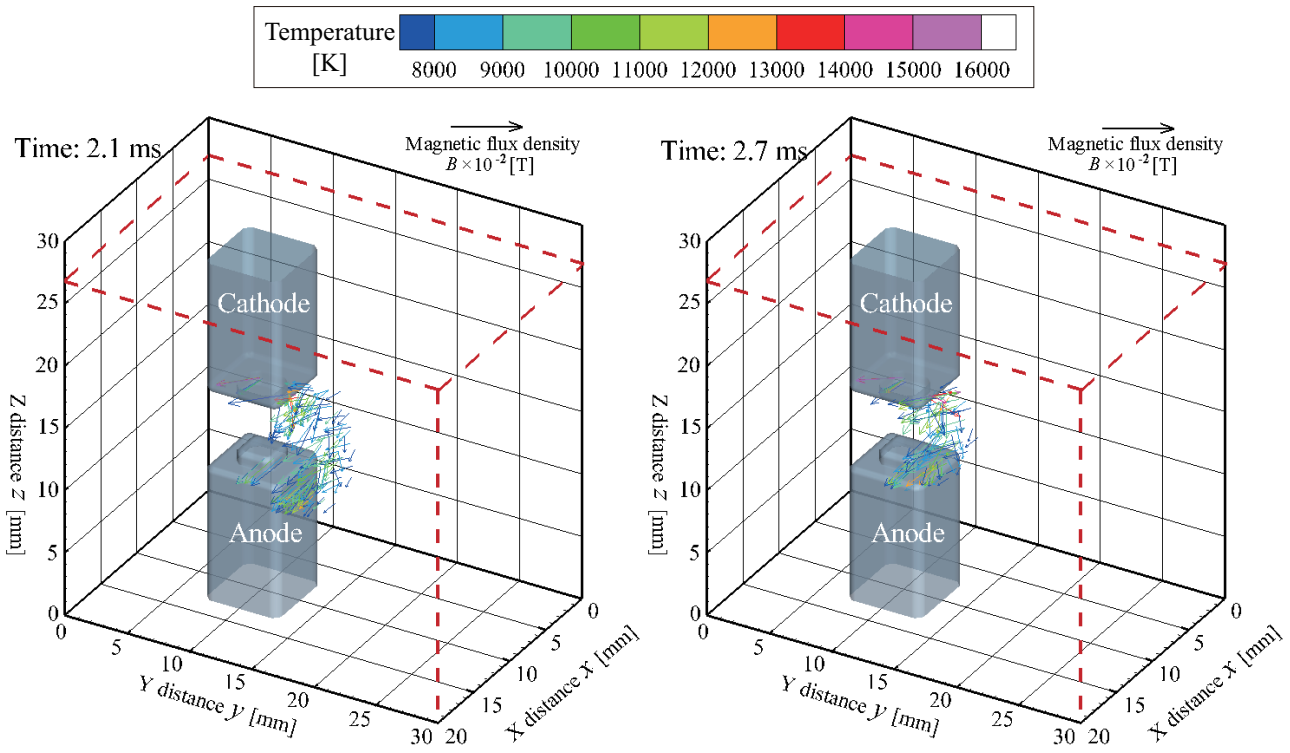

Fig. 62 Variation of magnetic flux density distribution with metal vapor [56].

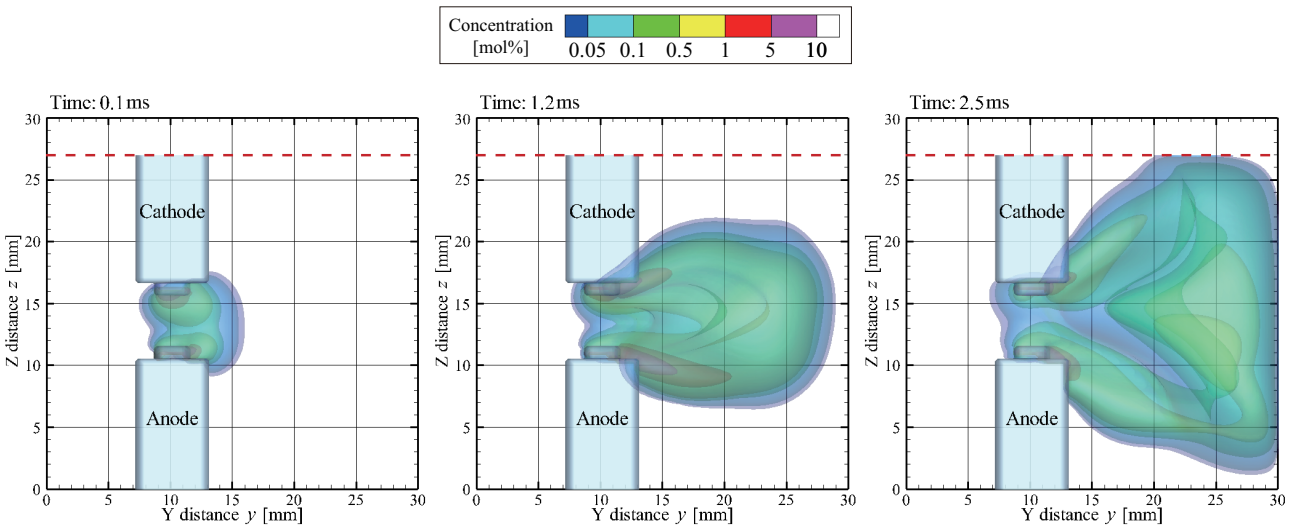

Fig. 63 Variation of metal vapor distribution with metal vapor [56].

4.1.2 Cathode spot backward movement with applying strong external magnetic field intensity

According to Ref. [52], the electrical conductivity of air is affected by the contamination rate of Cu vapor and gas temperature. If the gas temperature is less than 10,000 K, the electrical conductivity of the gas is proportional to the metal vapor concentration rate when the contamination rate is less than 10%. However, this relationship becomes inverse when the contamination rate is greater than 10%. This is because the Cu atom has a large reaction cross-section, which causes an increase in the number of collisions between electrons and other particles. The mean free path of the electron decreases based on the calculation formulas for the gas electrical conductivity in Ref. [93]. If the temperature is more than 10,000 K, the electrical conductivity is hardly affected by the Cu vapor concentration, and it increases with an increase in temperature. In this calculation, the gas temperature is approximately 6,500-7,500 K on the gas surface at the cathode side, and the highest metal vapor concentration is approximately 50%. Therefore, it is assumed that the gas electrical conductivity of the inner corner on the forward side becomes lower than that of the inner corner on the backward side. This is because the metal vapor is transported forward by the external magnetic field, which causes a higher metal vapor concentration at the inner corner on the forward side. Consequently, the cathode spot stagnates on the inner corner on the back side instead of moving forward, as shown in Fig. 64 [56]. Fig. 65 [56] shows the temperature distribution immediately after the arc ignition with applied different external magnetic field densities. It can be observed that the cathode spot shifts to the inner corner on the forward side when a 3 mT external magnetic field is applied. Conversely, when a 5 mT external magnetic field is applied, the cathode spot shifts to the inner corner on the backward side. The metal vapor concentration difference between the inner corner on the forward and backward sides becomes smaller when a weaker external magnetic field is applied. Moreover, the gas temperature of the inner corner on the forward side increases because the arc column stretches forward. Therefore, even if the metal vapor concentration of the inner corner on the forward side is higher than that on the backward side, its gas electrical conductivity is higher because of the higher gas temperature, which causes the cathode spot to move to the inner corner on the forward side. These cathode spot movement differences imply that there is an optimal-applied external magnetic field density for driving the arc into the extinguishing chamber.

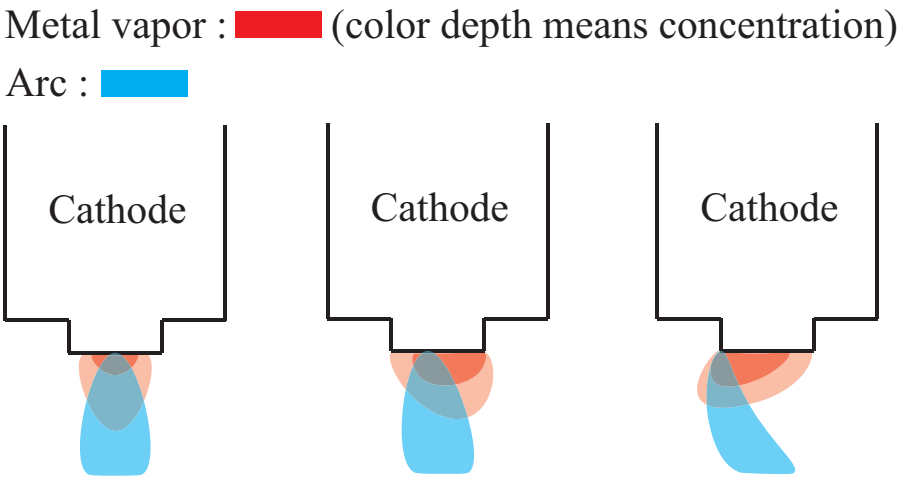

Fig. 64 Schematics of cathode spot retreat movement after arc ignition [56].

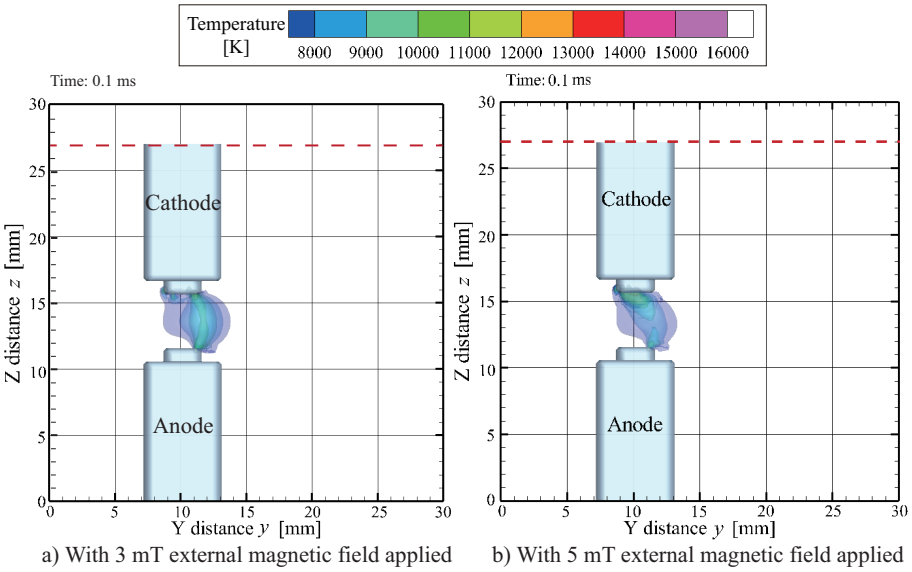

a) With 3 mT external magnetic field applied b) With 5 mT external magnetic field applied

Fig. 65 Comparison of temperature distribution after arc ignition with metal vapor [56].

4.1.3 Continuous occurrence of reattachment phenomenon on anode corner area

Another reason for the sluggish movement of arc when considering metal vapor is the continuous occurrence of reattachment. This is because the metal vapor particles have a low ionization voltage, and their existence causes high gas electrical conductivity in the corner area even after the arc is stretched into the extinguishing chamber. Fig. 66 [56] and Fig. 67 [56] show the variation of metal vapor concentration and gas electrical conductivity of the anode corner area. It can be observed that the metal vapor concentration of the inner or outer corners remains high even after the arc stop stagnating on it. The gas electrical conductivity of the anode corner area has severe vibration because of the recurring reattachment phenomenon.

The arc voltage variations with and without consideration of the metal vapor are shown in Fig. 68 [56]. It can be observed that the arc voltage rapidly increases and reaches 19.4 V immediately before its extinguishment in the case without considering metal vapor. This is because the arc movement is fast under the effect of an external magnetic field. As for the case of considering metal vapor, the arc voltage continues increasing before 2.0 ms because the electrode spots moved toward the outer corner on the forward side, and the arc length continues to increase during this period. From 2.0 ms to 4.0 ms, the reattachment phenomenon continued to occur and cause the fluctuation of the arc voltage in this period, which leads to the arc stopping from stretching into the extinguishing chamber and remaining between the electrodes as shown in Fig. 68 [56]. Meanwhile, the metal vapor and gas electrical conductivity of the corner area continued to decrease, as shown in Fig. 66 [56] and Fig. 67 [56]. Finally, the reattachment phenomenon stopped occurring and the arc stretched into the extinguishing chamber, and its arc voltage increased to 23.2 V immediately before its extinguishment.

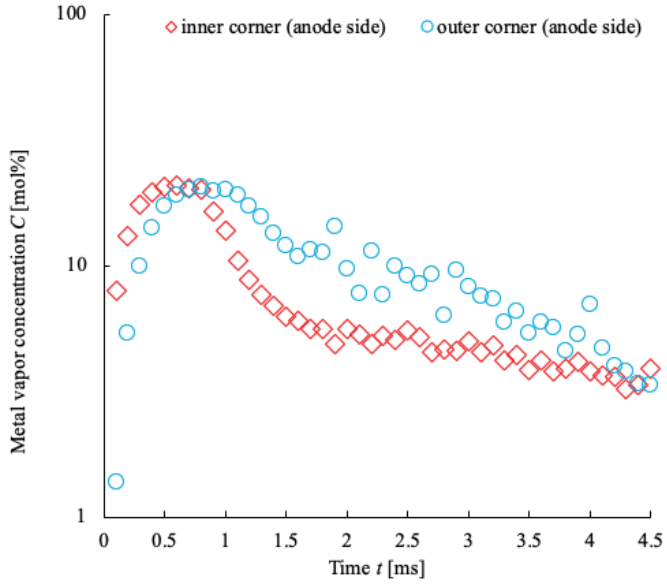

Fig. 66 Variation of metal vapor concentrations of anode corner area [56].

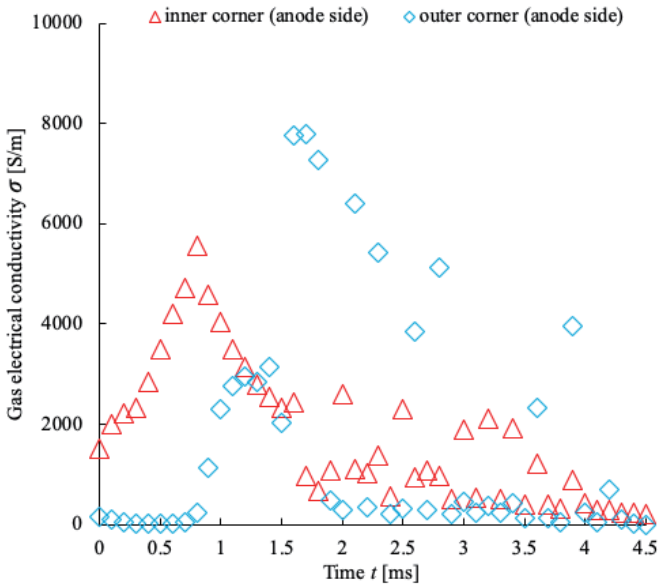

Fig. 67 Variation of gas electrical conductivities on anode corner area [56].

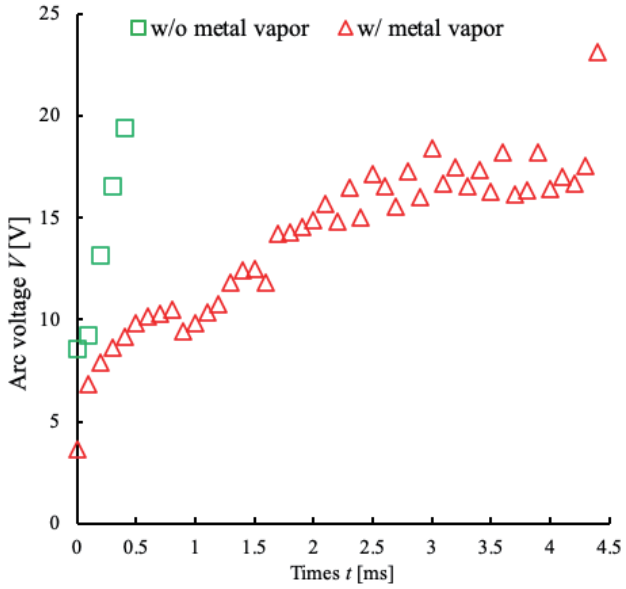

Fig. 68 Comparison of arc voltage between without and with metal vapor [56].

4.2 Three circumstances of DCCB interruption process

4.2.1 Interruption success circumstance: arc plasma extinguished without re-strike occurrence

Fig. 69 shows the temperature, flow velocity, and metal vapor concentration distribution before the arc plasma extinguish when the electrode opening velocity was 10 m/s with 1 mT external magnetic field applied. According to Fig. 69(a), it can observe that the arc plasma first moved to the corner where the electrical field is concentrated, and then moved backward (specifically the anode side) because the existence of wall causes the reversed flow velocity distribution as shown as the blue vector on the peripheral of arc plasma in Fig. 69(b).

It also can see that the arc plasma remained in the inter-electrode area during the interruption process and was extinguished while it moved around the edge of the inner corner. These simulation results were caused by the pinch effect of arc plasma and the insufficient magnetic force derived from the applied external magnetic field. To be specific, the density of charged particles inside the arc plasma decreases along with the electrode opening process and leads to the kinetic pressure decrease, which became insufficient to resist the magnetic pressure derived from the arc plasma itself [94]. As a result, the radius of the plasma cylinder was forced inwards and the plasma column was pinched in the inter-electrode area.

Based on Fig. 69(a) and (c), the variation of metal vapor concentration distribution could not follow the temperature distribution and move forward, because the metal vapor in this study is composed of ion (Cu^+) and neutral (Cu) particles, which are heavier than the charged particles (e^-, N_2^+, N^+, N^{2+}, O_2^+, O^-, O^+, O^{2+}, and NO^+) of arc plasma and caused the hysteresis.

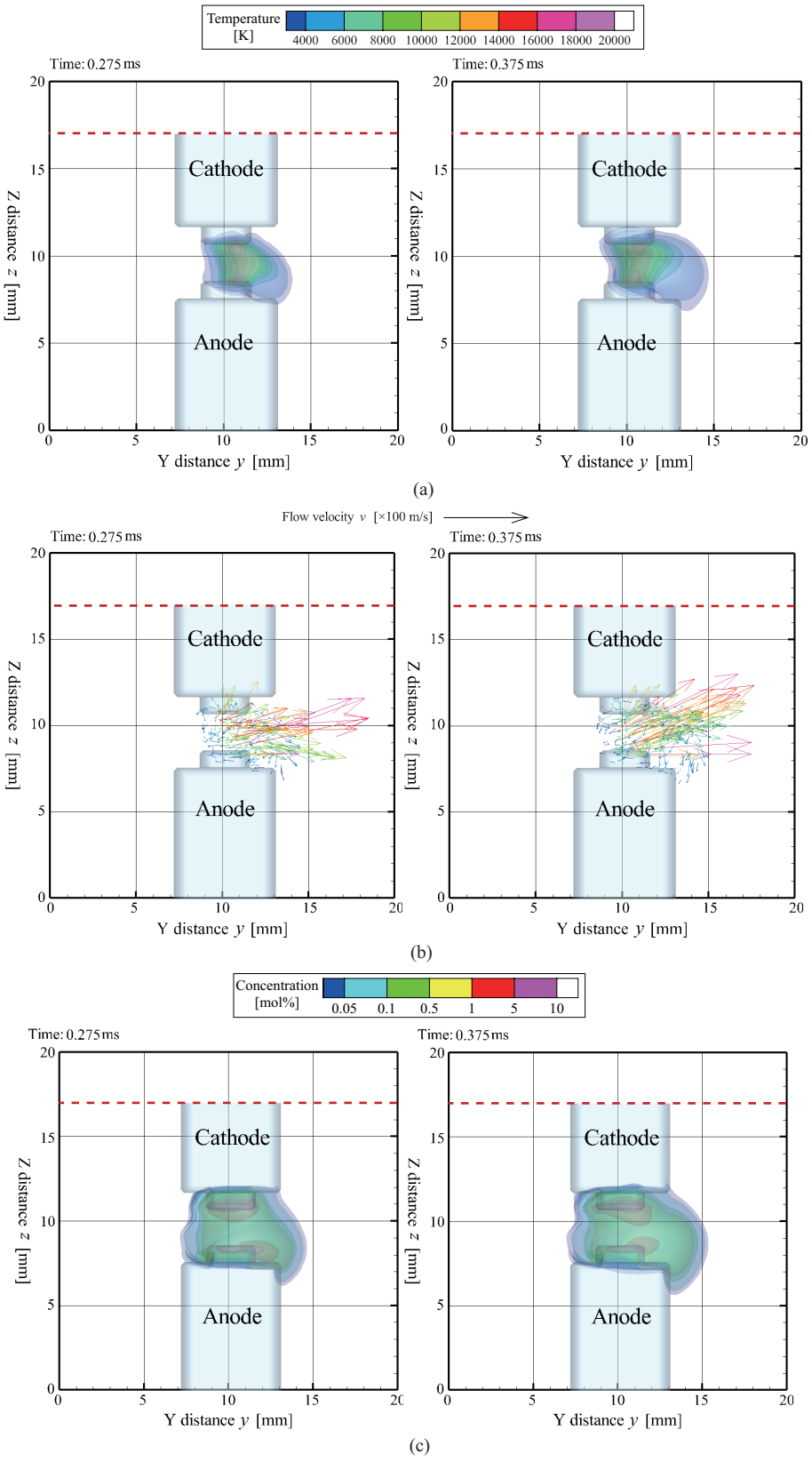

Fig. 69: Simulation results of temperature, flow velocity and metal vapor concentration distribution when electrode opening velocity was 10 m/s and with 1 mT external magnetic field applied. (a) Temperature distribution. (b) Flow velocity distribution. (c) Metal vapor concentration.

4.2.2 Interruption success circumstance: arc plasma extinguished with re-strike occurrence

Fig. 70 presents the temperature distribution of arc plasma during the occurrence of the re-strike phenomenon in different interruption conditions. It can observe that the re-strike phenomenon occurred, in which the branch of arc plasma on the outer corner kept decreasing and the new branch of arc plasma in the inter-electrode area kept increasing, and the arc plasma branches were both extinguished eventually. According to the simulation results, the re-strike phenomenon occurred at 212.5 μs when the electrode opening velocity was 20 m/s with 5 mT external magnetic field applied, and at 152.0 μs when the electrode opening velocity was 30 m/s with 9 mT external magnetic field applied. For elucidating the reason for the re-strike phenomenon occurrence of the above two circumstances, the variation of gas temperature, electrical conductivity, and metal vapor concentration of the center point of the new appeared arc plasma branch were summarized in Fig. 71.

The electrical conductivity of the re-strike location gradually increased even before the occurrence of the re-strike phenomenon as shown in Fig. 71 (b), which was caused by the increased of gas temperature according to Fig. 71 (a). As for the reason for these gas temperature increments, it is because of the reversed flow velocity distribution on the peripheral of arc plasma as discussed above. The occurred timing of the re-strike phenomenon became faster along with the applied external magnetic field intensity increasing. Based on Fig. 71 (c), it can observe that the metal vapor concentration first increased rapidly because of evaporation of molten metal bridge, and the second gradually increments was because of the metal vapor generated from the electrodes. Meanwhile, the metal vapor concentration decreased because of the diffusion and convection effect.

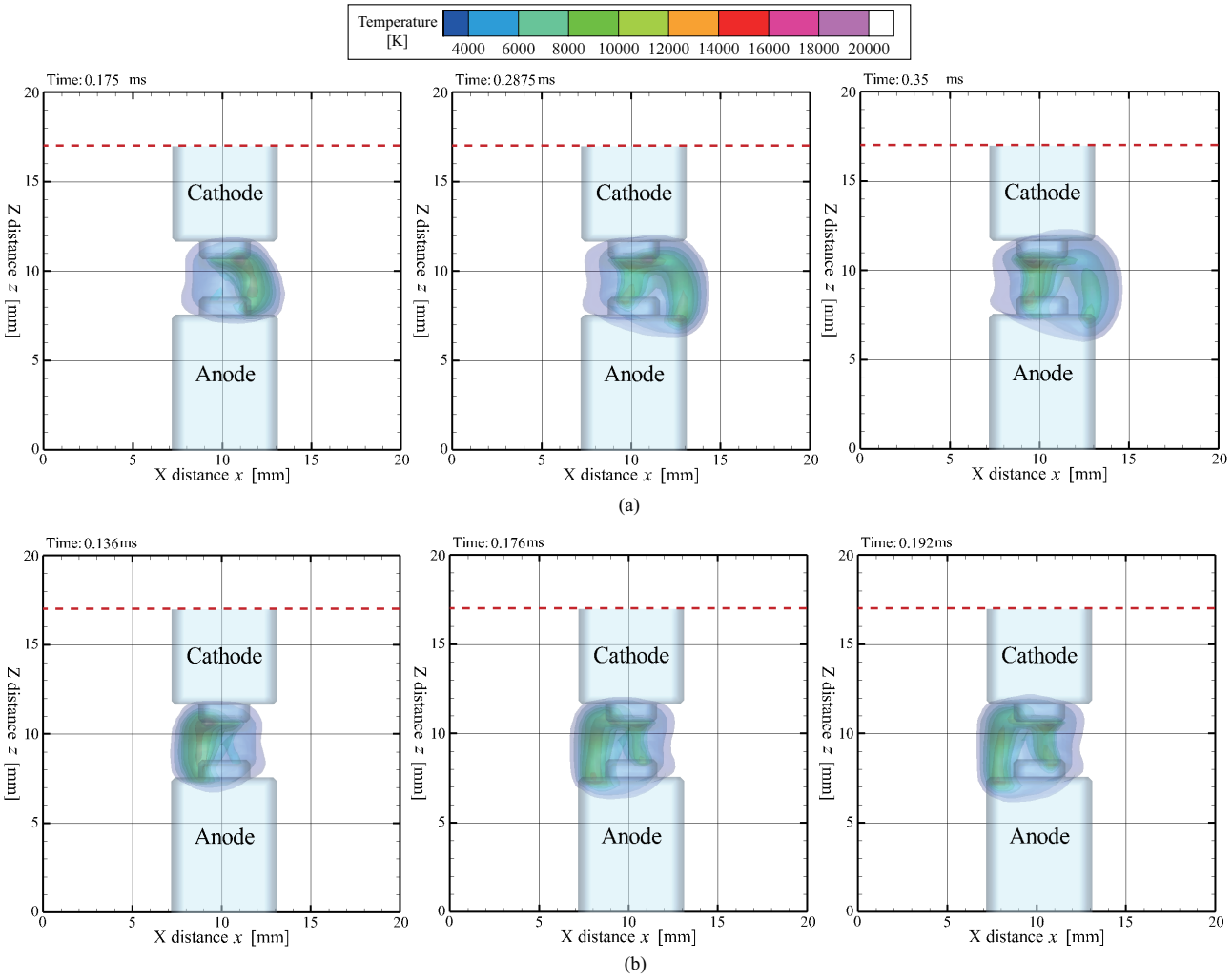

Fig. 70: Simulation results of temperature distribution of re-strike phenomenon occurrence in different interruption conditions. (a) Electrode opening velocity: 20 m/s, applied external magnetic field intensity: 5 mT. (b) Electrode opening velocity: 30 m/s, applied external magnetic field intensity: 9 mT.

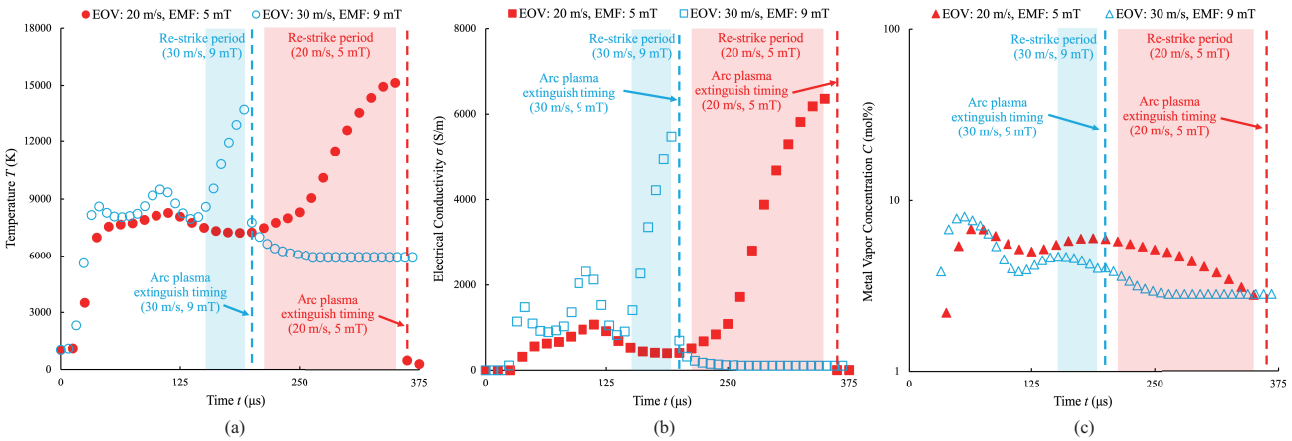

Fig. 71: Variation of physical properties of center point of new appeared arc plasma branch during re-strike phenomenon occurrence. (a) temperature variation. (b) Electrical conductivity variation. (c) Metal vapor concentration variation.

4.2.3 Interruption failure circumstance: arc plasma stagnation

Fig. 72 presented the simulation results of temperature, flow velocity, and metal vapor concentration distribution in the case without applying an external magnetic field, when the electrode opening velocity was 20 m/s. It can observe that the arc plasma shifted to the inner corner and remained existing based on Fig. 72 (a), because of the lack of electromagnetic force to drive the arc plasma into the extinguishing chamber. Moreover, the reversed flow velocity distribution on the peripheral of arc plasma as shown in Fig. 69 (b) did not formed in this case as presented in Fig. 72 (b). As for the metal vapor, its range and concentration were border and higher on the cathode side than anode side, because of the strong buoyancy of high gas temperature and the strong anode jet as shown in Fig. 72 (b).

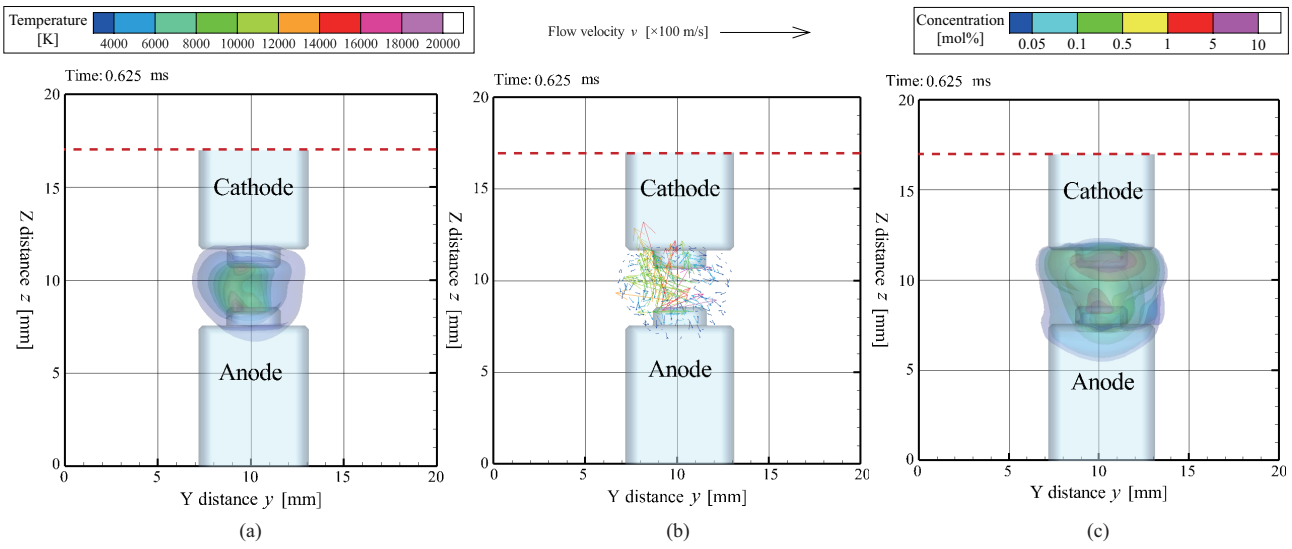

Fig. 72: Simulation results of temperature, flow velocity, and metal vapor concentration distribution in the case of without applying an external magnetic field. (a) Temperature distribution. (b) Flow velocity distribution. (c) Metal vapor concentration.

4.3 Variation of arc plasma physical properties during DCCB interruption process

4.3.1 Physical properties variation of inter-electrode area

Next, the hypothetical model (Chapter 1.5, Fig. 10 [57]) that the cross-sectional area is broader in the case of low electrode opening velocity was verified. The temperature distribution for different electrode opening velocities was obtained without external magnetic field application. The result is presented in Fig. 73 [57], which the arc plasma shifts to the right side of the electrode with time even without applying an external magnetic field. It is because a virtual high temperature (15,000 K) cylinder area is constructed in the first calculation cycle for igniting the arc plasma between electrodes after the broken molten metal bridge, which is difficult to locate the perfect center. After all, the number of control volumes of inter-electrode width is even (8 control volumes). Moreover, the corner of the electrode has concentrated electrical field density, which leads to the arc plasma being drawn to the right corner with time variation. It can be seen that the temperature distribution is broader for higher electrode opening velocities in the high-temperature or low-temperature areas in Fig. 73 [57], which is inconsistent with the hypotheses proposed in Chapter 1. Because the diffusion effect was not dominant, the flow velocity distribution at different electrode opening velocities was investigated without external magnetic field application for the convection effect analysis. The result is shown in Fig. 74 [57]. It can be seen that the flow velocity was dominated by the anode jet before the electrode opening process was complete, as shown in Fig. 74 (b) and (c) [57]. This is because the cathode kept moving upward and the cathode jet could not be formed stably. From the comparison of Fig. 73 [57] and Fig. 74 [57], it can see that the arc form (especially, the low-temperature part) is determined and bent forward by the synthetic flow, which is formed by the cathode and anode jets. Hence, the increment rate of the arc voltage per unit length can be influenced by this synthetic flow because the cross-sectional area and the electrical conductivity both change with the arc form.

Fig. 75 [57] and Fig. 76 [57] present the current densities of the control volume with the highest temperature on electrode surface for different electrode opening velocities without external magnetic field application. The control volume with the highest temperature on the electrode surface has the lowest current density when the electrode opening velocity is 25 m/s because in this case, the metal vapor concentration is significantly higher in the inter-electrode area, as shown in Fig. 77 [57]. When the electrode opening velocity is 25 m/s, the metal vapor concentration of the inter-electrode area is still dominated by the metal vapor generated from the molten metal bridge and remains at the high-concentration level because of insufficient time for metal vapor diffusion. As a result, the current path of the arc becomes dispersed. When the electrode opening velocity was 5 or 2.5 m/s, the metal vapor generated from the electrodes was dominant, which resulted in the current density increase on the electrode surface. According to Fig. 75 [57] and Fig. 76 [57], it can be seen that the current density of control volume with highest temperature on electrode surface both kept increasing when the electrode opening velocity was 2.5 or 5 m/s. This is because the electrode spots shifted to the electrode

corners, leading to the current density increase. However, the current density of the control volume with the highest temperature on the anode surface kept decreasing when the electrode opening velocity was 25 m/s because the amount of metal vapor generated from the anode kept increasing, leading to the current density dispersion at the anode surface. As for the cathode side, the current density of the control volume with the highest temperature on the cathode surface first decreased because of the high metal vapor concentration derived from the molten metal bridge. Subsequently, it increased because the cathode kept moving upward, weakening the influence of the metal vapor generated from the molten metal bridge on the cathode side.

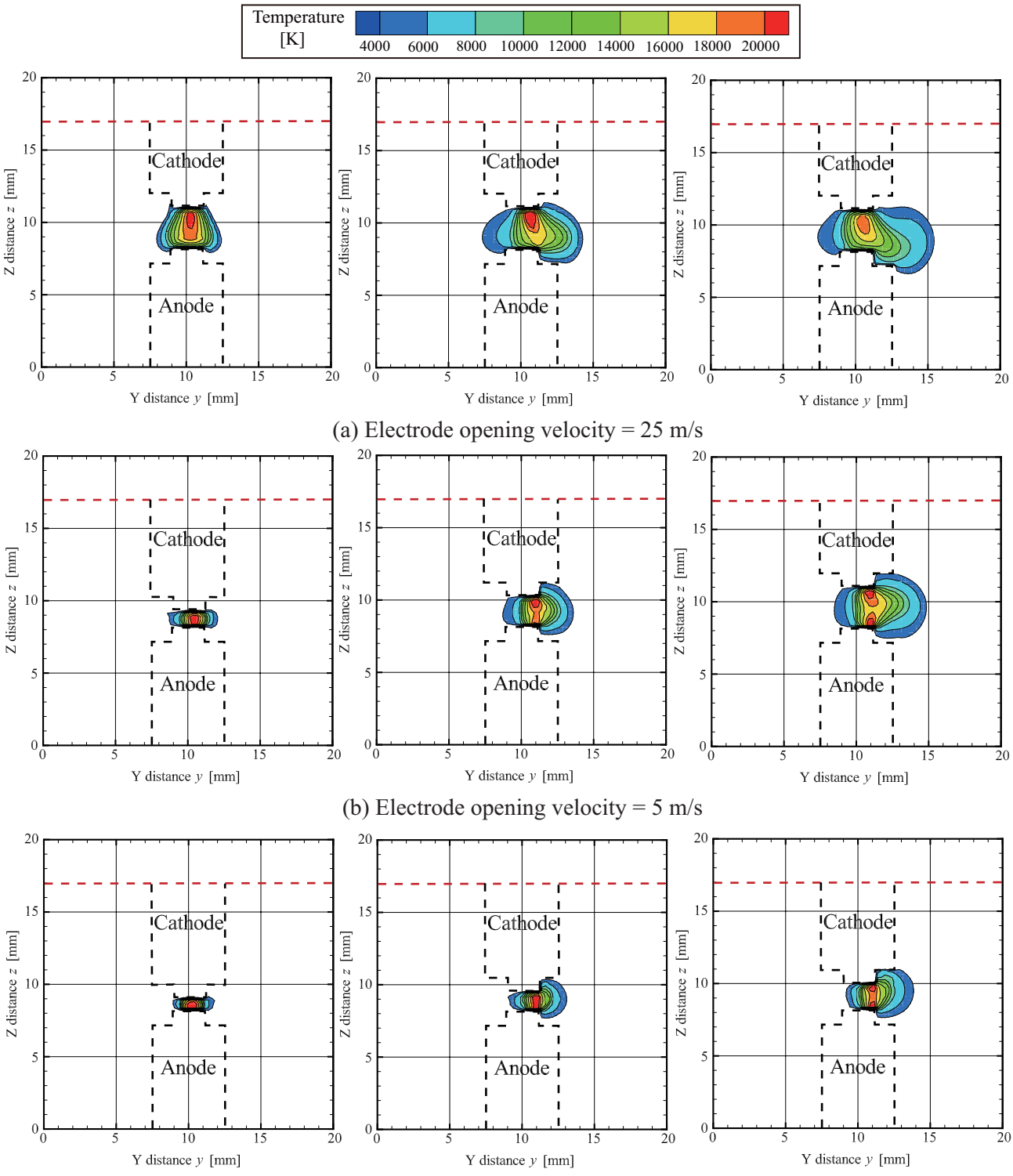

Fig. 73: Temperature distribution for different electrode opening velocities without external magnetic field application [57].

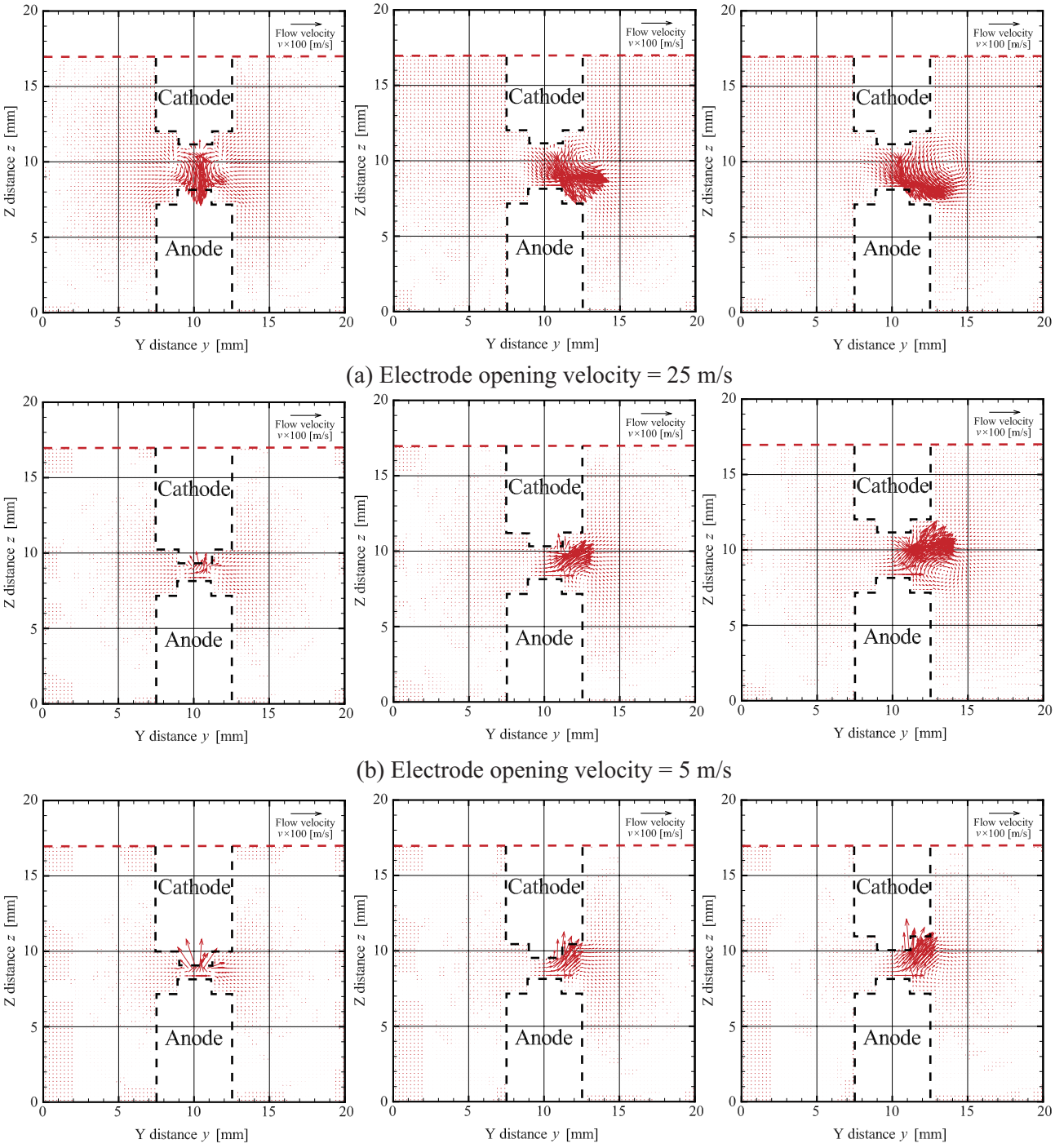

(a) Electrode opening velocity = 25 m/s

(b) Electrode opening velocity = 5 m/s

(c) Electrode opening velocity = 2.5 m/s

$t = 0.1$ ms $t = 0.3$ ms $t = 0.5$ ms

Fig. 74: Flow velocity distribution for different electrode opening velocities without external magnetic field application [57].

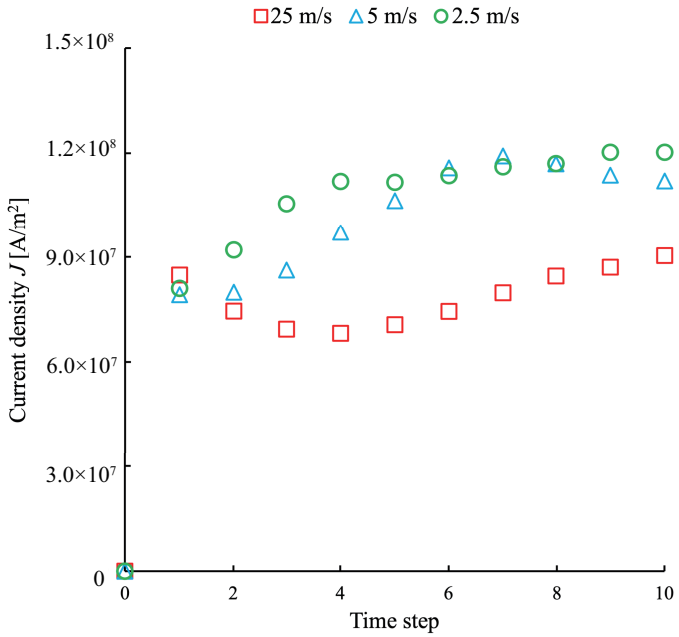

Fig. 75: Current density of the control volume with the highest temperature on cathode surface at different electrode opening velocities without external magnetic field application [57].

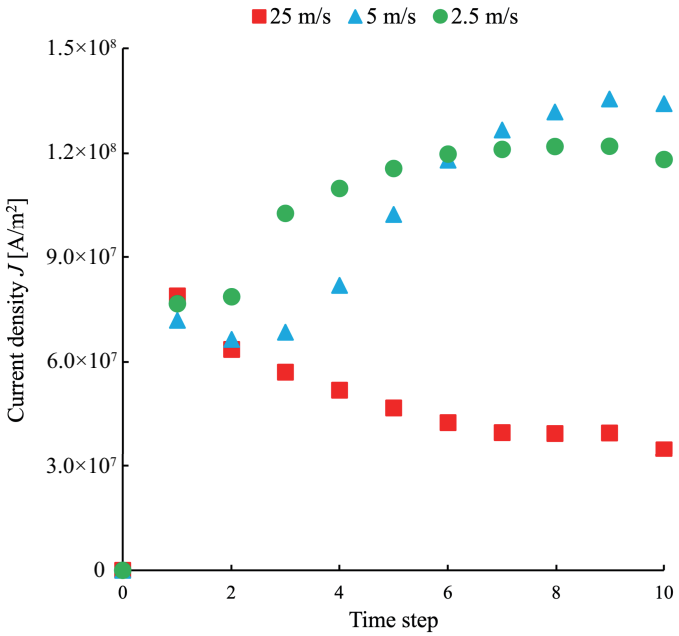

Fig. 76: Current density of the control volume with the highest temperature on anode surface at different electrode opening velocities without external magnetic field application [57].

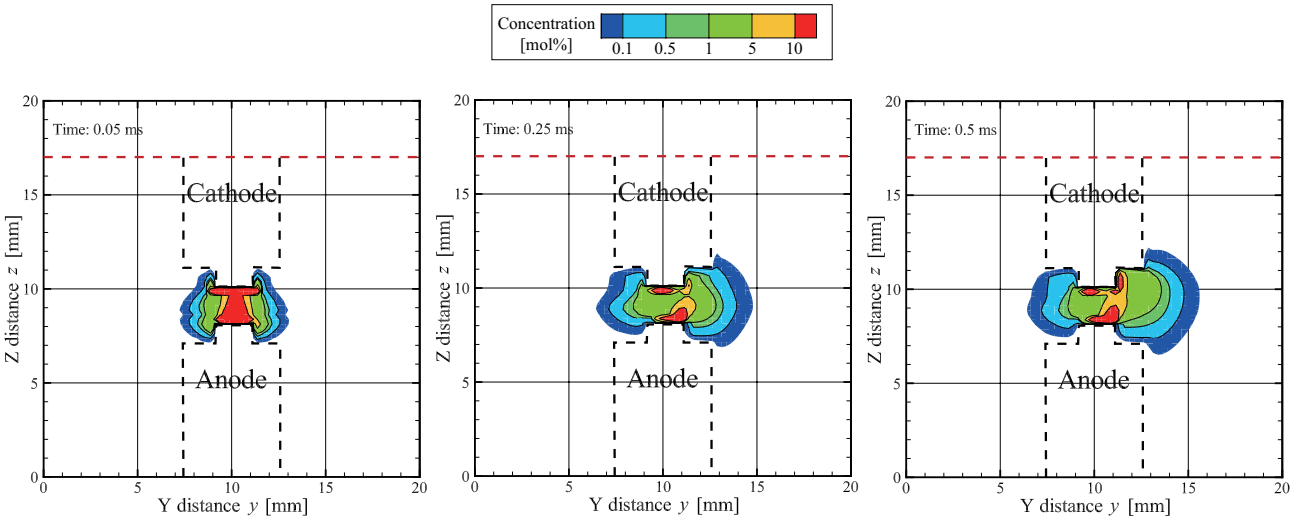

(a) V_{open} = 25 m/s (b) V_{open} = 5 m/s (c) V_{open} = 2.5 m/s

Fig. 77: Metal vapor concentration distribution at different electrode opening velocities without external magnetic field application at the fifth time step [57].

4.3.2 Increment rate of arc voltage per unit length

Table 6 [57] shows a summary of the increment rates of the arc voltage per unit length in different circumstances. From Table 6 [57], it can see that the increment rate of the arc voltage per unit length increases with the electrode opening velocity regardless of the electrode opening process completion. According to Eq. 1, the arc voltage is determined by its length, cross-section area, and electrical conductivity. When the external magnetic field was not applied, the increment rate of the arc voltage per unit length was 1.75 times faster (1.54×10^7 V/m·s, as compared with 8.79×10^6 V/m·s) when the electrode opening velocity was increased from 5 m/s to 25 m/s. The increment rate of the arc voltage per unit length was smaller than the increment rate of the electrode opening velocity (which was 5 times faster at 25 m/s, as compared to that at 5 m/s) before the electrode opening process was complete. This is because the cross-sectional area of the arc increased with increasing electrode opening velocity, as mentioned before. Furthermore, the metal vapor concentration remained high at the inter-electrode area immediately after the molten bridge breaking, as shown in Fig. 78 [57]. Hence, the electrical conductivity of this area remained high. For the same reasons, the increment rate of the arc voltage per unit length was 3.29 times faster (1.54×10^7 V/m·s, as compared with 4.69×10^6 V/m·s) when the electrode opening velocity was increased from 2.5 m/s to 25 m/s. In comparison, it was small than the increment rate of the electrode opening velocity, which was 10 times (25 m/s, as compared with 2.5 m/s) before the electrode opening process completion. After the electrode opening process completion, the increment rate of the arc voltage per unit length was higher for faster electrode opening because the arc received more kinetic energy during the electrode opening process.

Table 6 Increment rate of the arc voltage per unit length under different circumstances [57].

E.M.F.I. [mT]	E.O.V. [m/s]	A.V.I.R. before E.O.P. finished [V/m·s]	A.V.I.R. after E.O.P. finished [V/m·s]
0	25	1.54×10^{7}	2.34×10^{7}
	5	8.79×10^{6}	1.70×10^{7}
	2.5	4.69×10^{6}	6.51×10^{6}
3	25	2.15×10^{7}	2.22×10^{7}
	5	8.28×10^{6}	6.84×10^{6}
	2.5	2.71×10^{6}	2.55×10^{6}
5	25	2.60×10^{7}	2.43×10^{7}
	5	7.81×10^{6}	1.30×10^{7}
	2.5	3.09×10^{6}	1.21×10^{7}

* E.M.F.I.: External magnetic field intensity
** E.O.V.: Electrode opening velocity
*** A.V.I.R.: Increment rate of the arc voltage per unit length
**** E.O.P.: Electrode opening process

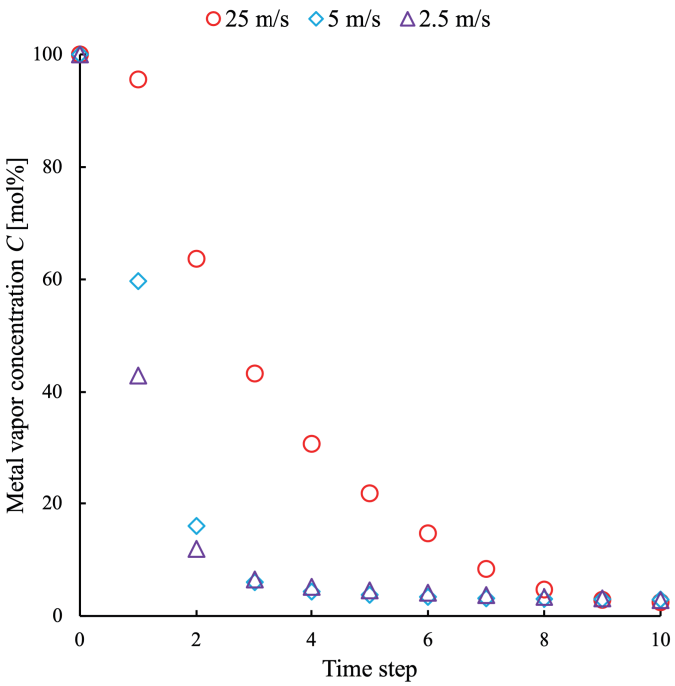

Fig. 78: Metal vapor concentration at the center point of the inter-electrode area at different electrode opening velocities without external magnetic field application [57].

4.3.3 Increment rate of arc length

A summary of the arc length increment rate in different circumstances is presented in Table 7 [57]. It can be seen that the arc length increment rate is approximately equal to the electrode opening velocity before the electrode opening process completion when the external magnetic field is not applied. When an external magnetic field was applied, the difference in the arc length increment rate at different electrode opening velocities became smaller before the electrode opening process was completed. However, the difference in the increment rate of the arc voltage per unit length at different electrode opening velocities became larger, as shown in Table 6 [57]. The metal vapor concentration was low and constant when the electrode opening process was completed for all electrode opening velocities (the influence of metal vapor became more slightly when an external magnetic field was applied), as shown in Fig. 78 [57]. This observation indicated that the electrical conductivity was determined by the gas temperature. According to Fig. 79 [57], the arc temperature decreased when the external magnetic field was applied, and this decrement became more significant at slow electrode opening. It can also be seen that the current path became more concentrated when the electrode opening velocity was 25 m/s, and it became more dispersed when the electrode opening velocity was 5 or 2.5 m/s, as shown in Fig. 80 [57]. In conclusion, the increment rate of the arc voltage per unit length increased for an electrode opening velocity of 25 m/s when an external magnetic field was applied because the arc temperature and the cross-sectional area decreased. In contrast, the increment rate of the arc voltage per unit length decreased for an electrode opening velocity of 5 or 2.5 m/s when an external magnetic field was applied. This is because the increment of the cross-sectional area was more significant than the decrement of the arc temperature. After the electrode opening process was completed, the variation in the arc length increment rate was dominated by the intensity of the applied external magnetic field.

Table 7 Arc length increment rate under different circumstances [57].

E.M.F.I. [mT]	E.O.V. [m/s]	A.L.I.R. before E.O.P. finished [m/s]	A.L.I.R. after E.O.P. finished [m/s]
0	25	25.0	0.5
	5	5.1	2.3
	2.5	2.6	1.0
3	25	25.5	15.6
	5	12.7	22.0
	2.5	12.1	15.2
5	25	28.5	18.9
	5	18.8	19.8
	2.5	16.8	18.1

* A.L.I.R.: Arc length increment rate

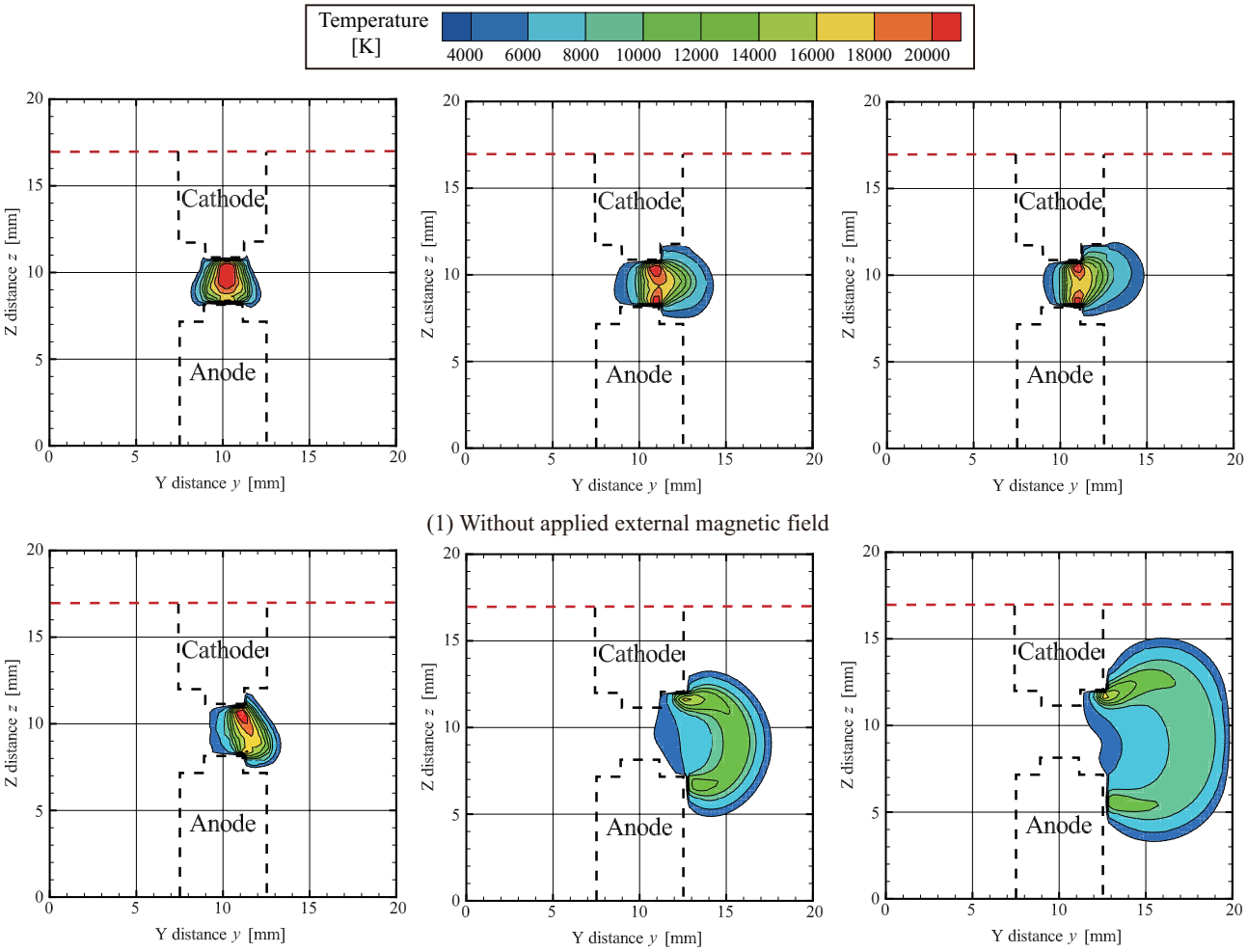

Fig. 79: Temperature distribution at different electrode opening velocities when the electrode opening process was complete [57].

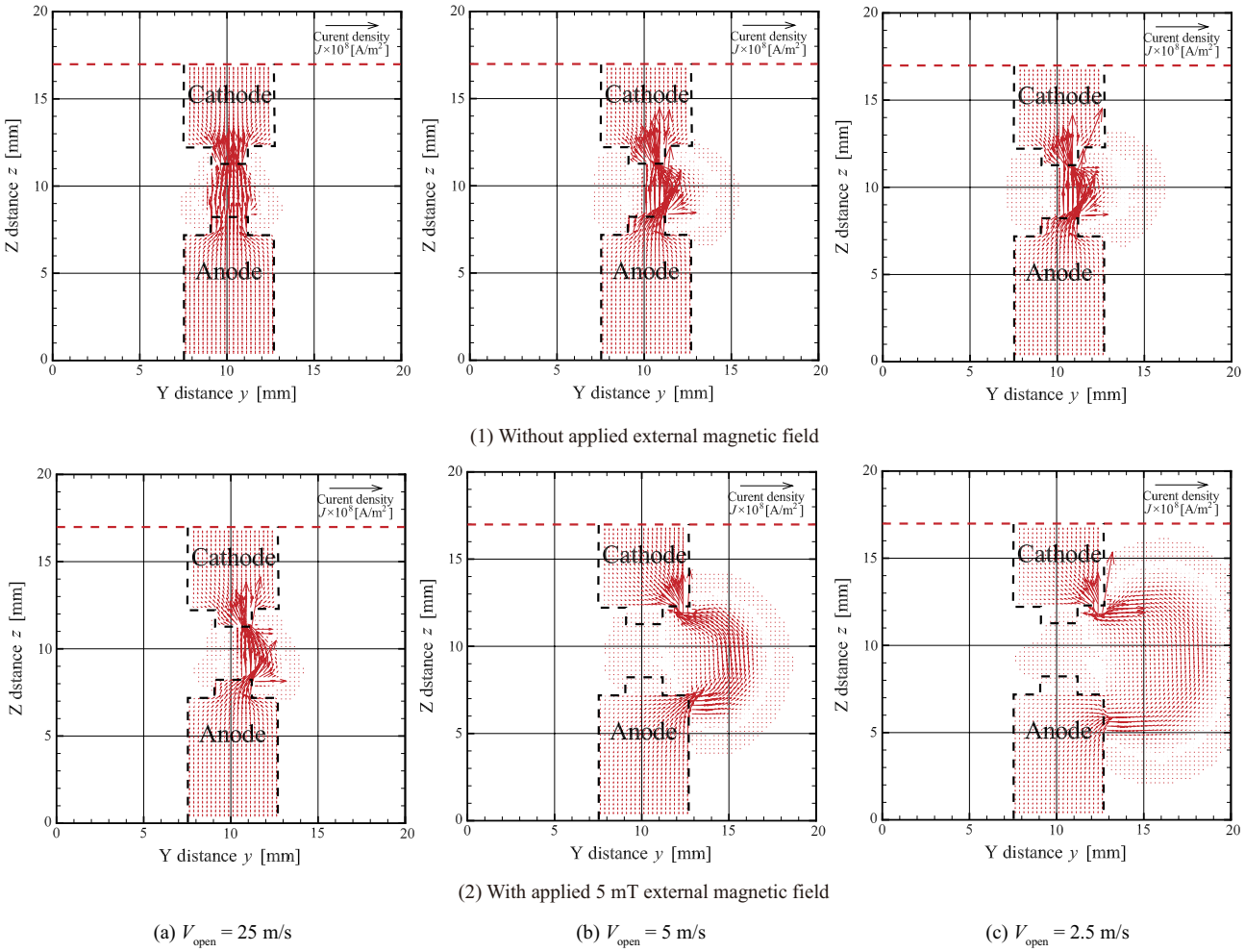

Fig. 80: Current density distribution at different electrode opening velocities when the electrode opening process was complete [57].

Chapter5 Develop of AI models and cyber-physical system for creating next-generation DCCB

5.1 Development of artificial intelligence program for locating arc plasma extinguish timing

The DCCB interruption process could be simulated in virtual space as discussed in Chapter 4. Hence, the parameters that affect the performance of DCCB interruption such as electrode opening velocity, applied external magnetic field intensity, and extinguish chamber size were adjusted and analyzed for finding out the most optimal combination.

To improve the analysis efficiency of the simulation results, an artificial intelligence model was established and applicated as shown in Fig. 81 [97]. The existence (150 figures) and extinguish (150 figures) sample figures were selected based on whether the current path continuity was satisfied or not, and applied as the training data. and then, the supervised machine learning model (SMLM) was established by using the convolutional neural network (CNN) in MATLAB R2022a [95][96]. The selected figure is a 2D overview of the isothermal surface which neglected the electrode and enlarged the layout ratio based on the 3D temperature data. Next, the simulation results of the arc plasma temperature distribution under different electrode opening velocities (EOV) and applied external magnetic field intensity (AEMFI) were classified as existing or extinguish by using this SMLM. The extinguishing timing of arc plasma in case of a successful interruption could be identified as the time of the first figure of the extinguishing category.

Table 8 [97] summarizes the differentiation results obtained under various interruption conditions. The SMLM differentiated the extinguish timing of the arc plasma as 280.0 and 200.0 μs in cases 5 and 6, respectively; these were different from the manual results which differentiate the arc plasma existence if the continuous high-temperature area (higher than 8,000 K) existed. For verifying the reliability of the differentiation result obtained using the SMLM, the current density distribution before and at the extinguish timing in cases 5 and 6 is presented in Fig. 82 [97]. It can observe that the current density at 280.0 and 200.0 μs in cases 5 and 6 decreased significantly from the previous timing, which means the broken current path continuity. Therefore, the differentiated extinguish timing by SMLM in cases 5 and 6 are accurate. The misjudgment of the manual differentiation was caused by differentiating the residual high-temperature gas as arc plasma existence even after extinguishment.

Moreover, the arc plasma movement was significantly affected by the application of an external magnetic field, and the results in Table 8 [97] indicated that increasing AEMFI was more effective than increasing EOV. However, the application of a strong AEMFI is not structurally feasible; instead, the adjustment of the electrode structure to use its self-electromagnetism as a driving force is recommended.

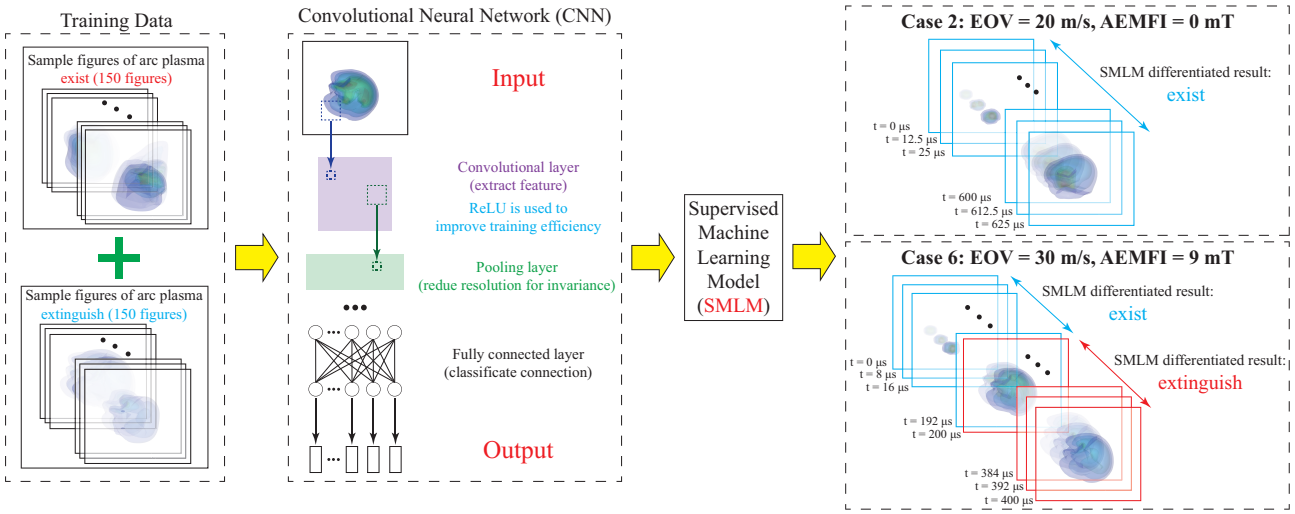

Fig. 81: Schematic of establishment and application of supervised machine learning model used in this study [97].

Table 8 Differentiation results obtained under various interruption conditions using SMLM [97].

Case	EOV [m/s]	AEMFI [mT]	Differentiated result	Extinguish timing [μs] (SMLM)	Extinguish timing [μs] (manual)
1	10	1	◯	400.0	400
2	20	0	×	-	-
3	20	5	◯	362.5	362.5
4	25	0	×	-	-
5	25	7	◯	280.0	290
6	30	9	◯	200.0	216
7	40	0	×	-	-

◯: Interruption success
×: Interruption failure

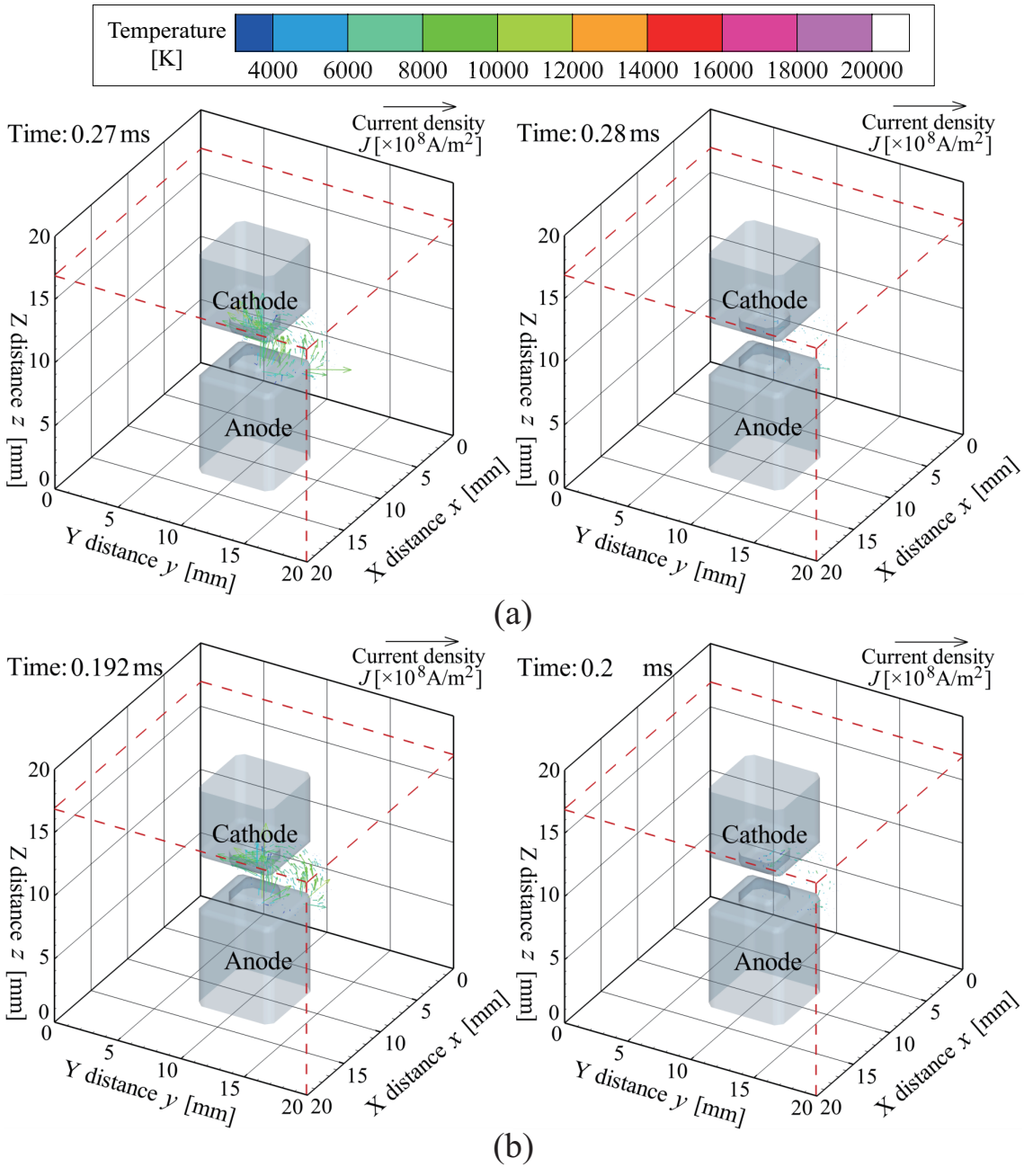

Fig. 82 Current density distribution at extinguish timing: (a) Case 5 and (b) Case 6 [97].

5.2 Prediction of interruption result in different circumstances by using artificial intelligence

The simulation program of this study can mimic the DCCB interruption process accurately, and analyze the time variation of various physical properties qualitatively. However, the consuming time for obtaining the interruption result of each calculation condition is large, because the amount of control volume is mass and the number of the time step is plenty (the time step is short for capturing the rapid movement of arc plasma). In the current circumstance, it takes about 136 hours to finish the interruption simulation of one calculation condition, in which the total amount of control volume is 470,680 and the number of the time step is 50. Moreover, the actual size of the DCCB is 2.5 times larger than this calculation model, and the number of time steps will be larger because the arc plasma movement is more complicated, and needs shorter time steps for analyzing it. Under the above consideration, the consumption time will increase to more than 700 hours, which is a great problem for iterating the current DCCB to the next generation.

The method of using AI to predicate the interruption result in different circumstances was proposed and shown in Fig. 83. To be specific, the variation of R, G, and B values of each pixel of the simulation result (which is temperature distribution in this study) of DCCB interruption at the preliminary stage were extracted. Then, the long short-term memory model was constructed by using MATLAB 2022a based on the extracted R, G, or B values, and predicts the R, G, and B values of each pixel at a specific time. Finally, the temperature distribution figure can be configured based on the predicted R, G, and B values.

Fig. 84 shows the comparison between the simulation result of temperature distribution and the AI prediction result at 100 dt. It can observe that the resolution of the AI prediction figure was low, because the input figure is 228×256 pixels for rapidity. Although the predicted figure did not have high resolution, it still can observe that the temperature distribution at the inter-electrode area had similar distribution when the electrode opening velocity is 20 m/s without applying an external magnetic field. Even the form of arc plasma remained in the predicted figure when the electrode opening velocity is 20 m/s with applying a 5 mT external magnetic field, there is no high-temperature area existing between the inter-electrode area which implies the extinguish of arc plasma. Therefore, the current AI prediction model's quality and accuracy can be improved by increasing the resolution of the input figure and using a high-specification Graphics Processing Unit.

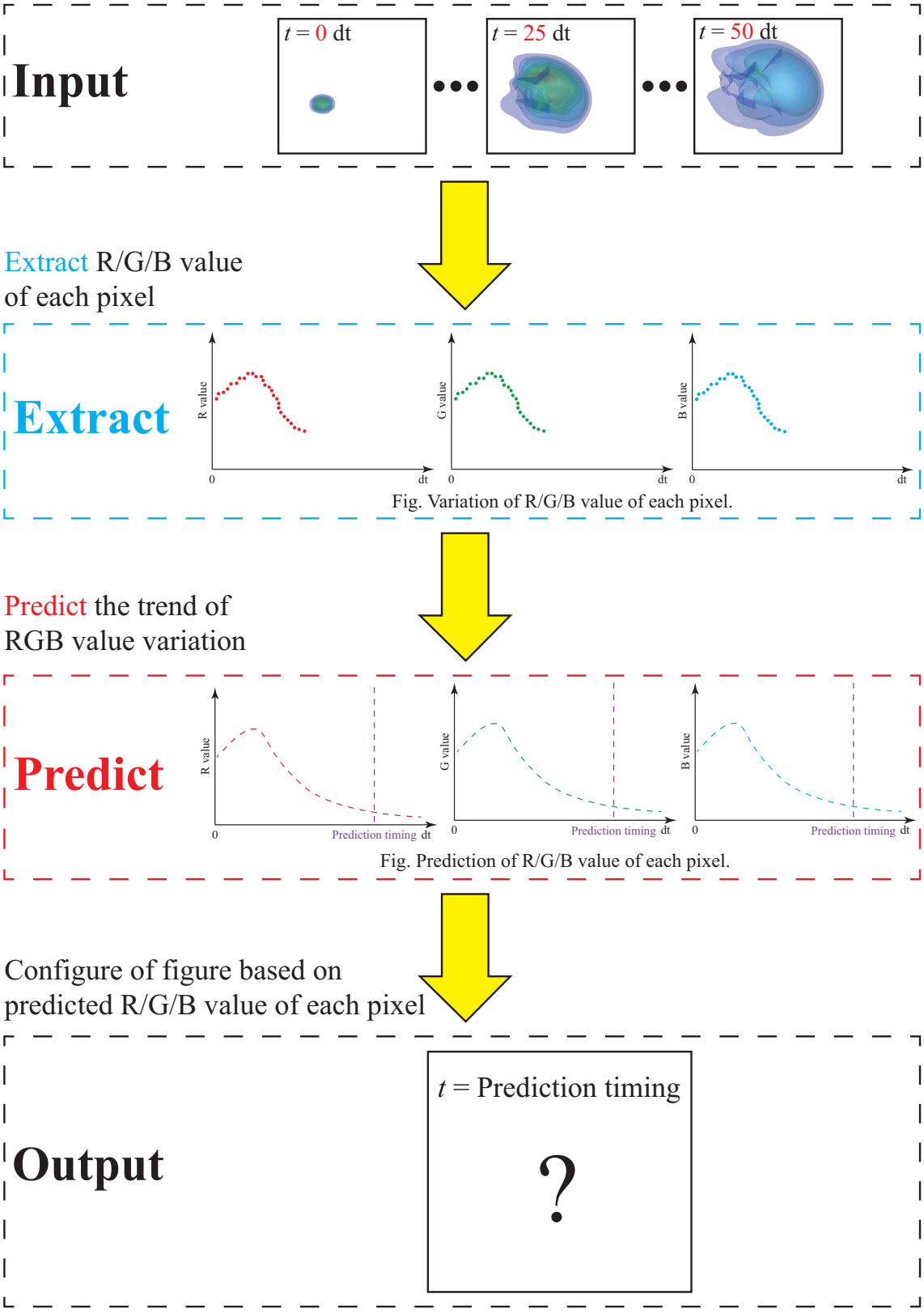

Fig. Variation of R/G/B value of each pixel.

Fig. Prediction of R/G/B value of each pixel.

Fig. 83 Schematic of predicting DCCB interruption result based on preliminary simulation results.

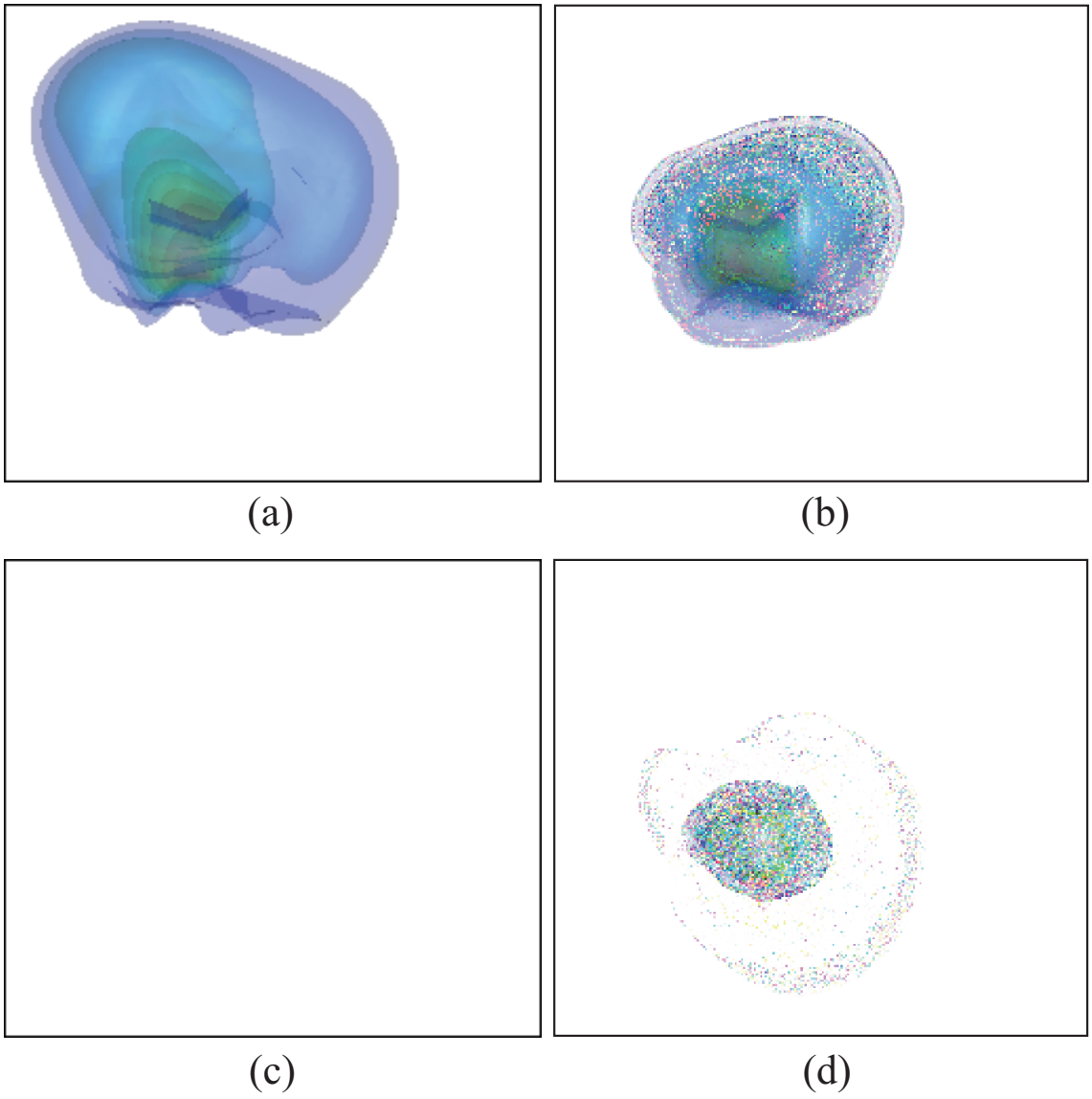

Fig. 84: Comparison between simulation result of temperature distribution and AI prediction result at 100 dt. (a) Simulation result: 0 mT, 20 m/s. (b) AI prediction: 0 mT, 20 m/s. (c) Simulation result: 5 mT, 20 m/s. (d) AI prediction: 5 mT, 20 m/s.

5.3 Construction and application of cyber-physical system for DCCB

Fig. 85 shows the diagram of the cyber-physical system for creating next-generation DCCB [99][100]. The first step for developing this CPS is measuring or sensing the data of the actual product and creating its digital twin in the virtual space, which is the function of the developed three-dimensional electromagnetic thermal fluid simulation in this study. Meanwhile, the knowledge of different fields such as material, structural, industrial design, etc. can be input into this simulation program to improve its accuracy.

As presented in Chapter 1.3, a series of simulations of various circumstances can be simultaneously implemented in the virtual space which can significantly decrease the time cost of the design phase. The dangerous experiment and tests can be implemented in the virtual space, which can substantially improve the safety of the manufacturing phase. As for after the product was put into use, its maintenance cost can be decreased by predicting the status of different parts of the equipment based on time series data, which can significantly improve product performance [98].

Moreover, this cyber-physical system does not only can be applied in the creation of next-generation DCCB but also can be expanded into other products and fields, and provide proposals of the optimal solution of design and operation to shorten the development iteration period and improve product performance.

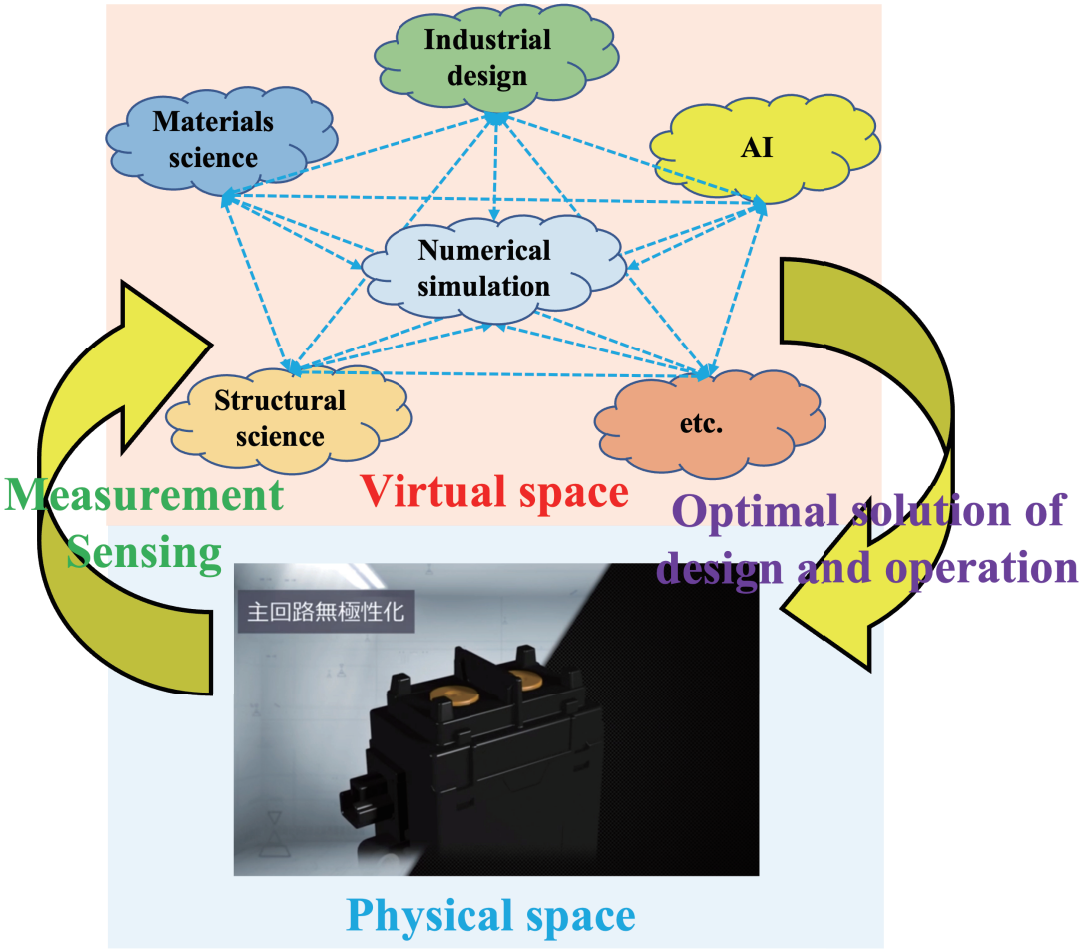

Fig. 85 Diagram of cyber-physical system for creating next-generation DCCB.

Chapter6 Summary and future topics

The construction of Society 6.0 should be started by different individuals, who locate their interested field and try to become an expert in that field. Then, the next-generation products can be generated through the cooperation and inspiration of knowledge from different fields. Those next-generation products will connect and constitute a sustainable infrastructure, which can provide a sufficient and unlimited environment for us to enjoy a life full of opportunity and excitement. This process will form a positive circle to create Society 6.0.

In this study, the application of DCCB in the electric railway system, the electric vehicle, and the solar photovoltaic system was investigated, which can to the conclusion that the need for next-generation DCCB is simultaneously satisfying four characteristics, which are rapid, reliability, miniaturization, and high capacity. Along with the development of modern manufacturing technology, the fabrication of next-generation DCCB can be significantly improved with the assistance of big data and digital twin technology. Hence, the fundamental arc plasma movement and its physical property variation were analyzed by numerical simulation, and the interruption process of DCCB was simulated in the virtual world. To be specific, the movements of the cathode spot, anode spot, and arc column were focused and their mechanisms were elucidated from the hypothesis model to simulation reproduction and experimental verification at the end. Moreover, the complicated phenomena of the primary stage of DCCB interruption, which includes the molten metal bridge, metal vapor generation, and electrode opening process were considered. Then the different circumstances of arc plasma during the interruption process were analyzed and classified into extinguish, re-strike, and stagnation. Therefore, the object of this study is to propose a design for next-generation DCCB that simultaneously satisfies four characteristics. Three tasks need to be accomplished: elucidate the movement and physical property variation of magnetic driven arc, construct the numerical simulation for simulating the interruption process of DCCB, and develop an AI model for differentiating and predicting the interruption result. The goal of this study is to construct a digital twin for proposing a next-generation DCCB design.

In Chapter 2, the basic assumption, governing equation, flow chart, calculation area, and boundary condition was presented. Moreover, two different metal vapor calculation methods were presented and the energy balance on the electrode surface due to the evaporation was discussed. For better simulating the electrode spot movement, the arc root model for the non-local thermal equilibrium effect on the electrode surface, and the thermal field theory application on the cathode surface were implemented. Based on the different movement mechanisms and characteristics of cathode and anode spots, the calculation setting of current density and the advanced threshold was set. For mimicking the interruption process as similar as possible to the actual phenomenon, the consideration of metal vapor generated from the molten metal bridge,

the electrode opening process, and the application of recovery voltage was implemented.

1. A three-dimensional electromagnetic thermal fluid simulation program was developed to simulate the magnetic driven arc movement and analyzed the variation of its physical properties.

2. The arc root model for simulating the non-local thermal equilibrium effect on the electrode surface was constructed, and the current density on the cathode surface was decided by the thermal field theory.

3. Cathode and anode spots' movements were simulated based on their different characteristics in the case of parallel electrodes circumstance, and the interruption process of DCCB was simulated from its preliminary stage to the arc plasma extinguish.

In Chapter 3, the cathode spot movement of atmospheric arc plasma after the ignition was analyzed. It found that the movement of the cathode spot was decided by the directions of total electromagnetic force (self and external) on the two sides of the center point of the cathode spot, and the cathode spot advances when the direction of the electromagnetic force on the right side control volume points forward. As for the effect of the application of an external magnetic field, it is to break the electromagnetic force balance. As for the cathode spot movement after its ignition, the charged particles advance under the influence of the applied external magnetic field, which causes the increase of current density derived from field emission and leads to cathode spot movement. In the case of analyzing the anode spot movement, the re-strike phenomenon was mimicked based on the experiment figures and then based on the electrical conductivity distribution. It found that the electrical conductivity of the re-strike point increased because of the transport of heavy particles, however, the detriment factor of the re-strike phenomenon occurrence was the increment of the electrical field between the arc column and the anode surface. Afterward, the simulation result compares with the experiment figure and data for verification.

1. The cathode spot's first step occurred when the electromagnetic force balance was broken by the application of an external magnetic field or the self-magnetic field derived from the parallel electrodes.

2. Cathode spot velocity was in proportion to the division factor, which is calculated by the driving electromagnetic force (points forward and promotes the cathode spot movement) divide by the flow velocity of the cathode jet (points downward and obstructs the cathode spot movement).

3. The current density of the re-strike point area increased before the occurrence of the re-strike phenomenon, which was caused by the electrical conductivity and electric field increments and the latter had a more significant influence on the re-strike occurrence.

4. The increments of electrical conductivity and electric field density of the re-strike point area were caused by the transport of heavy particles (ions and neutral particles), which was dominated by the cathode jet.

In Chapter 4, the behavior of atmospheric arc plasma during the interruption process of DCCB was analyzed. It found that the existence of high concentration metal vapor on the electrodes' surface causes the cathode spot to shift to the inner corner on the backward side after ignition, and the multiple occurrences of the reattachment phenomenon at the anode side. Those two phenomena led to the multiple occurrences of the reattachment phenomenon at the anode side and increased the interruption time. Moreover, the interruption process of DCCB was divided into three circumstances: extinguishing, re-strike, and stagnation. As for the increment rate of arc voltage per unit length, it was found that the increment rate of the arc voltage per unit length became more rapid when the electrode opening velocity was higher. The difference in the increment rate of the arc voltage per unit length at different electrode opening velocities became more significant with the application of an external magnetic field.

1. Metal vapor increases the interruption time because of its adverse influence on the electrode spot movement, where the cathode spot shifted to the inner corner on the backward side after ignition, and the multiple occurrences of the reattachment phenomenon at the anode side.

2. A certain external magnetic field intensity is necessary to drive the arc plasma into the extinguishment chamber, and the shape and position of the DCCB wall should be adjusted to prevent the formation of a rebound flow velocity distribution.

3. The cross-sectional area of the arc became larger and the metal vapor concentration of the inter-electrode area remained high when the electrode opening velocity was higher. Therefore, the increment rate of the arc voltage per unit length increased less than the increment ratio of the electrode opening velocity without external magnetic field application.

4. The difference in the arc length increment rate at different electrode opening velocities became smaller when an external magnetic field was applied. However, the difference in the increment rate of the arc voltage per unit length at different electrode opening velocities became more significant.

In Chapter 5, an AI model for differentiating the condition of arc plasma during the interruption process, and locating the extinguish timing in successful interruption circumstance was developed. It significantly increases the analysis efficiency and had better accuracy than manual differentiation. Furthermore, another AI model was developed for predicting the interruption result in different circumstances, which can rapidly decrease the consumption time of numerical simulation and manufacturing cycle. The construction of cyber-physical system can become a hotbed for the knowledge from different fields to fuse and inspire with each other, and lead to the creation of next-generation DCCB.

1. AI models were constructed for differentiating arc plasma conditions and locating the extinguishing timing, and predicting the interruption result in different interruption circumstances. A cyber-physical system was constructed for the creating of next-generation DCCB.

2. The data from physical space is transformed to cyber space by measuring or sensing, then knowledge from different fields under various circumstances and conditions were fused and the useful information was extracted and the optimal solution can be proposed to the design of next-generation DCCB.

According to the above-obtained results and insights which were summarized in Fig. 86, three tasks of this study were accomplished and a digital twin for proposing a next-generation DCCB design was constructed. Therefore, the object of this study of proposing a design of next-generation DCCB that simultaneously satisfies four characteristics was achieved.

Furthermore, several research topics still require further adjustment and development, which are summarized as follows.

1. In this study, the simulation was implemented under the assumption of an uncompressed gas situation. However, the physical properties of arc plasma change along with the pressure variation and influence the arc plasma movement. Along with the miniaturization of DCCB, the simulation of arc plasma movement and its physical property variation in compressed gas situations should be considered.

2. In this study, the developed arc root model on the anode surface was based on the known phenomenon and equation of cathode surface which was well researched. However, the mechanism of charged particles and neutral particles on the anode surface is different from the cathode surface, a independent arc root model for the anode surface should be developed.

3. In this study, the method of metal vapor generated from the molten metal bridge was implemented under the assumption of maximum generation. However, the broken of molten metal bridge happens faster than the calculation setting. The broken timing of the molten metal bridge and the generation volume of metal vapor in this process should be adjusted based on the experiment data.

4. In this study, continuous cathode spot movement and intermittent anode spot movement (re-strike phenomenon) were successfully simulated in parallel copper electrode situations, the advanced methods of electrode spots should be applied in various electrode shapes and materials for further generality.

5. In this study, the calculation area of DCCB is smaller that the actual product for simplicity and rapid calculation. To better reproduce the complicit arc plasma movement inside the actual DCCB, which has two arc plasma generated simultaneously. A larger and more complex calculation area should be constructed.

6. In this study, numerical simulation models and AI models were respectively developed and configured because of their different functions. For the wider application of this digital twin technology in other product development, the numerical simulation models and AI models should be integrated into one program to improve availability.

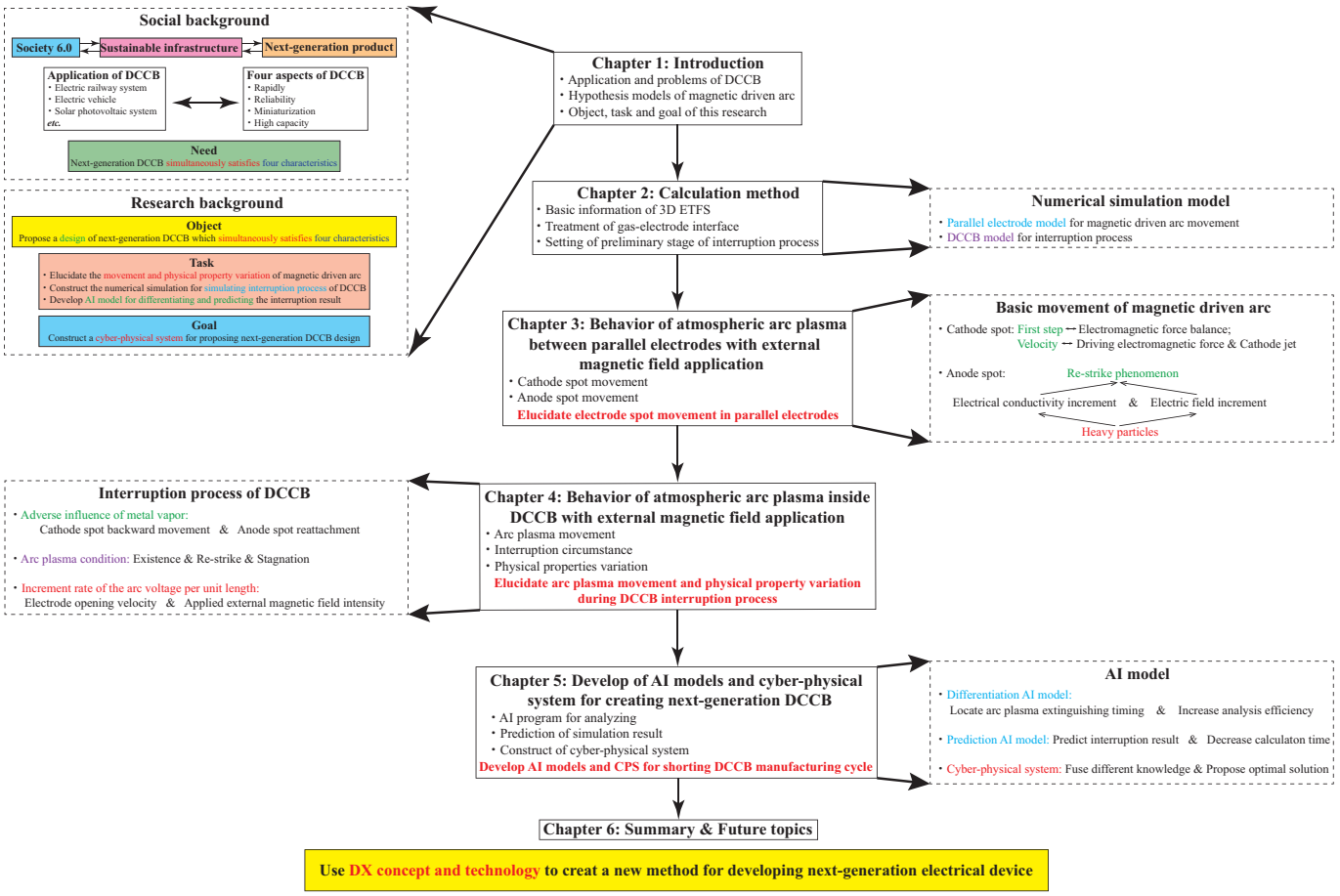

Fig. 86 Summary flow chart of this study.

Acknowledgements

About this research, I would like to express my deepest appreciation to Prof. Iwao. During the regular meeting and research presentations at the laboratory, Prof. Iwao gave me plentiful guidance and advice to help me construct a solid knowledge foundation to implement this research. Moreover, Prof. Iwao has shown me the possibility and innovation of integrating the foundation of physical research with cutting-edge technology such as AI, big data, and DX technology. Meanwhile, Prof. Iwao not only provided his support in the academic field, but also showed me the importance of having a passion for life and developing sustainable relationships with people around me. I joined the HiCEL DX laboratory with trepidation and uncertainty five years ago, and graduated as a capable and responsible person who can provide support and unite others to lead the social transformation in this DX trend. The ability to merge different kinds of technologies and create new research topics are the most important attainments of a researcher. As a great role model and pioneer, Prof. Iwao instructed me in these attainments by practicing them such as jointed international academic conferences and exchanging ideas with foreign scholars in all kinds of the research area, solving technical problems for companies, and training the students by including them into these joint research projects, and created and impelled the "Hirameki, Koto, Mono, Hito" creation program to initiate a new method for nurturing the next-generation leader. By observing the effort of Prof. Iwao impelled these projects and events and joining them, I managed to develop my ability to research, communicate, cooperate, and innovate. Thanks to the guidance and advice from Prof. Iwao, I have spent five meaningful years in the HiCEL DX laboratory at Tokyo City University.

In the meantime, I would like to express my gratitude to Prof. Tatsuhito Nakajima, Prof. Hiroshi Nohira, Assoc. Prof. Kenji Suzuki, and Lecturer Surantha Nico, gave me many advice and encouragement based on an engineering perspective, which improved my thesis structure and presentation skill. Because of their support, I was able to consider my research from different viewpoints and make my presentation easier to understand for people from other research fields. Also, I would like to express my gratitude to Prof. Reggie Cobarrubia Gustilo from De La Salle University, who spent one year in the HiCEL DX laboratory and gave much advice on my research topic and presentation skills. Moreover, he continuously supported and discussed the content of my research paper as a co-author, even after returning to De La Salle University. Meanwhile, I also want to express my gratitude to Mr. Shinji Yamamoto, Mr. Gaku Asanuma, and Mr. Toshiyuki Onchi from Fuji Electric Co., Ltd., who gave me a lot of advice based on the knowledge and insight of developing and applicating the actual electrical products.

At the beginning of my research, the graduated Ph.D. student Mr. Yoshifumi Maeda taught and helped me construct the three-dimensional electromagnetic thermal fluid simulation programs, which were used to elucidate the arc plasma phenomenon qualitatively and quantitatively as the cornerstone of my research. Also, I would like to thank Yuhi Asano, Yuya Ishikawa, Soshi Iwata, Yoshiyuki Zama, Yuti Naito, and Takashi Yamato who graduated in 2019 with their master's degrees. Those senior students showed me that focus and persistence are key factors for achieving accomplishment. With them as my examples, I set up my mind and persisted in my efforts during my master's studies.

I would also like to thank Tomonari Iwasaki, Kazuki Kawasaki, Shota Kokubo, Yuji Komai, Yuriko Takeda, Shogo Tokunaga, Shoya Nishizawa, and Yusuke Nemoto who are master's students in the same grade with me during the master period. We discussed and helped each other not only with our research but also in our daily life, and we joined a lot of academic conferences and symposiums together. Even though we chose different career paths, I believe our relationship will remain and our paths will cross someday in the future. Also, I would like to express my thankfulness to Yusuke Nemoto again, because we pursued our Ph.D. degrees together and shared a lot of experiences. I sincerely hope he can achieve remarkable achievements in the academic area.

Here, I also like to thank the students who committed to managing the events of our laboratory and university, which made me able to focus on my research. They are fourth-year Ph.D. students: Zhendong Yuan, Yuki Suzuki, and Hirotoshi Sato. The third-year Ph.D. students: Masahiro Takagi and Honoka Morishita. The second-year master students: Susumu Ichinose, Makoto Kaneko, Hideaki Sugekawa, Humiya Sekiguchi, Junya Tanaka, Masaya Toyota, Wataru Fuse, Gyoukan Horikawa, and Tomomasa Minamizawa. The first-year master's students: Ken Urushizaka, Miyoshiyuki Kusakari, Taisei Kudo, Akira Kouno, Kenshin Saigo, Reitairo Shirada, Yuto Suzuki, and Ki Maruta. The fourth-year bachelor students: Kazuya Ida, Koudai Ishikawa, Nozomi Ishihara, Hiroto Oinuma, Asuka Kawasaki, Sougo Saito, Daiki Takayama, Kaito Tateishi, and Motoki Tanaka. The third-year bachelor's students: Koto Isomi, Kazuki Kuran, Ying Sun, Sota Hosokawa, Naoto Masudo, Yohei Mitsuyama, and Satoshi Murayama. Also, Kanashiro Tang Takehide, Masashi Shimazaki, Yuki Sugiyama, Yu Shi, Takuya Tashiro, and Koki Matsumoto graduated in 2021 with their master's degrees. Shinichiro Kashiwagi, Koki Kouchi, Junpei Oya, and Hisatsugu Kaneko graduated in 2022 with their master's degrees.

My parents gave me full financial and emotional support during my graduate school period. Without their understanding and encouragement, I can't finish my master's and doctoral programs in Japan. Let alone joined academic conferences and symposiums all around the world. Meanwhile, I would like to thank Ms. Siyao Hong who gave me full support in emotion and daily life. Therefore, I am always grateful for their support and keep trying to become a better person who can contribute to society.

Finally, I would like to express my sincere thanks to the people who have helped me during my five years graduate school period.

References

[1] Society 5.0.
https://www8.cao.go.jp/cstp/society5_0/

[2] Gubbi J, Buyya R, Marusic S, Palaniswami M: "Internet of Things (IoT): A vision, architectural elements, and future directions," *Future Generation Computer Systems*, 2013, **29**(7):1645-1660. https://doi.org/10.1016/j.future.2013.01.010

[3] Wu G, Talwar S, Johnsson K, Himayat N, Johnson KD: "M2M: From mobile to embedded internet," *IEEE Communications Magazine*, 2011, **49**(4):36-43. https://doi.org/10.1109/MCOM.2011.5741144

[4] Murphy AB: "A Perspective on Arc Welding Research: The Importance of the Arc, Unresolved Questions and Future Directions," *Plasma Chem Plasma Process*, 2015, **35**:471-489. https://doi.org/10.1007/s11090-015-9620-2

[5] Freton P, Gonzalez JJ, Camy Peyret F, Gleizes A: "Complementary experimental and theoretical approaches to the determination of the plasma characteristics in a cutting plasma torch," *Journal of Physics D : Applied Physics*, 2003, **36**:1269. https://doi.org/10.1088/0022-3727/36/11/307

[6] Palama D, Verbakel W, Otto K, Senan S: "New developments in arc radiation therapy: A review," *Cancer Treatment Reviews*, 2010, **36**(5):393-399. https://doi.org/10.1016/j.ctrv.2010.01.004

[7] Yang F, Rong M, Sun H, Murphy AB, Ren Z, Niu C: "Low-voltage circuit breaker arcs – simulation and measurements," *Journal of Physics D : Applied Physics*, 2013, **46**:273001. https://doi.org/10.1088/0022-3727/46/27/273001

[8] Li X, Zhao H, Murphy AB: "SF6-alternative gases for application in gas-insulated switchgear," *Journal of Physics D : Applied Physics*, 2013, **51**:153001. https://doi.org/10.1088/1361-6463/aab314

[9] Homma M, Sakaki M, Kaneko E, Yanabu S: "History of vacuum circuit breakers and recent developments in Japan," *IEEE Transactions on Dielectrics and Electrical Insulation*, 2006, **13**(1):85-92. https://doi.org/10.1109/TDEI.2006.1593405

[10] Sasaki H, Toya N, Nakata T, Sagara Y, Toba S, Tanala S, Kamino Y, Yamaji Y: "Development of a High-Speed Circuit Breaker for DC Railway Substations," 2019

*IEEE Third International Conference on DC Microgrids*4 (*ICDCM*), 2019, pp.1-4. https://doi.org/10.1109/ICDCM45535.2019.9232706

[11] Sagara Y, Nakada K,Kobayashi M, Tohya N, Sasaki H, Nakata T, Toba s, Tanaka S: "High-speed Breaking Technic of DC High-speed Circuit Breaker for Railway Substation," *The* 2017 *Annual Meeting of The Institute of Electrical Engineers of Japan*, 2017, No.5-189 (in Japanese).

[12] Nakata T, Tohya N, Sasaki H, Sagara Y, Nakada K, Toba S, Tanaka S: "Arc-extinguishing Technique of DC High-speed Circuit Breaker for Railway Substation," *Joint Technical Meeting on Electrical Discharges*, *Switching and Protecting Engineering*, *High Voltage Engineering*, 2017, No.HV17073 (in Japanese).

[13] Naka Y, Shiba Y, Sakurai Y: ""SVE135" sealed high-voltage contactor having high overcurrent withstand capability," *Fuji Electric Review*, 2017, **63**(3):174-179.

[14] Tu H, Feng H, Srdic S, Lukic S: "Extreme Fast Charging of Electric Vehicles: A Technology Overview," *IEEE Transactions on Transportation Electrification*, 2019, **5**(4):861-878. https://doi.org/10.1109/TTE.2019.2958709

[15] Khalid M, Alam M, Sarwar A, Asghar M: "A Comprehensive review on electric vehicles charging infrastructures and their impacts on power-quality of the utility grid," *eTransportation*, 2019, **1**:100006. https://doi.org/10.1016/j.etran.2019.100006

[16] Deb N, Singh R, Brooks R, Bai R: "A Review of Extremely Fast Charging Stations for Electric Vehicles," *Energies*, 2021, **14**(22):7566. https://doi.org/10.3390/en14227566

[17] Lu S, Phung B, Zhang D: "A comprehensive review on DC arc faults and their diagnosis methods in photovoltaic systems," *Renewable and Sustainable Energy Reviews*, 2018, **89**:88-98. https://doi.org/10.1016/j.rser.2018.03.010

[18] Klement K: "DC Arc Flash Studies for Solar Photovoltaic Systems: Challenges and Recommendations," *IEEE Transactions on Industry Applications*, 2015, **51**(5):4239-4244. https://doi.org/10.1109/TIA.2015.2431639

[19] Rong M, Ma R, Chen J, Hou C, Sun Y: "Numerical Investigation on Arc Behavior in Low-Voltage Arc Chamber Considering Turbulence Effect," *IEEE Transactions on Plasma Science*, 2014, **42**(10):2716-2717. https://doi.org/10.1109/TPS.2014.2334694

[20] Sun H, Rong M, Chen Z, Hou C, Sun Y: "Investigation on the Arc Phenomenon of Air DC Circuit Breaker," *IEEE Transactions on Plasma Science*, 2014, **42**(10):2706-2707. https://doi.org/10.1109/TPS.2014.2343257

[21] Ma R, Rong M, Yang F, Wu Y, Sun H, Yuan D, Wang H, Niu C: "Investigation on Arc Behavior During Arc Motion in Air DC Circuit Breaker," *IEEE Transactions on Plasma Science*, 2013, **41**(9):2551-2560. https://doi.org/10.1109/TPS.2013.2273832

[22] Wu Y, Rong M, Sun Z, Wang X, Yang F, Li X: "Numerical analysis of arc plasma behaviour during contact opening process in low-voltage switching device," *Journal of Physics D : Applied Physics*, 2007, **40**:795. https://doi.org/10.1088/0022-3727/40/3/016

[23] Yang F, Rong M, Wu Y, Murphy AB, Pei J, Wang L, Liu Z, Liu Y: "Numerical analysis of the influence of splitter-plate erosion on an air arc in the quenching chamber of a low-voltage circuit breaker," *Journal of Physics D : Applied Physics*, 2010, **43**:434011. https://doi.org/10.1088/0022-3727/43/43/434011

[24] Yang F, Rong M, Wu Y, Murphy AB, Chen S, Liu Z, Shi Q: "Numerical Analysis of Arc Characteristics of Splitting Process Considering Ferromagnetic Plate in Low-Voltage Arc Chamber," *IEEE Transactions on Plasma Science*, 2010, **38**(11):3219-3225. https://doi.org/10.1109/TPS.2010.2070084

[25] Lindmayer M, Marzahn E, Mutzke A, Ruther T, Springstubbe M: "The process of arc-splitting between metal plates in low voltage arc chutes," *IEEE Transactions on Components and Packaging Technologies*, 2004, pp.28-34. https://doi.org/10.1109/HOLM.2004.1353090

[26] Hayasaka T, Kubota Y: "Influence of Breaking Arc on Mass and Surface Condition of Current-Collecting Materials," *IEEJ Transactions on Industry Applications*, 2012, **132**(2):163-169 (in Japanese). https://doi.org/10.1541/ieejias.132.163

[27] Hayasaka T, Akagi H: "Influence of Arc Discharge on the Surface of a Contact Wire," *IEEJ Transactions on Industry Applications*, 2015, **135**(4):327-334 (in Japanese). https://doi.org/10.1541/ieejias.135.327

[28] Hayasaka T, Morishita H, Ren Z, Iwao T: "Size of Molten Metal Bridge Conducting DC Current in Different Contact Strip Materials," *IEEJ Transactions on Electrical and Electronic Engineering*, 2022, **17**(7):1083-1084. https://doi.org/10.1002/tee.23598

[29] Morishita H, Maeda Y, Ren Z, Nemoto Y, Hayasaka T, Iwao T: "Development of Calculation Method for Melting Amount Mass of Contact Wire Caused by Melting and Evaporation of Molten Metal Bridge and Arc Generation," *IEEJ Transactions on Industry Applications*, 2022, **142**(5):410-417 (in Japanese). https://doi.org/10.1541/ieejias.142.410

[30] Morishita H, Maeda Y, Ren Z, Nemoto Y, Hayasaka T, Iwao T: "Development of Calculation Method for Melting Amount Mass of Contact Wire Caused by Melting and Evaporation of Molten Metal Bridge and Arc Generation," *Electrical Engineering in Japan*, 2022, **215**(3):?????-?????. https://doi.org/10.1002/eej.23403

[31] Lindmayer M, Springstubbe M: "Three-dimensional-simulation of arc motion between arc runners including the influence of ferromagnetic material," *IEEE*

Transactions on Components and Packaging Technologies, 2002, **25**(3):409-414. https://doi.org/10.1109/TCAPT.2002.804604

[32] Wu Y, Rong M, Li X, Murphy AB, Wang X, Yang F, Sun Z: "Numerical Analysis of the Effect of the Chamber Width and Outlet Area on the Motion of an Air Arc Plasma," *IEEE Transactions on Plasma Science*, 2008, **36**(5):2831-2837. https://doi.org/10.1109/TPS.2008.2004040

[33] Lindmayer M, Paulke J: "Arc motion and pressure formation in low voltage switchgear," *IEEE Transactions on Components and Packaging Technologies*, 1998, **21**(1):33-39. https://doi.org/10.1109/95.679030

[34] Zeller PR, Rieder WF: "Arc structure, arc motion, and gas pressure between laterally enclosed arc runners," *IEEE Transactions on Components and Packaging Technologies*, 2001, **24**(3):337-341. https://doi.org/10.1109/6144.946476

[35] Qi Q and Tao F: "Digital Twin and Big Data Towards Smart Manufacturing and Industry 4.0: 360 Degree Comparison," *IEEE Access*, 2018, **6**:3585-3593. https://doi.org/10.1109/ACCESS.2018.2793265

[36] Gandomi A and Haider M: "Beyond the hype: Big data concepts, meth- ods, and analytics," *International Journal of Information Management*, 2015, **35**(2):137-144. https://doi.org/10.1016/j.ijinfomgt.2014.10.007

[37] Grieves M: "Digital twin: Manufacturing excellence through virtual factory replication," *White Paper*, 2014.

[38] Ohno H, Ito H, Tange T, Naito K, Yokomizu Y, Matsumura T: "Travelling Characteristics of Electromagnetically Driven Arc Burning between the Edges of Parallel Flat Electrodes in Atmospheric Pressure," *IEEJ Transactions on Power and Energy*, 2000, **120**(11):1504-1512 (in Japanese). https://doi.org/10.1541/ieejpes1990.120.11_1504

[39] Chang Y, Liu X, Lu L, Babkin AS, Lee B, Gao F: "Impacts of external longitudinal magnetic field on arc plasma and droplet during short-circuit GMAW," *The International Journal of Advanced Manufacturing Technology*, 2014, **70**:1543-1553. https://doi.org/10.1007/s00170-013-5403-1

[40] Moriai H: "Interruption Technology of Breakers for High-voltage Direct Current," *Fuji Electric Review*, 2012, **58**(3):127-132.

[41] Sato Y: "No-Polarity Interruption Technology of Breakers for High-Voltage Direct Current," *Fuji Electric Review*, 2014, **60**(3):174-178.

[42] Iwao T, Nemoto A, Yumoto M, Inaba T: "Plasma Image Processing of High Speed Arc Movement in a Rail-Gun," *IEEE Transactions on Plasma Science*, 2005, **33**(2):430-431. https://doi.org/10.1109/TPS.2005.845292

[43] Ren Z, Kokubo S, Maeda Y, Yamamoto S, Iwao T: "Three-dimensional electromagnetic thermal fluid simulation of re-strike phenomenon in magnetic driven arc between parallel electrodes with edges," *IEEJ Transactions on Electrical and Electronic Engineering*, 2020, **15**(5):789-795. https://doi.org/10.1002/tee.23118

[44] Ren Z, Nemoto Y, Maeda Y, Yamamoto S, Asanuma G, Onchi T, Iwao T: "Cathode spot velocity of atmospheric arc plasma after arc ignition affected by self and external electromagnetic force between parallel electrodes using 3D numerical simulation," *IEEJ Transactions on Electrical and Electronic Engineering*, 2021, **16**(12):1656-1663. https://doi.org/10.1002/tee.23469

[45] Coulombe S, Meunier JL: "Thermo-field emission: A comparative study," *Journal of Physics D : Applied Physics*, 1997, **30**:776-780. https://doi.org/10.1088/0022-3727/30/5/009

[46] Murphy EL, Good RH: "Thermionic emission, field emission, and the transition region," *Physics Review*, 1956, **102**(6):1464-1473. https://doi.org/10.1103/PhysRev.102.1464

[47] Ren Z, Nemoto Y, Maeda Y, Yamamoto S, Asanuma G, Onchi T, Iwao T: "Analyzing Cathode and Anode Spot Movements of Atmospheric Arc Plasma in Parallel Electrodes Using Thermal Field Theory and Thermal Nonequilibrium Model," *IEEJ Transactions on Electrical and Electronic Engineering*, 2022, **17**(6):934-944. https://doi.org/10.1002/tee.23584

[48] Boxman RL, Martin PJ, Sanders DM: "Handbook of vacuum arc science and technology," New York: William Andrew Publishing, 1995

[49] Miller HC, Meunier JL: "Values of fowler-Nordheim emission functions v(y), t(y) and s(y), " *Journal of the Franklin Institute*, 1966, **282**:382-388. https://doi.org/10.1016/0016-0032(66)90043-3

[50] Nemoto Y, Iwata S, Maeda Y, Iwao T: "Analysis of electron and heavy particle velocity distribution under consideration of nonthermal equilibrium arc," *Electronics and Communications in Japan*, 2019, **102**(11):9-15. https://doi.org/10.1002/ecj.12214

[51] Nemoto Y, Iwata S, Maeda Y, Iwao T: "Analysis of electron and heavy particle velocity distribution under consideration of nonthermal equilibrium arc," *IEEJ Transactions on Power and Energy*, 2019, **139**(9):562-567 (in Japanese). https://doi.org/10.1541/ieejpes.139.562

[52] Sakuta T, Kito Y, Miyachi I: "Electrical and thermal conductivities and enthalpy of high-temperature air contaminated by copper vapor," *The Transactions of the Institute of Electrical Engineers of Japan A*, 1981, **101**(4):241-248 (in Japanese). https://doi.org/10.1541/ieejfms1972.101.241

[53] Tanaka T, Maeda Y, Yamamoto S and Iwao T: "Contribution of Metal Vapor Mass at Periphery Part of Pulsed Arc to Electromagnetic Force in Weld Pool," *Electrical Engineering in Japan*, 2019, **207**(1):15-23. https://doi.org/10.1002/eej.23199

[54] Tanaka T, Maeda Y, Yamamoto S and Iwao T: "Contribution of Metal Vapor Mass at Periphery Part of Pulsed Arc to Electromagnetic Force in Weld Pool," *IEEJ Transactions on Fundamentals and Materials*, 2018, **138**(11):562-569. https://doi.org/10.1541/ieejfms.138.562

[55] Sakuta T, Kito Y and Miyachi I: "Enhancement of Electron Density in High Temperature Air Contaminated by Copper Vapor", *The Transactions of the Institute of Electrical Engineers of Japan.A*, 1978, **98**(4):209-214 (in Japanese). https://doi.org/10.1541/ieejfms1972.98.209

[56] Ren Z, Nemoto Y, Suzuki Y, Yamamoto S, Asanuma G, Onchi T, Iwao T: "Analysis of Adverse Influence of Metal Vapor to Arc Movement Between Electrodes with External Magnetic Field Applied by Numerical Simulation," *IEEJ Transactions on Electrical and Electronic Engineering*, 2022, **17**(2):183-193. https://doi.org/10.1002/tee.23498

[57] Ren Z, Nemoto Y, Suzuki Y, Takagi M, Morishita H, Iwao T: "Numerical Simulation of External Magnetic Field Effect on Arc Plasma After Molten Metal Bridge Breaking under Different Electrode Opening Velocities," *AIP Advance*, 2022, **12**:035239. https://doi.org/10.1063/5.0079263

[58] Murphy AB: "Thermal plasmas in gas mixtures," *Journal of Physics D : Applied Physics*, 2001, **34**:R151-73. https://doi.org/10.1088/0022-3727/34/20/201

[59] Boulos M, Fauchais P, Pfender E: "Thermal Plasmas: Fundaments and Applications," New York, NY: Springer, 1994

[60] Gleizes A, Gonzalez JJ and Freton P: "Thermal plasma modelling," *Journal of Physics D : Applied Physics*, 2005, **38**:R153-83. https://doi.org/10.1088/0022-3727/38/9/R01

[61] Murphy AB, Tanaka M, Yamamoto K, Tashiro S, Sato T, Lowke JJ: "Modelling of thermal plasma for arc welding: The role of the shielding gas properties and metal vapour," *Journal of Physics D : Applied Physics*, 2009, **42**:194006. https://doi.org/10.1088/0022-3727/42/19/194006

[62] Murphy AB: "Transport coefficients of air, argon-air, nitrogen-air, and oxygen-air plasmas," *Plasma Chemistry and Plasma Processing*, 1995, **15**:279-307. https://doi.org/10.1007/BF01459700

[63] Tanaka Y, Fujino T, Iwao T: "Review of thermal plasma simulation technique," *IEEJ Transactions on Electrical and Electronic Engineering*, 2019, **14**(11):1582-1594. https://doi.org/10.1002/tee.23040

[64] Maeda Y, Iwao T: “Analysis of flow velocity distribution in arc affected by transverse magnetic field with lateral gas flow for elucidation of arc deflection,” *IEEJ Transactions on Fundamentals and Materials*, 2020, **140**(5):269-275 (in Japanese). https://doi.org/10.1541/ieejfms.140.269

[65] Maeda Y, Iwao T: “Contribution of axial arc pressure gradient near cathode on enthalpy flow of arc to axial direction with lateral gas,” *IEEJ Transactions on Power and Energy*, 2019, **139**(5):309-315 (in Japanese). https://doi.org/10.1541/ieejpes.139.309

[66] Yamamoto S, Iwata S, Iwao T, Ehara Y: “Energy balance on current density distribution of cathode spot in vacuum arc,” *IEEJ Transactions on Power and Energy*, 2019, **139**(5):302-308 (in Japanese). https://doi.org/10.1541/ieejpes.139.302

[67] Iwao T , Mori Y , Okubo M, Sakai T , Tashiro S, Tanaka M, Yumoto M: “Modelling of metal vapour in pulsed TIG including influence of self-absorption,” *Journal of Physics D : Applied Physics*, 2010, **43**:434010. https://doi.org/10.1088/0022-3727/43/43/434010

[68] Ikeda K, Amakawa T, Shibuya M: “Analysis of argon arc radiance under high pressure and high temperature,” *IEEJ Transactions on Fundamentals and Materials*, 2000, **120** − *A*:414-419 (in Japanese). http://doi.org/10.1541/ieejfms1990.120.4_414

[69] Wilbers ATM, Kroesen GMW, Timmermans CJ, Schram DC: “The continuum emission of an arc plasma,” *Journal of Quantitative Spectroscopy & Radiative Transfer*, 1991, **45**:1-10. https://doi.org/10.1016/0022-4073(91)90076-3

[70] NIST Atomic Spectra Database Lines Form. https://physics.nist.gov/PhysRefData/ASD/lines_form.html

[71] Wilke CR: “A viscosity equation for gas mixtures,” *The Journal of Chemical Physics*, 1959, **18**:517-519. https://doi.org/10.1063/1.1747673

[72] Ren Z, Nemoto Y, Suzuki Y, Iwao T: “Numerical Simulation for Analyzing Re-strike Phenomenon of Arc Plasma Considering Application of Recovery Voltage at Direct Current Circuit Breaker,” *IEEJ Transactions on Electrical and Electronic Engineering*, 2022, **17**(4):611-613. https://doi.org/10.1002/tee.23548

[73] Mori Y, Iwo T, Yumoto M, Tashiro S, Tanaka M: “Effects of Metal Vapor for Temperature Distribution of Transient Arc in Pulsed TIG Welding,” *quarterly Journal of the Japan Welding Society*, 2009, **27**(2):8-2. https://doi.org/10.2207/qjjws.27.8s

[74] Tanaka M, Yamamoto K, Tashiro S, Nakata K, Yamamoto E, Yamazaki K, Suzuki K, Murphy AB, Lowke JJ: “Time-dependent calculations of molten pool formation and thermal plasma with metal vapour in gas tungsten arc welding,” *Journal of Physics D : Applied Physics*, 2009, **43**:434009. https://doi.org/10.1088/0022-3727/43/43/434009

[75] Enami Y, Sakata M: "Simulation of arc in molded-case circuit breaker with metal vapor and moving electrode," *2nd International Conference on Electric Power Equipment - Switching Technology*, 2013, 1-4. http://doi.org/10.1109/ICEPE-ST.2013.6804390

[76] Aihara T: "Principles of Heat Transfer," Japan: SHOKABO Co., Ltd., 1994

[77] Lowke JJ, Morrow R, Haidar J: "A simplified unified theory of arcs and their electrodes," *Journal of Physics D : Applied Physics*, 1997, **30**(14):2033-2042. https://doi.org/10.1088/0022-3727/30/14/011

[78] Rong M, Yang F, Wu Y, Murphy AB, Wang W, Guo J: "Simulation of arc characteristics in miniature circuit breaker," *IEEE Transactions on Plasma Science*, 2010, **38**(9):2306-2311. https://doi.org/10.1109/ TPS.2010.2050703

[79] Amemiya H: "Basic concept of sheath formation," *Plasma Physics and Fusion Technology*, 1992, **24**(16):550-555 (in Japanese). https://doi.org/10.1585/jspf1958.68.550

[80] Okamoto Y: "Fundamentals of processing plasma," *Journal of the Vacuum Society of Japan*, 2016, **59**(7):161-170 (in Japanese). https://doi.org/10.3131/jvsj2.59.161

[81] Yokomizu Y, Matsumura T, Henmi R, Kito Y: "Total Voltage Drops in electrode fall regions of SF6 arcs between electrodes of Cu-W, Cu, Fe, Ti, C and W in current range from 10 to 20,000A," *IEEJ Transactions on Power and Energy*, 1996, **16**(10):1197-1203. https://doi.org/10.1541/ieejpes1990.116.10_1197

[82] Morrow R, Lowke JJ: "A one-dimensional theory for the electrode sheaths of electric arcs," *Journal of Physics D : Applied Physics*, 1993, **26**:634. https://doi.org/10.1088/0022-3727/26/4/016

[83] Dickson DJ, von Engel A: "Resolving the electrode fall spaces of electric arc," *Proceedings of the Royal Society of London. Series A. Mathematical and Physical Sciences*, 1966, **300**:316-325. https://doi.org/10.1098/rspa.1967.0172

[84] Dinulescu HA, Pfender E: "Analysis of the anode boundary layer of high intensity arcs," *Journal of Applied Physics*, 1980, **51**(6):3149-3157. https://doi.org/10.1063/1.328063

[85] Ushio M: "Arc discharge and its applications," *Iron and Steel*, 1987, **73**(10):1309-1315. https://doi.org/10.2355/tetsutohagane1955.73.10_1309

[86] Ohno H, Ito H, Tange T, Naito K, Yokomizu Y, Matsumura T: "Travelling Characteristics of Electromagnetically Driven Arc Burning between the Edges of Parallel Flat Electrodes in Atmospheric Pressure," *IEEJ Transactions on Power and Energy*, 2000, **120**(11):1504-1512. https://doi.org/10.1541/ieejpes1990.120.11_1504

[87] Nemoto Y, Suzuki Y, Ren Z, Maeda Y, Iwao T: "Analysis of Arc Electron and Heavy Particle Temperature Distribution with Lateral Flow Velocity for Elucidation of Restrike," *IEEJ Transactions on Power and Energy*, 2022, **142**(4):228-234 (in Japanese). https://doi.org/10.1541/ieejpes.142.228

[88] Langlois Y, Chapelle P, Jardy A, Gentils F: “On the numerical simulation of the diffuse arc in a vacuum interrupter,” *Journal of Applied Physics*, 2011, **109**:113306. https://doi.org/10.1063/1.3587180

[89] Braginskii SI: “Transport process in a plasma,” Reviews of Modern Plasma Physics, 1965, **1**:205-311.

[90] Subramaniam V, Panneerchelvam P, Raja LL: “Modeling of thermalization phenomena in coaxial plasma accelerators,” *Journal of Physics D : Applied Physics*, 2018, **51**:215203. https://doi.org/10.1088/1361-6463/aabd94

[91] Chapman S, Cowling TG: “The Mathematical Theory of Non-uniform Gases Third edition,” Cambridge University Press, New York, 1970.

[92] Trelles JP, Pfender E, Heberlein JVR: “Modelling of the arc reattachment process in plasma torches,” *Journal of Physics D : Applied Physics*, 2007, **40**(18):5635-5648. https://doi.org/10.1088/0022-3727/40/18/019

[93] Gupta RN, Yos JM, Thompson RA: “A review of reaction rates and thermodynamic and transport properties for the 11-species air model for chemical and thermal nonequilibrium calculations to 30,000K,” *Tech. Rep*, February, 1989, NASA

[94] Bittencourt JA: “Fundamentals of Plasma Physics,” New York, NY: Springer, 2004

[95] Krizhevsky A,Sutskever I, Hinton GE: “ImageNet classification with deep convolutional neural networks,” *Communications of the ACM*, 2017, **60**(6):84-90. https://doi.org/10.1145/3065386

[96] Matsuyama E: “Deep Learning for Image Recognition with MATLAB Implementation,” *Medical Imaging and Information Sciences*, 2019, **36**(2):44-49 (in Japanese). https://doi.org/10.11318/mii.36.44

[97] Ren Z, Nemoto Y, Suzuki Y, Takagi M, Morishita H, Reggie CG, Iwao T: “Differentiation of Numerical Simulation Result of Direct Current Circuit Breaker Interruption Process Using Artificial Intelligence,” *IEEJ Transactions on Electrical and Electronic Engineering*, 2023, **18**(1):147-149. https://doi.org/10.1002/tee.23707

[98] Chen B, Liu Y, Zhang C, Wang Z: “Time Series Data for Equipment Reliability Analysis With Deep Learning,” *IEEE Access*, 2020, **8**:105484-105493. https://doi.org/10.1109/ACCESS.2020.3000006

[99] TOSHIBA Cyber Physical Systems, https://www.global.toshiba/ww/cps/corporate.html (2022/09/23)

[100] Fuji Electric: “Release of High Voltage Contactor with the Highest Current Overload Capacity in the Industry”, https://www.fujielectric.com/company/news/2017/20170524090001600.html. (2022/12/28)

[101] Kanzawa J: “Plasma Heat Transfer,” Shinzansha Publisher Co.,Ltd., 1992

[102] Kojima K: “Foundation Chemistry Statistical Thermodynamics Approach to Molecular Assemblies,” Kodansha Scientific Ltd., 1990

[103] Kojima K, Ochi K: “Statistical Heat of Chemistry,” Baifukan Co., Ltd., 2003

[104] Atomic spectral line database from CD-ROM 23 of R. L. Kurucz. http://www.cfa.harvard.edu/amp/ampdata/kurucz23/sekur.html

[105] Kreyszig E: “Advanced Engineering Mathematics,” Baifukan Co., Ltd., 2003

[106] The Chemical Society of Japan: “Handbook of Chemistry: Pure Chemistry, 5th ed.,” Maruzen Publishing Co., Ltd., 2004

[107] Chapman S, Cowling TG: “The Mathematical Theory of Non-uniform Gases,” Cambridge University Press, 1991

[108] Abrahamson AA: “Born-Mayer-Type Interatomic Potential for Neutral Ground-State Atoms with Z=2 to Z=105,” *Physical Review*, 1969, **178**:76-78. https://doi.org/10.1103/PhysRev.178.76

[109] Monchick L: “Collision Integrals for the Exponential Repulsive Potential,” *The Physics of Fluids*, 1959, **2**(6):695-700. https://doi.org/10.1063/1.1705974

[110] Yos JM: “Transport Properties of Nitrogen, Hydrogen, Oxygen and Air to 30,000K,” *AVCO Tech. Mem. RAD − TM − 63 − 7, ASTIA Doc. AD − 435 − 053*, 1963

[111] Rapp D, Francis WE: “Charge Exchange between Gaseous Ions and Atoms,” *The Journal of Chemical Physics*, 1962, **37**(11):2631-2645. https://doi.org/10.1063/1.1733066

[112] Gupta RN, Yos JM, Thormpson RA, Lee KP: “A Review of Reaction Rates and Thermodynamic and Transport Properties for an 11-Species Air Model for Chemical and Thermal Nonequilibrium Calculations to 30,000K,” *NASA Reference Publication*, 1990, **1232**

[113] Itikawa Y: “Momentum-transfer cross sections for electron collisions with atoms and molecules: Revision and supplement, 1977,” *Atomic Data and Nuclear Data Tables*, 1978, **21**(1):69-75. https://doi.org/10.1016/0092-640X(78)90004-9

[114] Paul KC, Takashima T, Sakuta T: “Copper Vapor Effect on RF Inductively Coupled SF_6 Plasmas,” *IEEE Transactions on Plasma Science*, 1998, **26**(3):1000-1009. https://doi.org/10.1109/27.700881

[115] Mori T, Kawano H, Iwamoto K, Tanaka Y, Kaneko E: “Gas-Flow Simulation With Contact Moving in GCB Considering High-Pressure and High-Temperature Transport Properties of SF_6 Gas,” *IEEE Transactions on Power Ddelivery*, 2005, **20**(4):2466-2472. https://doi.org/10.1109/TPWRD.2005.852360

[116] Tanaka Y, Yamachi N, Matsumoto S, Kaneko S, Okabe S, Shibuya M: “Thermodynamic and Transport Properties of CO2, CO2-O2 and CO2-H2 Mixtures at Temperatures of 300-30,000K and at Pressures of 0.1-10MPa,” *IEEJ Transactions on Power and Energy*, 2006, **126**(1):80-90. https://doi.org/10.1541/ieejpes.126.80

[117] Saito T: “Application of Thermodynamics,” University of Tokyo Press, 1987

[118] Chase MW: “NIST-JANAF Thermochemical Tables Fourth Edition,” American Institute of Physics, 1998

[119] Yamamoto M, Murayama S: “Spectroscopic measurement of plasma,” Japan Scientific Societies Press, 1995

[120] Ikeda K, Amakawa T, Shibuya M: “Analysis of Argon Arc Radiance under High Pressure and High Temperature,” *IEEJ Transactions on Fundamentals and Materials*, 2000, **120**(4):414-419. https://doi.org/10.1541/ieejfms1990.120.4_414

[121] Devoto RS: “Transport coefficients of ionized argon,” *The Physics of Fluids*, 1973, **16**(5):616-623. https://doi.org/10.1063/1.1694396

[122] Mos'cicki T, Hoffman J, Szyman'ski Z: “Emission coefficients of low temperature thermal iron plasma,” *Czechoslovak Journal of Physics*, 2004, **54**(3):C677. https://doi.org/10.1007/BF03166470

[123] Yachkov LGD, Kurilenkov YK, Vitel Y: “Radiative continua of noble gas plasmas,” *Journal of Quantitative Spectroscopy and Radiative Transfer*, 1998, **59**(1-2):53-64. https://doi.org/10.1016/S0022-4073(97)00136-2

[124] Chang JS, Hobson RM, Ichikawa S, Kaneda T: “Atomic and Molecular Processes of Ionized Gases,” Tokyo Denki University Press, 1995

[125] Hou S: “Ionized Gas Theory,” The Institute of Electrical Engineers of Japan, 1969

[126] Sugai H: “Plasma Electronics,” Ohmsha Ltd., 2000

[127] Hinnov E, Hirschberg JG: “Electron-Ion Recombination in Dense Plasmas,” *Physical Review*, 1962, **125**(3):795-801. https://doi.org/10.1103/PhysRev.125.795

[128] Aldrovandi SMV, Pequignot D: “Radiative and Dielectronic Recombination Coefficients for Complex Ions,” *Astronomy and Astrophysics*, 1973, **25**:137-140. https://articles.adsabs.harvard.edu/pdf/1973A%26A....25..137A

[129] Makishima K: “Cosmic plasma phenomena and long-range interactions,” *Butsuri*, 2008, **63**(8):595-603.

[130] Venugopalan M: “Reactions under plasma conditions Vol.1,” Wiley-Interscience, 1971

Appendix 1: Physical Properties of Gas

Assumption for calculating particle composition, thermodynamic, transport and radiation properties

Generally, the gas temperature in the arc is as high as 3,000 - 30,000 K. Characteristics of this high-temperature gas are influenced by many external conditions, such as gas pressure, gas type, current, and input power. The components are as follows.

1. Thermodynamic properties: mass density, enthalpy, specific heat at constant pressure.
2. Transport properties: electrical conductivity, thermal conductivity, viscosity.
3. Radiation properties: line spectrum, continuous spectrum (bremsstrahlung, recombination radiation).

When a hot gas is in thermal equilibrium, these properties are functions of temperature and pressure and are called equilibrium properties [101]. The definition of thermal equilibrium is shown below [101].

1. Particle energy has Maxwell-Boltzmann distribution.
2. Temperatures of each particle are equal to the plasma temperature (Heavy particles temperature (T_h) = Electron temperature (T_e)).
3. Boltzmann distribution for the excited state.
4. The particle number density is the reaction equilibrium composition.

In this calculation, the high-temperature gas was assumed to be in local thermal equilibrium, similar to the atmospheric pressure arc. The calculation temperature range was between 300 and 30,000 K, and the calculation was performed in increments of 100 K. A database of these data for each temperature is read by the electromagnetic thermofluid simulation. The physical property values of temperature during this period were calculated by linear interpolation.

Partition function and particle composition of high-temperature gas

Two statistical thermodynamic methods are used to calculate the particle composition in thermal equilibrium.

1. Gibbs free energy of the system can be obtained by minimizing the particle composition of this system.
2. By combining Saha's equations for ionization equilibrium of each particle based on the equation of state to obtain the particle density.

The above two methods are under the constraint of the equation of state satisfaction and they have equivalent relationships. To calculate the particle composition and the thermodynamic, transport, and radiation properties in such a thermal equilibrium state, it is necessary to obtain the partition function of each particle.

Partition function

The partition function is the sum of all Boltzmann factors ($\exp(-\varepsilon_i/(kT))$ which the partition function includes all the energy values ε_0, ε_1, $\varepsilon_2 \cdots$) when the velocity (energy) distribution function of each particle group can assume the Boltzmann distribution. Therefore, the partition function is also called the sum of states, and its general expression is as follows.

$$Q = \sum \exp\left(-\frac{\varepsilon_i}{kT}\right) \tag{36}$$

Note that this sum is over all states, not over possible energy values. When continuous states are involved, the discrete sum above is expressed as an integral over the continuous variable.

In the case of considering the energy ε_i of a molecule as an ideal gas. Molecular motion forms include translational motion, rotational motion, and vibrational motion. These kinetic energies are expressed as translational energy $\varepsilon_{\text{trans}}$, rotational energy ε_{rot}, and vibrational energy ε_{vib}, respectively. Along with the electron orbital energy ε_{ele}, the energy ε_i of a molecule can be expressed as the sum of these four energies as follows.

$$\varepsilon_i = \varepsilon_{\text{trans}} + \varepsilon_{\text{rot}} + \varepsilon_{\text{vib}} + \varepsilon_{\text{ele}} \tag{37}$$

The partition function can be obtained based on a molecule's energy ε_i. The partition function obtained here is called the internal partition function (sum of internal states) because it is represented by the sum of the states inside the molecule. As for Eq. 37, it can be redefined as the internal partition function Q_i as the accumulation of the translational partition function q_{trans}, the rotational partition function q_{rot}, the vibrational partition function q_{vib}, and the electronic partition function q_{ele} as shown follows [102][103].

$$Q_i = q_{\text{trans}} \cdot q_{\text{rot}} \cdot q_{\text{vib}} \cdot q_{\text{ele}} \tag{38}$$

For diatomic molecules such as N_2 and O_2 and polyatomic molecules such as CO_2 and SF_6, the internal partition function Q_i can be obtained from Eq. 39. In the case of mon-atoms such as

Ar, W, and Fe, there is no vibrational or rotational motion, so the internal partition function Q_i is the product of the translation and electronic partition function.

$$Q_i = q_{\text{trans}} \cdot q_{\text{ele}} \tag{39}$$

From here on, the calculation of the translational partition function q_{trans}, rotational partition function q_{rot}, vibrational partition function q_{vib}, and the electronic partition function q_{ele} that make up the internal partition function will be described. Spectroscopy database [70][104] is required for calculation.

(1) Translational partition function

The translation partition function q_{trans} can be expressed by the following equation.

$$q_{\text{trans}} = \left(\frac{2\pi mkT}{h_P^2}\right)^{\frac{3}{2}} V \tag{40}$$

where m is the mass, k is Boltzmann's constant, h_P is Planck's constant, and V is the volume of the system. The translational partition function depends on the mass m of a molecule, the temperature T of the system, and the volume V of the system. In this study, the volume $V = 1\,\text{m}^3$. Substituting $V = 1\,\text{m}^3$ into the formula (40) corresponds to the middle term on the right side of Saha's formula (50) described later.

(2) Rotation Partition Function

Rotation is a form of internal molecular motion found in diatomic and larger molecules. When a diatomic molecule is used as a rigid rotor, the rotational energy level can be expressed by the following equation.

$$\varepsilon_{\text{rot}} = \frac{h_P^2}{8\pi^2 I_M} J(J+1) \qquad J = 0, 1, 2 \cdots \tag{41}$$

where J is the rotational quantum number and the ground state (J=0) has zero rotational energy. I_M is the moment of inertia (sum of [mass of atom]×[distance from the center of mass to the center of the atom]^2). The rotational energy level is degenerate, and the statistical weight (=degeneracy) g_J for the quantum number J is $2J+1$. Therefore, the following equation gives the rotational partition function q_{rot} of the diatomic molecule considering the statistical weight.

$$q_{\text{rot}} = \sum_{J=0}^{\infty} (2J+1) \exp\left(\frac{-J(J+1)\theta_\gamma}{T}\right) \tag{42}$$

$$\theta_\gamma = \frac{h_P^2}{8\pi^2 I_M k} \tag{43}$$

where θ_γ has the dimension of temperature and is called the rotational characteristic temperature. The rotation characteristic temperature is larger for lighter molecules and smaller for

heavier molecules. The rotational partition function $q_{\rm rot}$ of a diatomic molecule can be obtained by the following simple formula at high temperature $T \gg \theta_\gamma (T/\theta_\gamma \gg 1)$ can be done.

$$q_{\rm rot} = \frac{T}{\sigma_{\rm rot}\theta_\gamma} \tag{44}$$

$\sigma_{\rm rot}$ is a symmetric number ($\sigma_{\rm rot}$=1 for heteronuclear diatomic molecules, $\sigma_{\rm rot}$=2 for isonuclear diatomic molecules) be. From a comparative study of this equation (42) and (44), the region of high temperature $T \gg \theta_\gamma$ is estimated to be about $T/\theta_\gamma \gg 100$.

(3) Oscillating partition function

The vibrational energy levels of a diatomic molecule as a harmonic oscillator are given by the following equation.

$$\varepsilon_{\rm vib} = \left(v_{\rm vib} + \frac{1}{2} \right) h_P \nu \tag{45}$$

where $v_{\rm vib}$ is the vibrational quantum number, 0, 1, 2, 3$\cdots$. $v_{\rm vib}$=0 is the ground state energy, $h\nu/2$. A vibrational partition function $q_{\rm vib}$ is given based on the vibrational energy levels.

$$q_{\rm vib} = \frac{1}{1 - e^{-\theta_\nu / T}} \tag{46}$$

$$\theta_\nu = \frac{h_P \nu}{k} \tag{47}$$

where θ_ν is the vibration characteristic temperature with the dimension of temperature. The vibrational characteristic temperature of molecules is about θ_ν=300$\sim$6,000 K, which is high for light molecules and low for heavy molecules. In this study, the vibration characteristic temperature is extended up to 30,000 K.

(4) Electron partition function

The electron partition function is the state sum due to the orbital motion of electrons. It is known that electrons are degenerate [102][103], and the electron partition function is expressed by the following equation.

$$\begin{aligned} q_{\rm ele} &= g_0 \exp\left(-\frac{\varepsilon_0}{kT}\right) + g_1 \exp\left(-\frac{\varepsilon_1}{kT}\right) + g_2 \exp\left(-\frac{\varepsilon_2}{kT}\right) + \cdots \\ &= \sum g_{ei} \exp\left(-\frac{E_{ei}}{kT}\right) \end{aligned} \tag{48}$$

g_{ei} is the statistical weight and E_{ei} is the electron level energy. Also, the partition function of the electron itself is only the ground state and is determined as follows.

$$q_{\rm e} = 2 \tag{49}$$

Particle composition in thermal equilibrium

Calculation method of particle composition

In this study, the particle composition was calculated using the method of solving each particle density by combining Saha's equation for ionization equilibrium under the equation of state. Specifically, by numerically solving the following nonlinear simultaneous equations consisting of Saha's equation (ionization equilibrium equation), gas equation of state, and charge neutrality conservation equation. The electron densities $n_{\mathrm{e}}\,[\mathrm{m}^{-3}]$ and the particle densities of neutral particles and ions at different temperatures were obtained. The solution method at that time was the Newton-Raphson method[105]. · Saha's equation

$$\frac{n_{i+1}n_{\mathrm{e}}}{n_i} = \frac{Q_{\mathrm{e}}Q_{i+1}}{Q_i}\left(\frac{2\pi m_{\mathrm{e}}kT}{h_P^2}\right)^{\frac{3}{2}}\exp\left(-\frac{E_{i+1}-\Delta E_{i+1}}{kT}\right) \tag{50}$$

· State equation of gas

$$P = \left(n_{\mathrm{e}} + \sum n_i\right)kT \tag{51}$$

· Charge neutrality conservation formula

$$n_{\mathrm{e}} = \sum (\mathrm{Z}-1)n_i \tag{52}$$

The decrease in ionization energy ΔE_{i+1} due to the Stark effect and the Debye length λ_D, which are included in Saha's equation, were calculated using the following equations.

$$\Delta E_{i+1} = \frac{(i+1)e^2}{\varepsilon_0\lambda_D} \tag{53}$$

$$\lambda_D = \left\{\frac{\varepsilon_0 kT}{4\pi e^2\left(n_{\mathrm{e}} + \sum_i (i+1)n_{i+1}^2\right)}\right\}^{\frac{1}{2}} \tag{54}$$

where m_{e} is the electron mass, h_P is the Planck constant, E_{i+1} is the ionization energy, and $E_{D_{ij}}$ is the dissociation energy. Note that i indicates the type of element. ΔE_{i+1} is the ionization energy correction term (J), e is the elementary charge, λ_D is the Debye length, and (i+1) is the ion valence. , (i+1)=1, 2 is monovalent and divalent ions, respectively, (i+1)=0 represent an atom.

In addition, Table 9 shows the ionization voltage [106] of the gas used in this simulation.

Calculation of particle composition

Figure 87 shows the particle composition of the gas used in this simulation.

Table 9 Ionization energy of the gases [106].

N_2	$\Longleftrightarrow$	N	+	N	:	9.76 eV
O_2	$\Longleftrightarrow$	O	+	O	:	5.12 eV
NO	$\Longleftrightarrow$	N	+	O	:	6.51 eV
N	$\Longleftrightarrow$	N^+	+	e^-	:	14.53 eV
O	$\Longleftrightarrow$	O^+	+	e^-	:	13.62 eV
N_2	$\Longleftrightarrow$	${N_2}^+$	+	e^-	:	15.58 eV
O_2	$\Longleftrightarrow$	${O_2}^+$	+	e^-	:	12.07 eV
NO	$\Longleftrightarrow$	NO^+	+	e^-	:	9.27 eV
Cu	$\Longleftrightarrow$	Cu^+	+	e^-	:	7.73 eV

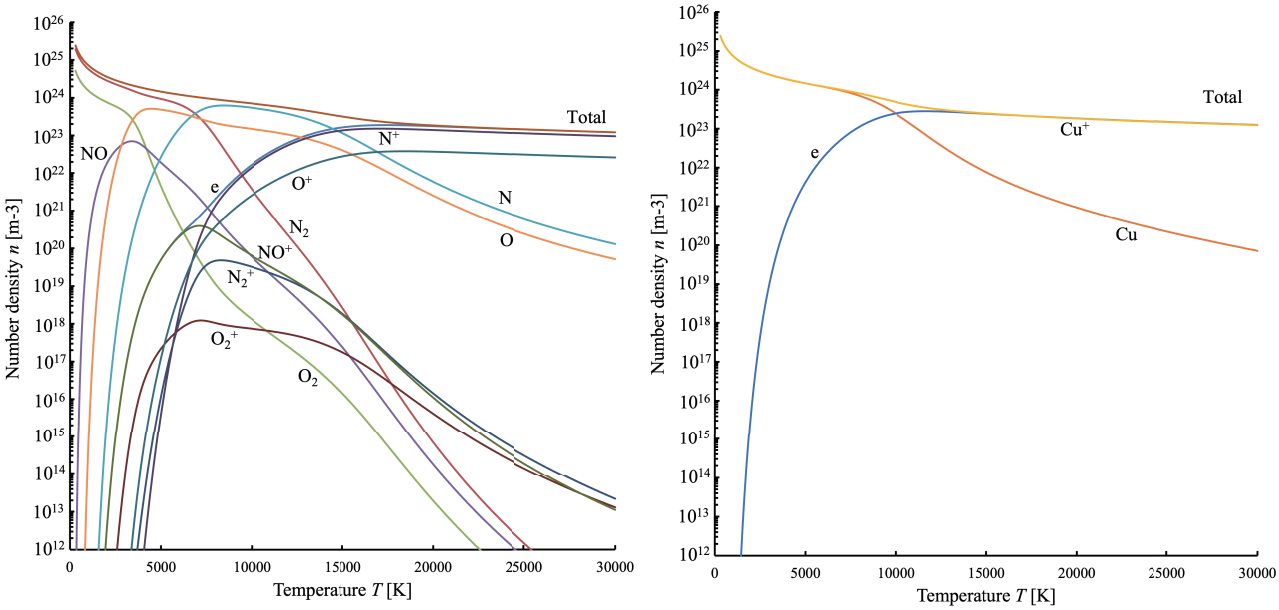

(a) Particle composition of Air

(b) Particle composition of Cu

Fig. 87 Particle composition of gases. (a) Air (b) Cu

Collision cross-section

In addition to the particle composition, the collision cross section is necessary to determine the transport properties of high-temperature gases. In a high-temperature gas, electrons, ions, molecules, atoms, etc. exist in a very wide temperature range of tens of thousands of Kelvin. Therefore, to determine the transport characteristics, in addition to the electron collision cross-section usually used for the analysis of low-pressure plasma, the collision cross-section between all these particles is necessary.

1. Collision cross-section between homogenous neutral particles
2. Homogeneous neutral particle-ion collision cross-section
3. Electron-neutral collision cross-section
4. Coulomb collision cross-section

Approximate calculation [107] by the Chapman-Enskog method is used to calculate the transport properties under thermal equilibrium. In this approximation, the collision cross section is treated in the form of a collision integral, which is called the effective collision cross-section. Therefore, it is necessary to obtain various collision cross sections based on the approximation of the Chapman-Enskog method.

Chapman-Enskog method

The following four assumptions are important in the Chapman-Enskog method.

1. Only bimolecular collisions
2. Molecular collisions should follow classical mechanics
3. Collisions must be elastic collisions
4. The intermolecular interaction potential function is spherically symmetric

The Chapman-Enskog theory considers the intermolecular interaction in detail, and the parameter expressing the effect is expressed by the collision cross section $\pi\overline{\Omega}_{ij}^{(l,s)}$. This accuracy is determined by the order (l, s) of the Sonine polynomial approximation, and the type of collision cross section required by this order also differs. The required collision cross sections for each order are summarized below.
First-order approximation: $\pi\overline{\Omega}_{ij}^{(1,1)}$, $\pi\overline{\Omega}_{ij}^{(2,2)}$
Second-order approximation: $\pi\overline{\Omega}_{ij}^{(1,1)}$, $\pi\overline{\Omega}_{ij}^{(1,2)}$, $\pi\overline{\Omega}_{ij}^{(1,3)}$, $\pi\overline{\Omega}_{ij}^{(2,2)}$
Third-order approximation: $\pi\overline{\Omega}_{ij}^{(1,1)}$, $\pi\overline{\Omega}_{ij}^{(1,2)}$, $\pi\overline{\Omega}_{ij}^{(1,3)}$, $\pi\overline{\Omega}_{ij}^{(1,4)}$, $\pi\overline{\Omega}_{ij}^{(1,5)}$, $\pi\overline{\Omega}_{ij}^{(2,2)}$, $\pi\overline{\Omega}_{ij}^{(2,3)}$, $\pi\overline{\Omega}_{ij}^{(2,4)}$
Here, when l=1, s=1 $\sim$ 5, the momentum transfer cross section is given and l=2, s=2 $\sim$ 4 gives the viscous cross section. In this study, the first-order approximation of the Chapman-Enskog method was adopted, which has the smallest number of collision cross-section calculations. Therefore, the required collision cross section is the momentum transfer cross section $\pi\overline{\Omega}_{ij}^{(1,1)}$ [m^2] and the viscous cross-section $\pi\overline{\Omega}_{ij}^{(2,2)}$ [m^2].

Collision cross-section between homogenous neutrals

The collision cross section between homogenous neutral atoms was calculated as follows. First, Mr. Abrahamson obtained the interaction potential between neutral atoms up to atomic number $2 \sim 105$ in the following Born-Mayer type[108].

$$U(R) = A \exp(-bR_{\mathrm{dis}}) \tag{55}$$

where A [J], b is $b \times 10^{-10}$ [m], R_{dis} is the internuclear distance and $R_{\mathrm{dis}} \times 10^{-10}$ [m]. Using these values of A and b, Mr. Monchick defines the parameters α and ρ for obtaining the collision cross section as follows.[109].

$$\alpha = \ln\left(\frac{A}{kT}\right) \tag{56}$$

$$\rho = \frac{1}{b} \tag{57}$$

where k is the Boltzmann constant and T is the absolute temperature. Monchick shows the value of the correction factor $I_{(l,s)}$ of the collision cross section for this α [109]. From $I_{(l,s)}$, obtain the momentum conversion cross section and the viscous cross section by the following formulas [109].

$$\sigma_R^2 \pi \overline{\Omega}_{ij}^{(l,s)} = \frac{8\pi\alpha^2\rho^2 I_{(l,s)}}{(s+1)!\left(1 - \frac{1}{2}\frac{1+(-1)^l}{1+l}\right)} \tag{58}$$

where σ_R is an arbitrary distance parameter defined by $U(R)$. In this study, σ_R=1 for all cases. In the case of l=1, s=1, given the momentum transfer cross section $\pi\overline{\Omega}_{ij}^{(1,1)}$, l=2, s= In the case of 2, it gives the viscous cross-section $\pi\overline{\Omega}_{ij}^{(2,2)}$.

Collision cross-section between heterogeneous neutrals

The momentum transfer cross sections $\pi\overline{\Omega}_{ij}^{(1,1)}$ and $\pi\overline{\Omega}_{ij}^{(2,2)}$ between heterogeneous neutrals are calculated as follows based on Empirical Combining Laws[110].

$$\pi\overline{\Omega}_{ij}^{(1,1)} = \frac{1}{2}\left(\pi\overline{\Omega}_{ii}^{(1,1)} + \pi\overline{\Omega}_{jj}^{(1,1)}\right) \tag{59}$$

$$\pi\overline{\Omega}_{ij}^{(2,2)} = \frac{1}{2}\left(\pi\overline{\Omega}_{ii}^{(2,2)} + \pi\overline{\Omega}_{jj}^{(2,2)}\right) \tag{60}$$

Collision cross-section between homogenous neutral particles-ions

(1) Homogeneous neutral particle-singly charged ion

The momentum transfer cross section $\pi\overline{\Omega}_{ij}^{(1,1)}$ between homogeneous neutral particles and monovalent ions was calculated by the following equation. First, the resonance charge exchange cross section is expressed in the following analytical form [111].

$$\sigma(v) = (K_2 - K_1 \ln v)^2 \tag{61}$$

where v represents the relative velocity. The effective cross-section between particles i and j was given by Gupta and Yos [112].

$$\pi\overline{\Omega}_{ij}^{(l,s)} = \frac{\int_0^\infty\int_0^\pi \exp(-v^2)v^{2s+3}(1-\cos^l x)4\pi\sigma_{ij}\sin x dx dv}{\int_0^\infty\int_0^\pi \exp(-v^2)v^{2s+3}(1-\cos^l x)\sin x dx dv} \tag{62}$$

$$v = \sqrt{\frac{m_i m_j}{2(m_i+m_j)kT}}\cdot g \tag{63}$$

here, $\sigma_{ij} = \sigma_{ij}(x,g)$ is the differential scattering cross-section between i-j particles, x is the scattering angle in the center-of-gravity system, g is the relative velocity of the colliding particle, and v is the reduced velocity. l=1, s=1 gives the momentum transfer cross section, and l=2, s=2 gives the viscous cross-section. Substituting the formula (62) into the formula (63) and integrating it analytically, the effective collision cross section is given by the following formula.

$$\pi\overline{\Omega}_{A-A^+}^{(1,1)} = (39.8K_1^2 - 17.8K_1K_2 + 2K_2^2) + (8.82K_1^2 - 2K_1K_2)\left[\ln\left(\frac{T}{M}\right)\right] + \frac{1}{2}K_1^2\left[\ln\left(\frac{T}{M}\right)\right]^2 \tag{64}$$

where M is the molecular weight and T is the absolute temperature. Regarding the constants K_1 and K_2, Rapp et al. gave a relationship diagram between the resonance charge exchange cross section $\sigma(v)$ and v with the ionization energy as a parameter. It was obtained by extrapolating to the figure. In other words, with v as a parameter, draw a relationship diagram between $\sigma(v)$ and ionization energy, and read the value of $\sigma(v)$ at the ionization energy of the target particle. The values of the constants K_1 and K_2 were obtained by converting to the relationship diagram of $\sigma(v)$ and v again. The viscous cross-section was assumed to be equal to the collision cross-section between neutral particles because there was no effect of charge exchange.

(2) Homogeneous neutral particles - doubly charged ions

Momentum transfer cross section $\pi\overline{\Omega}_{ij}^{(1,1)}$ between neutral particle and divalent ion, viscous cross-section $\pi\overline{\Omega}_{ij}^{(For2,2)}$. Since the temperature range in which the two coexist is small, they are assumed to be the same as those between neutral particles.

Collision cross-section between heterogeneous neutral particles - ions

The collision cross section between heterogeneous neutral particles and ions is a non-resonant charge exchange collision. Therefore, these collision cross sections were assumed to be equal to the collision cross sections between neutral particles.

Collision cross-section between electron - neutral particles

In the momentum transfer cross section $\pi\overline{\Omega}_{ij}^{(1,1)}$ between the electron and the Ar atom. It is necessary to consider the Ramsauer effect, in which the collision cross section becomes extremely small at electron energies around 1 eV. The collision cross-section of this case was extrapolated

from [113]. From [112], the momentum transfer cross section between electron and oxygen atom $\pi\overline{\Omega}_{ij}^{(1,1)}$ is treated as a constant hard-ball collision of $5.00\times10^{-20}\,\mathrm{m}^2$ at any temperature.

Coulomb collision cross-section

The electron - electron, electron - ion and ion - ion collision cross sections were obtained from the following equations regardless of the particle type.

$$\pi\overline{\Omega}_{ej}^{(l,s)}(T) = aQ_c(T) \tag{65}$$

$$Q_c(T) = \left(\frac{e^2}{kT}\right)^2 \ln\Lambda \quad (\mathrm{cm}^2) \tag{66}$$

$$\Lambda = \sqrt{\frac{9(kT)^3}{4\pi e^6 n_\mathrm{e}} + \frac{16(kT)^2}{e^4 n_\mathrm{e}^{\frac{2}{3}}}} \tag{67}$$

a is the correction coefficient, and $n_\mathrm{e}\,[\mathrm{m}^{-3}]$ is the electron density. Also here e=4.80×10^{-10} esu and $Q_c(T)\,\mathrm{cm}^2$ [112]. The collision cross section due to Coulomb scattering is for the case where the ions are stationary, and correction is required when the particles are in motion. Therefore, it is necessary to multiply the correction factor a for the relative velocity ratio of the particles. Correction coefficients are shown in table 10. M in the table represents the type of particles.

Table 10 Correction coefficient of Coulomb collision.

	e-e	e-M^+	e-M^{2+}	e-M^{3+}	M^+-M^+	M^+-M^{2+}	M^+-M^{3+}	M^{2+}-M^{2+}	M^{2+}-M^{3+}	M^{3+}-M^{3+}
$\pi\Omega_{i,j}^{(1,1)}$	0.800	0.800	2.700	0.708	0.800	2.700	0.708	12.80	28.04	62.65
$\pi\Omega_{i,j}^{(2,2)}$	0.750	0.750	2.100	6.650	0.300	0.840	6.650	4.800	26.25	58.73

Molecular collision cross-section

In the case of N_2, O_2 and Air, etc., the treatment of the collision cross section becomes more complicated because it is necessary to consider molecular collisions. Mr. Gupta has reported an approximate calculation method that handles this easily[112]. The approximation formula of momentum transformation cross-section $\pi\overline{\Omega}_{ij}^{(1,1)}$ and viscous cross-section $\pi\overline{\Omega}_{ij}^{(2,2)}$ were given by Gupta as follows.

$$\pi\overline{\Omega}_{ij}^{(1,1)} = \left[\exp\left(D_{\overline{\Omega}_{ij}^{(1,1)}}\right)\right] T^{\left[A_{\overline{\Omega}_{ij}^{(1,1)}}(\ln T)^2 + B_{\overline{\Omega}_{ij}^{(1,1)}}\ln T + C_{\overline{\Omega}_{ij}^{(1,1)}}\right]} \tag{68}$$

$$\pi\overline{\Omega}_{ij}^{(2,2)} = \left[\exp\left(D_{\overline{\Omega}_{ij}^{(2,2)}}\right)\right] T^{\left[A_{\overline{\Omega}_{ij}^{(2,2)}}(\ln T)^2 + B_{\overline{\Omega}_{ij}^{(2,2)}}\ln T + C_{\overline{\Omega}_{ij}^{(2,2)}}\right]} \tag{69}$$

where $A_{\overline{\Omega}_{ij}^{(1,1)}}$, $B_{\overline{\Omega}_{ij}^{(1,1)}}$, $C_{\overline{\Omega}_{ij}^{(1,1)}}$, $D_{\overline{\Omega}_{ij}^{(1,1)}}$, $A_{\overline{\Omega}_{ij}^{(2,2)}}$, $B_{\overline{\Omega}_{ij}^{(2,2)}}$, $C_{\overline{\Omega}_{ij}^{(2,2)}}$, $D_{\overline{\Omega}_{ij}^{(2,2)}}$ is a constant given by Mr. Gupta. In this study, the above equations were used to obtain the O_2 and O_2^+ related collision cross sections.

Thermodynamics and transport properties

Thermodynamic properties of high-temperature gases include mass density, enthalpy, and constant pressure-specific heat. The transport properties include electrical conductivity, thermal conductivity, and viscosity. These properties are calculated based on the following equations [59][110][114][115][116]. Figure 88 shows the thermodynamics and transport properties of the gas used in this simulation.

(1) Mass density

The mass density $\rho\,[\mathrm{kg/m^{-3}}]$ at a certain temperature $T\,[\mathrm{K}]$ is the particle density $n_i\,[\mathrm{m^{-3}}]$ and mass $m_i\,[\mathrm{kg}]$.

$$\rho = \sum_i m_i n_i \tag{70}$$

i represents the type of particle.

(2) Enthalpy

At constant pressure, heat applied to a substance is used to raise work and internal energy, and the sum of both is enthalpy. The enthalpy $h\,[\mathrm{J/kg}]$ is calculated from the internal partition function Q_i of the i seed particle and the standard enthalpy of formation $U_i\,[\mathrm{kJ/mol}]$ as follows.

$$h = \frac{1}{\rho}\sum_i h_i m_i n_i \tag{71}$$

$$h_i = \frac{1}{m_i}\left(\frac{5}{2}kT + kT^2\frac{\partial}{\partial T}(\ln Q_i) + U_i\right) \tag{72}$$

The standard enthalpy of formation is the heat of reaction when a compound is produced from constituent particles in the standard state (298 K, 0.1 MPa). As a reference, the enthalpy of a simple substance stable in the standard state is set to 0[106][117]. For example, the noble gases Ar and He can exist as monatoms in the standard state, so the standard enthalpy of formation U_i=0. For ions, the standard enthalpy of formation U_i corresponds to the ionization energy required from the reference state to an arbitrary excited state. These values are summarized in NIST - JANAF[118].

(3) Specific heat

Specific heat $C_p\,[\mathrm{J/(kg{\cdot}K)}]$ is the energy required to raise the temperature of a gas by 1 K per unit mass under constant pressure. Since it is obtained by differentiating the enthalpy under

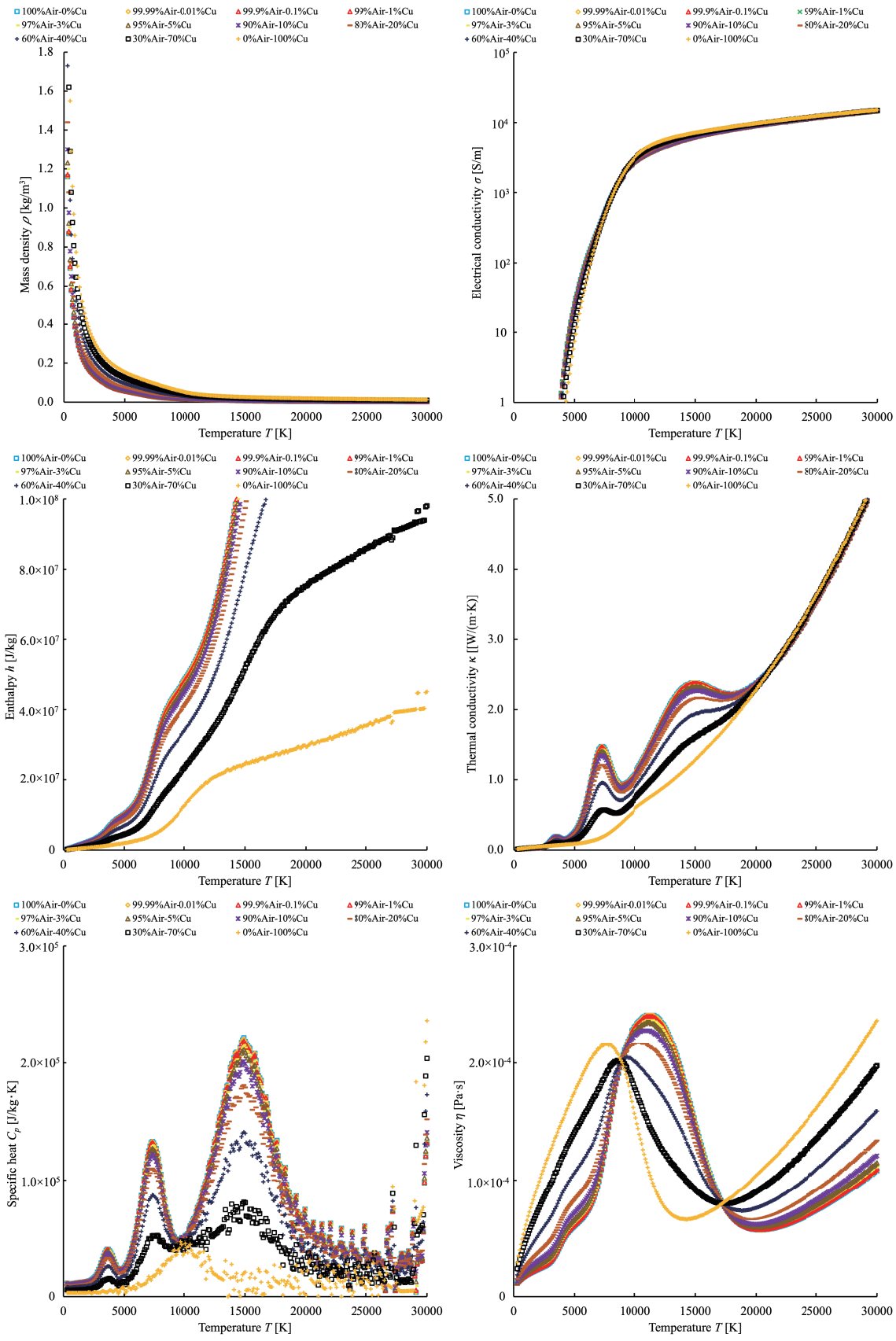

Fig. 88 Thermodynamics and transport properties of gas used in this study.

the same pressure concerning temperature, it shows a maximum value in the temperature range where dissociation/ionization reactions occur. In this calculation, the pressure was constant at 0.1 MPa, and the following equation was used.

$$C_p = \left.\frac{\partial h}{\partial T}\right|_{P=const} \tag{73}$$

(4) Electrical conductivity

- **Electrical conductivity**

Electrical conductivity is proportional to electron density, and when ionization occurs, electrons transport current and increase rapidly. The electrical conductivity $\sigma\,[\mathrm{S/m}]$ is given by the following equation.

$$\sigma = \frac{e^2}{kT}\frac{n_\mathrm{e}}{\sum_{\substack{j=1\\ j\neq \mathrm{e}}}^{N} n_j \Delta_{\mathrm{e}j}^{(1)}} \tag{74}$$

$$\Delta_{ij}^{(1)} = \frac{8}{3}\left(\frac{2m_i m_j}{\pi kT(m_i+m_j)}\right)^{\frac{1}{2}} \pi\overline{\Omega}_{ij}^{(1,1)} \tag{75}$$

e is the elementary charge, $\pi\overline{\Omega}_{ij}^{(1,1)}$ is the momentum transfer cross section between i - j seed particles.

- **Electrical conductivity of ion**

Ionic conductivity increases in proportion to ion density. The ionic conductivity $\sigma_i\,[\mathrm{S/m}]$ is given by the following equation.

$$\sigma_i = \frac{1}{kT}\sum_{\substack{i=1\\ i\neq \mathrm{e}}}^{N} \frac{{q_i}^2 n_i}{\sum_{j=1}^{N} n_j \Delta_{i,j}^{(1)}} \tag{76}$$

where $q_i\,[\mathrm{C}]$ is the charge of each particle, $n_i\,[\mathrm{m^{-3}}]$ is the ion number density, $n_j\,[\mathrm{m^{-3}}]$ is the number of colliding particles density.

(5) Thermal conductivity

The definition of thermal conductivity $\kappa\,[\mathrm{W/(m{\cdot}K)}]$ is the thermal energy passing through a unit area per unit time, that is, the physical quantity obtained by dividing the heat flux by the temperature gradient. If the heat flux is q and the temperature gradient is dT/dr, then the relationship between the thermal conductivity κ is given by the following equation.

$$q = -\kappa\frac{dT}{dr} \tag{77}$$

Heat transfer mechanisms in high-temperature gases include contact (translational) kinetic energy, internal energy, and reactions such as dissociation and ionization. Therefore, the thermal conductivity κ of high-temperature gas is calculated by the sum of these three.

$$\kappa = \kappa_{\mathrm{tr}} + \kappa_{\mathrm{int}} + \kappa_{\mathrm{re}} \tag{78}$$

where κ_{tr} is the contact thermal conductivity, κ_{int} is the internal thermal conductivity, and κ_{re} is the reaction thermal conductivity. In the case of monatoms, since there is no change in internal energy due to vibration or rotation, it can be obtained from the sum of the contact thermal conductivity and the reaction thermal conductivity.

(5-1) Contact thermal conductivity

$$\kappa_{\mathrm{tr}} = \kappa_{\mathrm{tr}}^{\mathrm{h}} + \kappa_{\mathrm{tr}}^{\mathrm{e}} \tag{79}$$

$$\kappa_{\mathrm{tr}}^{\mathrm{h}} = \frac{15}{4} k \sum_{i \neq \mathrm{e}}^{N} \frac{n_i}{\sum_{j}^{N} \alpha_{ij} n_j \Delta_{ij}^{(2)}} \tag{80}$$

$$\kappa_{\mathrm{tr}}^{\mathrm{e}} = \frac{15}{4} k \sum_{i = \mathrm{e}}^{N} \frac{n_{\mathrm{e}}}{\sum_{j}^{N} \alpha_{\mathrm{e}j} n_j \Delta_{\mathrm{e}j}^{(2)}} \tag{81}$$

$$\alpha_{ij} = 1 + \frac{\left(1 - \frac{m_i}{m_j}\right)\left(0.45 - 2.54\frac{m_i}{m_j}\right)}{\left(1 + \frac{m_i}{m_j}\right)^2} \tag{82}$$

$$\Delta_{ij}^{(2)} = \frac{16}{5}\left(\frac{2 m_i m_j}{\pi k T (m_i + m_j)}\right)^{\frac{1}{2}} \pi \overline{\Omega}_{ij}^{(2,2)} \tag{83}$$

(5-2) Internal thermal conductivity

$$\kappa_{\mathrm{int}} = k \sum_{i=1}^{N} \frac{\left(\frac{C_{pi} M_i}{R} - \frac{5}{2}\right) n_i}{\sum_{j=1}^{N} n_j \Delta_{ij}^{(1)}} \tag{84}$$

(5-3) Reaction thermal conductivity

$$\kappa_{\mathrm{re}} = k \sum_{l=1}^{N_{\mathrm{re}}} \frac{\left(\frac{\Delta H_l}{RT}\right)^2}{\sum_{i=1}^{N} \frac{\beta_{li}}{n_i} \left(\sum_{j=1}^{N} (\beta_{li} n_j - \beta_{lj} n_i) \Delta_{ij}^{(1)} \right)} \tag{85}$$

here, $\kappa_{\mathrm{tr}}^{\mathrm{e}}$ is the electron contact thermal conductivity, $\kappa_{\mathrm{tr}}^{\mathrm{h}}$ is the contact thermal conductivity of heavy particles, $\pi\overline{\Omega}_{ij}^{(2,2)}$ is the viscous cross section between i - j particles, C_{pi} [J/(kg·K)] is the constant pressure specific heat of the i particle, M_i is the molecular weight of i particle, R [J/(k·mol)] is the gas constant (=8.31 J/(k·mol)), N_{re} is the type of chemical reaction, β_{li} is the coefficient of the i particle in the lth chemical reaction, ΔH_l [J/mol] is the reaction energy per mol.

(6) Viscosity

Viscosity η [Pa·s] of high-temperature gas is obtained from the following equation.

$$\eta = \sum_{i=1}^{N} \frac{m_i n_i}{\sum_{j=1}^{N} n_j \Delta_{ij}^{(2)}} \tag{86}$$

Radiation coefficient of high-temperature gas

The radiation characteristics of thermal plasmas are determined by the behavior of electrons in high-temperature gas, and line spectra and continuous spectra are emitted. By performing these calculations, the radiation for the temperature and wavelength of the high-temperature gas can be obtained. At this time, the light emitted from the high-temperature part of the thermal plasma is again absorbed as energy by the low-temperature part of the plasma. This phenomenon is called self-absorption, and the calculation of the absorption coefficient is essential to take it into account. Particle composition and spectroscopic databases [70][104] are required to calculate the radiation coefficient. Figure 89 shows the radiation characteristics of the gas used in this simulation. The following section describes how to calculate the basic spectral emission coefficient.

Line spectra

The radiation characteristics of thermal plasmas are determined by the behavior of electrons in hot gases, and line spectra and continuous spectra are emitted. This is because electrons in atoms and ions, which are the constituent particles in the thermal plasma, acquire energy and are excited. There is a line spectrum generated by the de-excitation of the energy, and a

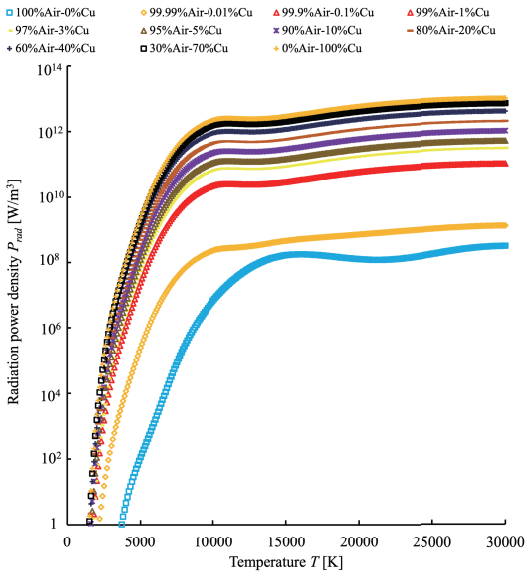

Fig. 89 Radiation power density of gas used in this study.

continuous spectrum generated by the Coulomb force generated between the free electrons in the gas and the ions. The following chapters describe line spectra and continuous spectra.

A line spectrum refers to a portion where the intensity of light near a certain wavelength is stronger or weaker than that of a continuous spectrum. Depending on the energy level of the atom or ion, each element has its electron configuration and emission spectrum. The energy states are given at discrete values determined by different quantum numbers. Spectral lines from atoms or ions are emitted at wavelengths specific to each element type as the electrons are changed (transitioned) by ionization or excitation. Also, by absorbing light, it transitions to a higher level. [59][119][120] which shows the theoretical formula of the radiation coefficient of the line spectrum.

$$\varepsilon_{\mathrm{rad}}^{\mathrm{line}} = \frac{n_i}{4\pi Q_i} \frac{h_P c}{\lambda_{mi}} g_{mi} A_{mni} \exp\left(-\frac{E_{mi}}{kT}\right) \tag{87}$$

where i represents the particle type, and $\varepsilon_{\mathrm{rad}}^{\mathrm{line}}$ [W/(m^3·sr)] is the line spectral radiation coefficient, n_i [m^{-3}] is the particle number density of i seed particles, Q_i is the partition function of i seed particles, h_P [J·s] is Planck's constant, c [m/s] is the speed of light, λ_{mi} [m] is the wavelength of the i seed particle, and g_{mi} is the statistical weight of m level (upper level) of i seed particle, E_{mi} [J] is the energy of m level of i seed particle, A_{mni} [s^{-1}] is the transition probability from the m level to the n level of the i seed particle (Einstein's A coefficient: spontaneous emission coefficient), λ_{mi} [m] is the wavelength of the i seed particle, k [J/K] is the Boltzmann constant, and T [K] is the temperature.

Continuous spectrum

Unlike line spectra, continuous spectra have a continuous intensity distribution over a wide wavelength range and are produced by two processes, recombination radiation, and bremsstrahlung. Ref. [69] shows the theoretical formula of each radiation coefficient below.

$$\varepsilon_{\mathrm{fb}} = \sum_i C_1 \frac{n_{\mathrm{e}} n_i}{\lambda^2 \sqrt{T}} {Z_{\mathrm{eff},i}}^2 \left[1 - \exp\left(-\frac{h_P c}{\lambda k T}\right)\right] \frac{g_{i,1}}{Q_i} \xi_{\mathrm{fb}}(\lambda, T, i) \Delta\lambda \tag{88}$$

$$\varepsilon_{\mathrm{ff}}^{ei} = \sum_i C_1 \frac{n_{\mathrm{e}} n_i}{\lambda^2 \sqrt{T_{\mathrm{e}}}} {Z_{\mathrm{eff},i}}^2 \exp\left(-\frac{h_P c}{\lambda k T_{\mathrm{e}}}\right) \xi_{\mathrm{ff}}(\lambda, T_{\mathrm{e}}, i) \Delta\lambda \tag{89}$$

$$\varepsilon_{\mathrm{ff}}^{ea} = C_2 \frac{n_{\mathrm{e}} n_a}{\lambda^2} \sqrt{T^3} S(T_{\mathrm{e}}) \left[\left(1 + \frac{h_P c}{\lambda k T_{\mathrm{e}}}\right)^2 + 1\right] \exp\left(-\frac{h_P c}{\lambda k T_{\mathrm{e}}}\right) \Delta\lambda \tag{90}$$

$$C_1 = \frac{1}{(4\pi\varepsilon_0)^3} \frac{16\pi e^6}{3c^2 \left(6\pi {m_{\mathrm{e}}}^3 k\right)^{\frac{1}{2}}} = 1.63 \times 10^{-43}\ \mathrm{Wm^4K^{\frac{1}{2}}/sr} \tag{91}$$

$$C_2 = \frac{1}{(4\pi\varepsilon_0)} \frac{32e^6}{3c^2} \left(\frac{k}{2\pi m_{\mathrm{e}}}\right)^{\frac{3}{2}} = 1.026 \times 10^{-34}\ \mathrm{Wm^4K^{\frac{3}{2}}/sr} \tag{92}$$

where $\varepsilon_{\mathrm{fb}}$ [W/(m^3·sr)] is the radiation coefficient of recombination radiation, $\varepsilon_{\mathrm{ff}}^{ei}$ [W/(m^3·sr)] is the electron - ion bremsstrahlung radiation coefficient, $\varepsilon_{\mathrm{ff}}^{ea}$ [W/(m^3·sr)] is the electron - atom bremsstrahlung radiation coefficient, C_1 is the electron - ion continuity constant, and C_2 is the electron - atom is a continuous constant of atomic density, n_e [m^{-3}] is electron density, n_i [m^{-3}] is the ion density of i species, λ [m] is the wavelength, and $Z_{\mathrm{eff},i}$ is $The effective charge number of the i$ seed particle, $S(T_{\mathrm{e}})$ [m^2] is the electron-neutral collision cross section [121], $\Delta\ lambda$ [m] is the wavelength step size, $g_{i,1}$ is the ground state weight of the i seed particle, $\xi_{\mathrm{fb}}(\lambda, T_{\mathrm{e}}, i)$ is the Biberman factor($=\xi_{\mathrm{ff}}(\lambda, T_{\mathrm{e}}, i)$)[122][123].

From this equation, the continuous spectrum is determined mainly by the product of electron density and ion density and statistical weights. Also, the Biberman factor becomes smaller in the ultraviolet and infrared regions [122][123].

Recombination radiation

Recombination radiation is the phenomenon by which charged particles recombine in space and return to their original atoms or ions. Free electrons are slowed down by the Coulomb force generated between them, and the electron velocity becomes zero when they recombine with the ions. When an ion is captured at a certain level, it releases excess energy and radiates the kinetic energy and excitation energy (de-excitation energy) at this time.

$$h_P \nu = E_k + eV_i \tag{93}$$

where ν [Hz] is the frequency, E_k [J] is the kinetic energy of the free electron, and eV_i [eV] is the excitation energy of the i particle.

In a high-temperature gas such as thermal plasma, particle collisions between ions and electrons are depending on the recombination mechanism, there are radiative recombination, two-electron recombination, three-body recombination, dissociative recombination, and charge exchange recombination.

Radiative recombination occurs when a free electron is trapped to a level in an ion. This is the reverse process of photoionization, in which the energy difference between before and after capture (the kinetic energy and ionization energy of electrons) is emitted as photons. Since the kinetic energy of captured free electrons has a continuous value, the wavelength of the emission line is also continuous.

Two-electron recombination once goes through a double exciting state in which two outer core electrons are simultaneously excited. Furthermore, some of them emit photons and become normal excitation or the ground state, which is the reverse process of auto-excitation. This occurs at high electron temperatures because the special case of double excitation does not occur unless the free electrons possess high energy.

Three-body recombination is the reverse process of electron impact ionization and is the same as radiative recombination in that free electrons are captured by ions. It does not emit a photon because the excess energy is received by another nearby electron or particle. The reaction formula is shown below[124].

(1) Recombination

$$\mathrm{A}^+ + e^- \rightarrow \mathrm{A} + h\nu \tag{94}$$

(2) Two-electron recombination

$$\mathrm{A}^+ + e^- \rightarrow \mathrm{A}'' \rightarrow \mathrm{A}^+ + e^- \tag{95}$$

$$\mathrm{A}^+ + e^- \rightarrow \mathrm{A}'' \rightarrow \mathrm{A}' + h\nu \tag{96}$$

(3) Three-body recombination

$$\mathrm{A}^+ + e^- + \mathrm{X} \rightarrow \mathrm{A} + \mathrm{X} \tag{97}$$

Recombination radiation in this paper assumes radiative recombination. However, comparing these three types of recombination, radiative recombination is generally thought to be less likely [125]. Therefore, let us consider the thermal motion of gas molecules that causes these phenomena.

- Maxwell distribution

Among n gas molecules, the number of particles with velocity from v to $v + dv$ is assuming dn pieces, this ratio is a function of velocity magnitude v and is expressed by the following formula.

$$\frac{dn}{n} = f_{\mathrm{M}}(v)dv \tag{98}$$

$f_{\mathrm{M}}(v)$ is [126] generally expressed by the following equation.

$$f_{\mathrm{M}}(v) = 4\pi \left(\frac{m}{2\pi k_{\mathrm{B}} T}\right)^{3/2} v^2 \exp\left(-\frac{mv^2}{2k_{\mathrm{B}} T}\right) \tag{99}$$

here, m [kg] is mass, k_{B} [J/K] is Boltzmann's constant, and T [K] is temperature.

This function f_{M} is the Maxwellian distribution, which is used as a function representing the particle velocity distribution and the particle energy distribution in a particle system in thermal equilibrium. Maxwell distribution can uniquely describe velocity distribution and energy distribution by defining the average temperature or average energy of the system. Expressing this f_{M} as a function of the energy ε, and transform $f_{\mathrm{M}}(v)dv$ from $\varepsilon = (1/2)mv^2$ and $dv = (1/(mv))d\varepsilon$ as following.

$$f_{\mathrm{M}}(\varepsilon) = \frac{2}{\sqrt{\pi}} \left(\frac{1}{k_{\mathrm{B}} T}\right)^{3/2} \sqrt{\varepsilon} \exp\left(-\frac{\varepsilon}{k_{\mathrm{B}} T}\right) \tag{100}$$

The electron energy distribution was calculated using the (99) formula. For reactions such as ionization to occur, electrons must have energy above a certain threshold. As the electron temperature T_{e} [K] increases, the proportion of low-energy electrons decreases, and the proportion of high-energy electrons increases. Focusing on 15000 K, the average is about 3 eV, and there are almost no electrons with an Ar ionization energy of 15.76 eV and a He ionization energy of 24.59 eV. Therefore, there are overwhelmingly many particles that are not ionized, and the $0 \sim 3$ eV side has a large effect on recombination.

- Recombination velocity coefficient

At this time, the susceptibility of these recombination events is determined by the recombination rate coefficient α_{ei} [cm^3/s], which expresses the degree of recombination in unit volume per unit time. The calculation formulas for the recombination rate coefficients for three-body recombination, radiative recombination, and two-electron recombination are shown below.

$$\alpha_{3B} \approx 5.6 \times 10^{-27} k T^{-\frac{9}{2}} N_e \tag{101}$$

$$\alpha_{rad} = 4.3 \times 10^{-13} \left(\frac{T_e}{10^4}\right)^{-0.672} \tag{102}$$

$$\alpha_{di} = 1.9 \times 10^{-3} T_e^{-\frac{3}{2}} \exp\left(-T_0/T_e\right) \times \left(1 + B_{di} \exp\left(-T_1/T_e\right)\right) \tag{103}$$

Here, α_{3B} [cm^3/s] is the recombination rate constant for three-body recombination [127], α_{rad} [cm^3/s] is the recombination rate coefficient of radiative recombination [128], α_{di} [cm^3/s] is the recombination rate coefficient for two-electron recombination[128], T_e [K] is electron temperature.

Considering three-body recombination, radiative recombination, and two-electron recombination, three-body recombination tends to occur at low temperatures below 0.7 eV. Two-electron recombination is dominant in the high-temperature region above 6 eV, but radiative recombination tends to occur in the arc region of $0.7 \sim 6$ eV. Since neither He nor Ar has excited levels at low energies, the recombination rate coefficient of Ar can be considered to be similar to that

of He. Therefore, radiative recombination should be considered in this temperature range, and recombination radiation is quite possible. At this time, the pressure like a high-pressure lamp is not taken into account, but in this study, which aims to clarify the physics, the pressure is assumed to be constant at 0.1 MPa. Based on the above, radiative recombination is dominant in this temperature range, so the radiation characteristics are calculated with recombination radiation taken into account.

Bremsstrahlung

Bremsstrahlung is generated when free electrons passing near ions are accelerated by the Coulomb force and their trajectories are bent. This is the process of transitioning to a lower-energy-free electronic state. Since free electrons alone cannot absorb (or supply) the energy and momentum of photons at the same time, ions take on the excess and deficiency of momentum. The energy values are stochastically distributed widely from zero to electron energy, forming a continuous spectrum [129]. When the electron's initial velocity is small, or when the electron passes very close to the ion's scattering center, the electron is bent significantly from its original trajectory. In such cases, high-energy photons are emitted. If the initial velocity of the electrons is high or the collision diameter is large, the trajectories of the electrons will be straight without deviating from their straight trajectories. Photons with very little energy emitted in such small angle scattering are emitted.

Figure 90 shows the transition process for the continuous spectrum. (1) and (2) in the figure are bremsstrahlung and inverse bremsstrahlung, (3) and (4) are radiative recombination and photoionization; (5) and (6) are spontaneous emission and photoexcitation, (7) and (8) are three-body recombination and electron collision excitation; (9) and (10) are collisional deexcitation and collisional excitation. Processes (7) and (11) occur simultaneously, and deexcitation in (12) is double electron recombination. Auto-excitation is the excitation in (14) and the simultaneous occurrence of processes (8) and (13). Radiation-related processes are shown with dashed lines, and collisional processes are shown with solid lines. All radiation processes have stimulated radiation · absorption processes.

Of the phenomena taken into account in the calculation of the continuous spectrum, the following are the phenomena (Gaunt factor, Biberman factor) that require special attention.

Continuous spectral phenomena

- **Gaunt factor**

The Gaunt factor is a quantum theoretical correction term that corrects the dependence on the electron orbital quantum number. $G_z(\nu, T_e)$ is called the Gaunt factor, which is written by the classical theory as follows [130].

$$G_z(\nu, T_e) = \int_{x_0}^{\infty} \exp(-x) \cdot g_z(u_0)\, dx \tag{104}$$

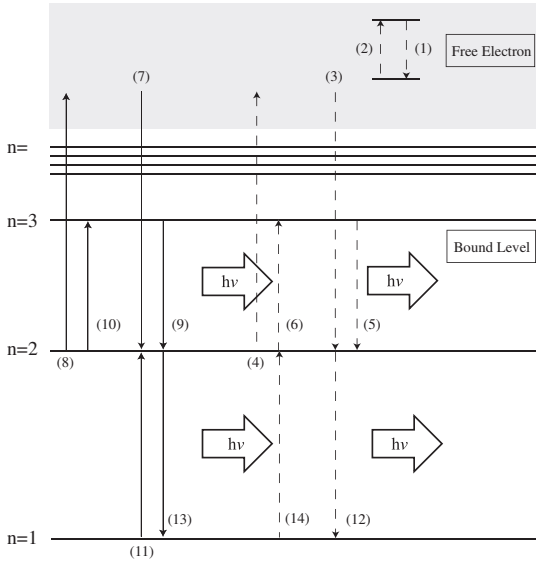

Fig. 90 Transition process.

where $x = mv^2/2kT_e$, $x_0 = h\nu/kT_e$, $u_0 = 2\pi\nu p_0/v$. Note that the collision coefficient ($p_0 = ze^2/mv^2$) corresponds to the deviation from 90°. $g_z(u_0)$ is expressed as a factor of u_0. At high frequency ($h\nu/kT_e \gg 1$), $g_z(u_0) \cong 1$ and $G_z(\nu, T_e) = \exp(-h\nu/kT_e)$, (88), (89), (90) formulas hold, and in the formula becomes 1.

- **Biberman factor**

The Biberman factor (hereafter referred to as the ξ factor) is the parameter that determines the shape of the continuous spectrum peculiar to the arc. The ξ factors are sometimes treated like constants, but strictly speaking, they are functions of wavelength and temperature. This ξ factor was calculated by Biberman and Norman of Russia in 1960 in the process of calculating the photoionization cross section of an atom. It was first introduced as the ratio of hydrogen to the photoionization cross-section.

Based on the fact that the quantum deviation decreases rapidly with increasing quantum numbers, Biberman-Norman proposed to divide the entire system of complex atomic energy levels into two groups. Group A contains levels with large quantum deviations, while Group B consists of levels with practically zero quantum deviations. The photo-isolation cross section for the Group B levels is equal to that for the corresponding levels of hydrogen. Therefore, it was derived that the correction for the difference between the photoionization cross section per atom and the cross-section of a hydrogen atom should be performed for the Group A levels. From this result, Biberman-Norman defined the ξ factor as a correction factor for the classical radiation theory. It was later applied in a slightly different way by Schlüter to a simple representation of the continuous spectra of non-hydrogen-like atoms. To date, much research has been carried out, mainly on noble gases. However, the ξ factor has an error of

$20 \sim 30\,\%$, which is different for each researcher. Also, the same element has different values depending on the valence [122]. In this paper, we extrapolate the calculation results by Mr. L.G.D'Yachkov[123], he has $\xi_{\mathrm{fb}}(\lambda, T_{\mathrm{e}}, i) = \xi_{\mathrm{ff}}(\lambda, T_{\mathrm{e}}, i)$).

Appendix 2: Physical Properties of Electrode

Fig. 91 shows the mass density, enthalpy, specific heat, electrical conductivity, and thermal conductivity of the copper electrode which used in this study. The interval values of these physical properties were calculated using a linear approximation based on the temperature variation.

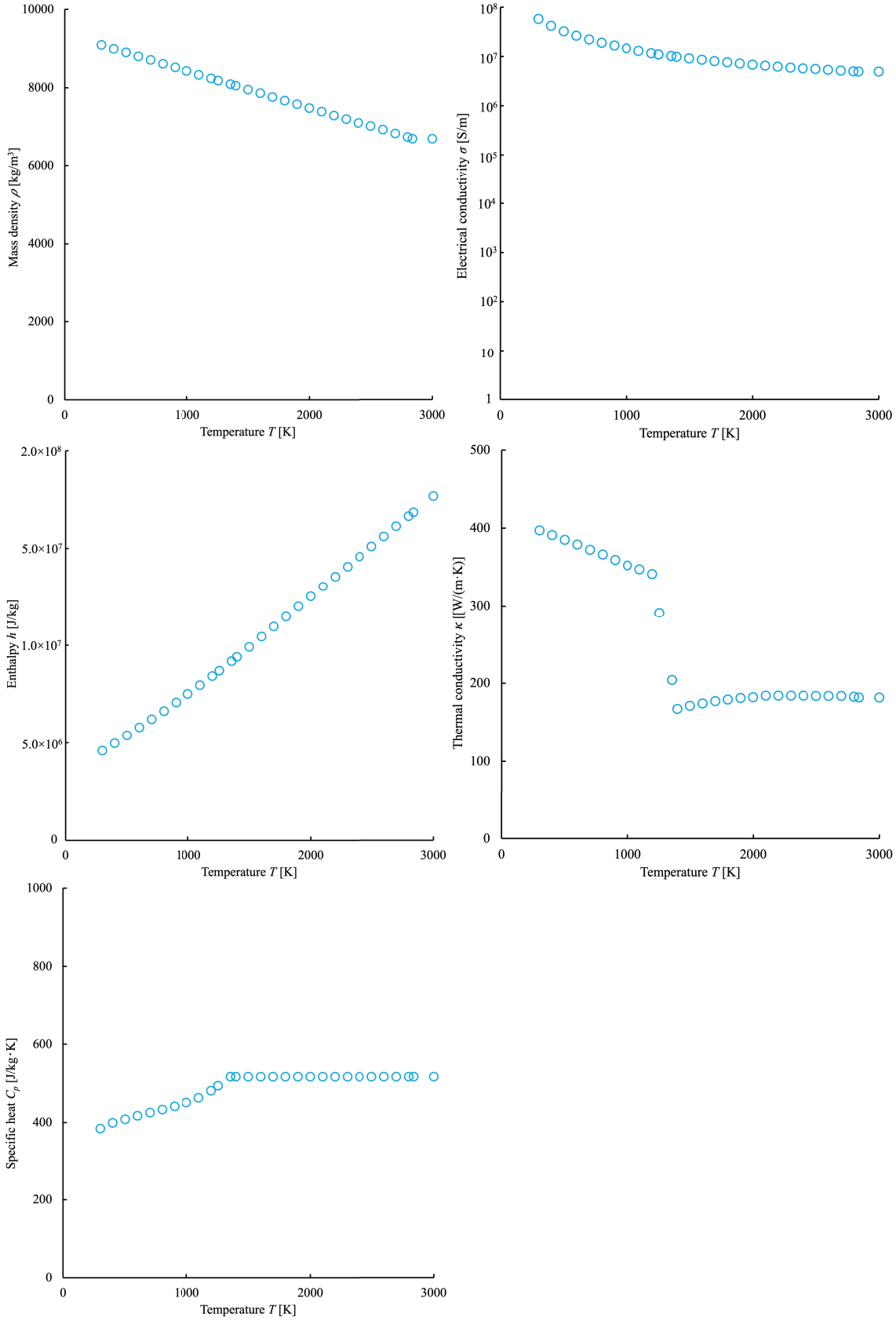

Fig. 91 Thermodynamics and transport properties of copper electrode used in this study.

Appendix 3: Method of Coupled Analysis of Velocity Field and Pressure Field

The SIMPLE (Semi-Implicit Method for Pressure-Linked Equations) method, which is one of the numerical analysis methods, is widely used in atmospheric pressure-free arc calculations. This paper uses SIMPLER (Semi-Implicit Method for Pressure-Linked Equations Revised), an improved version of the SIMPLE method. The advantages of the SIMPLER method are fast convergence, light computational load, and excellent stability. If the flow field is known, a general differential equation can be formulated concerning the dependent variable ϕ. However, it is generally impossible to define the flow field first. Therefore, the SIMPLER method performs iterative calculations and finally obtains the true velocity field. The velocity field is governed by the momentum conservation equation, which corresponds to one case of the general differential equation for ϕ. Therefore, we can solve the momentum conservation equation and thereby obtain the velocity field. The specific calculation method is to give the estimated value of the velocity field, solve the momentum conservation equation by iterative calculation, and obtain the velocity component.

Figure 92 shows the SIMPLER method algorithm. The description of the SIMPLER method used in past three-dimensional simulations of vacuum arcs resolved the coefficient a of the discretization equation when solving the algorithm's momentum conservation laws of 1 and 3. However, the values change as the flow velocities in the directions of x, y, and z are solved in order. Therefore, this value is used to calculate the coefficient of the discretization equation in the next direction, so the value of the coefficient changes.

However, there is a problem that the solution diverges because the velocity field that satisfies the law of conservation of mass cannot be calculated. In addition, the two-dimensional cylindrical coordinate system program, which was the mainstream in our laboratory in the past, uses the calculated coefficient in 1 in the algorithm to solve the momentum conservation law in 3, but the array of physical quantities is shared. Therefore, when the array of a certain variable is calculated, the values of the two variables change, making it difficult to follow the change of the coefficient, and the program becomes unclear to others.

In this study, in the three-dimensional Cartesian coordinate system, the coefficient value used in 1 in the algorithm was used to perform the calculation of 3. In addition, shared arrays were abolished and new settings were made to define the coefficients of separate discretization equations. Figure 93 shows an improved program description for the SIMPLER method that does not use shared arrays.

As in [2] of Figure 93, substitute the coefficient a_{pu} obtained in 1 into another coefficient a'_{pu}. Then, when solving the momentum conservation law of 3, the discretization equation of the

momentum conservation law is obtained by substituting a'_{pu} for a_{pu}. By these measures, the solution does not diverge, and the law of conservation of mass and law of momentum can be calculated.

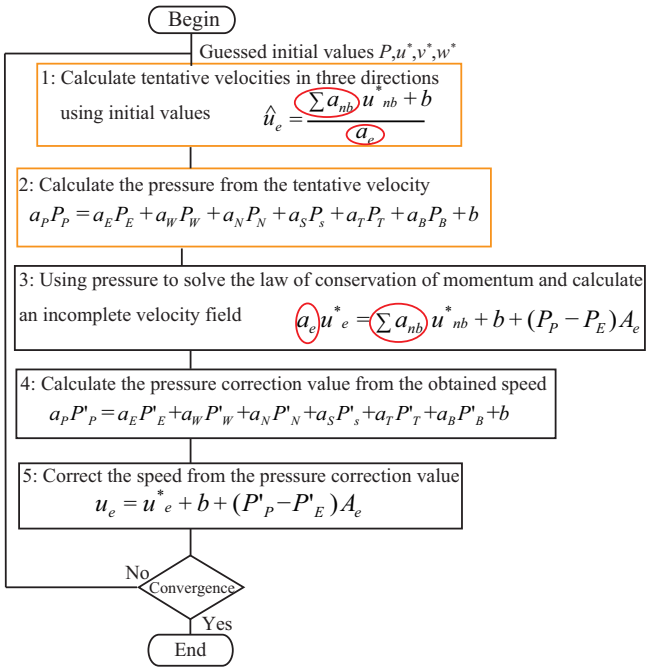

Fig. 92 Algorithm of semi-implicit method for pressure-linked equations revised.

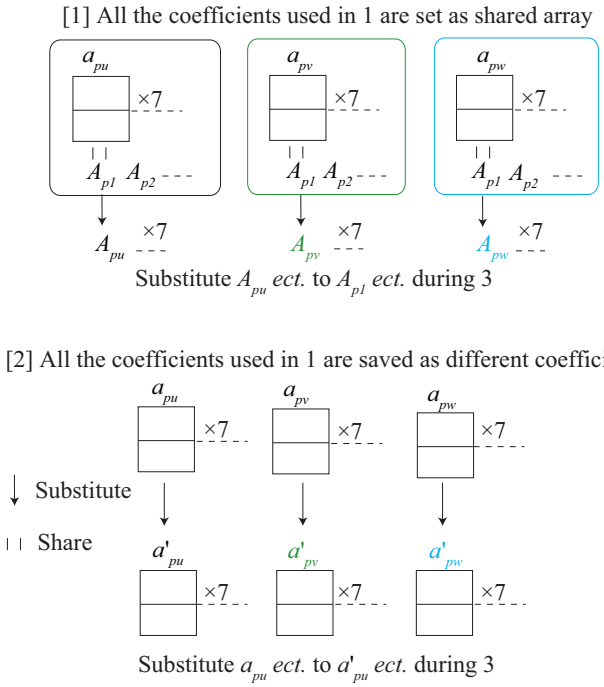

Fig. 93 Improvement plan of semi-implicit method for pressure-linked equations revised.

Publication, presentation, and award list

Publication paper (with review)

(1) Zhenwei Ren, Yusuke Nemoto, Yuki Suzuki, Masahiro Takagi, Honoka Morishita, Reggie Cobarrubia Gustilo and Toru Iwao: "Differentiation of Numerical Simulation Result of Direct Current Circuit Breaker Interruption Process Using Artificial Intelligence", *IEEJ Transactions on Electrical and Electronic Engineering*, Vol.18, No.1, pp.147-149 (2023)

(2) Honoka Morishita, Yoshifumi Maeda, Zhenwei Ren, Yusuke Nemoto, Takamasa Hayasaka, Toru Iwao: "Development of calculation method for melting amount mass of contact wire caused by melting and evaporation of molten metal bridge and arc generation", *Electrical Engineering in Japan*, Vol.215, No.3, pp.???-??? (2022)

(3) Takamasa Hayasaka, Honoka Morishita, Zhenwei Ren and Toru Iwao: "Size of Molten Metal Bridge Conducting DC Current in Different Contact Strip Materials", *IEEJ Transactions on Electrical and Electronic Engineering*, Vol.17, No.7, pp.1083-1084 (2022)

(4) Zhenwei Ren, Yusuke Nemoto, Yoshifumi Maeda, Shinji Yamamoto, Gaku Asanuma, Toshiyuki Onchi and Toru Iwao: "Analyzing Cathode and Anode Spot Movement of Atmospheric Arc Plasma in Parallel Electrode Using Thermal-field Theory and Thermal Non-equilibrium Model", *IEEJ Transactions on Electrical and Electronic Engineering*, Vol.17, No.6, pp.934-944 (2022)

(5) 森下穂香・真栄田義史・任振威・根本雄介・早坂高雅・岩尾徹：「溶融ブリッジの溶融蒸発とアークの発弧が及ぼすトロリ線の溶融量算出手法の開発」，電気学会論文誌D（産業応用部門誌），Vol.142，No.5，pp.401-407（2022）

(6) 根本雄介・鈴木祐揮・任振威・真栄田義史・岩尾徹：「リストライク現象の解明に向けた横風吹き付け時のアークの電子と重粒子温度分布の解析」，電気学会論文誌B（電力・エネルギー部門誌），Vol.142，No.4，pp.228-234（2022）

(7) Zhenwei Ren, Yusuke Nemoto, Yuki Suzuki and Toru Iwao: "Numerical Simulation for Analyzing Re-strike Phenomenon of Arc Plasma Considering Application of Recovery Voltage at Direct Current Circuit Breaker", *IEEJ Transactions on Electrical and Electronic Engineering*, Vol.17, No.4, pp.611-613 (2022)

(8) Zhenwei Ren, Yusuke Nemoto, Yuki Suzuki and Toru Iwao: "Numerical Simulation of External Magnetic Field Effect on Arc Plasma After Molten Metal Bridge Breaking under Different Electrode Opening Velocities", *AIP Advances*, **035239** (2022)

(9) Zhenwei Ren, Yusuke Nemoto, Yuki Suzuki, Shinji Yamamoto, Gaku Asanuma, Toshiyuki Onchi and Toru Iwao: "Analysis of Adverse Influence of Metal Vapor to Arc Movement Between Electrodes with External Magnetic Field Applied by Numerical Simulation", *IEEJ Transactions on Electrical and Electronic Engineering*, Vol.17, No.2, pp.183-193 (2022)

(10) Zhenwei Ren, Yusuke Nemoto, Yoshifumi Maeda, Shinji Yamamoto, Gaku Asanuma, Toshiyuki Onchi and Toru Iwao: "Cathode Spot Velocity of Atmospheric Arc Plasma after Arc Ignition Affected by Self and External Electromagnetic Force between Parallel Electrodes Using 3D Numerical Simulation", *IEEJ Transactions on Electrical and Electronic Engineering*, Vol.16, No.12, pp.1656-1663 (2021)

(11) Zhenwei Ren, Shota Kokubo, Yoshifumi Maeda, Shinji Yamamoto and Toru Iwao: "Three-Dimensional Electromagnetic Thermal Fluid Simulation of Re-strike Phenomenon in Magnetic Driven Arc between Parallel Electrodes with Edges", *IEEJ Transactions on Electrical and Electronic Engineering*, Vol.15, No.5, pp.789-795 (2020)

Publication paper (without review)

(1) 岩尾徹・任振威・根本雄介・鈴木祐揮・高木真宏・森下穂香：「超高温プラズマに関する 3 次元電磁熱流体シミュレーション技術」，エレクトロヒート，Vol.239，pp.562-569（2021）

Presentation of academic conference

(1) Honoka Morishita, Asuka Kawasaki, Masahiro Takagi, Yuki Suzuki, Zhenwei Ren, Yusuke Nemoto, Takamasa Hayasaka and Toru Iwao: "Calculation of Temperature Distribution of Electrodes Surface Affected by Stagnation Time of Disconnection Arc", 放電・プラズマ・パルスパワー/静止器/開閉保護合同研究会, EPP-22-075 SA-22-042 SP-22-010 (July, 2022)

(2) 任振威:「あらゆる先進技術で次世代製品の物作り方法」，超異分野学会東京大会 2022，P-109（March, 2022）

(3) Zhenwei Ren, Yusuke Nemoto, Yuki Suzuki, Shinji Yamamoto, Gaku Asanuma, Toshiyuki Onchi and Toru Iwao: "Numerical Simulation for Analysis Electron and Heavy Particle Temperature Variation before Re-strike Occurrence in Parallel Electrode", *The 74th Annual Gaseous Electronics Conference*, TF14.00008 (October, 2021)

(4) Zhenwei Ren, Yusuke Nemoto, Yuki Suzuki and Toru Iwao: "Analysis of Arc Voltage Increment Rate with Applying External Magnetic Field in Different Electrode Opening Velocities", 令和 3 年 電気学会 基礎・材料・共通部門大会, 3-D-p1-3 (September, 2021)

(5) Zhenwei Ren, Yusuke Nemoto, Yuki Suzuki and Toru Iwao: "Numerical Simulation for Analyzing Current Density Variation of Arc Plasma with Different Applying Timing of Recovery Voltage at DCCB", 令和 3 年 電気学会 電力エネルギー部門大会, 308 (August, 2021)

(6) Zhenwei Ren, Yusuke Nemoto, Yuki Suzuki and Toru Iwao: "Analysis of Arc Reignition Phenomenon of DCCB with Applied Recovery Voltage after Arc Extinguishment by Numerical Simulation", 放電・プラズマ・パルスパワー/静止器/開閉保護合同研究会, ED-21-072 SA-21-041 SP-21-013 (July, 2021)

(7) Zhenwei Ren, Yusuke Nemoto, Yoshifumi Maeda and Toru Iwao: "Electrical Conductivity for First Step of Cathode Spot Movement after Molten Metal Bridge Stage Using Numeral Simulation", 令和 3 年 電気学会 全国大会, 1-087 (March, 2021)

(8) Zhenwei Ren, Yusuke Nemoto, Yoshifumi Maeda, Shinji Yamamoto, Gaku Asanuma, Toshiyuki Onchi and Toru Iwao: "Cathode Spot Velocity after Arc Ignition Affected by Self and External Electromagnetic Force Between Parallel Electrodes Using 3D Numerical Simulation", 放電/開閉保護/高電圧合同 (IWHV2020), EPP-20-100 SP-20-42 HV-20-86 (November, 2020)

(9) Zhenwei Ren, Yusuke Nemoto, Yoshifumi Maeda and Toru Iwao: "Analysis of Driven Factor of Cathode Spot Initial Movement in Parallel Electrodes by Numerical Simulation", *The 73rd Annual Gaseous Electronics Conference*, GEC20-2020-000146 (October, 2020)

(10) Zhenwei Ren, Honoka Morishita, Yusuke Nemoto, Yoshifumi Maeda and Toru Iwao: "Numerical Simulation for Analyzing Re-strike Phenomenon Occurrence Conditions in Magnetic Driven Arc", 令和 2 年 電気学会 電力エネルギー部門大会, 54 (September, 2020)

(11) Zhenwei Ren, Yusuke Nemoto, Yoshifumi Maeda and Toru Iwao: "Analysis of Arc Stagnation Phenomenon Caused by Metal Vapor from Electrodes Surface Using Numeral Simulation", 令和 2 年 電気学会 基礎・材料・共通部門大会, 3-B-a1-1 (September, 2020)

(12) Zhenwei Ren, Yusuke Nemoto, Yoshifumi Maeda and Toru Iwao: "Analysis of Dielectric Strength of Re-strike Phenomenon in Magnetic Driven Arc with External Magnetic Field by Numerical Simulation", *The 72nd Annual Gaseous Electronics Conference*, GEC19-2019-000071 (October, 2019)

(13) REN, Zhen Wei；KOKUBO, Shota；NEMOTO, Yusuke；MAEDA, Yoshifumi and IWAO, Toru: "Analysis of Magnetic Driven Arc Movement Affected by Metal Vapor Using 3-Dimensional Electromagnetic Thermal Fluid Simulation", *The International Council on Electrical Engineering (ICEE) Conference* 2019, ICEE19J-163 (July, 2019)

(14) Zhenwei Ren, Shota Kokubo, Yoshifumi Maeda, Shinji Yamamoto and Toru Iwao: "3-Dimensional Electromagnetic Thermal Fluid Simulation of Re-strike Phenomenon in Magnetic Driven Arc Between Parallel Electrodes with Edges", 放電/開閉保護/高電圧合同 (IWHV2018), ED-18-076 SP-18-028 HV-18-110 (November, 2018)

(15) Shinji Yamamoto, Shiko Kaneda, Arisa Takahashi, Yoshifumi Maeda, Zhenwei Ren and Toru Iwao: "Vacuum Arc Cathode Spot Movement Affected by Electromagnetic Repulsion Force", 放電/静止器/開閉保護合同研究会, ED-18-057 SA-18-040 SP-18-009 (June, 2018)

Award

(1) 任 振威；YOC 奨励賞, 電気学会, (2021 年 9 月)；Zhenwei Ren, Yusuke Nemoto, Yuki Suzuki and Toru Iwao: "Numerical Simulation for Analyzing Current Density Variation of Arc Plasma with Different Applying Timing of Recovery Voltage at DCCB", 令和 3 年 電気学会 電力エネルギー部門大会, 308 (August, 2021)

(2) 任 振威；開閉保護研究発表賞, 電気学会, (2021 年 3 月)；Zhenwei Ren, Yusuke Nemoto, Yoshifumi Maeda, Shinji Yamamoto, Gaku Asanuma, Toshiyuki Onchi and Toru Iwao: "Cathode Spot Velocity after Arc Ignition Affected by Self and External Electromagnetic Force Between Parallel Electrodes Using 3D Numerical Simulation", 放電/開閉保護/高電圧合同 (IWHV2020), EPP-20-100 SP-20-42 HV-20-86 (November, 2020)

(3) 任 振威；YOC 奨励賞, 電気学会, (2020 年 9 月)；Zhenwei Ren, Honoka Morishita, Yusuke Nemoto, Yoshifumi Maeda and Toru Iwao: "Numerical Simulation for Analyzing Re-strike Phenomenon Occurrence Conditions in Magnetic Driven Arc", 令和 2 年 電気学会 電力エネルギー部門大会, 54 (September, 2020)

(4) Ren Zhenwei；電気学会優秀論文発表賞, 電気学会, (2019 年 3 月)；Zhenwei Ren, Shota Kokubo, Yoshifumi Maeda, Shinji Yamamoto and Toru Iwao: "3-Dimensional Electromagnetic Thermal Fluid Simulation of Re-strike Phenomenon in Magnetic Driven Arc Between Parallel Electrodes with Edges", 放電/開閉保護/高電圧合同 (IWHV2018), ED-18-076 SP-18-028 HV-18-110 (November, 2018)